Magnetic fabrics from sheeted dikes reveal regional magma flow patterns, and the spacing and dimensions of ophiolite magma-chambers, Troodos ophiolite, Cyprus.

by
David Gauthier

Submitted in partial fulfillment of the requirements for the degree of

Master of Science

July 31, 2002

Supervisor: Dr. G.J. Borradaile

Geology Dept.
Lakehead University
Thunder Bay, ON P7B 5E1

Your file Votre référence
ISBN: 0-612-83407-7
Our file Notre référence
ISBN: 0-612-83407-7

ABSTRACT

Orientation-distributions of crystals were determined for 1289 specimens of the Sheeted Dike Complex of the Troodos ophiolite, located on the island of Cyprus. These were inferred from anisotropy of magnetic susceptibility (AMS). From these data the dispersion of magmatic flow fabrics with a mild tectonic overprint were recognized.

The study area (~400km^2) is located to the east of Mt. Olympus, and adjacent to a fossil transform fault (STTFZ) that was responsible for shearing of dikes and a change in their orientation from predominantly north-south to east-west as the fault is approached.

The predominantly magmatic AMS fabrics blend a flow-aligned paramagnetic component from mafic silicates with a ferromagnetic component from titanomagnetites. The inclination of magma-flow axes varies from near vertical to near horizontal throughout the area with predominantly steep magma flow regions separated from regions with predominantly shallow magma-flow. Fast Fourier Transform (FFT) analysis of steep-flow region spacing shows that the magma chambers that fed the dikes were *point-source* with minimal along-axis extent, and very short lived. FFT wavelength calculations suggest that they may have been spaced approximately every 4km along the ridge, and every 100,000 to 250,000 years in time. These results imply localized magma chambers, thereby supporting the slow-spreading origin of the Troodos crust, and refine models for slow-spreading ridge processes to include a point-source magma delivery system between magma reservoirs and the sheeted dike complex.

ACKNOWLEDGEMENTS

This research was financially supported by NSERC grants to Graham Borradaile. Fieldwork was possible with the encouragement and support of the Geological Survey of Cyprus, its Director Dr. George Petrides and his Liaison Officer Dr. Ioannis Panayides.

Special thanks to: Dr. Borradaile, Anne Hammond, Sam Spivak, France Lagroix, the good people of Askas and Palechori, Steve and Patty, Mike and Lorrie, and of course RB.

TABLE OF CONTENTS

TABLE OF FIGURES

1. Purpose

There has been much discussion in the past regarding the style of magmatism at oceanic spreading centres. Dilek et al. (1998) reviewed the current information on the subject, including comparisons between modern ocean crust and ophiolite sequences. They also considered the different mechanisms thought to control magmatism at both fast and slow-spreading ridges. Fast-spreading ridges are those with *full*-spreading rates of 9-18 cm/year, and slow-spreading ridges are those that spread at 1-5 cm/year (Moores & Twiss, 1995, p.104). Fast-spreading ridges are thought to be fed by an axial magma chamber that is continuous along the ridge, which causes vertical magma flow within the sheeted dike complex at all points along the ridge. The current model for slow-spreading ridges shows isolated non-continuous axial magma chambers to feed the sheeted dikes and axial volcanics (Dilek et al., 1998; Varga et al., 1998). Figure 1-1 shows how a sheeted dike complex fed by this mechanism would show a variation in flow directions, from vertical above a chamber, to near horizontal in peripheral areas.

The oceanic crust that makes up the Troodos ophiolite complex on the island of Cyprus is inferred to have formed at a slow spreading ridge. Evidence comes mainly from structural data that documents tectonic extension without associated magmatism or volcanism along the spreading axes, which implies that the ridge was intermittently magma-starved (Dilek et al., 1998). This feature of the spreading style of Troodos agrees with the slow-spreading ridge model described above, where segments of the ridge are not underlain by an axial magma chamber and accommodate spreading by means of brittle extension. Further evidence comes from geochemical studies which indicate that

all of the sheeted dikes of Troodos are not of the same provenance, implying that they had more than one penecontemperaneous source.

Many previous studies have used anisotropy of magnetic susceptibility (AMS) fabrics to study magma flow in granitic rocks, and rocks of volcanic origin (see Varga et al. (1998) for a literature review). Generally, it has been shown that the orientation of the axis of maximum susceptibility, k_{max}, is closely related to magmatic flow direction, and the plane containing k_{max} and k_{int} (magnetic foliation) is related to the flow plane. In this study, magmatic flow fabrics will be determined for sheeted dikes of the Troodos ophiolite to attempt to constrain the location of the axial magma chamber that was feeding them. The pattern of spatial variation in magma flow directions, and the conclusions drawn from it will either support or contradict many features of ocean crust generation models, and refine them to include details of the size, stability, and frequency of mid-ocean ridge magma chambers. An understanding of magma transport at ocean ridges has far reaching implications for both the geophysics and geochemistry of oceanic crust, and global tectonic processes.

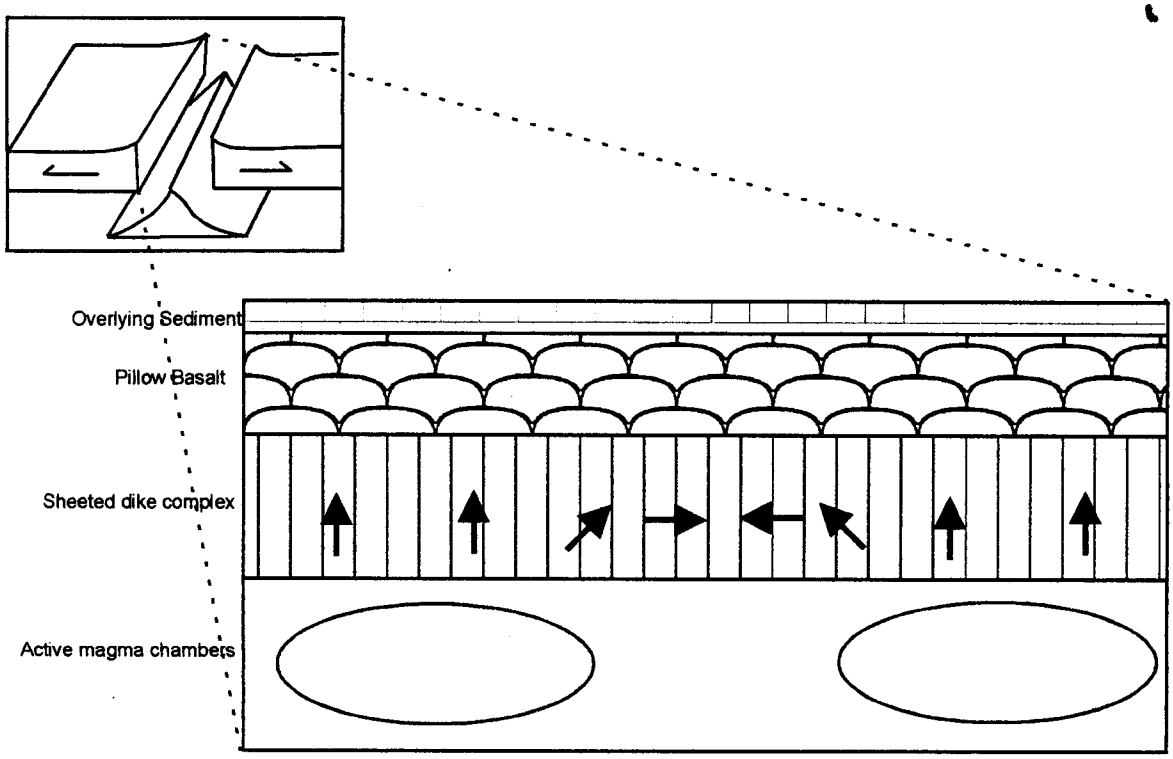

Figure 1-1. Schematic diagram illustrating slow-spreading ridge magma chamber model, with expected flow directions (bold arrows) in sheeted dike complex.

2. Geology of Cyprus

This chapter is intended to describe the regional geology of Cyprus, and establish the idea that the Troodos ophiolite terrane represents obducted oceanic crust and can therefore be used as an analogue for modern oceanic crust.

2.1. Terranes

The island of Cyprus is composed of four major geological regions: the Mamonia, Kyrenia, and Troodos tectonic terranes, and the weakly tectonized Circum-Troodos Sedimentary Succession (CTSS) (Figure 2-1). Of these four, the Troodos terrane has received the most interest from geologists, and is most pertinent to this study.

The Kyrenia terrane makes up the northernmost ranges of the island (Figure 2-1), and is a structurally complex assemblage of Late Paleozoic to recent sedimentary and minor metamorphic rocks (Robertson, 1990). The major tectonic terrane of southwestern Cyprus is the Mamonia complex (Figure 2-1). There are two broad groups of Mamonia rocks: 1) The Dhiarizos Group, made up of Triassic-age pillow lavas and intrusives, overlain by Triassic-Cretaceous sediments 2) The Ayios Photios Group, a sedimentary sequence of red mudstones and cherts. The Ayios Photios Group overlies the Dhiarizos Group (Swarbick, 1993). The Circum-Troodos Sedimentary Succession surrounds the Troodos Massif, with the exception of the northwestern most corner of the island (Figure 2-1). Numerous groups and formations have been identified, most of which represent deposition on the sea-floor above the amalgamated terranes during uplift to their present level. Excluding rare allochtonous umbers, the sedimentary facies of the succession vary from pelagic limestones and chalks, to sandstone and mudstone (Swarbick and

Robertson, 1980). The CTSS lies conformably atop rocks of the Troodos Terranes, and seals the tectonic contacts between Troodos and Mamonia, and Troodos and Kyrenia.

2.2. Troodos Ophiolite

The Troodos Massif conforms nearly perfectly to the definition of an 'ophiolite' as set out by the Geological Society of America's Penrose Field Conference in 1972, which defined the term as a distinctive sequence of rocks occurring in the following order:

Table 2-1. Ideal ophiolite stratigraphy, as described by the Penrose Conference (1972)

Stratigraphic Position	**Rock Type**
top of sequence	- chert, shale, and limestone
	- pillowed mafic volcanic complex
	- sheeted dyke complex
	- gabbroic complex (cumulus textures) containing pyroxenites and peridotites and less deformed than the ultramafic rocks
base of sequence	- ultramafic complex (harzburgite, lherzolite, dunite) with a metamorphic tectonite fabric

They also noted in their definition that "an ophiolite may be incomplete, dismembered, or metamorphosed", and went on to declare that "use of the term should be independent of its supposed origin", although the latter would no longer be disputed.

Gass (1968) and Moores and Vine (1971) were the first to propose that the Troodos complex represents oceanic crust formed at a mid-ocean ridge. They noted that the 'layer-cake' stratigraphy observed in the Troodos igneous sequences matched the layer cake model oceanic crust determined with geophysics in the ocean basins (Figure 2-2).

Vine and Matthew's (1963) sea-floor spreading models allowed them to link the Troodos 'stratigraphy' directly to an oceanic spreading centre.

As acceptance of this idea spread, each unit in the Troodos sequence could be associated with a specific feature of the mid-ocean ridge model. The ultramafic complex was shown to represent the uppermost mantle, with tectonized harzburgites thought to be refractory (Greenbaum, 1972), and the dunite bodies considered as frozen mantle diapirs (Allen, 1975). The mafic complex was assumed to represent the solidified magma reservoirs that fed the SDC and extrusives, with high level plagiogranites crystallizing from the residual liquids after fractionation of the reservoir magmas. Oceanic spreading centres became the only known geological environment capable of generating sheeted dike complex (Gass, 1968), as well as a thick, laterally extensive, overlying pillowed basalt sequence.

Miyashiro (1973) disagreed with the mid-ocean ridge formation of Troodos, arguing on the basis of geochemical data that the extrusive sequence was erupted *above* a subduction zone. Major-element geochemistry of the lavas indicated a crustal component in the melt, and therefore an island-arc setting was proposed. Most researchers argued that some type of fore-arc spreading could account for both the indisputable evidence for sea-floor spreading and supra-subduction zone associations found in Troodos rocks.

It is now well documented and accepted that the Troodos ophiolite was formed as oceanic crust, most probably at a supra-subduction zone spreading centre. Nomenclature of many of the igneous units has become genetic: the ultra-mafic complex is now commonly referred to as the 'Mantle sequence', while the mafic sequence, SDC, and extrusive sequence are known as the 'Crustal sequence'. These sequences are separated by a

'petrological moho', at a similar crustal level to the geophysical 'Mohorvicic (moho) discontinuity' observed in present day oceanic crust.

2.2.1. Ultramafic/Mantle Complex

Ultramafic rocks of the Troodos ophiolite are exposed at the very centre and highest elevations of the ophiolite massif (approximately 10% of Troodos exposure) (Figure 2-3). Tectonized harzburgite makes up 85% of the complex, with the remainder being mostly lherzolite and dunite. All are variably serpentinized. Harzburgite is generally medium to coarse-grained, composed of 70-85% olivine and 15-20% orthopyroxene, with accessory chrome spinel and clinopyroxene. Dunite 'intrusions' with sharp igneous contacts appear sporadically throughout the harzburgite unit. They are >98% olivine, with accessory chrome spinel.

There exists a penetrative tectonic foliation throughout the complex, manifested by a preferred orientation in orthopyroxene and spinel grains in harzburgite. Metamorphic segregation of the harzburgite into 0.5-5cm thick olivine-rich and orthopyroxene rich bands is commonly observed. Metamorphism and deformation apparently occurred at approximately 1000°C. The tectonic fabric passes uninterrupted between the harzburgite and dunite bodies.

2.2.2. Mafic Complex

The mafic complex, lying structurally above the ultra-mafic complex, but outcropping in a concentric ring around it (approximately 15% of exposure) (Figure 2-3), has been divided into a lower 'Layered Series' and and upper 'Non-Layered Series'.

2.2.2.1. Layered Series

Layered mafic rocks form a unit from 500m to >2km thick directly above the ultra-mafic complex. The lowest layered rocks are wehrlite, followed up section by dunite, gabbro-norite and gabbro. Rythmic igneous layering is generally 0.5-2cm thick (locally thicker), and flat lying at depth. Up section the layering steepens to near vertical at the contact with the non-layered series. Cumulus phases are generally olivine or clinopyroxene, while plagioclase is rare. Plagioclase, hornblende, orthopyroxene, and titanomagnetite make up the intercumulus phases. Cryptic variation in mineral compositions indicates that there was repeated influx of fresh magma into a fractionating magma chamber. This explains also the presence of the layering.

2.2.2.2. Non-Layered Series

Generally only 500 to 700m thick, non-layered mafic rocks lie above the layered series. Igneous textures are variable throughout the series, however layering is never present. Rock type is generally massive to brecciated amphibole-gabbro with minor plagiogranite intrusions. At the base of the non-layered series there may be a more noritic gabbro, which is transitional into the layered series.

2.2.3. Sheeted Dike Complex (SDC)

The majority of the outcrop area (>50%) of the Troodos terrane is of the Sheeted Dike Complex (SDC) (Figure 2-3). It is approximately 1-1.5km thick and composed entirely of steeply dipping 30cm-1m wide diabase dikes. At its top and bottom the SDC is transitional into adjacent units, with gabbro screens mixed with dikes at the contact with the mafic complex below, and a thick 'Basal Group (BG)' of 50% dikes and 50% lava screens marking the transition into the extrusive sequence above. A detailed description of the petrology and structure of the SDC is given in chapter 3.

2.2.4. Extrusive Sequence

The Extrusive Sequence volcanic rocks ring the periphery (~10% of exposure) of the Troodos ophiolite (Figure 2-3). It is made up of predominantly pillowed basalts, rarely mixed with deep sea chemical sediments at the upper levels. Flows generally have shallow dips, and are overlain by the Circum Troodos Sedimentary Succession. Two suites of chemically distinct flows have been identified: the Upper pillow lavas (UPL) or depleted suite, and the Lower pillow lavas (LPL) or the non-depleted suite (Robinson et al., 1983). The terms 'depleted' and 'non-depleted' were used by Robinson et al. (1983) to describe the state of the mantle source of the volcanic units, where a depleted mantle source may have already generated a batch of basaltic magma. Most of the volcanic sequence has suffered the effects of low-temperature alteration, and is the host of Cyprus-type volcanogenic massive sulfide deposits. These deposits are formed by chemical deposition of material exhaled by black-smoker vents along a mid-ocean ridge.

2.2.5. Southern Troodos Transform Fault Zone (STTFZ)

2.2.5.1. Arakapas Fault Belt (AFB)

The Arakapas Fault Belt (AFB) is marked by a 35km east-west oriented valley at the south of the Troodos terrane (Figure 2-4). Lava flows and volcanoclastic sediments from erosion of fault scarps are common within the belt. The basement rock is brecciated dikes of the SDC, with large rotated fault blocks and horst and graben structures common.

2.2.5.2. Western Limassol Forest Complex (WLFC)

The western areas of the Limassol Forest Complex (Figure 2-4) are mainly serpentized harzburgite, surrounded by mafic plutonic rocks similar to those described

above from Troodos proper. There is an east-west structural fabric (Murton, 1986) manifest by ductile shear zones and serpentinized mélange zones, both related to block rotations along the AFB. Ophiolitic fragments (ie. sheeted dikes with no pillows or gabbros in contact) are also present, with tectonised ultramafic, mafic plutonic, and dike/volcanic rocks cropping out around the main serpentized areas.

2.2.5.3. Eastern Limassol Forest Complex

Tectonically disrupted ophiolite fragments make up much of the Eastern Limassol Forest Complex (ELFC) (Figure 2-4), with rare tectonized harzburgites. The same east-west trending serpentized melange zones seen in the WLFC are found here, as are minor volumes of volcanic rocks and fault-scarp sediments in areas adjacent to the AFB.

In 1971, Moores and Vine first proposed that the Arakapas fault belt (AFB) was a fossil transform fault. Simonian and Gass (1978) speculated that the AFB was only the northern margin of a wider fault zone, now termed the Southern Troodos Transform Fault Zone (STTFZ). They noted also that the generally ridge-parallel, north-south strikes of dikes in the sheeted dike complex of Troodos underwent a gradual swing to the west into alignment with the AFB as they approached it. Two mechanisms were proposed to explain the swing in dike orientations, a dextral shear model and a primary intrusion into a sigmoidal stress field model. In the first model dextral motion along the transform was proposed, causing horizontal drag of the dikes along the fault. The second model involved intrusion of the dikes into the sigmoidal stress field of a sinistrally slipping transform, the dikes acting as maximum stress trajectories opening parallel to relative tension. Considerable discussion followed, with some authors supporting the sigmoidal

intrusion mechanism (e.g., Dilek et al., 1990) and others supporting the fault-drag model (e.g., Bonnhommet et al., 1988; MacLeod et al., 1990; Morris et al., 1990). MacLeod and Murton (1995) compiled the evidence related to the sense of slip of the STTFZ, and concluded that the majority of evidence from the STTFZ is for dextral motion, which is now generally accepted. Their conclusions were based on paleomagnetic, structural, and kinematic data. MacLeod and Murton (1995) explained the rare but documented sinistral kinematic indicators of the Limassol Forest Complex by considering fault blocks (small size relative to the shear zone) within the STTFZ. These blocks were rotated clockwise with response to dextral shear along the transform, and set up local small-scale sinistral slip along block boundaries.

2.2.6. Spreading Structure

Following the establishment of the idea that Troodos was formed at an oceanic spreading centre, many researchers began attempting to document the features of sea-floor spreading, using Troodos as an analogue for mid-ocean processes. Early investigations into the SDC found that the complex could be divided into domains based on areas that contain dikes of similar orientation (Versoub and Moores, 1981). They also noted major extensional detachment faults at the base of the SDC, indicating that the upper part of the crust was decoupled from the lower crust during formation. The similarity of dip within dike domains, but differences between domains, was attributed to tilting by listric normal faults, which were thought to coallesce at depth into the detachment surfaces. This showed that extensional faulting plays a role in crustal growth at ocean ridges. Varga and Moores (1985) also noted dike domains, but also found three graben (west to east: Solea, Mitsero, and Larnaca; see Fig. 3-4), with dikes on either side

dipping towards the axis. These grabens were considered to represent fossil ridge-axis valleys, related by ridge-jumping during their formation. Citing evidence for extensive amagmatic spreading around the graben structures, they proposed that the Troodos crust was formed at a slow-spreading ridge.

The first coherent model (and after minor refinements the currently accepted model) to describe the spreading history of Troodos, proposed by Allerton and Vine (1987, 1991), is summarized in the following sequence of events:

1) Magmatic spreading at the Solea axis, with minor normal faulting, related to crustal loading and adjustment (Figure 2-5(A))

2) Magma supply to Solea axis stops, with extension continuing amagmatically through faulting. The Solea graben and Kakopetria detachment form due to extensional faulting at ridge

3) A 'ridge-jump' occurs to the Larnaca axis, which forms a new magmatic spreading ridge (Figure 2-5(B))

4) Off axis extension on the flanks of the Larnaca ridge creates the Mitsero graben (Figure 2-5(C))

This sequence of events was thought to occur at a fast to intermediate spreading ridge, due to what Allerton and Vine (1991) interpret as dike domains throughout the SDC that are neither deformed, rotated, nor faulted. This was an indication that magma supply was only periodically interrupted, and therefore amagmatic extension was only a minor feature of Troodos construction. Off-axis graben formation in the Solea area was supported by subsequent studies (e.g. Hurst et al., 1992). Van Everdingen and Cawood (1995) refined this model following detailed investigations of the dike domain structure

in the Mitsero area. Their model suggests that the Mitsero axis does represent a fossil ridge, with the formation of the graben off axis following an eastward ridge jump. They also proposed a ridge jump to the east for the anti-Troodos crust (ophiolite fragments of the Limassol Forest complexes), requiring that the STTFZ did not have a dextral sense of motion throughout its history (Figure 2-6)

2.3. Tectonic evolution of Cyprus

Below is a summary of the tectonic evolution of the geological terranes of Cyprus as presented by Robertson (1990). This synthesis is based on the work of many authors, which are reviewed extensively by Robertson (1990).

2.3.1. Permian (286-245 Ma)

Shallow water shelf limestones are deposited within the Paleo-Tethys Sea, separating Gondwanaland to the south and Laurasia to the north. These sediments become part of the Kyrenia terrane.

2.3.2. Triassic (245-208 Ma)

Continental rifting of the northern margin of Gondwanaland, at the Permian-Triassic boundary, forms the Neo-Tethys Sea. This rifting creates many small microcontinents which separate the Neo- and Paleo-Tethys Seas. Rocks that are now part of the Mamonia Terrane may have been formed on the margin of one of these microcontinents, with rift-related sediments and volcanics.

2.3.3. Jurassic/Early Cretaceous (208-125 Ma)

The Neo-Tethys continues to open, while the African plate begins moving east relative to Eurasia. This means that both spreading and strike-slip motion affect the Neo-Tethys basin. After 119 Ma, Africa begins moving north relative to Eurasia, initiating

subduction in the Neo-Tethys (Figure 2-7). Dilek et al. (1990) claimed that this subduction was south dipping, while more popular models (e.g. Robertson, 1990) indicate a northward dip of the subduction zone.

2.3.4. Late Cretaceous (100-65 Ma)

The oceanic crust that will make up the Troodos ophiolite is formed at a spreading centre above the subduction zone. Rotation of the Troodos microplate is initiated, with >60° anticlockwise rotation completed by 65 Ma (Moores and Vine, 1971; Clube and Robertson, 1986). Many mechanisms have been proposed for the cause of this rotation: subduction of a microcontinent (Moores et al., 1984; Murton, 1987; Robinson, 1987), offset collision of the Troodos microcontinent with another small island or microcontinent (Murton, 1990), rotation during continued spreading, or by offset collision with the Levant continental margin of northern Africa (Robertson, 1990; Figure 2-8a). Amalgamation and suturing of the Mamonia and Troodos terranes begins during this time (Malpas et al., 1993).

2.3.5. Paleocene (66-58 Ma)

The Mamonia and Troodos rocks are sutured and sealed by a shallowing upward sedimentary sequence.

2.3.6. Eocene (58-37 Ma)

Final 30° of anticlockwise rotation of Troodos/Mamonia completed. Rocks of the Kyrenia terrane to the north are uplift and thrust to south, closer to Troodos/Mamonia, possibly due to the collision of the Anatolian microcontinent with the Eurasian margin.

2.3.7. Oligocene/Miocene (36-6 Ma)

With continued subduction in the Neo-Tethys area, Africa begins to be underthrust beneath the Eurasian plate. Underthrusting at a shallow angle (no arc magmatism) results in the uplift of Troodos/Mamonia to a shallow sea environment, and causes some subsidence in the Kyrenia terrane. It appears that the Arakapas Fault belt is active at this time, however not necessarily as an oceanic transform, but probably to accommodate stresses in the region. In the late Miocene the Polis Graben forms in west Cyprus. Sudden uplift of Troodos/Mamonia to above sea level takes place at this time.

2.3.8. Pliocene (5-1 Ma)

Troodos rocks are locally uplifted, while the Kyrenia terrane is likely a low landmass to the north, fringed by carbonates deposited in the shallow sea separating Kyrenia from Troodos/Mamonia.

2.3.9. Pleistocene-Recent (1Ma-present)

During the Pleistocene the terranes of Cyprus are uplifted as a unit, centered on the Troodos Massif at Mt. Olympus. The cause of this uplift is related to both underthrusting of a seamount and serpentinization and dilation of the Troodos mantle sequence rocks (Figure 2-8b). Compression in the Kyrenia range results in uplift, which is also related to underthrusting beneath Cyprus.

Many details of the model of Robertson (1990) presented above have been debated and refined (e.g. Swarbick, 1993; Malpas et al., 1993; Dilek et al., 1990; more recently Morris et al., 1998; Whitchurch et al., 1996; Robertson et al., 1996), however the main features as described here are generally accepted

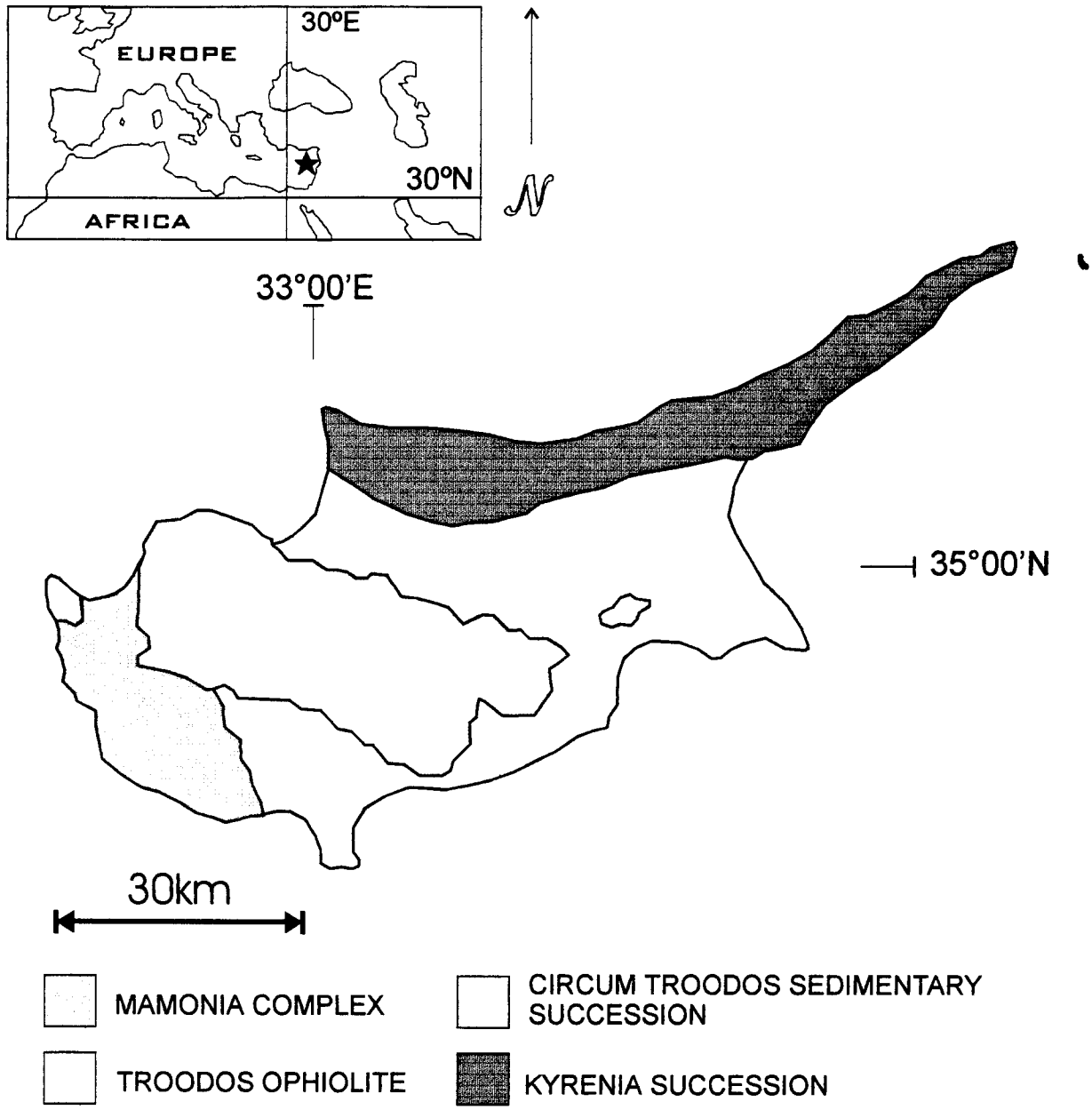

Figure 2-1. Main geological terranes of Cyprus.

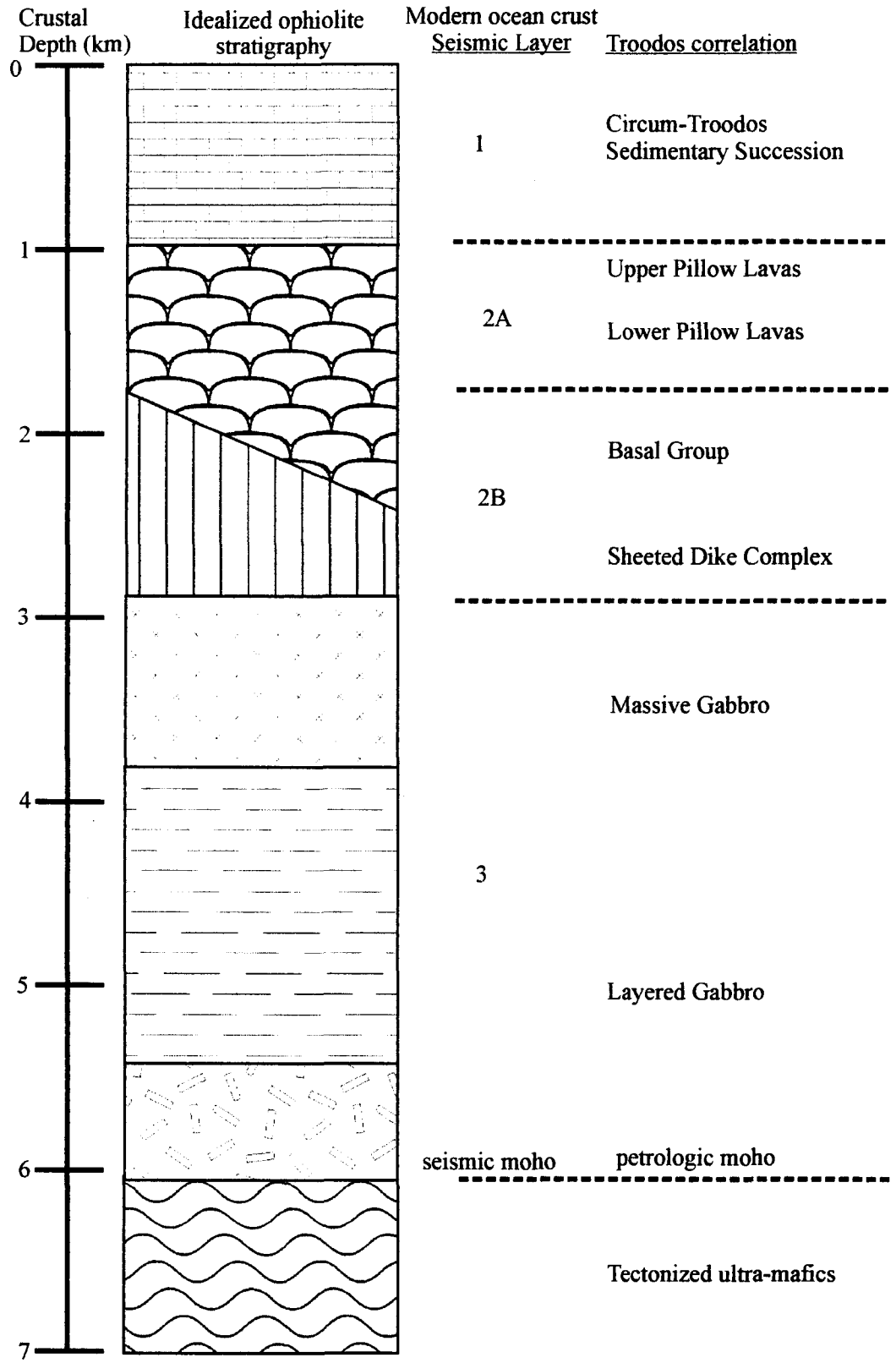

Figure 2-2. Idealized ophiolite stratigraphy, with comparison to modern oceanic seismic layer, and Troodos ophiolite correlation.

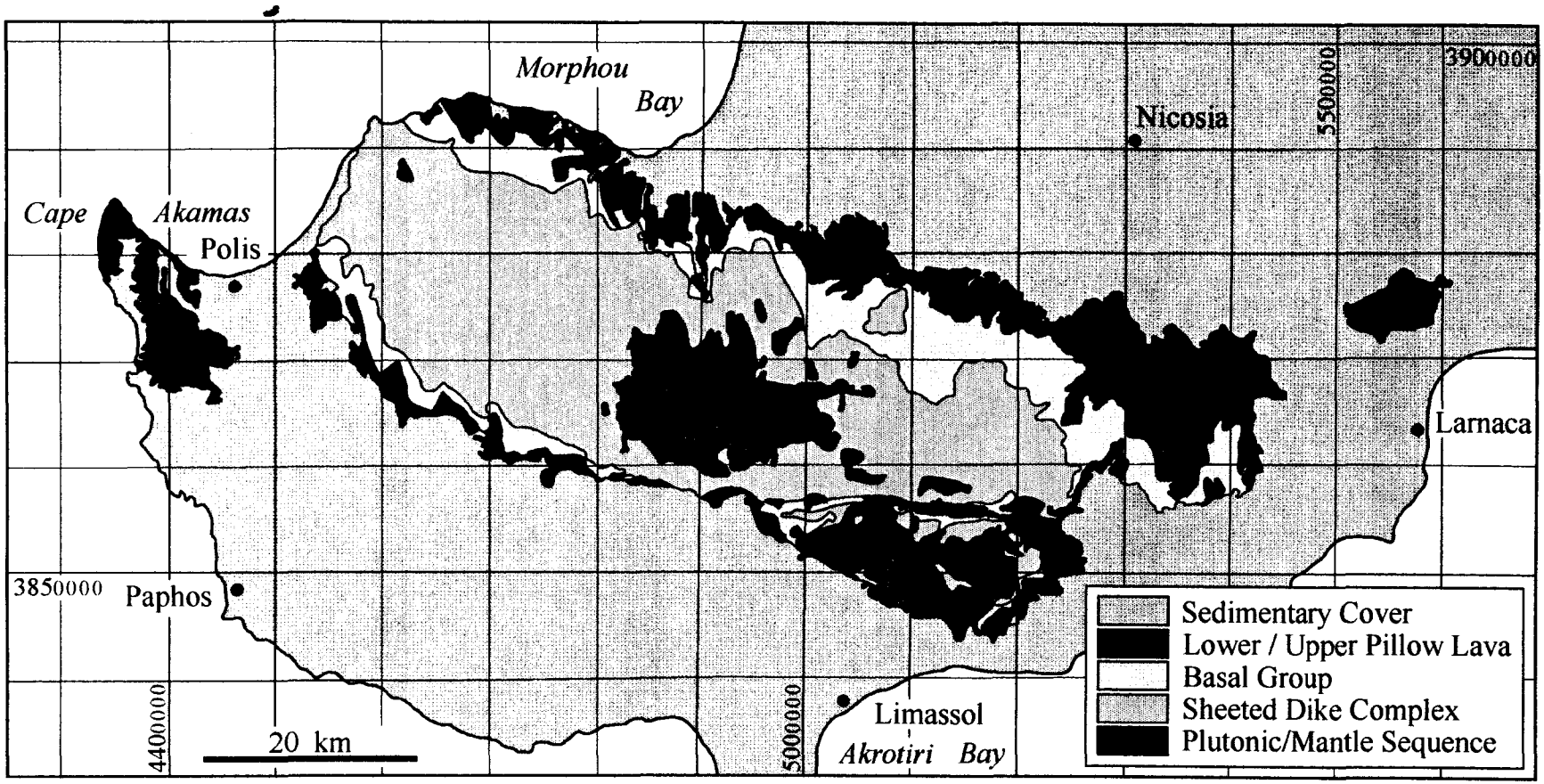

Figure 2-3. Geology of the Troodos Ophiolite.

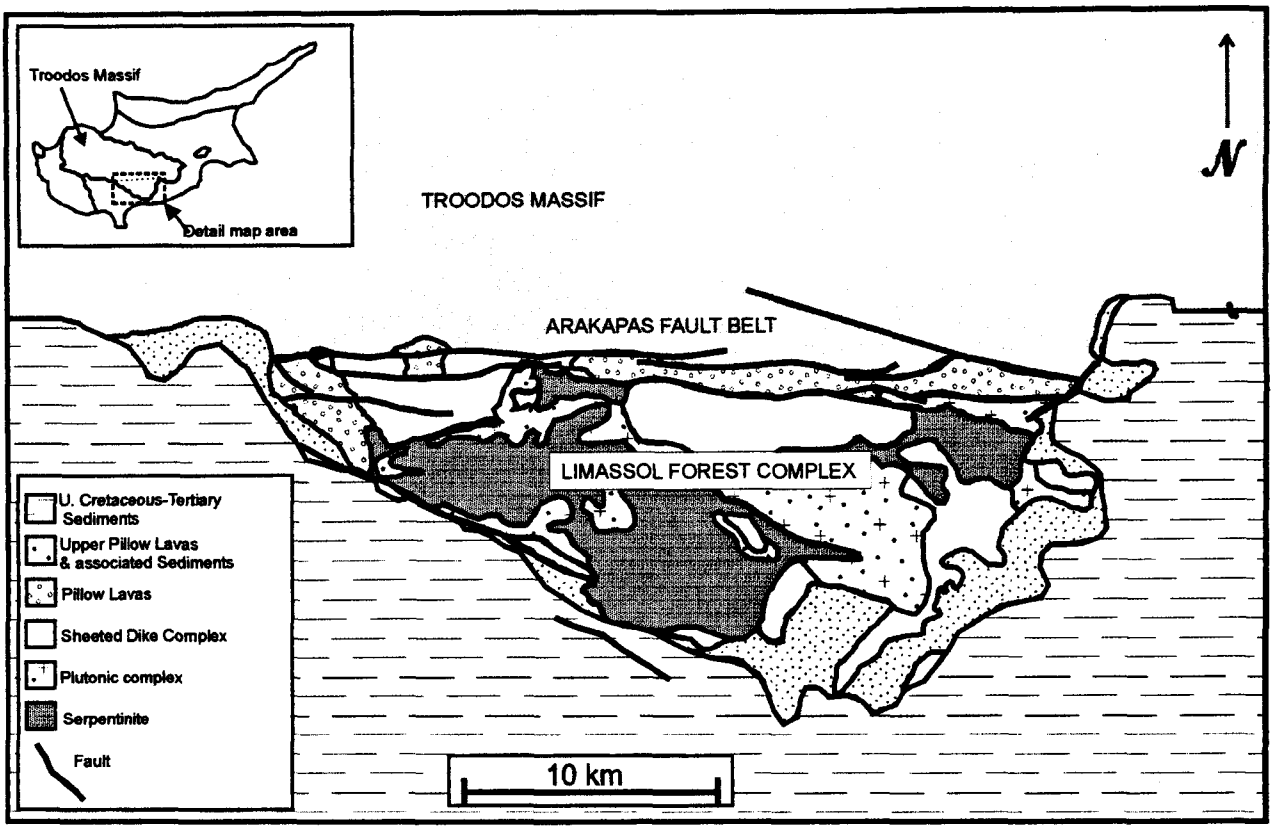

Figure 2-4. Limassol Forest Complex and Arakapas fault belt geology (After Simonian and Gass, 1978).

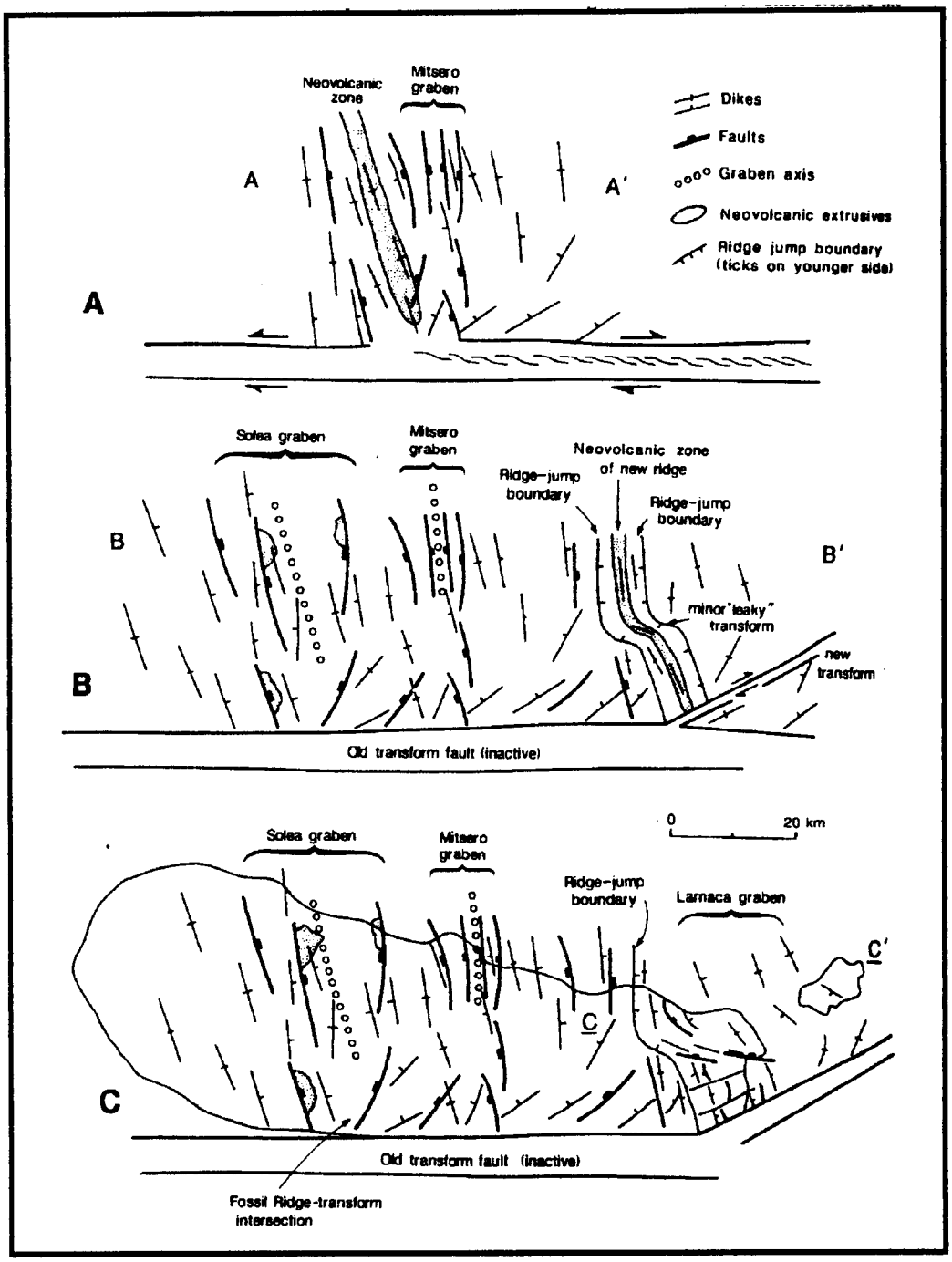

Figure 2-5. Spreading model for Troodos of Allerton and Vine (1991). A) Spreading centred on Solea axis, with off-axis formation of the Mitsero graben. The Southern Troodos Transform Fault is active with dextral motion. B) Ridge jump to Larnaca axis, while Solea graben forms via off-axis extension. C) Paleo-spreading features as observed in Troodos ophiolite at present

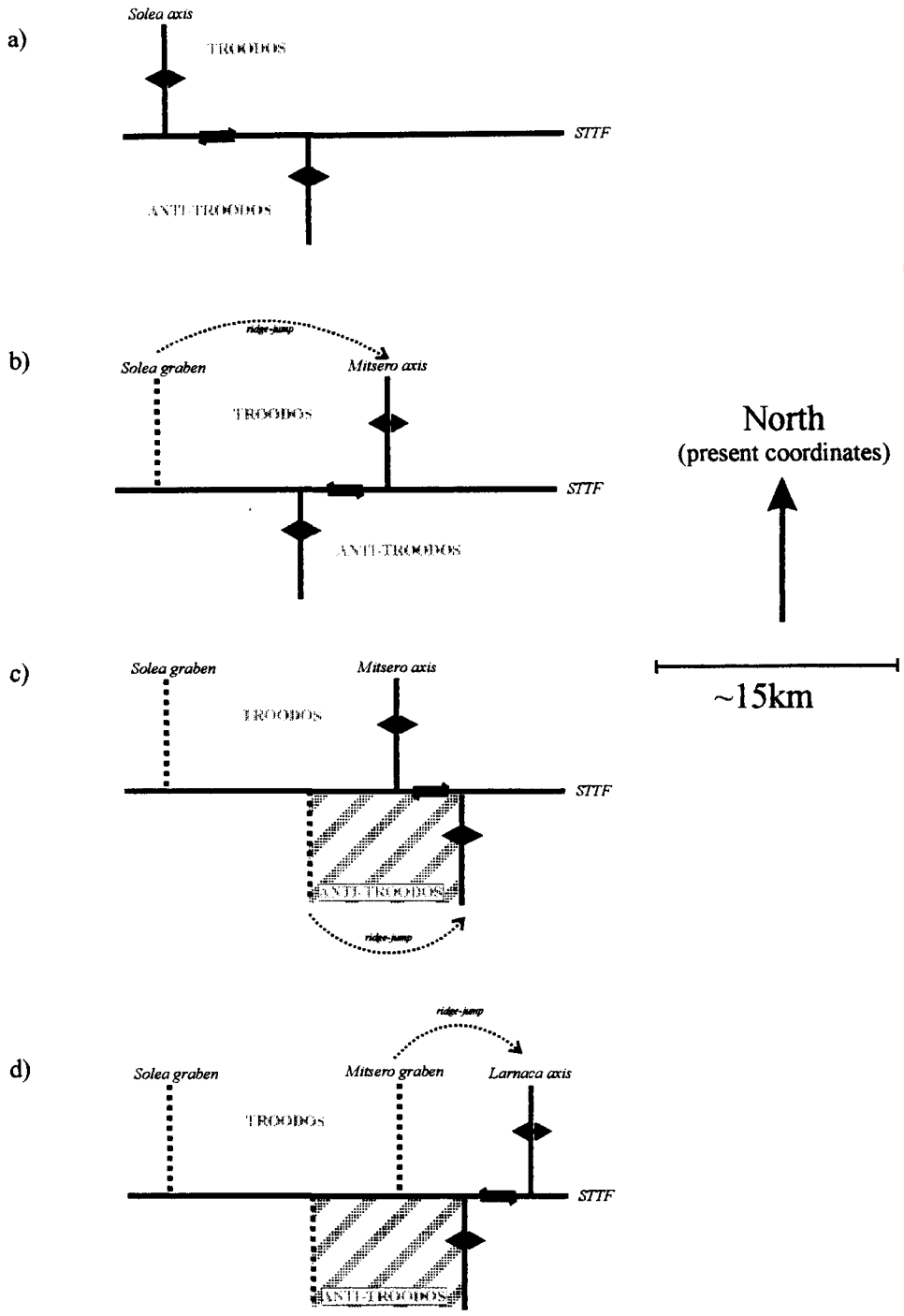

Figure 2-6. Spreading structure model of van Everdingen and Cawood (1995). (a) Magmatic spreading at Solea axis and an anti-Troodos axis south of a dextrally slipping transform fault. (b) Ridge jump from Solea axis to Mitsero axis, which is east of the active anti-Troodos axis, causing the transform to slip sinistrally. (c) Anti-Troodos ridge jump to the east causing dextral slip along transform. (d) Troodos ridge jump from Mitsero to Larnaca axis, east of anti-Troodos active axis, leading to sinistral slip on the transform fault.

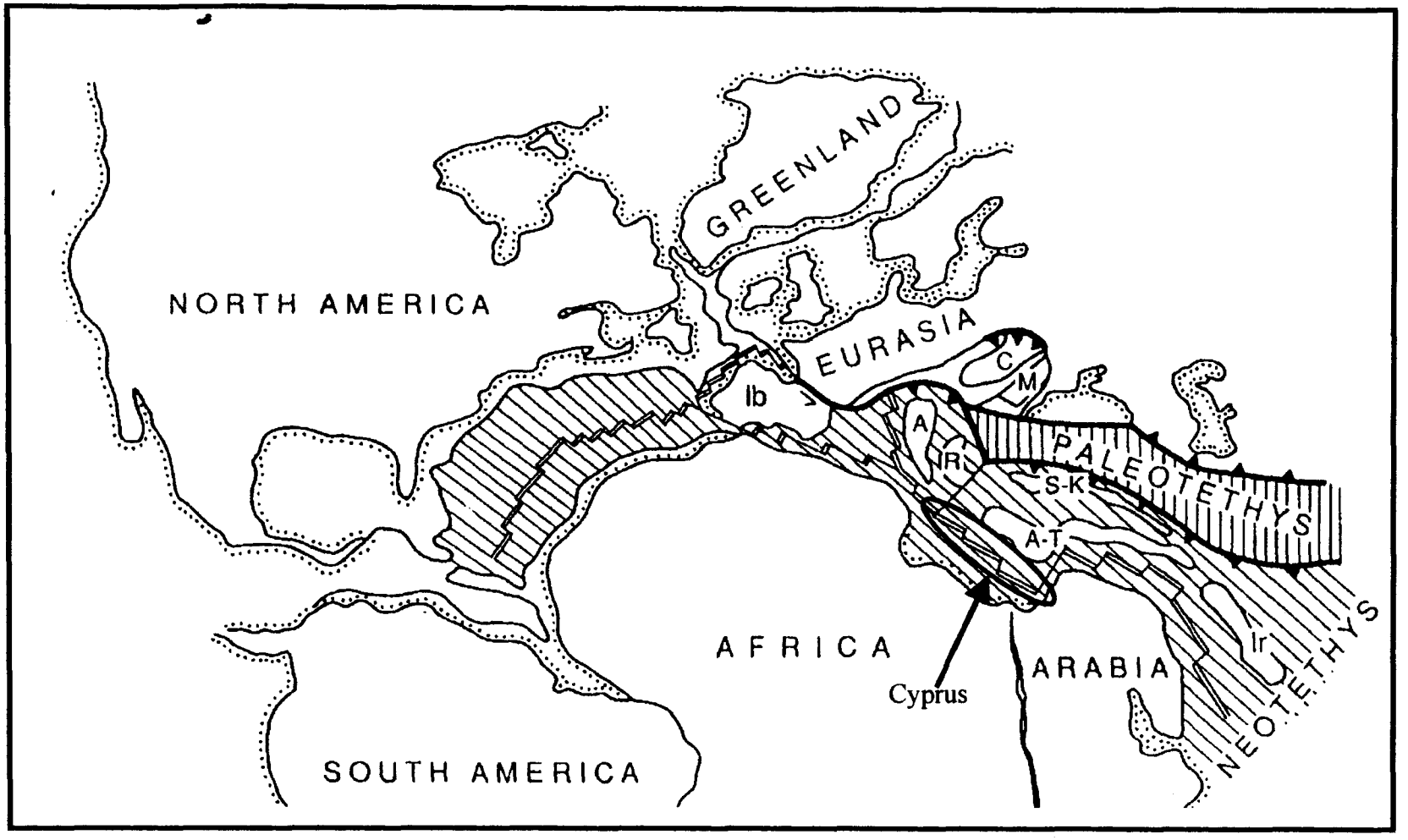

Figure 2-7. Paleogeographic reconstruction for the Early Cretaceous (~140Ma). Oval region marked 'Cyprus' indicates the mid-ocean ridge along which the rocks of Cyprus formed/were forming (from Dilek et al., 1990).

a)

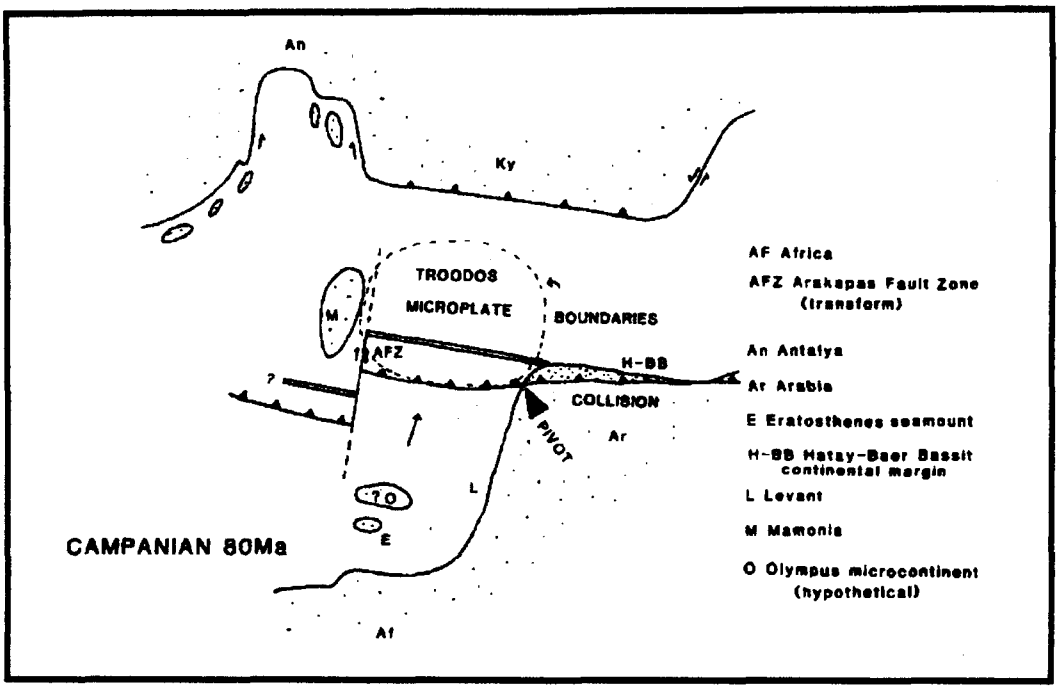

b)

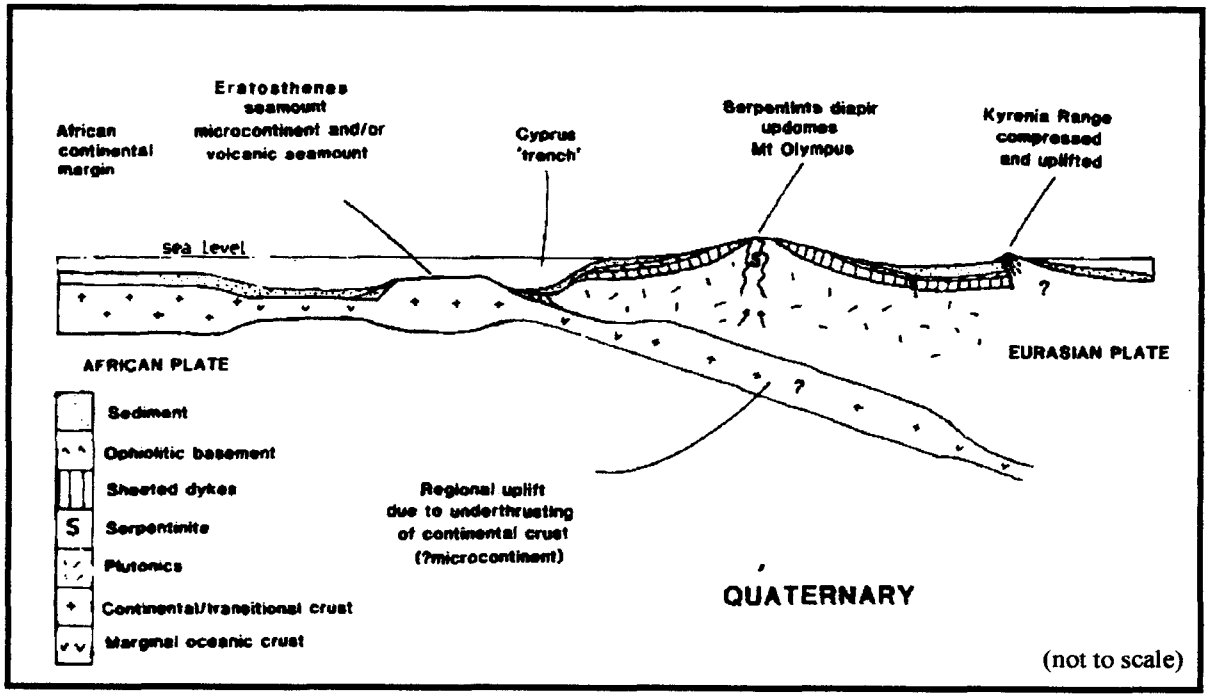

Figure 2-8. (a) Map view sketch of model for the rotaion of the Troodos microplate (from Robertson, 1990). (b) N-S cross section sketch of Quaternery tectonics in the Mediterranean region around Cyprus, describing possible causes of localized intense uplift of Troodos rocks, and regional uplift of Cyprus (from Robertson, 1990).

3. Study area geology

3.1. Present study

During the 1999 field season, Dr. Graham Borradaile (Lakehead University, Canada) collected 82 oriented samples from 79 sites over a 60km^2 area located in the Arakapas-Sykopetra-Agios Konstantinos area (Borradaile and Gauthier, 2001). Dike orientations were measured at each site. This pilot-study area is located almost entirely within the Arakapas dike domain of Varga and Moores (1985, 1990).

In 2000, 440 oriented samples were obtained from 356 locations, yielding 1289 standard size cores. In addition, 1169 dike orientation measurements were made. The approximately 400km^2 area sampled covers most of the SDC exposure on the east half of the Troodos ophiolite, as well as the base of the BG in some cases (Figure 3-1). Two particularly well-exposed locations with relatively fresh and sub-parallel dikes, at Panagea and Konia, were sampled in detail (Borradaile and Gauthier, 2002).

On an outcrop scale, sheeted dikes vary between 30cm and 3m thick, and are sub-parallel and generally steeply dipping. Signs of forceful injection are never observed, whereas dike-intruding-dike tensional infilling structures are common (Baragar et al., 1990). Kidd and Cann (1974) suggested that chilled margins of dikes should be one-sided, due to 'half dikes' being separated at the ridge and carried in opposite directions as new dikes are intruded, an idea that at present seems unduly optimistic. Baragar et al. (1987) searched for this phenomenon at a single location in the SDC, but found no statistical preference for directions of chilled margins. The dikes are commonly fractured, with dike parallel cooling joints as well as dike perpendicular columnar joints,

both of which decrease in length and frequency with depth in the sequence (van Everdingen, 1995).

In many outcrops, a steep set of dikes can be found cross-cutting a shallower set (Figure 3-2a). In other places, the age relationship between dike sets is not as clear, however the steeper set is generally considered to be the younger (Moores et al., 1990). More rarely, outcrops with two oppositely dipping sets of steep dikes are found with no obvious age relationship (Figure 3-2b). It is often assumed that all of the dikes of the SDC were originally vertical, however in some locations age relationships between dike sets seem to contradict this idea (Figure 3-2c).

3.1.1. Spatial-averaging of dike orientation data

Due to the extensive road-cut exposure and common secondary and tertiary roadways within the study area, the majority of samples were obtained from roadside outcrops. We sampled with the aim of achieving a uniform distribution of samples across the area of interest. A χ^2 test of sample distribution (Figure 3-1) showed that it was indistinguishable from a uniform distribution at the 95% confidence level.

In order to smooth local variations in the dike orientations measured in the field, the data was spatially-averaged. The intent of this procedure is to:

1) Smooth the data, reducing local variations and 'noise' in the data; and

2) To interpolate average dike orientations between sample locations, but avoid extrapolating orientations outside of the study area.

Figure 3-3 shows several test maps that were generated in order to determine the appropriate smoothing parameters. In all tests, averages were calculated at points with 1km grid spacing, using a moving circle method, with data weighted at each station

according to the inverse of their distance from the station. Thus, data closer to an averaging station contribute more to the average calculated at that station. The radius of the averaging circle was varied between tests and results visually examined to find the appropriate parameters to meet the criteria described above. The orientation data were averaged by using circle-radii of 5km (Fig. 3-2a), 3.75km (Fig. 3-2b), 2.5km (Fig. 3-2c) and 1.25km (Fig. 3-2d). By comparing the sample distribution of Figure 3-1 with Figure 3-3a, it is obvious that a 5km radius circle tends to over-smooth the data, and extrapolates data for many points on the periphery of the plot where no data was actually collected. A 3.75km radius circle (Fig. 3-3b) resolves regional patterns in the data better than the 5km circle, however the 'edge effect' is still prominent. At 2.5km (Fig. 3-3c) gaps in the distribution have been filled, regional patterns are recognizable, and the border of the averaged data closely follows the outline of the original data, thereby subduing any edge effects. An averaging circle of 1.25km (Fig. 3-3d) does a poor job of smoothing the data, regional patterns are only partially observable, and gaps in the original distribution persist in the averaged distribution.

The spatial averaging parameters of 1km station spacing, inverse distance weighted averaging in 2.5km radius moving circles (Fig. 3-2c) appears to smooth the data best without subduing regional patterns, or introducing any ambiguous edge effects. Smoothed dike orientation data using the above described parameters are presented relative to the dike domains and graben axes/boundaries of Varga and Moores (1985, 1990) on Figure 3-4. The dike orientations that were used to originally map the domains and grabens match well with those observed in this study, and the gradual swing in orientation described by Simonian and Gass (1978) can be seen as the SSTFZ and the

Arakapas dike domain are approached. This study area is located within the Makheras, Mitsero, and Arakapas dike domains, and samples across the Mitsero graben axis and the Mitsero graben east boundary. Refinements of the Mitsero domain by van Everdingen and Cawood (1993) cannot be resolved with the data presented here, as sample frequency within the domain is too coarse to observe small scale variations in attitude.

3.1.2. Faults

Due to the extensional nature of the near-ridge oceanic crust, normal faulting is found throughout the SDC (Figure 3-5). These faults generally dip shallower than the dikes that they cut, and are most often planar in nature. In some locations, they are observed to be listric, shallowing with depth to coalesce into low-angle detachment surfaces near the base of the SDC. This basal detachment may be only 1-5m wide, marked by a highly altered brecciation zone. In other locations low angle faults are found to be subparallel, but do not coalesce into a major detachment (Moores et al., 1990). Dietrich and Spencer (1993) performed a very detailed investigation into the patterns and scale of faulting in the SDC. Some of their data seems to contradict previous studies, however their conclusions appear to be valid:

1) common meter-scale planar dike parallel faults show a 'ramp and flat' geometry, following dike margins for the majority of their length and stepping across dikes at a high angle to continue along another margin
2) larger than meter scale dike parallel to sub-parallel faults link with sub-horizontal shear zones

3) listric normal faults coalescing at depth (as described above) are not as common as other fault types, however they can accommodate more spreading than other faults.

They also pointed out that some previous extension models must have oversimplified the actual system, as extension is only possible in the hanging walls of listric normal faults.

It is generally assumed that all of the dikes in the SDC were originally intruded vertical and ridge-parallel, and any departure from that orientation seen today must be a result of either sea-floor or obduction related processes. Normal faulting is often cited as the cause of much of the variability in dike orientations (see Figure 3-2).

3.2. Petrology

3.2.1. Petrography

Robinson et al. (1983) and Baragar et al. (1987) investigated both the primary and secondary minerals in the rocks of the sheeted dike complex. They found that plagioclase is a ubiquitous phenocryst throughout the suite. Dikes with higher proportions of MgO (>5.5%) were found to be olivine-phyric, while in those with less MgO (<5.5%) magnetite was a phenocryst phase. Quartz is present in most dikes with MgO less than 7%. Baragar et al. (1987) consider the primary mineralogy to have been principally plagioclase + clinopyroxene, ± quartz/olivine/magnetite depending on MgO concentrations. They found a metamorphic assemblage comprising: plagioclase + actinolite +chlorite + magnetite. The plagioclase is calcic ($An_{>50}$), with altered pyroxenes and (titano)magnetite with sphene alteration rims.

3.2.2. Magmatic chemistry

When investigating the chemical characteristics of Troodos volcanic rocks, Robinson et al. (1983) found in their analyses that there is a composition break in the volcanics at between 4 and 5.5% MgO. Apparently, no petrological process could account for the discontinuity in compositions, leading to the idea that there were in fact two genetically distinct lava suites. These were termed the Upper Pillow Lavas (UPL) and the Lower Pillow Lavas (LPL). Field relationships show that the UPL cross-cuts the LPL, and further analyses showed that the UPL is derived from a depleted suite mantle source, while the LPL is derived from primitive mantle material (Robinson et al., 1983). In the SDC, Baragar et al. (1987) found that while dike compositions generally matched the compositions of the volcanics, there was no gap in the analyses corresponding to the one observed between the LPL and UPL. Furthermore, they observed that depleted dikes do not consistently crosscut primitive dikes in the field. One possibility, they suggested, was that there were two laterally discontinuous magma sources available to the dikes and lavas at the same time.

3.2.3. Petrogenesis

Despite the obvious petrogenetic ambiguities introduced by metamorphism and alteration, Thy et al. (1989) put forth a model for generation of the SDC that called for an open-system fractionating magma chamber feeding the dikes. This model could explain most of the petrological features of the SDC, all except for the problematic TiO_2 and rare-earth element (REE) abundance (Baragar et al., 1990). It was suggested by Baragar et al. (1990) that TiO_2 and REE abundance could be explained if the magma chambers were replenished from variable sources. Following an example described by Bender et al.

(1984) for the East Pacific Rise (EPR) they also suggested that a 'Transform fault effect' caused the rapid cooling of the crust close to an active transform fault, which can explain the REE pattern in the SDC of Troodos.

More recent studies (Thy and Ebeson, 1993) have disputed previous chemical analyses of the SDC rocks, claiming that 98% of the dikes can be shown to be related to the LPL 'non-depleted' lava suite. If this is the case, then the UPL 'depleted' suite of lavas and dikes may have been an off-axis phenomenon, unrelated to a major spreading event (Thy and Ebeson, 1993).

As the underlying plutonic complex is thought to represent the solidified magma chambers that were feeding the dikes, it may be instructive to investigate its petrology. Laurent (1990) showed that the parental magma to the plutonic complex found in the CY-4 drillhole was a low-alkali basaltic andesite, and that all of the sections that were sampled were of a continuous and co-magmatic suite. Laurent (1990) suggested a closed system-fractionation source, with a crystallization sequence olivine → clinopyroxene → orthopyroxene → plagioclase, similar to that expected for the SDC (Baragar et al., 1987).

3.3. Metamorphism and alteration

3.3.1. Metamorphism

Metamorphic grade in the SDC is commonly considered greenschist or amphibolite. Baragar et al. (1990), however, state that the mineral assemblage in the dikes is closer to the actinolite facies of Elthon and Stern (1978), indicating metamorphism under low water-rock ratios. Metamorphic conditions vary with depth through the volcanics and SDC. Generally, the volcanics (UPL and LPL) and basal group (BG) are permeable to seawater and far removed from any significant heat source.

Therefore, metamorphism takes place under low-temperature, but high water-rock ratio conditions. At depth in the SDC, vertical and lateral water flow is confined to faults and detachments. Low water-rock ratios therefore prevail, with a much higher temperature due to proximity to a heat source (magma chamber) below (Baragar et al., 1990). The basal detachment surface separating the SDC from plutonic rocks below is often thought to be a physical boundary of seawater circulation in the crust. Gillis and Roberts (1999) suggest that the lower limit of circulation may not be restricted to the detachment surface, but may be related to a convective boundary between magmatic and hydrothermal heating and cooling.

3.3.1.1. Hydrothermal alteration of magnetic minerals

The effect of hydrothermal alteration on the primary magnetic mineralogy in the SDC has been studied in detail by Hall et al. (1987). Based on a traverse through the volcanics and SDC to the plutonic suite in the northern part of the current study area, they showed that:

- Within this study section, maximum susceptibilities should be observed in the uppermost *and* lowermost samples, whereas minimum values of susceptibility should be found in the mid-depth samples.
- The effects of hydrothermal alteration should be at a maximum in higher level samples, and at a minimum in those from the deepest parts of the section.
- In the uppermost samples from this study, primary and secondary magnetite should be in roughly equal proportions, with an increasing dominance of secondary over primary with increasing depth. The lowest samples should have little or no primary magnetite

3.3.1.1.1. Magnetite alteration

Primary titanomagnetite (TM_{60}; $Fe_{2.4}Ti_{0.6}O_4$) in seafloor basalts (Butler, 1992) may follow one of two alteration paths (Shau et al., 2000):

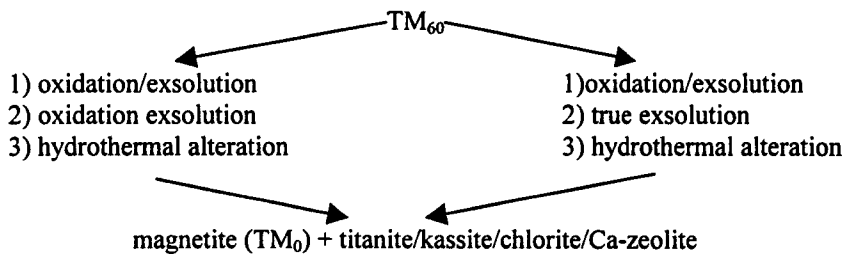

Butler (1992) describes the deuteric oxidation of primary titanomagnetite as occurring during cooling of the rock, mainly due to non-equilibrium of temperature and oxygen conditions between the grains and their surroundings. The result of oxidation of primary TM_{60} grains is the exsolution of ilmenite, leading to a composite grain of $TM_{<60}$ with Ti-rich ilmenite lamellae. This process takes place at approximately 750°C. Butler (1992) also states that true exsolution also takes place on cooling, a result of the breakdown of the titanomagnetite solid solution between pure magnetite and ulvospinel. Above approximately 600°C the solid solution is complete, and all compositions between magnetite and ulvospinel are stable. Below 600°C however, compositional gaps form causing unstable regions to unmix into Fe and Ti rich regions. The result again is a composite grain. Low-temperature oxidation, or hydrothermal alteration, takes place below 200°C, and results in the weathering of magnetite or TM_{60} to maghemite or titanomaghemite (TMH), respectively (Butler, 1992). Titano-maghemite is compositionally titano-hematite, but maintains the spinel structure of titano-magnetite.

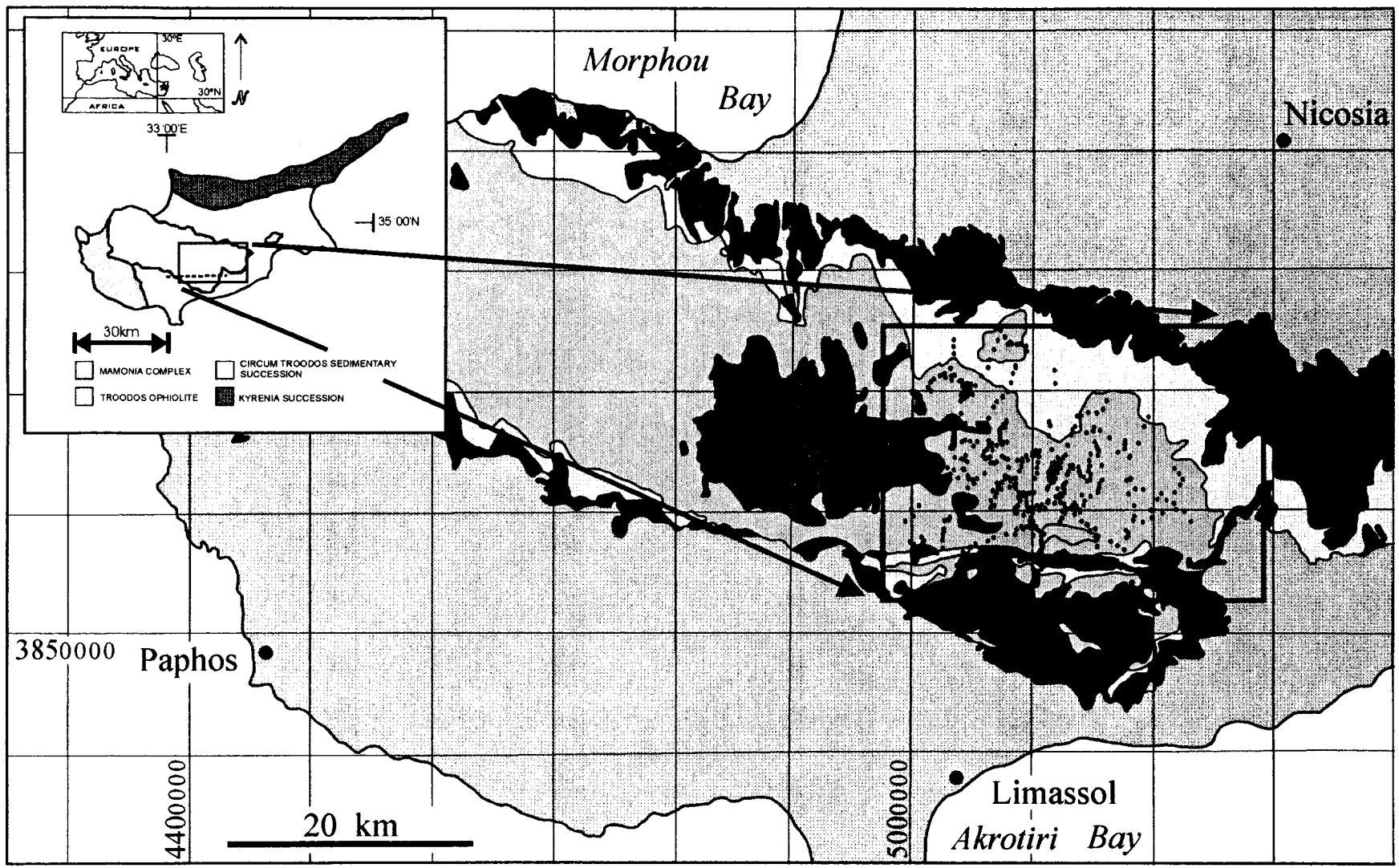

Figure 3-1. Map of geology of part of the Troodos Ophiolite (legend as per figure 2-3), showing the present study area (thick square), and sampling locations (black circles). A total of 435 sites were visited during the field seasons of 1999 and 2000, with 522 oriented samples retrieved, and 1248 dike orientation measurements recorded.

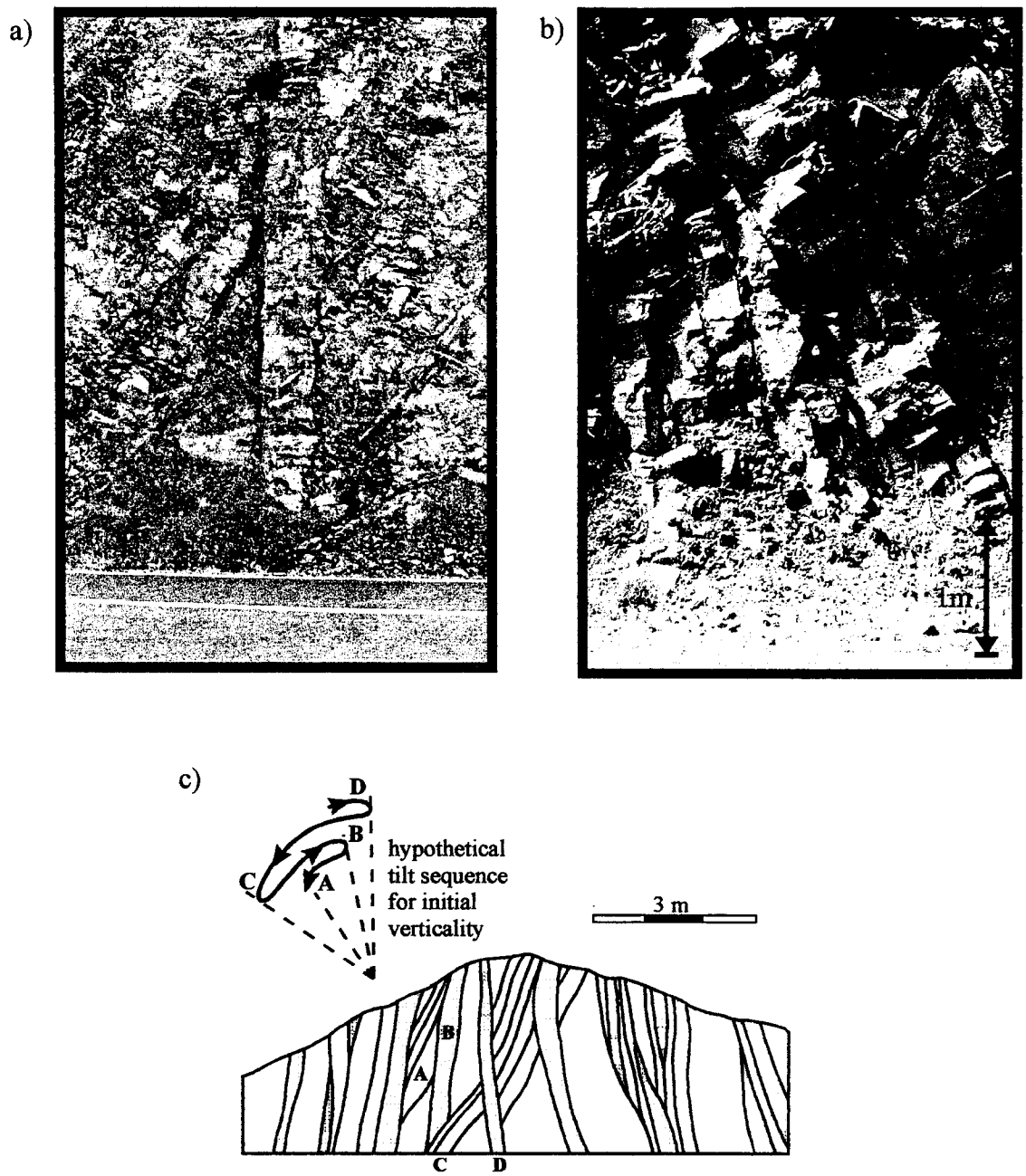

Figure 3-2. (a) Photograph of a roadcut exposure near Zoopigi with a vertical dike crosscutting a dipping set of dikes. (b) Photograph of a roadcut exposure near Platanistasa showing dikes of same generation with opposing dips, as well as a dike closure. (c) Sketch of a roadcut exposure with dikes of variable dip. Dikes of different ages cannot be uniformly restored to vertical primary orientations, as this would require a complex history of rotations and counter rotations The range of dips may therefore be considered a primary feature, implying that not all dikes were originally vertical.

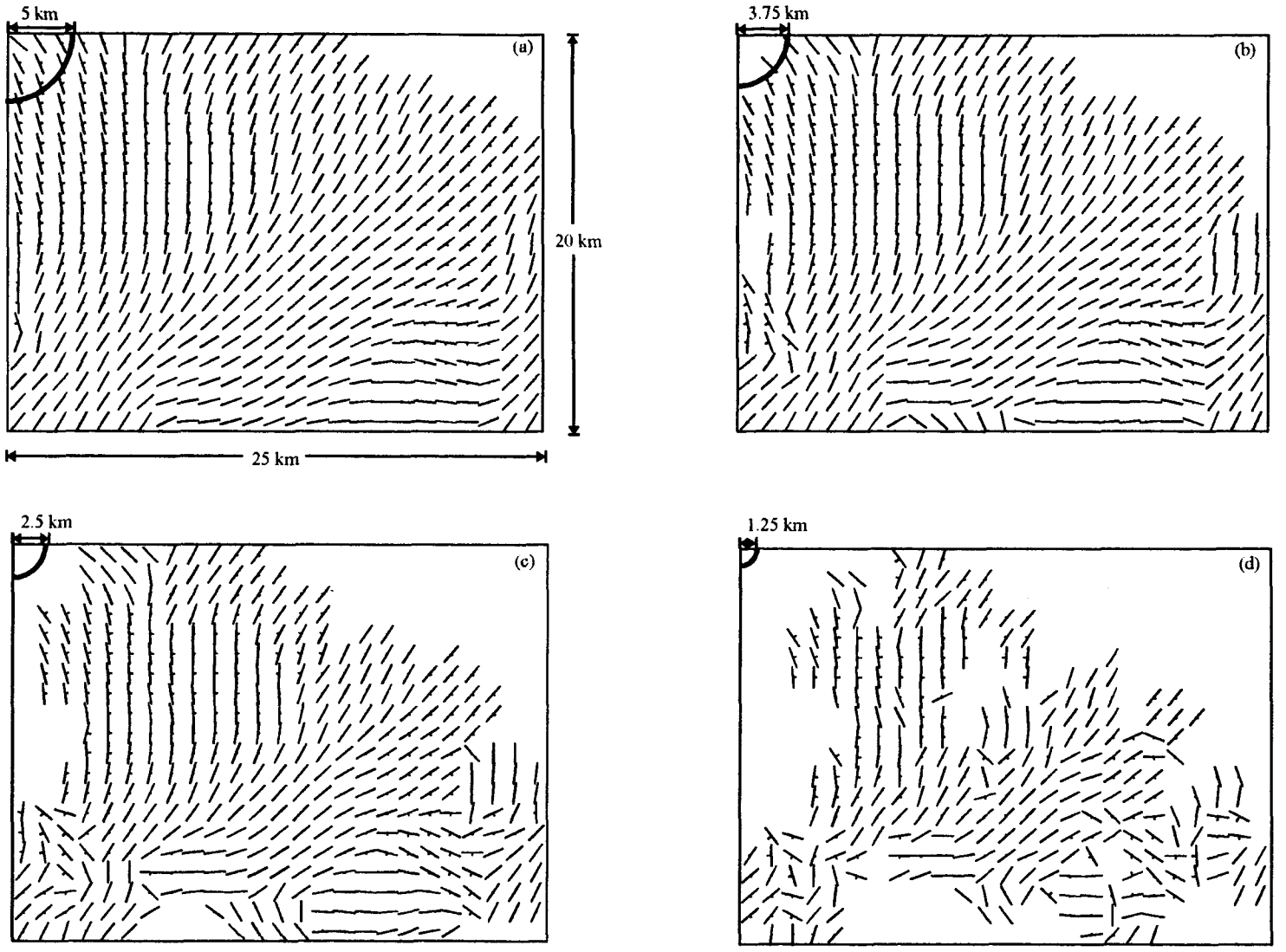

Figure 3-3. Maps of spatially averaged dike orientation data collected at the locations shown in Figure 3-1(1km grid spacing, moving circle method, inverse distance weighting). (a) 5km radius sampling circle for each grid station. (b),(c),(d) 3.75km, 2.5 km, 1.25km radius respectively. Edge-effects and interpolation errors are minimized in (c).

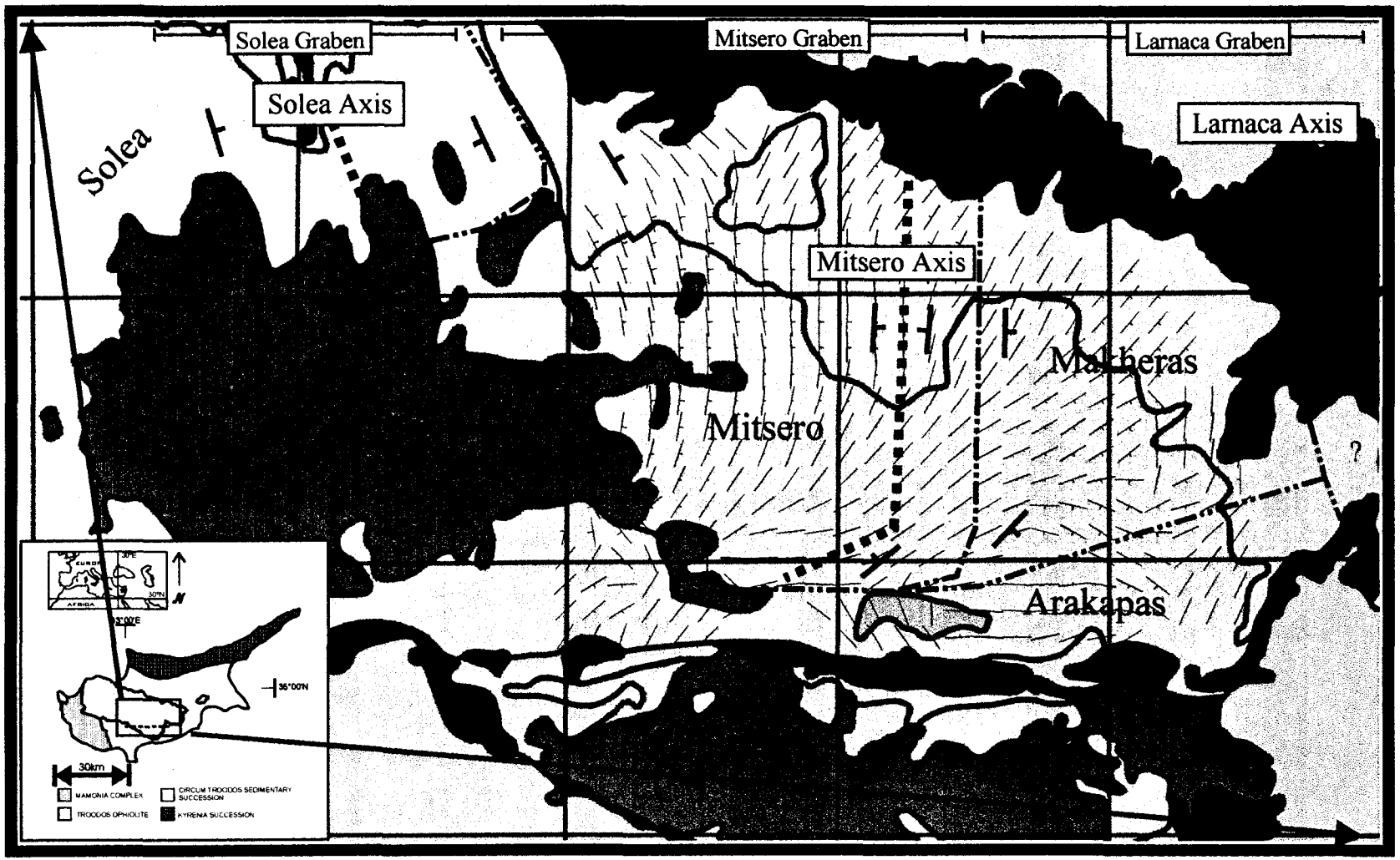

Figure 3-4. Spatially averaged dike orientations superimposed on Troodos Geology. Dikes are represented by thin lines (strike) with small hatch marks to indicate dip-direction and amount (shorter hatch = steeper dip). Thin dashed lines represent graben boundaries, thick dashed lines represent paleo-spreading axes, as defined by Varga and Moores (1990). The data presented here agrees well with the existing domain boundaries, and the gradual swing in orientation as the STTFZ is approached can be see clearly.

a)

b)

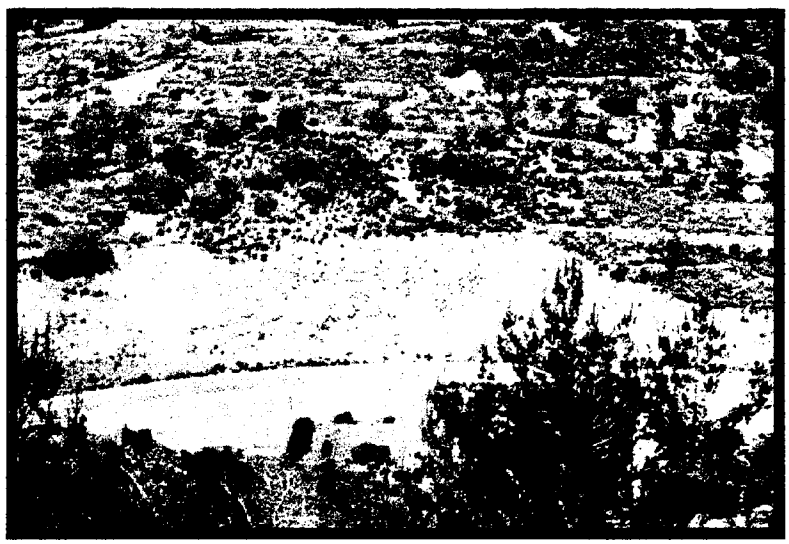

Figure 3-5. (a) Photograph of a roadcut exposure showing a normal fault cutting rocks of the SDC(b) Photograph of a roadcut exposure near Palekhori showing a low-angle normal fault cutting rocks of the SDC. This location is close to the base of the SDC, near its contact with a window into the plutonic section.

4. Magma flow and magnetic fabrics

It is the aim of this study investigate magmatic flow orientations using the anisotropy of magnetic susceptibility. To this length, one to three oriented hand samples were collected from each of the 435 sites (see Figure 3-1) located within a 400km^2 area of SDC, east of Mt. Olympus. Each sample was re-oriented in the laboratory, where several cylindrical cores, 25.4mm in diameter by 21mm high were drilled. 1289 cores were retrieved from the samples collected in 2000, and 291 from those gathered in 1999. Anisotropy of magnetic susceptibility (AMS) measurements were made on each of these cores, while a limited number were subjected to further analysis of magnetic properties.

There are two main concepts that allow this experiment to work:

1) AMS measurements faithfully records the *orientation distribution* of grains within a sample
2) Magmatic flow in dikes will tend to cause an alignment of particles within the dike, leading to a flow derived petrofabric.

These two concepts will be reviewed in the following sections in hopes of showing that AMS is a valuable petrofabric tool, and that the results of AMS determinations *may* be used to determine flow axes in the sheeted dikes of Troodos. The results of this experiment will be presented in Chapter 5.

4.1.Magma-flow kinematics

Since Jeffrey (1922) began the study of the motion of ellipsoidal particles in a flowing matrix, a large volume of both theoretical and practical research has been compiled. Nicolas (1992) reviewed many aspects of the kinematics of magmatic rocks,

including the alignment of particles in a flowing matrix. He states that in two-dimensional models of magmatic flow the longest axis of particles affected by the flow tend to align with the flow axis. Furthermore, he describes how Passchier (1987) and Fernandez and Laporte (1991) have shown that three-dimensional models have similar implications. It is generally accepted that the long axes of triaxial particles will tend to align with flow direction, while the shortest axes of these particles will align perpendicular to the flow plane. To model the effects of magmatic flow, the situation is often considered in terms of the rotation of a rigid marker (particle) during shear (Fig. 4-1). A preferred dimensional orientation (PDO) arises due to variability in the angular velocity of the rotating particles in such a way that each spends more time aligned with flow than perpendicular to it (Nicolas, 1992), resulting in a net tendency for particles to be aligned with flow. In geological terms, the orientation of the *magmatic lineation* in a dike should be close to parallel with the orientation of magmatic flow in that dike, while the *magmatic foliation* should lie close to parallel with the plane of flow in the dike. In dikes 1-3m wide, such as those sampled in this study, flow could only be expected to be within the dike plane, implying that the *magmatic foliation* should lie parallel with the dike plane itself. The implications of this idea are paramount to the current study, and will be revisited in section 4.3.

4.2.Anisotropy of magnetic susceptibility (AMS)

4.2.1. Magnetization of rocks

In the presence of an applied external magnetic field (H), any substance acquires a magnetization (M). Different substances respond differently to the external field (see below). Magnetic susceptibility (k) is a measure of how easily the applied field can

induce a magnetization in a given substance. M and H are related by k in all substances: linearly (constant k) in the diamagnetic and paramagnetic response, and generally non-linearly in the ferromagnetic response. Susceptibility is dimensionless. It is important to note that, for a given material in a given applied field, the value of susceptibility will be larger in a larger volume sample. Therefore, when a susceptibility determination is made in the laboratory or in the field, it is the susceptibility of the whole sample that is measured, and must be divided by the sample volume (in m^3 in the SI system). For convenience, in this thesis v*olume susceptibility* (χ) is simply referred to as *susceptibility* (k). A sample of known mass (where *mass* susceptibility is measured) is multiplied by sample density to normalize the measurement to refer to the susceptibility of a substance, on a volume basis, or SI. All materials can be grouped into the following physical classifications, based on their response to an applied external magnetic field.

All substances respond to an external field by acquiring a very weak magnetization that opposes the applied field (Figure 4-2a). In an isotropic material the strength of the induced field (M) is linearly related to the applied field (H) by:

M=kH (Figure 4-3a) **(4-1)**

4.2.1.1. Diamagnetic

The diamagnetic response is a result of the effect of the applied field on electron orbital motions in the sample, and is therefore lost when the external field is removed. In elements that have even atomic numbers, or complete electron shells, diamagnetism is the only response. Pure quartz, calcite, and feldspar are examples of common diamagnetic rock forming minerals, which record small negative susceptibilities (Table 4-1). In nature, however, these minerals are rarely (if ever) pure, and commonly contain Fe-oxide

inclusions, which may mask their diamagnetic response. The theoretical diamagnetic susceptibility (k_{dia}) is -13.6 x 10^{-6} SI.

4.2.1.2. Paramagnetic

Substances with incomplete electron shells respond to the external field by acquiring a magnetization that is parallel to and supports the applied field (Figure 4-2b). Induced magnetization is linearly related to the applied field by equation 4-1 (Figure 4-3b). Values of susceptibility are positive and usually much greater than values for diamagnetic materials (Table 4-1). The Curie law of paramagnetic susceptibility,

$$\chi = J/H = NM^2/3kT \qquad (4\text{-}2)$$

(where χ is the paramagnetic susceptibility, J is the magnetization, H is the applied field, N is the atomic moments per unit volume of the sample, M is the magnetic moment, k is Boltzmann's constant, and T is the temperature in Kelvin), describes the paramagnetic response of a substance to an applied field, and states that the susceptibility of paramagnetic substances decreases proportionally with increasing temperature. For example, paramagnetic susceptibility decreases 0.34% per C° at room temperature. Butler (1992) describes how, in a paramagnetic substance, thermal energy causes atomic magnetic moments to oscillate randomly, and the way in which an applied field will tend to exert an aligning torque on the moments. This results in a biased distribution of magnetic moments parallel to the applied field. When the field is removed, the oscillations are returned to random, leaving no net magnetization. Most rock-forming mafic silicates are paramagnetic (Table 4-1), with susceptibilities generally <2000 μSI. As with diamagnetic minerals, however, in nature most paramagnetic silicates contain

Fe-oxide inclusions. This can lead to increase in theoretical susceptibility values (Lagroix and Borradaile, 2000; Werner and Borradaile, 1994; Borradaile, 1994).

4.2.1.3. Ferromagnetic

Ferromagnetic substances respond to an external field by acquiring a very strong magnetism parallel to the applied field (Table 4-1), and are capable of maintaining their magnetism after the field has been removed. As with all magnetism, this type is related to the spin moments of electrons. Ferromagnetism arises because of an interaction between electrons, such that they are 'coupled' to one another and can affect the spin moments of their neighbours. This coupling allows them to be both easily magnetized in an external field and maintain that magnetism in the absence of the field. Different spin configurations lead to the further classification of *ferromagnetic*, *ferrimagnetic*, and *antiferrimagnetic* responses. Parallel coupling between adjacent layers of atomic moments results in a ferromagnetic response to an applied field (Figure 4-2c), while anti-parallel coupling of unequal and equal moments respectively produce the ferrimagnetic and antiferrimagnetic response (Figure 4-2e and d, respectively).

Remanent magnetization, or the magnetization that is maintained after removal of the external field, can be observed by plotting magnetization M versus the applied field H as in Figure 4-3c. At very low fields (up to 5mT) for an isotropic medium the relationship is linear (M=kH, Figure 4-3c), but at higher fields the magnetization becomes a non-linear function of H and eventually saturates. Upon removal of the applied field, the magnetization of a ferromagnetic substance does not return to zero (as in diamagnetic and paramagnetic material), but instead follows an irreversible decrease to M_R (remanent magnetization) which thus forms part of a 'hysteresis loop' (Figure 4-3c).

The saturation magnetization for a given substance decreases as temperature is increased, and at the Curie Temperature (T_c) is zero. At any temperature above T_c a ferromagnetic mineral behaves paramagnetically

Table 4-1. Examples of susceptibilities of some common rock forming minerals. Note that in most cases the susceptibilities of a given mineral species can vary greatly. D, P, and F in parentheses indicate diamagnetic, paramagnetic, and ferromagnetic responses, respectively.

	Susceptibility (μSI)	**Reference**
Biotite (P)	1000-1300	Borradaile et al. (1987)
Chlorites (P)	70-1500	Borradaile et al. (1987)
Amphiboles (P)	300-9000	Borradaile (1987)
Pyroxenes (P)	500-5000	Rochette et al. (1992)
Quartz (D)	-13.4	Hrouda (1986)
Feldspars (D)	-14.0	Borradaile et al. (1987)
Magnetite (F)	2.8×10^6	Borradaile and Henry (1997)
Ilmenite (P)	$0.1\text{-}0.2 \times 10^6$	Borradaile and Henry (1997)
Titanomagnetite (TM_{78}) (F)	50,000	Dr. M. Jackson, pers. comm.
Chromite (F)	3000-100000	Carmichael (1982)
Hematite (F)	< 6000	Borradaile and Henry (1997)
Maghemite (F)	2.0×10^6	Borradaile and Henry (1997)

The magnitude of susceptibility in magnetically isotropic substances is equal in all directions. Any material for which the magnitude of susceptibility varies with orientation of the material is anisotropic with respect to susceptibility. The magnetization and the response now have a direction and a magnitude, meaning that both M and H are vectors, and equation 4-1 must be re-written as:

$$\vec{M} = k\vec{H} \qquad (4\text{-}3)$$

Magnetic susceptibility is generally measured by comparing induction in a coil when a low-field (~0.1 mT) is applied to a sample within the coil, with induction in the coil when the same low-field is applied to air. Several commercial instruments are available, but the most popular systems use the same basic principle of measuring coil induction. Susceptibility measurements for this study were made using a Sapphire Instruments SI2B (Canada) at 19,200Hz, with an RMS field of ~ 1 Oersted.

AMS measurements determine the maximum, intermediate and minimum susceptibility directions (k_{max}, k_{int}, and k_{min} respectively) of each sample, which are orthogonal and define the axes of a magnitude ellipsoid of the second rank tensor of magnetic susceptibility. In order to determine the AMS ellipsoid of a sample, it is necessary to measure the susceptibility of the sample in several different orientations. Borradaile and Stupavsky (1995) describe a 7-orientation measurement scheme that brings all of the extremities of a sample equally close to the coil during the measurements, subduing the effects of sample heterogeneity. As the AMS ellipsoid is described by a symmetrical second rank tensor, the 7-orientation scheme of Borradaile and Stupavsky (1995) provides more than the six independent terms needed to solve the tensor for the orientations and magnitudes of the principal susceptibility axes.

4.2.2. Magnetic fabrics and orientation-distributions

4.2.2.1. AMS specimen fabrics

Anisotropy of magnetic susceptibility (AMS) of a rock sample represents the combined response to the applied field from all minerals in the sample. The specimen's AMS tensor must, therefore, represent the sum of the AMS tensors for the individual

minerals that make up that sample (Jackson, 1991). Each mineral in a sample contributes to the samples overall AMS signal based on:

(1) Its relative abundance in the sample

(2) Its susceptibility compared to other minerals in the sample

(3) Its own AMS, both in terms of shape and intensity

(4) Its orientation distribution or degree of alignment with other grains (Jackson, 1991)

Generally, it is the degree of alignment, or *orientation distribution,* of crystals in a specimen that is of interest, as with other petrofabric techniques. In the simplest possible case, where a specimen is monomineralic, the orientation-distribution of the crystals is the sole control on the specimen's AMS fabric. For example, if a group of magnetically anisotropic grains of one mineral were randomly oriented, the specimen's AMS fabric would be isotropic (Figure 4-4a). On the other hand, if the orientations of the grains was saturated in a given direction, i.e. all perfectly parallel, the AMS fabric of the specimen would be equivalent to the AMS of the crystal, both in shape and intensity (Figure 4-4b). Orientation distributions in a sample can vary between random and perfectly saturated, and every degree of alignment would produce a corresponding AMS fabric. In the case of diamagnetic and paramagnetic minerals, the AMS response represents the *preferred crystallographic orientation* (PCO), whereas in magnetite grains it is the *preferred dimensional orientation* (PDO) of grains that defines the AMS. This is because the AMS of individual diamagnetic and paramagnetic grains is a *crystalline anisotropy*, and a *shape anisotropy* in magnetite.

4.2.2.1.1. Crystalline anisotropy

Crystalline anisotropy is a result of lattice forces allowing spin configurations to align more readily in certain crystallographic directions than others. A crystal's response to an external field is therefore stronger in the 'easy' direction (Tarling and Hrouda, 1993), leading to a direction-dependent difference in susceptibility. The relationship between symmetry-system and susceptibility principal axes is summarized in table 4-2.

Table 4-2 Relationship between crystal and AMS principal axes (Nye, 1957)

Optical system	Crystal symmetry	Expected principal susceptibilities	Selected examples
Isotropic	Cubic	$k_{max}=k_{int}=k_{min}$	Garnet
Uniaxial	Tetragonal	$k_{max,int,min} \parallel$ a, b, c	Anthophyllite
Uniaxial	Hexagonal	k_{max} or $k_{min} \parallel$ c	Beryl
Uniaxial	Trigonal	k_{max} or $k_{min} \parallel$ c	Calcite, dolomite, quartz, tourmaline
Biaxial	Orthorhombic	$k_{max,int,min} \parallel$ a, b, c	Zoisite, cordierite, olivine, andalusite
Biaxial	Monoclinic	one of $k_{max,int,min} \parallel$ b	Micas, chlorite, hornblende, augote, epidote, orthoclase
Biaxial	Triclinic	none of $k_{max,int,min} \parallel$ a, b, c	Plagioclase, microcline, kyanite

4.2.2.1.2. Shape anisotropy

The application of an external field can align spin-moments in such a way that the grain is polarized. The magnetostatic (self-demagnetizing) force is weakest with the poles further apart, so that in a non-symmetric grain the surface poles will disperse to the ends of the long-axis of the grain. The induced field is therefore oriented preferentially parallel to the long-axis (Tarling and Hrouda, 1993). The result is that the AMS signal of a grain of multi-domain magnetite directly corresponds to the shape of the grain, and is not related to any crystallographic controls (Rochette, 1991). The transition between crystallographic and shape control on AMS is related to intrinsic susceptibility (k_i). Shape effects are negligible where $k_i<100{,}000\mu SI$, while shape control dominates where $k_i>2000 \times 10^6$ μSI. Pure magnetite may have k_i values in the hundreds or thousands,

while in TM_{78} titanomagnetite intrinsic susceptibility may be around 50,000μSI. Therefore, shape effects can only be ignored for very titanium rich compositions (pers. comm., Dr. Mike Jackson, IRM, University of Minnesota, Minneapolis). Shape anisotropy should dominate the AMS of both pure magnetite and TM_{60} found in ocean-floor basaltic rocks.

While the single-mineral example above is useful for illustrative purposes, most often in nature rocks are composed of two (or more) minerals, each of which contributes to the overall AMS of the rock. In this case, the AMS signal of the sample is a combination of the AMS signals of two groups of grains. If both groups have a paramagnetic response and are perfectly aligned with one another, the addition of the two signals is straightforward:

$K = kd + a_xPk_x + a_zPk_z$ (after Borradaile & Henry, 1997) (4-4)

where K is the overall susceptibility of the sample, kd is the diamagnetic contribution of the two groups, a is the proportion of each mineral x and z, Pk is the susceptibility of each mineral x and z. The slightly more complicated situation with the two groups having distinct but saturated orientation distributions requires similar but much more complicated mathematics, including the use of tensors:

$\mathbf{K} = \mathbf{p_a k_a} + \mathbf{p_b k_b}$ (after equation 2.6 of Tarling & Hrouda, 1993) (4-5)

where **K** is the susceptibility tensor of the sample, **p** is the proportion of mineral **a** and **b** in the sample, and **k** is the susceptibility tensor for the minerals **x** and **z**. Since each group in this example is perfectly aligned within itself, the tensor for the group is at its maximum and can be represented by the tensor for the mineral (as described above). Tensors are required because the alignment of the two groups is not coaxial, and direction as well as magnitude must be considered when summing their contributions to the overall

AMS of the sample. These equations imply that when more than one mineral is present in a sample their relative abundance or proportions can help define the samples AMS. Both the magnitude of susceptibility and intensity of anisotropy for the minerals remain an important factor, but the amount of each become a factor as well.

Other than quartz and feldspar, which only respond diamagnetically, most of the common rock forming minerals are paramagnetic, and have similar susceptibilities and anisotropies. This means that they will tend to mix (or compete) in the AMS signal of a sample, such that only when there is a significant difference in abundance or degree of preferred orientation does one mineral dominate the overall fabric. The special case is when a ferromagnetic mineral is included in the sample. The most common ferromagnetic minerals found in rocks (magnetite, hematite) rarely occur as more than a trace fraction (Jackson, 1991), but they always contribute greatly to the overall fabric of the rock. While the proportion term for these minerals (equation 4-5) is very small, their tensors are enormous in terms of susceptibility compared to the paramagnetic minerals. In igneous rocks the ferromagnetic minerals often crystallized at high temperature while the rest of the rock was still somewhat fluid (Butler, 1992), commonly resulting in a strong PDO due to magmatic flow. One can imagine how even a few parts per million of strongly oriented magnetite in a sample could completely overwhelm the paramagnetic signal in the sample (Borradaile, 1987).

The AMS tensors for each of the groups of minerals in a sample are equal to the AMS tensor of the minerals only when each has a perfect PDO or PCO. If the degree of alignment within each group is not saturated, then it too must be considered. The AMS for the sample would then be dependent on all four of the factors described by Jackson

(1991): the susceptibilities and anisotropies of the minerals, their orientation distributions, and their proportions in the sample.

Increasing the number of minerals in the sample to any number greater than two simply increases the number of terms in equation 4-5, extending the length of the calculation but not its complexity. Just as any number of combinations of minerals with different susceptibilities and anisotropies can exist in rocks, so too can any combination of degree of alignment and proportion of the minerals exist. It is the way in which these factors interact in equation 4-5 that determines the AMS fabric of any sample. Note that when AMS measurements are made in the laboratory, it is the overall or global AMS fabric of the sample that is determined, and while the aforementioned arguments are still valid, without further investigation neither the contribution nor the individual fabrics of minerals within a sample can be determined.

When examining the AMS response of a homogenous petrofabric, the concepts of shape and crystalline anisotropy lead to the interpretation that k_{max} may represent a mineral alignment, and k_{min} may define the pole to a mineral foliation (Borradaile & Henry, 1997). Jelinek (1981) presented a method of graphically representing the degree of eccentricity and shape of the AMS ellipsoid. The plot compares the parameter Pj, which describes the eccentricity of a fabric (Pj = 1 for a perfect sphere), to the shape parameter Tj (Tj = +1 for a perfect disk or oblate fabric and Tj = -1 for a perfect rod or prolate fabric).

Rochette et al. (1992) reviewed various aspects of the interpretation of AMS data, including the possibility of encountering 'inverse' fabrics. This situation may arise if a sample contains minerals that have k_{min} parallel to their long axis, opposite to that

predicted by shape anisotropy. A sample whose magnetism is carried solely by minerals such as Fe-bearing carbonates, cordierite, goethite, or SD-magnetite will have an inverse AMS fabric, with the k_{min} and k_{max} axes interchanged. Intermediate fabrics are possible in situations where both normal and inverse minerals contribute to a sample's susceptibility. It is, therefore, important to determine the mineralogical sources of magnetism in samples with AMS fabrics that do not correlate with fabric orientations (Rochette et al., 1992). Non-correspondence of AARM (Section 4.4.2 below) and AMS principle axes characterizes an inverse fabric, whereas in normal fabrics the principal axes of AMS and AARM correspond, e.g. k_{max} with $AARM_{max}$ (Borradaile & Henry, 1997).

4.2.2.2. AARM specimen fabrics

Remanent magnetism is that which ferromagnetic substances retain in the absence of an external field (M_R in Figure 4-3c). The causes of AARM are similar to those outlined for AMS, however the technique for measuring AARM is quite different. The first step is to erase any previously acquired remanence, or NRM, from the sample. This is accomplished using a Sapphire Instruments SI-4 AF demagnetizer. In this study a peak AF field of 200 mT in three orientations was required to ensure complete demagnetization of the samples. An anhysteretic remanent magnetism (ARM) is then applied to the sample in the seven directions of the Borradaile and Stupavsky (1995) scheme. The ARM was applied over a window of 60 mT to zero, with a constant DC bias field of 0.1 mT superimposed on a decaying AF with a peak field of 200 mT. Remanence was measured after ARM is applied in each orientation, using a Molspin spinner magnetometer. Werner and Borradaile (1996) showed that AF demagnetization

is not always necessary between each orientation. The AARM fabric can then be calculated by comparison of the strength of the remanence in each direction.

AARM was determined for 40 cores collected from two sites, Panagea and Konia (Borradaile and Gauthier, 2002). AARM isolates the ferromagnetic response to an applied field, which makes it possible to distinguish (qualitatively at least) between the ferromagnetic and paramagnetic/diamagnetic contributions to the overall magnetic fabric of the rock. Borradaile and Gauthier (2002) compared AARM fabrics of the two sites mentioned above with AMS and other rock magnetic data in order to aid in interpretation of AMS data. Care must be taken to recognize inverse fabrics or other anomalous fabrics before reliable interpretations can be made (Borradaile et al., 1999).

4.2.2.3. Spatial variation of magnetic fabrics

Generally speaking, magnetic fabrics are homogenous on an outcrop scale, such that in this study the orientations of the three principal susceptibility axes of the 3 to 6 oriented cores recovered from each outcrop visited show little variation. However, the magnetic fabrics tend to vary between outcrops and structural domains. It is this *spatial variation* that is of interest here; some areas may be expected to have generally steeply inclined maximum susceptibility axes, while other areas may have dominantly shallow maximum susceptibility axes.

The characterization of the orientation distribution of a group of sample fabrics requires tensor-statistics, as traditional density-contoured stereonets may yield false means for the principal axes (Borradaile, 2001). The tensor-statistical approach requires that the means of each axis remain mutually perpendicular, and allows for the calculation of cones of confidence about each mean axis. Traditionally, it is the 95% confidence

limit that is plotted (Figure 4-4c,d). The sense of symmetry of these confidence regions, when plotted on a stereonet, may allow the fabric to be characterized as oblate (S>>L; Figure 4-4c) or prolate (L>>S; Figure 4-4d). In these cases, it is the directional uncertainty in the principle axes that may define the shape of the fabric. For example, if a given sample of prolate shaped specimen fabrics have strongly aligned minimum susceptibility axes, yet some freedom in the orientation of the maximum and intermediate axes, an oblate shaped fabric would result (Figure 4-4c).

Due to the high-variability in intensity of bulk susceptibilities between specimens, it may be useful to normalize the specimens according to their bulk susceptibility (Borradaile, 2001). This process ensures that each specimen's principal axes contribute equally to the mean orientation of the principal axes, based strictly on orientation. Neglecting this step could result in a poorly defined but highly susceptible sub-fabric masking a well-defined and pertinent petrofabric.

4.3. Requirements for primary flow determination

In the preceding sections it has been shown that the longest axes of particles (mineral grains) suspended in flowing magma in a dike will tend to become aligned with the flow direction. Also, their shortest axes will tend to align perpendicular to the flow plane. Furthermore, the idea that AMS fabrics can faithfully detect the preferred orientation distribution of flow-aligned grains has been established. In the simplest terms, k_{max} (*magnetic* lineation) is expected to correspond to the *magmatic* lineation, while k_{min} may be parallel to the pole of the *magmatic* foliation. The simple thought experiment, which requires magma flow, and therefore flow lineation, to be within the dike plane (section 4.1), also requires that k_{max} lie within the flow (dike) plane. k_{min} may

(depending on the shape of the fabric) be parallel to the dike pole, in which case the *magnetic* foliation (k_{max}-k_{int} plane) should be co-planar with the dike. Some departure from these theoretical requirements may be expected, however a simple test of whether or not AMS fabrics are successfully recording flow-alignment is this:

- if k_{max} does not lie within the dike plane, or convincingly close to it, then it must be assumed that a primary flow fabric has not been determined, and therefore may not be used to infer the location of magma source
- a mineral lineation (k_{max}) that lies within or convincingly close to the dike plane is assumed to represent a primary flow fabric, as in the absence of penetrative deformation there are no geologically reasonable causes of a mineral lineation within the dike plane other than flow.

Many previous authors have used AMS fabrics to determine the orientations of magmatic flow in igneous rocks (see Varga et al., 1998 for a literature review). Three main conclusions that are particularily pertinent to this study can be drawn from the previous research:

(1) AMS is a useful technique for determining magma and solid state flow orientations in the sheeted dike complex, gabbro, and mantle sequence rocks of ophiolites. Many authors, such as Rochette et al. (1991, 1992), Studigel et al. (1992) and Varga et al. (1998) have shown that, in sheeted dike rocks, k_{max} is convincingly close to parallel with the magma flow axis. Abelson et al. (2001) and Borradaile and Lagroix (2001) determined petrofabrics using AMS in the gabbro and mantle suites respectively, and found a strong agreement between AMS and macroscopic and microscopic magmatic and tectonic fabrics.

(2) Rochette et al. (1991, 1992) were able to prove that where a pattern in magma flow directions exists, it can be discovered by determining the AMS of many samples on a scale appropriate to the scale of the mechanism that created the pattern. They were able to observe a strong preference for vertical magma flow in sheeted dikes from the Semail ophiolite, Oman, supporting the fast-spread origin of the Semail crust

(3) In the sheeted dike complex of the Troodos ophiolite, Cyprus, Staudigel et al. (1992, 1999), Varga et al. (1998), and Tauxe et al. (1998) observed both shallow and steep magma flow, indicating that centralized magma sources and along ridge lateral magma transport may have been a feature of the Troodos oceanic crust, supporting the slow-spread origin of the ophiolite. No regional pattern in flow directions could be determined however, due to the highly focussed and/or the broad extent of the studies.

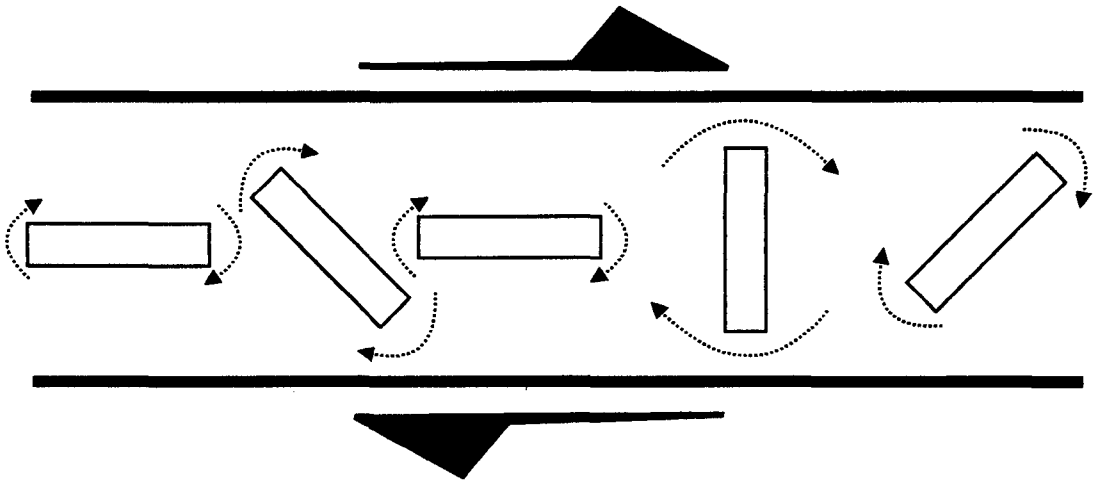

Figure 4-1. Model of rigid particle rotation due to shear of Nicolas (1987). Arrows around particles indicate sense of rotation, and the length of the arrows are proportional to angular velocity. Note that a particle perpindicular to shear (flow) rotates more quickly than one parallel to shear.

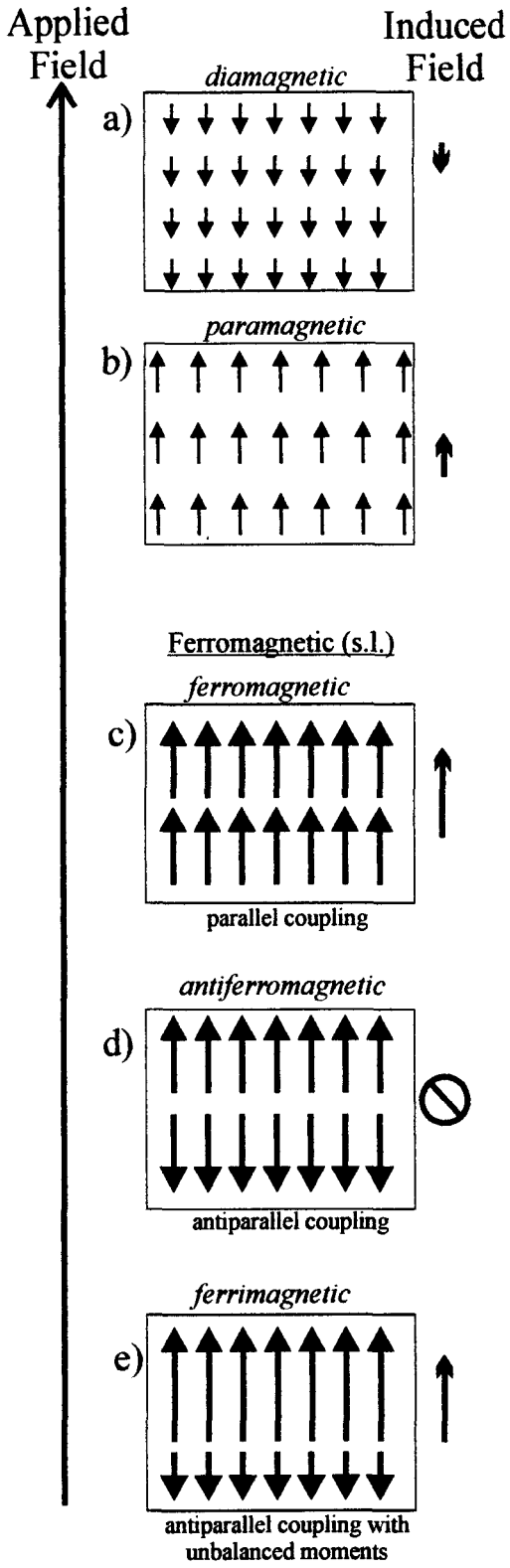

Figure 4-2. Schematic diagram relating applied field to induced field for (a) diamagnetic, (b) paramagnetic, and (c),(d),(e) ferromagnetic (*sensu lato*) responses.

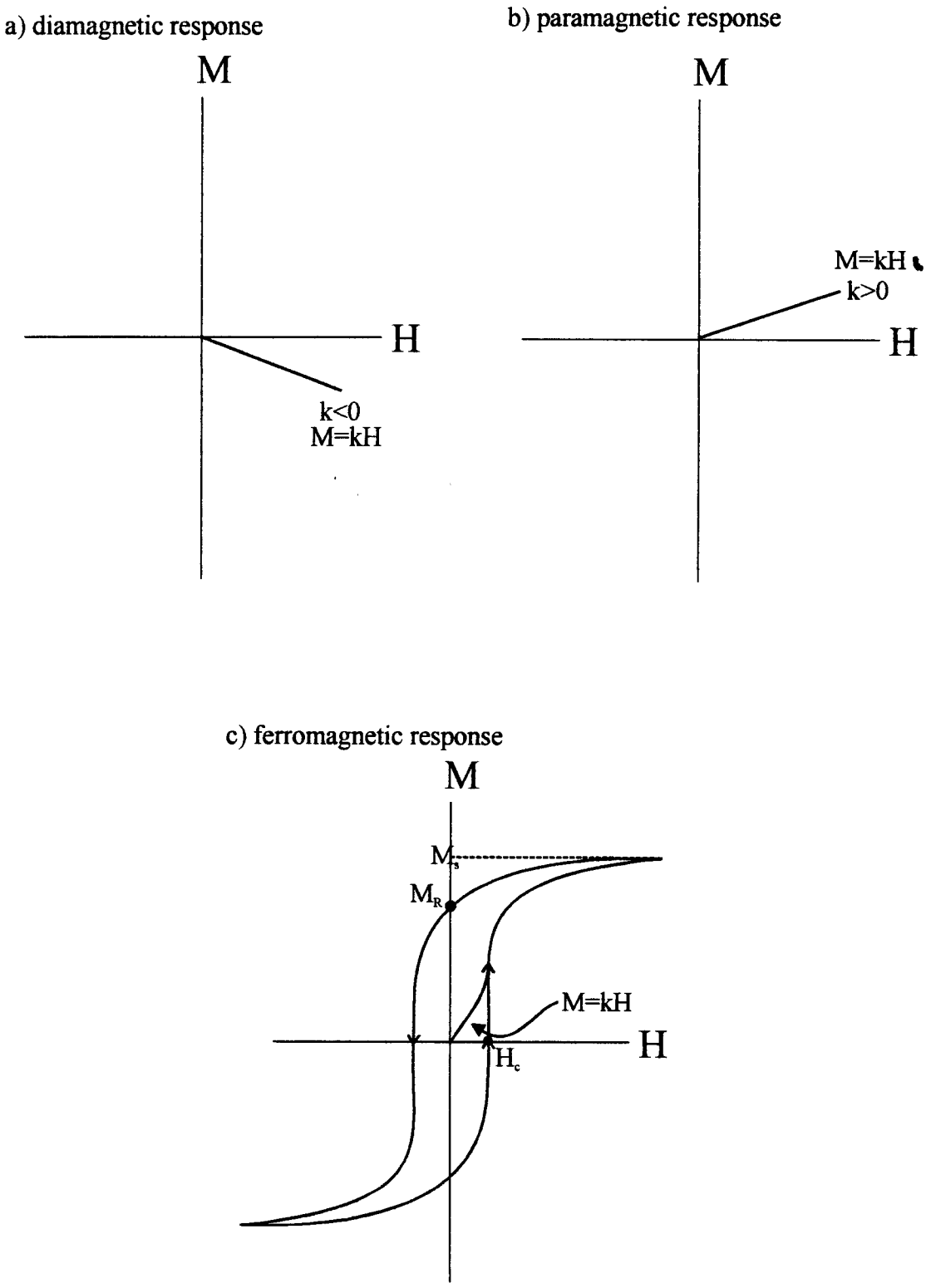

Figure 4-3. Plots of applied field (H) versus induced field (M) for (a) diamagnetic, (b) paramagnetic, and (c) ferromagnetic responses.

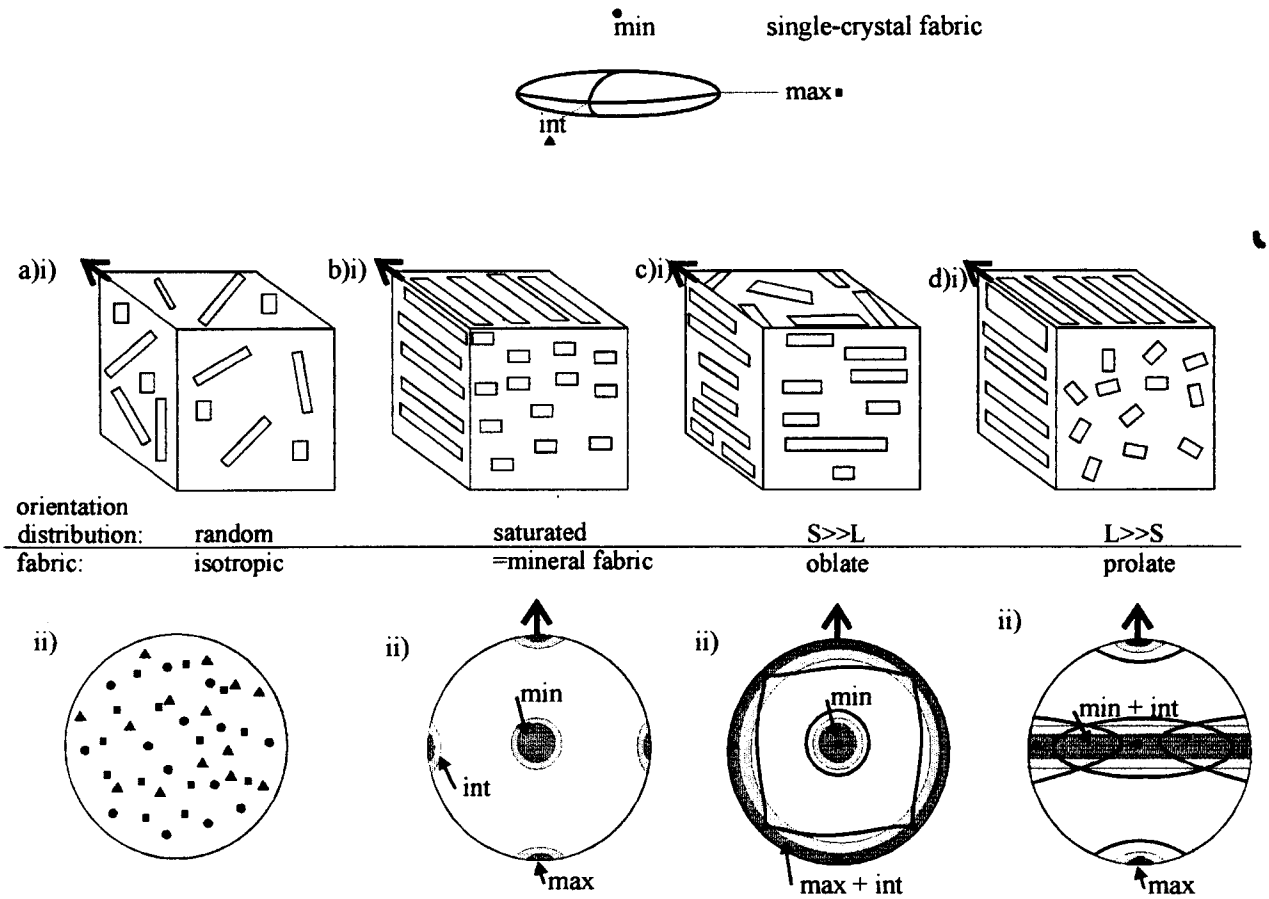

Figure 4-4. Block diagrams (i) and resulting fabric (ii) of (a) random mineral orientations in a sample, (b) saturated alignment of minerals in a sample, (c) S>>L orientation distribution of sample fabrics, and (d) L>>S orientation distribution of sample fabrics. Shaded regions represent density contours, and thick lines represent possible 95% confidence regions about mean-tensors. (After Borradaile, 2001)

5. Results

This chapter describes the results of AMS measurements made on 1289 oriented cores recovered from 440 hand samples collected in 2000. The AMS and AARM results of the 291 cores collected in 1999 can be found in Borradaile and Gauthier (2001). As the intent of this study is to recognize patterns in the orientation-distributions of the principal susceptibility axes of the specimens, the data will spatially analyzed and grouped into homogenous sub-areas. The orientation of dikes and magnetic fabrics will be described for each sub-area individually, and each will be evaluated in terms of the criteria described for primary magmatic flow (Section 4.3).

5.1. Statistics

The descriptive statistics for bulk susceptibility of specimens, which is given by the average susceptibility of the 7 measurements made during AMS determinations, are listed below, in Table 5-1, and plotted graphically in Figure 5-1i. The frequency distribution of k_{mean} results (Figure 5-1) shows that the sample has a positively skewed distribution, similar to a log-normal distribution (Figure 5-1ii). A log-normal distribution commonly arises where a rare component, such as a sub-population of high-susceptibility specimens, may be combined with a population of lower susceptibility specimens. In this case, a high-susceptibility ferromagnetic accessory mineral may be competing with a paramagnetic matrix.

Table 5-1. Descriptive statistics of bulk susceptibility data; see also Figure 5-1

Descriptive Statistic	Value (μSI)
Count (n)	1289
Mean	41 461
Median	37 801
Mode	42 500
Range	165 207
Maximum	165 590
Minimum	383
Standard error	783
Standard deviation	28 126
95% Confidence Level (about mean)	1 537

5.1.1. Jelinek plot

Jelinek (1981) presented a method of graphically representing the degree of eccentricity and shape of the AMS ellipsoid. The plot compares P_j, which describes the eccentricity of a fabric ($P_j = 1$ for a perfect sphere), to the shape parameter T_j ($T_j = +1$ for a perfect disk or oblate fabric and $T_j = -1$ for a perfect rod or prolate fabric). A density contoured (count per 1% area) Jelinek plot of the AMS fabrics measured in this study is presented in Figure 5-2. As seen in Table 5-2, fabric shapes vary from nearly perfectly prolate to nearly perfectly oblate (T_j range from 0.992 to -0.961). Interestingly, the more anisotropic specimens tend to be preferably oblate in shape (Figure 5-2).

Table 5-2. Descriptive statistics of Jelinek (1981) parameters P_j and T_j for AMS fabrics in this study; se also Figure 5-2.

Descriptive Statistic	Value (μSI)	
	Pj	Tj
Count (n)	1289	1289
Mean	1.022	0.097
Median	1.017	0.123
Mode	1.012	0.102
Range	0.131	1.953
Maximum	1.133	0.992
Minimum	1.002	-0.961
Standard error	0.0005	0.012
Standard deviation	0.016	0.416
95% Confidence Level (about mean)	0.0009	0.023

5.2. Spatial-averaging of k_{max}

In order to identify spatial patterns in the orientation of the maximum susceptibility axes, k_{max} orientations were spatially averaged over the study area. To ensure that meaningful comparisons with dike orientations (Section 3.1.2) could be made, the same averaging parameters were used to smooth k_{max} data as were used to smooth dike orientations. As expected, the moving circle method (5km radius, 1km spacing) weighted by nearest neighbour smoothing parameters provided the best balance between smoothing and undesired edge-effects (Figure 5-3). At first inspection, a spatial pattern in k_{max} orientations is obvious, in both trend and plunge. There are clear regions of steeply inclined k_{max} (short arrows on Fig. 5-3), and adjacent areas of shallowly inclined k_{max} axes (longer arrows). The trend of steeply inclined axes is difficult to observe (or indeterminate when vertical), whereas there is trend variation in the shallowly inclined axes. There are regions of generally north-south oriented k_{max} axes, as well as areas with east-west trends dominating.

5.2.1. Sub-area classification

When dealing with a large number of specimens spread over a large areal extent, it is important to evaluate AMS data in structurally homogenous groups. This is especially important in this study, as the intent is to differentiate between areas of generally steep k_{max} inclinations and areas of generally shallow k_{max} inclinations. In addition, filtering AMS data into sub-areas with similar k_{max} orientations *and* similar dike orientations will facilitate the evaluation of AMS as an indicator of magmatic flow as described in Section 4.3. An axial magma chamber may have underlain areas with both steep k_{max} *and* AMS fabrics that satisfy the criteria laid out in Section 4.3. Conversely,

areas with both shallow k_{max} *and* AMS fabrics that meet the criteria for primary flow may have been located at some distance from an axial magma chamber.

By plotting spatially averaged k_{max} orientations (Figure 5-3) and dike orientations (Figure 3-2c) on the same map, it is possible to simultaneously observe patterns in the AMS and dike data, and assign the data to corresponding sub-areas. First, regions of predominantly steep k_{max} are filtered out of the entire data set (coloured boxes in Figure 5-4). These areas are then sub-divided further to contain both consistent AMS data and consistent dike orientation, and are designated as primarily steep k_{max} sub-areas with the letters A through F (Figure 5-4). Regions of the study area not included in the steep k_{max} sub-areas are also grouped according to fabric and dike orientation. As dike orientation tends to vary systematically east to west and north to south (with proximity to the STTFZ), the most logical grouping scheme follows this pattern. The study area is therefore divided into four north-south columns (designated I through IV) and four east-west rows (designated 1 through 4). Boundaries of each column and row are conveniently placed so that within each intersection (e.g. I-1, II-2, III-3 etc.) dike and fabric orientations are consistent (Figure 5-4). Some variability in both parameters is permitted at this point, as the actual (not spatially averaged) AMS data and dike orientations within each sub-area will be evaluated further.

In the following sections, both the sub-areas with predominantly *steep* k_{max} (A to F) and those with predominantly *shallow* k_{max} (I-1 to IV-4) will be evaluated in terms of the flow-kinematic model described in section 4.3. The dike and magnetic fabric orientations within each will be described, followed by a brief discussion of the potential for each

sub-area's AMS fabrics to faithfully represent the orientation of primary magmatic flow, and if applicable, the orientation of that flow-axis.

5.3. AMS results

Stereonets: All of the density contoured stereonets presented here are equal-area lower hemisphere projections, contoured at 0E, 2E, 4E...etc., where E is the expected uniform density, i.e. the density expected for an isotropic orientation-distribution of the points. Because k_{min} may define the pole to foliation, and k_{max} may define a mineral alignment (Borradaile & Henry, 1997), minimum axes are commonly interpreted as poles to foliation, and maxima as lineations. Of course, for perfectly prolate fabric ellipsoids there could be no foliation, and for perfect oblate ellipsoids there is no lineation.

Tensor statistics: The stereonets presented here for tensor data are equal-area, lower hemisphere projections of 95% confidence limits about the mean tensors of the principal AMS axes. The mean tensor is calculated in such a way as to take both the orthogonal nature of the axes and the magnitude of each sample's principal axes into account during the calculation (Jelinek, 1978; using SI201.exe program algorithm). To account for the considerable range in anisotropy values, the tensors have been normalized by dividing the value for each axis by the mean value of that sample. This treatment ensures that each sample's anisotropy contributes equally to the orientation of the mean tensors, regardless of the magnitude of the sample's susceptibility. The foliation plane included in each stereonet represents the plane that contains the maximum and intermediate principal axes. For prolate ($T_j < 0$) or weakly oblate (T_j slightly > 0) the foliation plane is not geologically meaningful (i.e. the rock may not show a well-developed foliation).

5.3.1. Primarily steep k_{max} sub-areas

5.3.1.1. Sub-area A

At ~13km^2 in area, sub-area A is the most northwesterly of the steep-k_{max} regions identified (Figure 5-4). Specimens were collected from both the Sheeted Dike Complex and the Basal Group, in the vicinity of the town of Laghoudera (UTM ref. 501000E 3869000N). Twelve dike orientations were measured, and AMS determinations made on 21 individual cores. Dikes in this subarea have a relatively constant N/NW strike and ~45° dips to the northeast (Figure 5-5a). A slight smear towards the south and steeper dip in the contoured dike poles is present, and indicates that a small number of dikes in this area strike to the west and dip shallowly to the north. A strong clustering of k_{max} axes plunging to the east and lying close to the dike plane is present, with any variability in the data tracing a very weak plane that is coplanar with the mean dike plane (Figure 5-5b). A similarly strong cluster of k_{int} axes plunges very shallowly to the north, and lies close to the mean dike plane (Figure 5-5c). Some anomalous axes plot steeper and easterly along the dike plane, while a small number of points plot close to the cluster of mean dike poles, close to where k_{min} axes would be expected. A strong cluster of k_{min} data does in fact plot near the cluster of mean dike poles, however a small number of points plunge shallowly to the north, close to the main cluster of k_{int} axes (Figure 5-5d). Mean tensors of the principal susceptibility axes plot close to the main clusters observed in Figures 5-5b-d. The 95% confidence regions about the principal axes are small, and show a slightly oblate symmetry (maximum and intermediate cones elongated towards each other) (Figure 5-5e). The confidence cones are not perfectly orthogonal, possibly indicating the existence of multiple competing sub-fabrics (Borradaile, 2001). In general, while only a small number of data are included, the AMS results of sub-area A fulfill the

theoretical requirements for magma-flow described in Section 4.3. k_{max} and k_{int} lie close to the dike plane, and k_{min} lies close to the pole to the mean dike. The *magnetic* lineations, and therefore the *magmatic* (or flow) lineations, show a definite preference for steep inclination.

5.3.1.2. Sub-area B

Sub-area B is located adjacent to and south of sub-area A, and is ~30km^2 in area (Figure 5-4). Fifty-one dike orientation measurements were made at exposures within this sub-area, and 91 oriented cores were obtained. The mean dike plane strikes north-south, and dips to the east at ~60°. A very strong clustering of dike poles is evident for this orientation (Figure 5-6a). There is a slight smearing of dike poles towards the south, indicating that some of dikes in this subarea have a more northwesterly strike, and dip to the northeast. Maximum susceptibility axes are well clustered around an east trend and ~60° plunge, and lie within the dike plane (Figure 5-6b). A portion of the distribution of k_{max} data seems to trace a plane perpendicular to the mean dike plane, however the majority of the data do coincide with the mean dike. A very weak cluster in k_{int} axes is present, although in general the data is widely scattered (Figure 5-6c). A small number of k_{min} axes plot close to the mean dike pole, however the data is scattered (Figure 5-6d). The strongest clustering of points actually lies within the dike plane, close to the weak k_{int} cluster. It appears that while k_{max} axes are well constrained, k_{int} and k_{min} are not confined to either the mean dike plane, or parallelism with the mean dike pole, respectively. The mean tensor confidence cones about the three principal axes show a strong prolate (L>>S) symmetry, explaining the high variability in intermediate and minimum axes compared to maximum (Figure 5-6e). As with sub-area A, the tightly constrained k_{max}

axes that plunge steeply within the dike plane meet the requirements for indicating primary magmatic flow, and as such sub-area B is considered to be a region of steep magmatic flow.

5.3.1.3. Sub-area C

Sub-area C is ~18km^2 in area (Figure 5-4), and is centred around the town of Palekhori (UTM ref 508000E 3865000N). 118 oriented cores suitable for AMS measurements were recovered. The 131 dike orientations measured in this sub-area have a bimodal distribution, with one set of dikes striking almost north-south, and another north-northeast (Figure 5-7a). The stronger cluster of dike poles is related to the north-northeast set, resulting in the mean dike for the sub-area having this orientation. Maximum susceptibility axes show similar bi-modality, with a strong cluster of points plunging north at around 60° (related to the north-south vertical dikes) and a dispersed but significant group plunging steeply within the mean dike plane (Figure 5-7b). k_{int} axes are widely scattered, however a weak cluster exists that is close to the cluster of dike poles for the north-northeast striking dike set (Figure 5-7c). The remaining intermediate axes trace a crude plane perpendicular to the mean dike plane. Strongly clustered k_{min} axes plunge gently north and south. The only obvious variability in k_{min} data relates to the bimodality of dike orientations, with a smear in minimum axes between the north-south set and the north-northeast set (Figure 5-7d). Confidence cones about mean tensors of AMS data are small, and have a moderate oblate symmetry (S>L) with intermediate and maximum confidence cones extending towards each other (Figure 5-7e). The mean tensor of k_{max} plunges near vertical, and close to both the mean dike plane and the north-south striking subset. Mean tensors of k_{int} and k_{min} axes depart significantly from

expected, appearing to 'swap' orientations with k_{min} lying within the dike plane and k_{kint} co-linear with the pole to the mean dike. This fact does not exclude the AMS of sub-area C from consideration as a magmatic flow indicator, as the axes of maximum susceptibility meet the requirements laid out for primary flow (Section 4.3).

5.3.1.4. Sub-area D

Sub-area D covers ~ 16km^2, and includes 112 oriented core samples. This sub-area is directly south of sub-area C, and from Figure 5-4 appears to have similar AMS fabrics to C. There is a significant difference, however, in the orientations of dikes between the two. Sub-area D includes 133 dikes from within a few kilometers of the Arakapas Fault Belt (AFB), meaning that the mean strike of dikes is closer to east-west than in areas further from the fault (Figure 5-4). Nearly all of the dikes measured in this area dip close to vertical, while a slight smear in strike from east-west towards northeast-southwest is evident (Figure 5-8a). k_{max} axes cluster strongly close to vertical (Figure 5-8b), and as most dikes are close to vertical k_{max} must lie within them. There is significant variability (unrelated to dike-strike) in the data, with a poorly defined distribution tracing a plane perpendicular to that of the mean dike plane. Intermediate susceptibility axes are highly variable, with a scatter of points between north/horizontal (close to the mean dike pole cluster) and east-northeast shallow (within the mean dike plane)(Figure 5-8c). As with previously described sub-areas, k_{min} axes show a similar pattern to k_{int}. A weak cluster of k_{min} axes close to the group of mean dike poles combined with a stronger cluster plunging shallowly to the west (close to the mean dike plane) makes up the distribution (Figure 5-8d). Again, like other subareas, the mean tensor maximum axis is close to vertical and close the mean and secondary dike planes, while intermediate and

minimum mean tensors are in unexpected orientations (Figure 5-8e). In this case, the apparent 'swapping' of minimum and intermediate axes seen previously is incomplete, with both lying between their expected and swapped orientations. Nonetheless, the *magnetic* lineation (k_{max}) likely records the primary *magmatic* lineation.

5.3.1.5. Sub-area E

With the town of Odhou at it's centre (UTM ref 515000E 3860000N), this ~20km^2 sub-area includes sites from within ~100m of the AFB (Figure 5-4). Of the 87 dike orientations measured in the field, those closest to the AFB strike almost east-west and are approximately vertical. In the northern part of this sub-area dikes strike northeast-southwest and are approximately vertical. The stronger cluster of dike poles marks the northeast-southwest striking dikes, with a smearing of the remaining data towards poles to east-west striking dikes (Figure 5-9a). The mean dike plane is nearly vertical and strikes east-northeast, between the east-west and northeast-southwest groups. Eighty-six oriented cores were obtained form sub-area E. Maximum susceptibility axes cluster within the mean dike plane, plunging very steeply to the southwest (Figure 5-9b). There is some variability in k_{max} orientations, which weakly trace a plane perpendicular to the mean dike plane. k_{int} axes are widely scattered, however they do seem to weakly trace a plane similar to that which k_{max} data traces (Figure 5-9c). Minimum susceptibility axes are less scattered than k_{int}, and have a good clustering of points within the dike plane, trending east and plunging close to horizontal. Scattering of minimum axes defines a horizontal girdle, with a poor cluster close to the pole to the mean dike (Figure 5-9d). The elongation of the maximum and intermediate tensor confidence regions towards one another, and the very small confidence region around the minimum mean tensor axis

indicate a strong oblate symmetry (S>>L) for this sub-area (Figure 5-9e). The magnetic foliation described by the symmetry of the tensor confidence cones is oriented perpendicular to the mean dike plane. As the mean tensor for k_{max} lies within the dike plane and is close to vertical, the assumption that it represents alignment by magmatic flow is valid.

5.3.1.6. Sub-area F

Sub-area F is relatively large at ~30km^2 (107 oriented cores), and occupies much of the northeastern portion of the study area (Figure 5-4). The 37 dikes measured here have an almost constant northeast strike and ~60° dip to the southeast (Figure 5-10a). While the distribution of k_{max} axes traces a plane almost perpendicular to the mean dike plane, there is a good clustering of points within the dike plane, plunging >45° to the east-northeast (Figure 5-10b). k_{int} axes are poorly grouped around the dike plane, with a generally shallow plunge to the southwest (Figure 5-10c). A further pattern in the distribution of intermediate axes may be the tracing of a similar plane to that which k_{max} data traces, however this is weak at best. The distribution of minimum susceptibility axes roughly traces a horizontal girdle, with two weak clusters of data (Figure 5-10d). One of these clusters lies within the dike plane (shallow plunge to the southwest, as per k_{int}), while the other groups close to the pole to the mean dike. Confidence regions about the mean tensors of the principal susceptibility axes are small, and mean tensor axes lie close to the theoretical case described in section 4.3 (Figure 5-10e). The maximum and intermediate mean axes lie within the mean dike plane, and the minimum close to the dike pole. A slight clockwise offset of the dike plane from the magnetic foliation plane is within error limits of measurement, or may be related to brittle re-orientation of dikes as

described by Borradaile and Gauthier (2002). Sub-area F is interpreted here to be a region of generally steep magma-flow.

5.3.2. Primarily shallow k_{max} sub-areas

5.3.2.1. Sub-area I-1

Located in the extreme northwest corner of the study area, sub-area I-1 contains only 2 sites (Figure 5-4). A total of 6 dike orientation measurements were made, and 6 oriented cores were recovered for AMS determinations. The small number of sites (and specimens) in this sub-area preclude it's data from being meaningfully interpreted. The six dikes included in this area are all close to vertical, with strikes ranging from NW-SE to N/NW-S/SE. AMS principal axes show a relationship to the mean dike plane which is opposite to that expected from magma kinematics, with k_{max} corresponding to the dike poles, and k_{int} and k_{min} lying in the dike plane (Figure 5-11a). As such, AMS data from this sub-area may not represent magma-flow within the dikes.

5.3.2.2. Sub-area I-2

Geographically, much of sub-area I-2 has been included in sub-areas A and B (Figure 5-4). Fifty-one oriented cores make up the shallow k_{max} set from this area, and are therefore part of this sub-area. Fifty-three dike orientations were measured in the field, and a relatively constant north-south strike and ~60° dip was recorded. While inclinations are generally shallow, k_{max} axes trend east and west, and rarely lie convincingly close to the mean dike plane. In cases where k_{max} is close to the dike plane, it trends to the east and plunges ~60°, appearing to be a steep axis rather than a shallow one. The axes of intermediate susceptibility have an interesting distribution that is masked by the location of the mean tensor. Some points group to trace the mean dike

plane, while others cluster around the main group of dike poles. k_{min} axes, however, rarely correspond to the dike poles, grouping instead within the dike plane, trending south and plunging close to horizontal. This fabric appears to be blended, with each principal AMS axis in an unexpected orientation relative to the mean dike plane. Some of the data included in this sub-area *may* faithfully record magmatic flow (if so these specimens should be included in sub-area A), however the relationship between AMS and flow-alignment is ambiguous at best.

5.3.2.3. Sub-area I-3

Variability is the rule for sub-area I-3, which is located along the western side of the study area. The 51 dikes are generally steeply dipping, but their strike varies between north-south and almost east-west. The mean dike plane is therefore almost vertical and strikes slightly north of northeast. 44 oriented cores were collected from this area. k_{max} orientations are highly scattered, with a weak grouping of data plunging shallowly to the south, and scattered throughout the dike plane. The trend of intermediate axes are scattered as well, however they generally have a shallow plunge. k_{min} group weakly around a west trend with moderate plunge, close to the poles to north-south dikes. Large 95% confidence cones about the mean tensors reflect the high variability in the data. The mean tensor maximum susceptibility axis lies close to the dike plane, plunging ~45° to the southeast, with its confidence cone elongated parallel to the mean dike plane. The intermediate mean tensor axis is horizontal and trends southwest-northeast, close to the dike plane. Plunging ~30° to the northwest is the mean tensor for k_{min}. The confidence region around k_{min} encloses the majority of the dike poles. Despite variable dike orientations and high variability in the AMS data, the magnetic fabric of this subarea may

be regarded to approximate magmatic flow, as k_{max} and k_{int} mean orientations are generally related to the mean dike plane, and k_{min} axes plot close to dike poles.

5.3.2.4. Sub-area I-4

As with sub-area I-3, the dike orientations measured in I-4 are highly variable, however in this sub-area the scatter is clearly related to proximity to the AFB, and the gradual swing in dike-strikes to parallelism with it as described first by Simonian and Gass (1978). Dips are generally greater than 60°, and strikes vary between north-south and east-west. Only northeast dipping dikes are absent. Despite the variability, a strong cluster of dike poles relate to a northeast-southwest striking mean dike plane for the area that dips very steeply. The extent of variability in dike orientations is not present in the distributions of principal susceptibility axes. k_{max} and k_{min} axes group strongly, with k_{max} axes plunging gently to the south (and north) and k_{min} axes gently to the west (and east). The intermediate susceptibility axes do show high scatter, with only a weak clustering of points plunging ~45° to the north. Mean tensors of principal susceptibility axes confirm this. 95% confidence regions are generally small, and show a slightly non-orthogonal but prolate (L>S) symmetry. The magnetic fabrics of this sub-area fit very well the criteria described in Section 4.3 for primary magmatic flow, however only in the case of a north-south vertical dike. As stated previously, dike orientations vary between north-south and east-west, with a mean dike plane that is near vertical and strikes northeast-southwest. It would appear that that magnetic fabrics that originated in north-south dikes have become misaligned by cataclastic shearing of some dikes to a more east-west orientation. This can be explained by considering dike trends that may shear on an outcrop scale, whereas on the specimen scale the rotation is accomplished by the formation of a cataclastic

foliation. This process has been shown to lead to the loss of parallelism between dike planes and magnetic fabrics, without the disruption of the primary nature of the fabric (Borradaile and Gauthier, 2002; see Chapter 6). As magmatic flow ceased prior to dike rotation (Bonhommet et al., 1988), the AMS fabrics of this sub-area may be used as a flow indicator. Shallowly plunging k_{max} axes within the dike plane indicate lateral magma-flow.

5.3.2.5. Sub-area II-1

Sub-area II-1 is located along the northern margin of the study area. 39 dike orientations were measured and 52 oriented core samples were collected from this area. The dikes are of generally constant orientation, dipping steeply and striking to the north-northeast. Contrary to the high scatter seen in the I-group sub-areas (above), AMS principal axes in this sub-area are well constrained. A strong grouping in k_{max} axes plunges moderately to the south. The remainder of the distribution traces a north-south vertical plane, with minor groupings of points shallow to the north. Intermediate susceptibility axes are distributed along the trace of the mean dike plane for the area, with weak clusters of data dipping moderately/steeply to the north and south. A very strong grouping of k_{min} axes trending east-west and plunging close to horizontal is offset anti-clockwise from the dike pole groups by less than 15°. A strongly oblate (S>>L) symmetry of the fabrics is evident from the tightly constrained 95% confidence region around the mean tensor minimum axis and high elongation, within the magnetic foliation plane, of k_{max} and k_{min} confidence regions. The mean tensor of k_{max} plunges very shallowly to the north, and lies within 15°of the mean dike plane, indicating that magmatic flow was likely the main control on generating these magnetic fabrics. The

clockwise offset of the mean dike plane from the magnetic foliation plane is similar to that expected as a result of cataclastic shear close to the AFB (see sub-area I-4 above). The generally northeast strike of dikes in this sub-area, however, may not be related to shear along the STTFZ.

5.3.2.6. Sub-area II-2

Sub-area II-2 includes specimens from both the Basal Group and Sheeted Dike Complex, and is located in the north-central portion of the study area. Many of the specimens within the boundaries of this sub-area are included in sub-areas A, B, and C. Sampling density here is high, leaving 181 oriented cores and 134 dike orientation measurements within II-2. Dikes are of very constant orientation, striking north-south and dipping approximately 75° to the east. Rare dikes in this area dip to the west or strike north-northeast or north-northwest. The orientation-distribution of k_{max} axes in this sub-area traces the mean dike plane, with strong groupings of points dipping very shallowly to the north and south. The distribution of intermediate susceptibility axes weakly traces the mean dike plane, however the data is scattered compared with k_{max}. A moderate grouping of data occurs dipping steeply to the east, within the mean dike plane. k_{min} axes show a similar variability in orientation as k_{int}, however group strongly around the dike pole cluster for the area. k_{min} orientations tend to scatter around the periphery of the stereonet, with a weak group occurring at south/horizontal, within the dike plane and close to a group of k_{max} points. Inspection of the mean tensor axes and 95% confidence regions shows that the AMS data are clearly related to the mean dike orientation in this sub-area. The mean tensor k_{max} and k_{int} axes lie within the mean dike plane, and their confidence regions are elongated within the dike plane. This means that the *magnetic*

foliation is co-planar with the mean dike, and as such the mean tensor of the minimum susceptibility axis lies parallel to the pole to the mean dike. Despite some scatter in k_{min} data, the confidence cone about its mean tensor axis is very small. The symmetry of the confidence regions of the three principal susceptibility axes indicates a strongly oblate (S>>L) regional fabric. There is little departure in this data from the theoretical case described in section 4.3, and therefore the *magnetic* fabrics of sub-area II-2 must represent a primary *magmatic* flow fabric. The strong grouping of k_{max} axes plunging very shallowly to the north indicates nearly horizontal magma-flow.

5.3.2.7. Sub-area II-3

As with II-2, many of the sites within II-3 have been included in previous sub-areas (C and D). 42 sites with 128 dike measurements and 135 oriented cores are included here. Dike orientations are extremely consistent. The mean dike plane for the area strikes northeast-southwest and dips very steeply to the northwest. Only a small number of dikes in this subarea depart from the mean dike. AMS axes are scattered, however a pattern is detected in their orientation-distribution. k_{max} axes trace weakly a north-south/steep plane, with several weak clusters dipping both steeply and shallowly. Despite slightly more scatter in k_{int} axes than k_{max}, they tend to trace a plane similar in orientation to the mean dike plane. One moderate grouping of k_{int} axes occurs dipping shallowly on a southwest trend, within the mean dike plane. Scatter is high in the distribution of k_{min} axes, however two patterns are recognized: a moderate grouping of points at east/horizontal and the trace of an east-west vertical plane. The shallowly dipping cluster may be related to the cluster of dike poles for the area as there is a smear in the density contours towards the southeast and the dike poles, and the main groups are offset by less

than 45° trend. The trace of an east-west striking plane may be related to the existence of multiple sub-fabrics, which tend to cause an apparent axis swapping, and lead to the non-orthogonal nature of mean tensor confidence regions. While the 95% confidence region about the mean tensor minimum susceptibility axis is very small (and offset ~30° anti-clockwise from the dike pole group), the confidence regions about the maximum and intermediate axes are large and elongated toward each other. The elongation is not perfectly co-planar, however, with some offset in each from the *magnetic* foliation plane. This may be the effect of multiple sub-fabrics contributing to the fabric for the subarea, indicating a slight heterogeneity within the sub-area. As observed in other sub-areas, there is a clockwise offset of the dike plane form the AMS fabric that may be due proximity to the AFB (see above). In fact, the main departure of the data from that expected for a primary flow fabric is related to shear of dike orientations along the STTFZ with no disruption to the magnetic fabric. The AMS data for sub-area II-3 is considered to represent an area with a preference for lateral magma-flow.

5.3.2.8. Sub-area II-4

Only 5 oriented cores were recovered from this sub- area, which is located in the very south of the study area adjacent to the AFB. The east-west strike of the 30 dikes measured, the fact that k_{max} axes are parallel with dike poles for much of the area, and the very low number of specimens make this area unsuitable for interpretations or speculations in terms of magmatic flow.

5.3.2.9. Sub-area III-1

Due to minor edge-effects in the spatial-averaging process, one smoothed point lies within this area, however no data was actually collected here.

5.3.2.10. Sub-area III-2

Sub-area III-2 covers a large area of the northeastern part of the study area, and contains samples of the Basal Group and Sheeted Dike Complex. 71 dike orientations were measured, which, while steeply dipping, vary between east-west and north-south strike. A mean dike plane with a vertical dip and northeast-southwest strike is supported by a moderate grouping of dike poles trending northwest and dipping very shallowly. k_{max} axes, while scattered, are generally confined to broad groupings that plunge shallowly to the north and south. Points that are not part of these groups dip shallowly at various orientations, weakly tracing an horizontal girdle around the periphery of the stereonet. Intermediate susceptibility axes do not group together, however their distribution weakly traces a vertical north-south plane. A weak cluster of points occurs with a vertical plunge, within the dike plane. k_{min} axes are generally shallow-dipping, with groups of data trending east and west. A small number of points cluster around a vertical plunge, close to the strongest grouping of k_{int} axes. This leads to the k_{min} data weakly tracing an east-west vertical plane. The main shallow dipping groups may be related to the strongest dike pole clusters, with the difference being a small (<45°) anticlockwise offset. Mean tensor axes and their confidence regions show a weak prolate symmetry (L>S). The mean tensor of k_{max} plunges near horizontal to the north, with k_{int} and k_{min} vertical and east/horizontal, respectively. The general northeast-southwest strike of dikes in this sub-area relates to shear along the STTFZ, and as such the mean dike plane is offset ~45° clockwise from the magnetic fabric. Otherwise, the magnetic fabrics appear to be primary, as described in section 4.3, with a preference for lateral flow (shallow k_{max}) assumed for the area.

5.3.2.11. Sub-area III-3

Much of sub-area III-3 has been included in sub-areas E and F (above). The 21 remaining sites that are within III-3 have predominantly east-northeast striking dikes that dip steeply to the south-southeast. A small number of the 60 dikes measured in the field dip to the north-northwest. k_{max} axes of the 96 oriented cores from this sub-area form a steeply dipping group, that is part of an overall distribution that weakly traces a plane perpendicular to the mean dike plane. Intermediate axes are quite scattered, with a distribution that very weakly traces a nearly vertical southwest striking plane. Two poorly defined groups of points occur, one having a shallow plunge to the northeast, the other close to vertical. k_{min} axes are scattered as well, with a bimodal distribution pattern. The data can be seen to group close to the main group of dike poles for the area, and can be seen to trace an east-west striking and ~30° dipping plane. The strongest grouping of points occurs at east/horizontal, within the mean dike plane. The orientations of the mean tensor principal susceptibility axes are as expected for the data described above, however a prolate symmetry (L>S) is observed based on the elongation of their confidence regions. With k_{max} dipping steeply within the dike plane, this sub-area seems more suited to inclusion in an area of generally steeply inclined k_{max}. In terms of the primary (flow derived) nature of the magnetic fabric, this has a problem; k_{min} is expected to coincide with the pole to the mean dike, and k_{int} is expected to lie within the dike plane. In this case, k_{min} lies within the dike plane and k_{int} close to the pole to the mean dike. Regardless, the magnetic fabric is clearly related in some way to the mean dike plane. The magnetic fabrics may be reconciled with magmatic origin (see Chapter 6), and it can be seen from Figure 5-4 that steep-k_{max} sub-areas E and F nearly overlap within III-3. This implies that predominantly steep k_{max}, and therefore an extension of the steep magmatic flow regions

of E and F is not unreasonable for this area. The most conservative interpretation would be that III-3 has ambiguous magnetic fabrics and cannot be considered to represent an area of shallow magma-flow.

5.3.2.12. Sub-area III-4

Located directly adjacent to the AFB, much of this area is included in sub-area F (above). The 20 dikes included in III-4 have strikes ranging from north-south to east-west, and may dip between 90° and 30°. The mean dike for the area is vertical and oriented almost east-west. A bimodal distribution describes k_{max} axes (n=24), with a group of points plunging shallowly northeast and southwest, and a second weaker grouping lying close to the dike plane through the NW quadrant of the stereonet. k_{int} axes almost evenly distributed throughout the stereonet, as implied by the fact that the highest density of points is only twice the expected for an isotropic distribution. Nonetheless, there is a weak preference for shallow dips in the distribution. k_{min} orientations are somewhat scattered, with a strong grouping of points close to the dike plane and plunging close to horizontal. A second group occurs plunging northeast at ~45°. Large confidence regions about the mean tensor maximum and intermediate axis is clear, as is an oblate (S>>L) symmetry of the fabrics. While in this case k_{max} does lie within the dike plane and dip shallowly, the mean tensor k_{min} axis lies within the dike plane and k_{int} lies nearly collinear with the pole to the mean dike plane. This is not necessarily the configuration expected for primary flow, however there is a clear relationship between AMS and the mean dike plane. As mentioned previously (and described below), multiple sub-fabrics competing for the orientation-distribution of principal axes can cause an apparent swapping of k_{min} and k_{int} axes. If this is the case here, then k_{max} represents the magmatic

flow axis and flow was indeed shallow. One further source of ambiguity relates to how the magnetic fabric and dike plane remained aligned after dike rotation due to shear along the STTFZ.

5.3.2.13. Sub-area IV-1

Due to minor edge-effects in the spatial-averaging process, smoothed points lie within this area, however no data was actually collected here.

5.3.2.14. Sub-area IV-2

Due to minor edge-effects in the spatial-averaging process, smoothed points lie within this area, however no data was actually collected here.

5.3.2.15. Sub-area IV-3

This sub-area is located within the Sheeted Dike Complex along the western boundary of the study area. Of the 31 dikes included in this sub-area (28 oriented cores), the majority strike northeast-southwest and dip very steeply. A small group of dikes strike east-west and dip ~60° to the south. k_{max} axes group with northeast and southwest trends, plunging shallowly and close to the mean dike plane. Data that does not group tends to be scattered throughout the stereonet. Intermediate axes are generally shallowly dipping, and form a horizontal girdle around the periphery of the stereonet, with a weak grouping trending southeast. Despite some scatter, k_{min} axes tend to cluster around vertical, and within the mean dike plane. Mean tensors for this data tell much the same story, with a tightly constrained maximum axis trending southwest and plunging very shallowly. Elongation of the confidence regions about the mean tensor k_{min} and k_{int} axes indicate a strong prolate symmetry (L>>S). The intermediate and minimum axes do not correspond to any particular relationship with the mean dike plane (such as k_{min} colinear

with the dike pole). Despite this, k_{max} is horizontal and within the dike plane, and the prolate symmetry of the fabric does not require that k_{min} and k_{int} lie within or perpendicular to the dike plane. In fact, the minimum and intermediate confidence regions together trace a plane perpendicular to the mean dike plane. This data, therefore, meets the requirements for magmatic origin. In this area flow may have been close to horizontal.

5.3.2.16. Sub-area IV-4

With only 4 oriented cores recovered from this subarea, and its proximity to the AFB, no interpretations can be based on it. The magnetic fabrics found here match those determined for sub-area IV-3. Therefore, by extension, any interpretations made for IV-3 will apply to IV-4 as well.

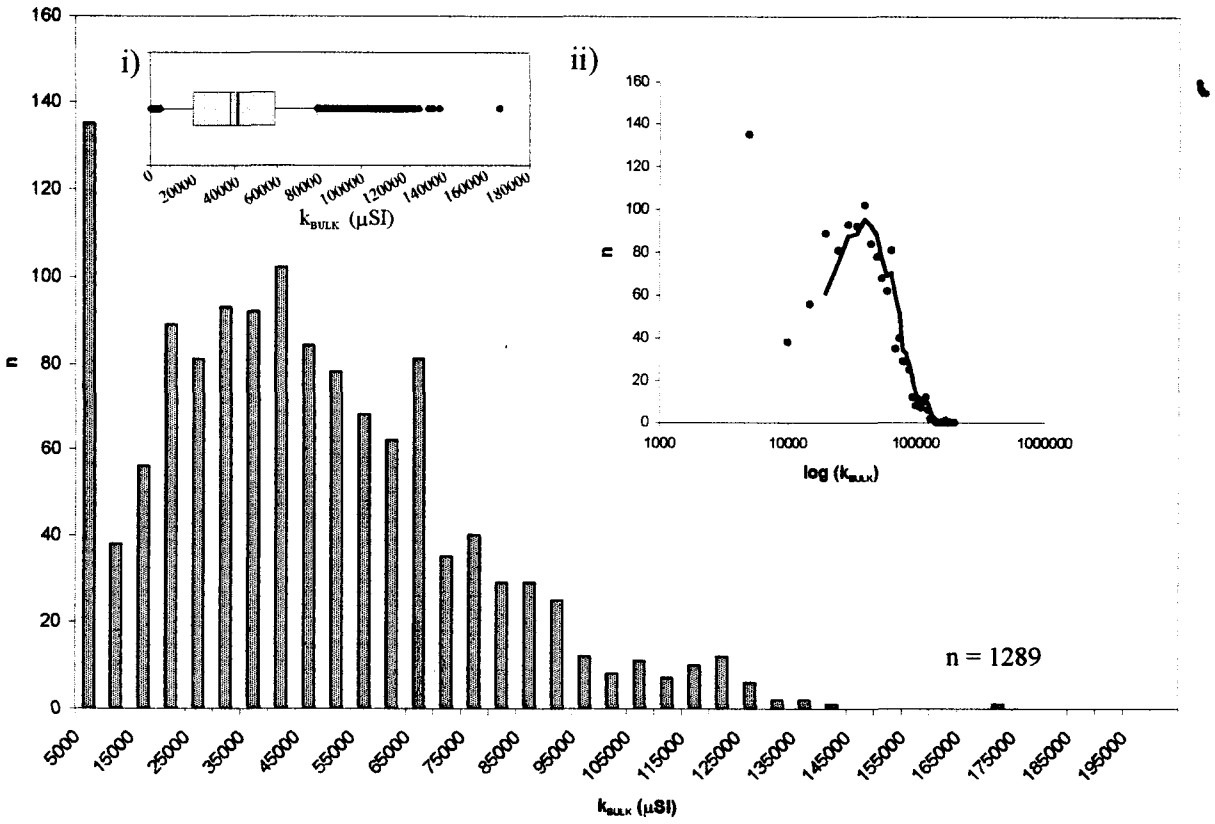

Figure 5-1. Histogram of k_{BULK} data, with insets of (i) 'box and whiskers' plot of data, where lower and upper 'whiskers mark the 5th and 95th percentiles, respectively, the upper and lower borders of the 'box' mark the 25th and 75th percentiles, respectively, and the thin and thick vertical line mark the median and mean, respectively; and (ii) histogram of log(k_{BULK}), showing a log-normal distribution. See text for discussion.

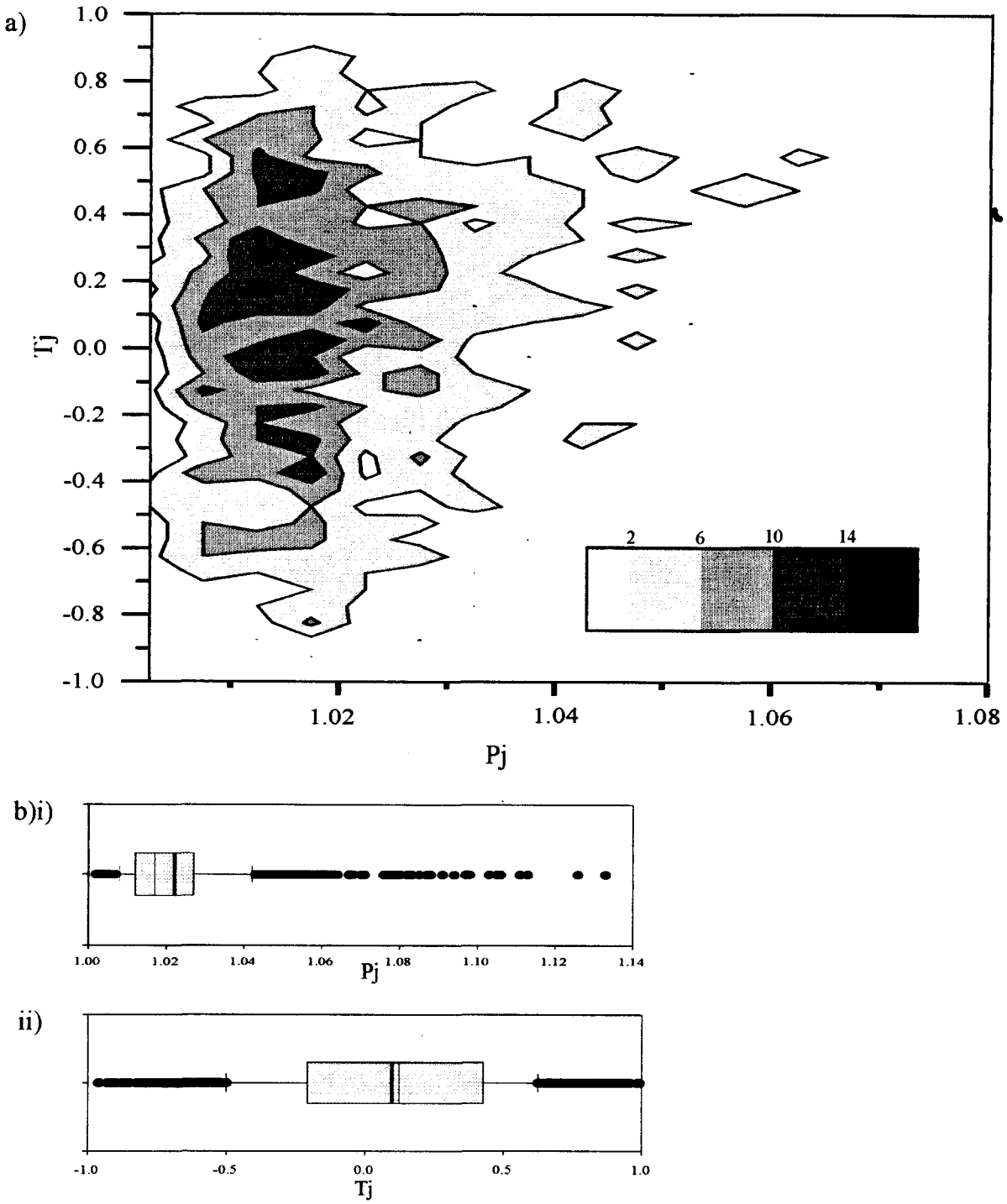

Figure 5-2. a) Density contoured Jelinek plotfor all data (n=1289). Note that higher Pj specimens generally have Tj >0. Data is contoured at count per 1% area. Tj=+1 for a perfect oblate or disk shape, Tj=-1 for a perfect prolate or rod shape, Pj=1 for a sphere or isotropic fabric. b) 'box and whiskers' plot of Pj (i) and Tj (ii) distribution. Plot parameters as per Fig. 5-1i.

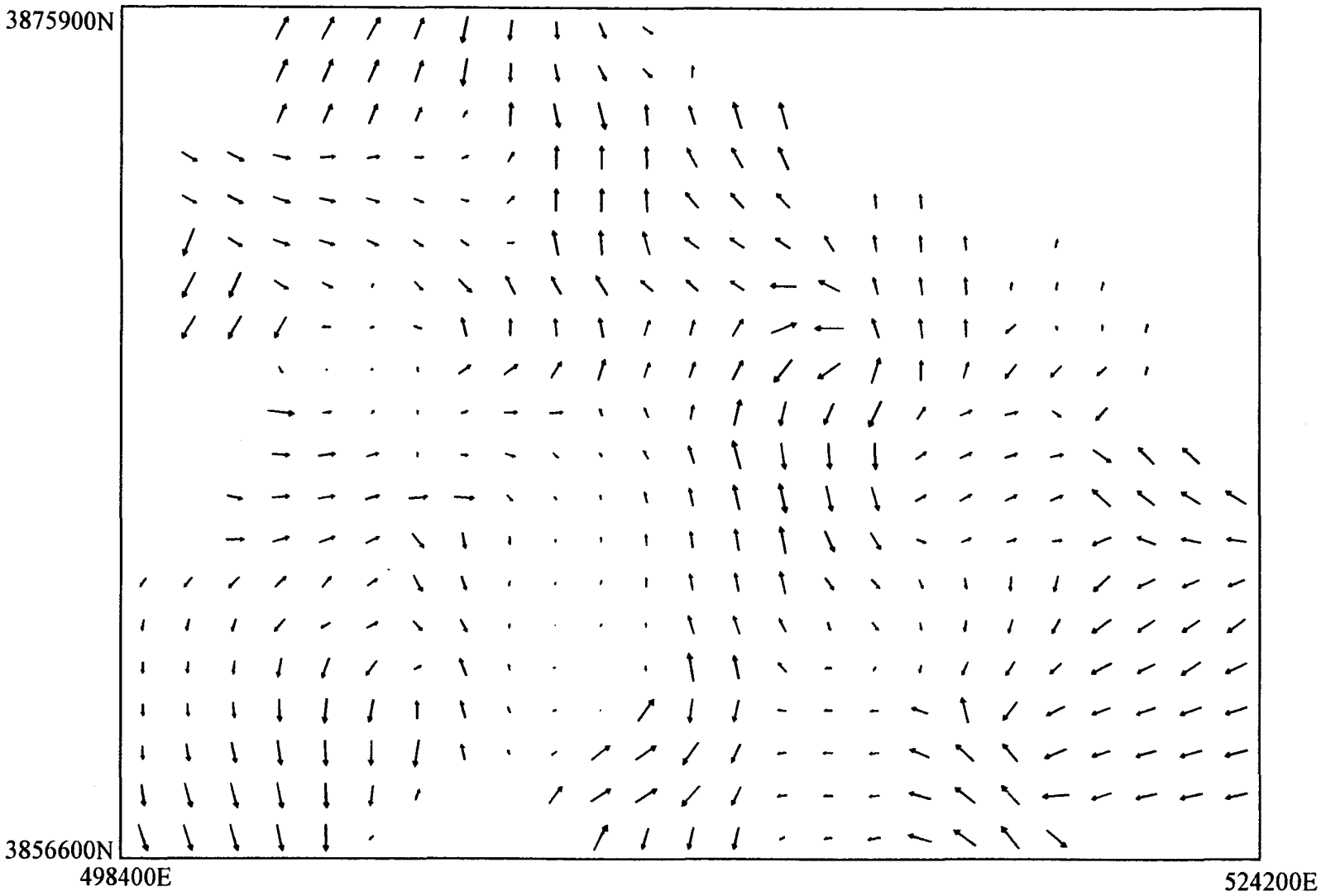

Figure5-3. Spatially averaged k_{max} data for entire study area. Raw data was smoothed using a moving circle method (5km radius, 1km spacing) weighted by inverse distance (nearest neighbour) to station. Longer arrows indicate shallower plunge, shorter arrows indicate steeper plunge.

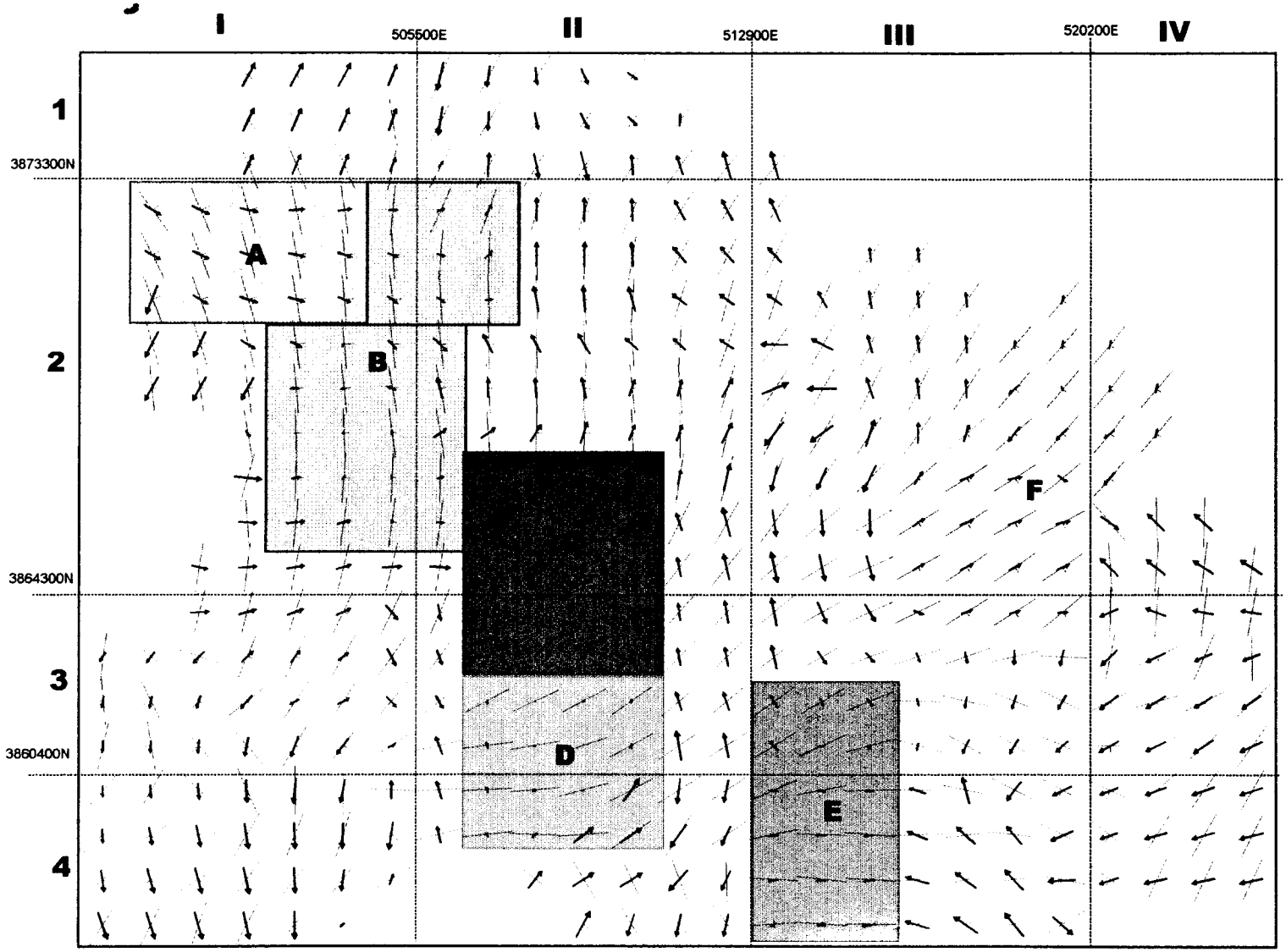

Figure 5-4. Spatially averaged dike orientation and k_{max} data. Nubered (I-1, I-2, etc.) regions are sub-areas of shallowly plunging k_{max} axes and homogenous dike orientations. Lettered (A, B, etc.) regions are sub-areas of generally steeply plunging k_{max} axes and homogenous dike orientations.

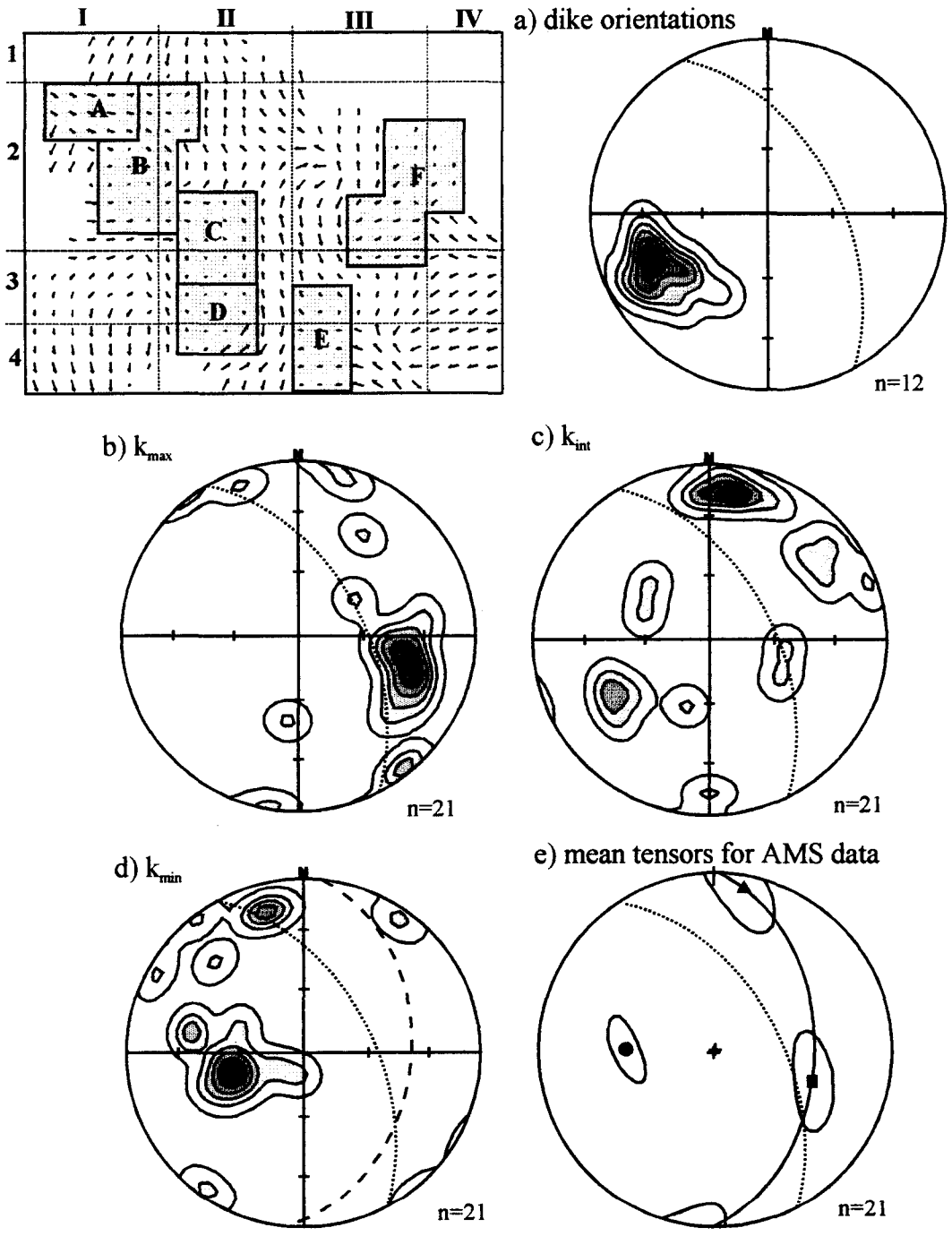

Figure 5-5. AMS data for sub-area A. Density contoured stereonets for dike orientations (a), k_{max} (b), k_{int} (c), k_{min} (d), and mean tensors and 95% confidence regions (e). Fine dashed plane represents the mean dike for this sub-area, coarse dashed plane (d) and solid plane (e) represent magnetic foliation plane. Solid squares, triangles, and circles represent mean tensor maximum, intermediate, and minimum axes, respectively (e).

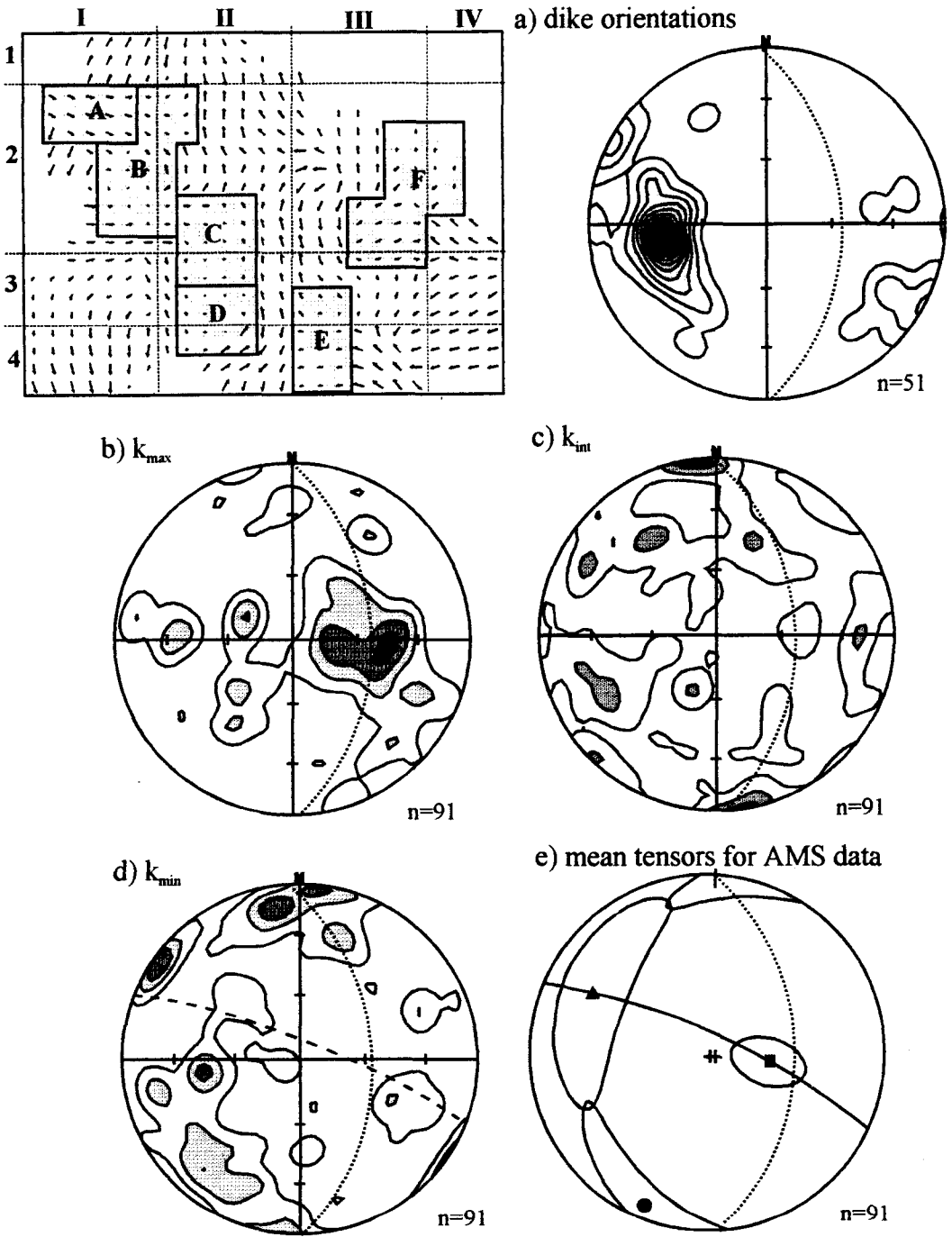

Figure 5-6. AMS data for sub-area B. Density contoured stereonets for dike orientations (a), k_{max} (b), k_{int} (c), k_{min} (d), and mean tensors and 95% confidence regions (e). Fine dashed plane represents the mean dike for this sub-area, coarse dashed plane (d) and solid plane (e) represent magnetic foliation plane. Solid squares, triangles, and circles represent mean tensor maximum, intermediate, and minimum axes, respectively (e).

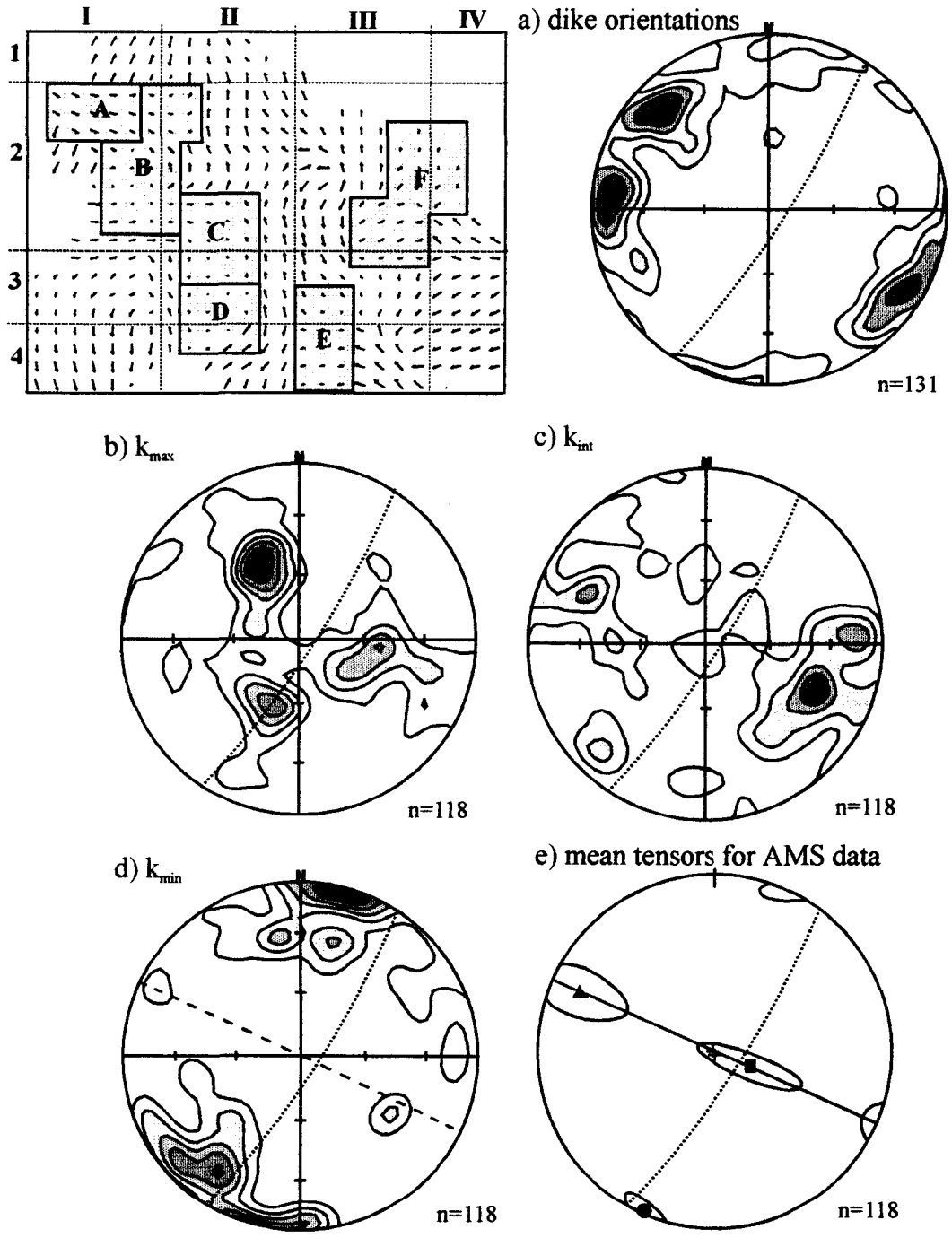

Figure 5-7. AMS data for sub-area C. Density contoured stereonets for dike orientations (a), k_{max} (b), k_{int} (c), k_{min} (d), and mean tensors and 95% confidence regions (e). Fine dashed plane represents the mean dike for this sub-area, coarse dashed plane (d) and solid plane (e) represent magnetic foliation plane. Solid squares, triangles, and circles represent mean tensor maximum, intermediate, and minimum axes, respectively (e).

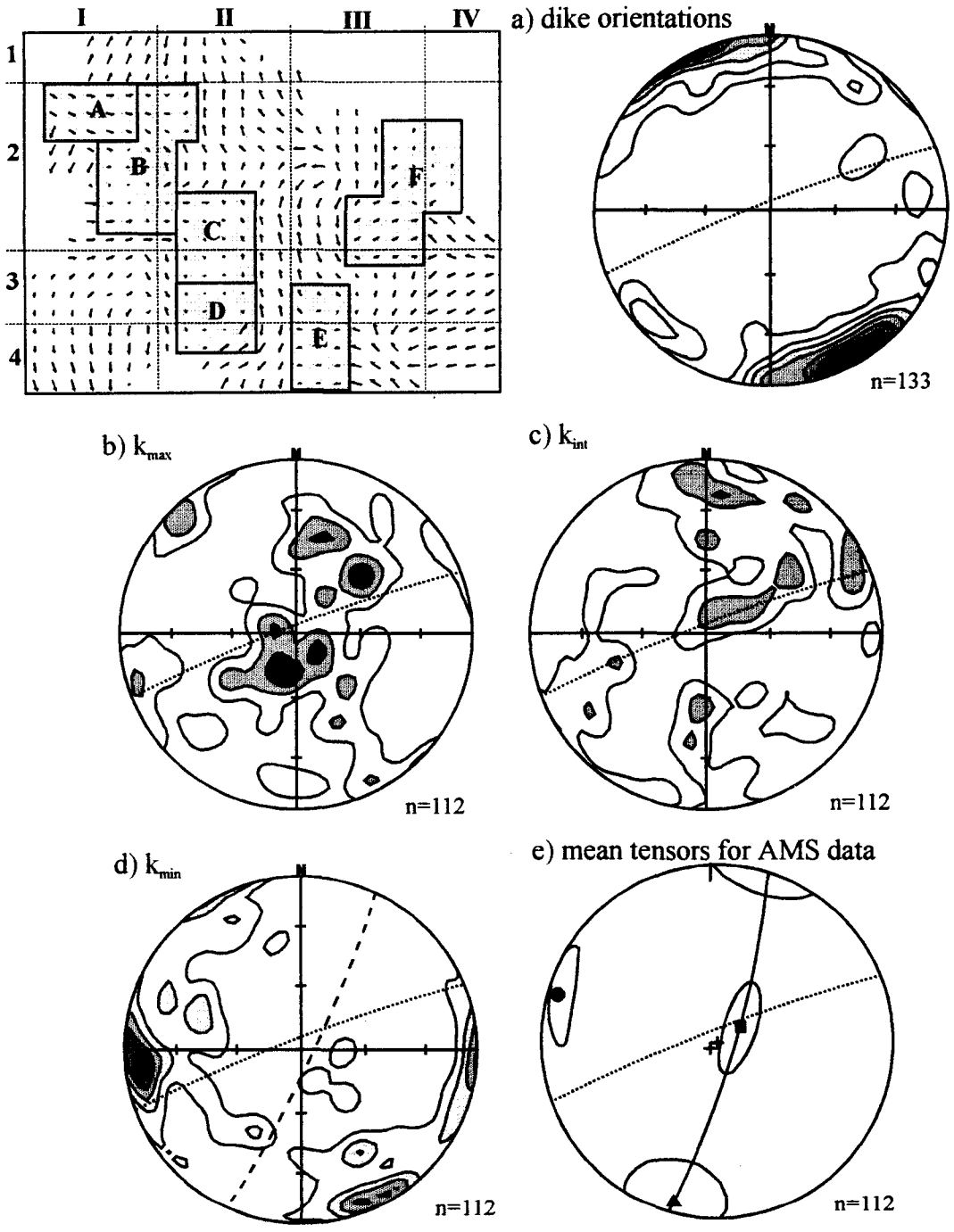

Figure 5-8. AMS data for sub-area D. Density contoured stereonets for dike orientations (a), k_{max} (b), k_{int} (c), k_{min} (d), and mean tensors and 95% confidence regions (e). Fine dashed plane represents the mean dike for this sub-area, coarse dashed plane (d) and solid plane (e) represent magnetic foliation plane. Solid squares, triangles, and circles represent mean tensor maximum, intermediate, and minimum axes, respectively (e).

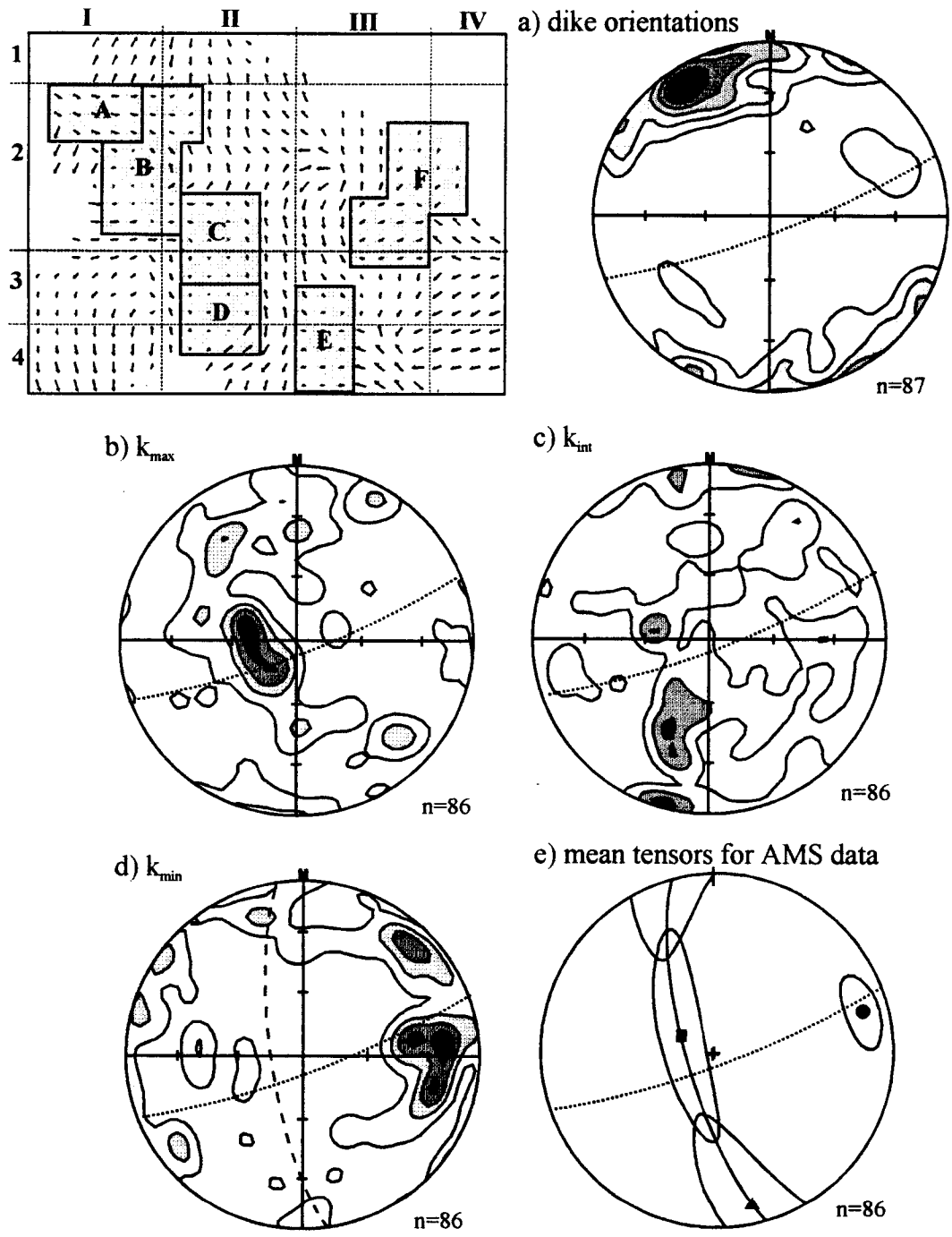

Figure 5-9. AMS data for sub-area E. Density contoured stereonets for dike orientations (a), k_{max} (b), k_{int} (c), k_{min} (d), and mean tensors and 95% confidence regions (e). Fine dashed plane represents the mean dike for this sub-area, coarse dashed plane (d) and solid plane (e) represent magnetic foliation plane. Solid squares, triangles, and circles represent mean tensor maximum, intermediate, and minimum axes, respectively (e).

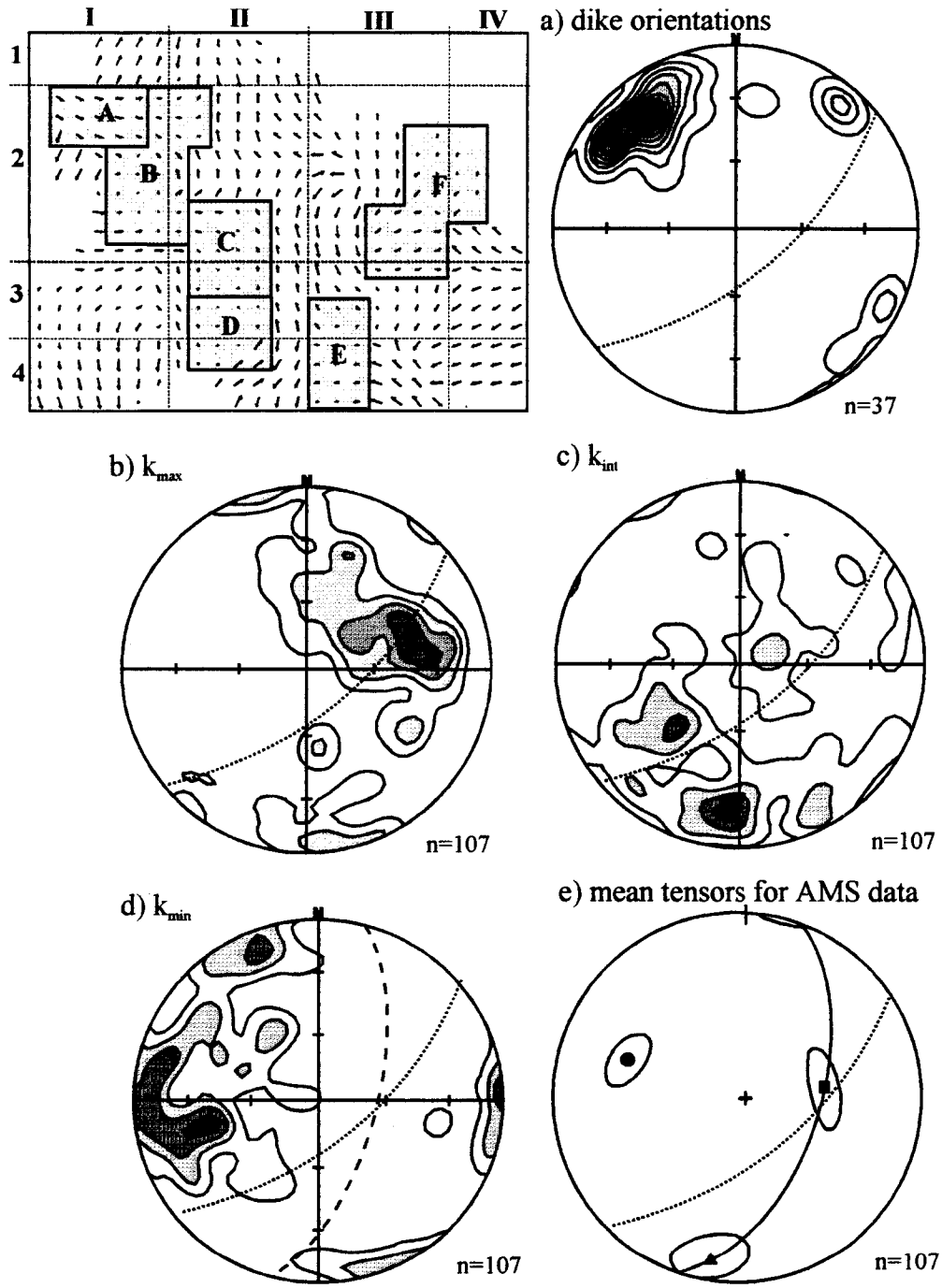

Figure 5-10. AMS data for sub-area F. Density contoured stereonets for dike orientations (a), k_{max} (b), k_{int} (c), k_{min} (d), and mean tensors and 95% confidence regions (e). Fine dashed plane represents the mean dike for this sub-area, coarse dashed plane (d) and solid plane (e) represent magnetic foliation plane. Solid squares, triangles, and circles represent mean tensor maximum, intermediate, and minimum axes, respectively (e).

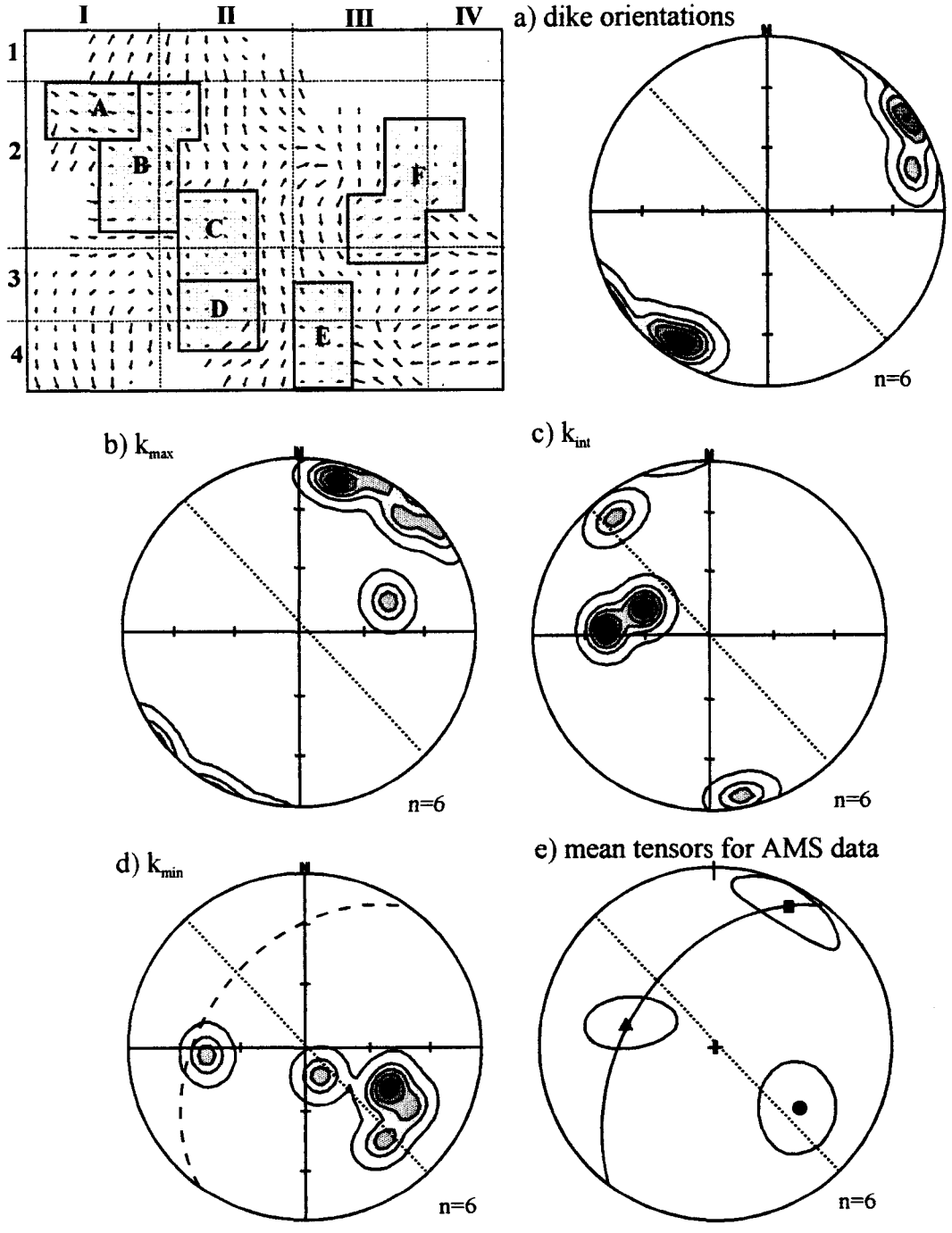

Figure 5-11. AMS data for sub-area I-1. Density contoured stereonets for dike orientations (a), k_{max} (b), k_{int} (c), k_{min} (d), and mean tensors and 95% confidence regions (e). Fine dashed plane represents the mean dike for this sub-area, coarse dashed plane (d) and solid plane (e) represent magnetic foliation plane. Solid squares, triangles, and circles represent mean tensor maximum, intermediate, and minimum axes, respectively (e).

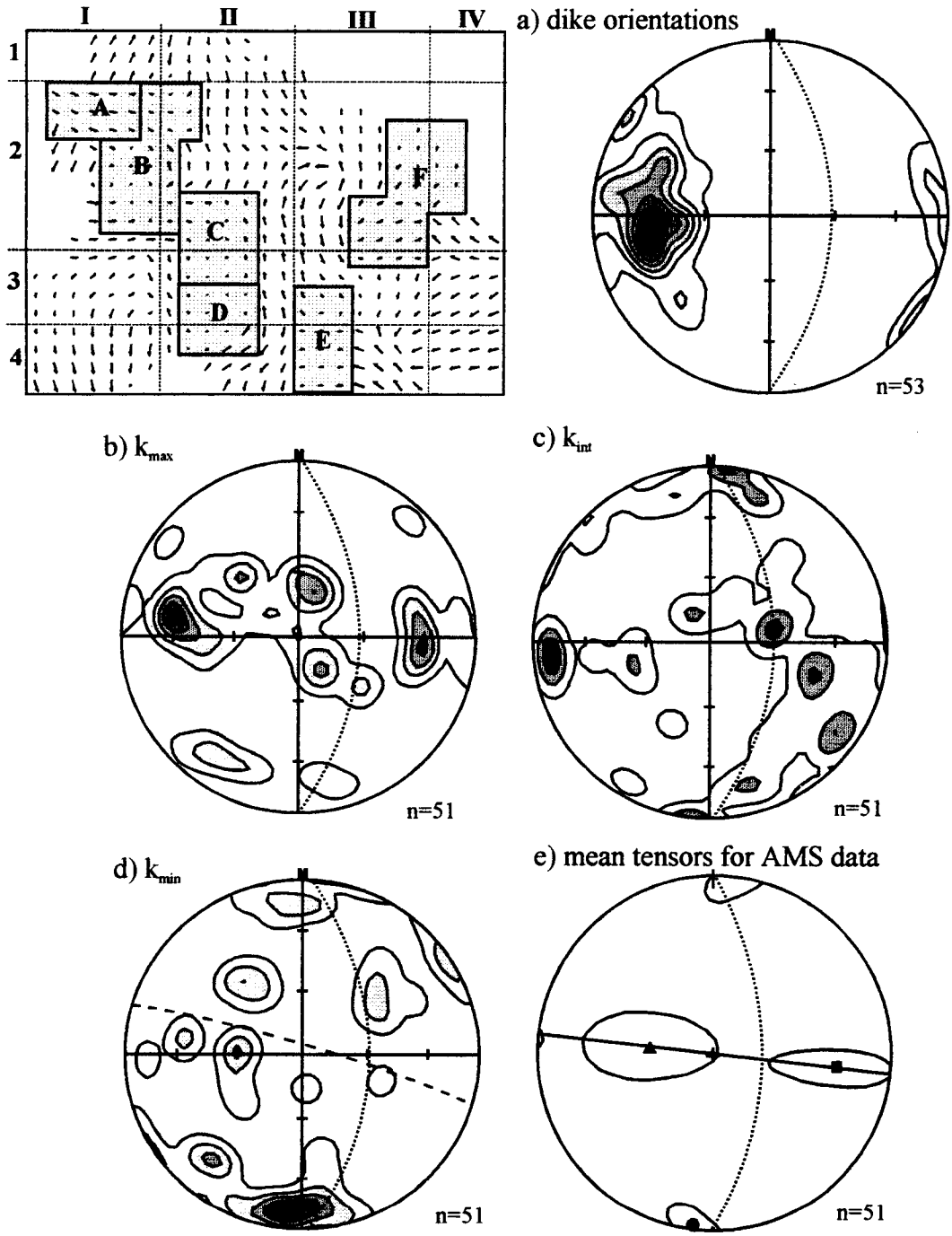

Figure 5-16. AMS data for sub-area I-2. Density contoured stereonets for dike orientations (a), k_{max} (b), k_{int} (c), k_{min} (d), and mean tensors and 95% confidence regions (e). Fine dashed plane represents the mean dike for this sub-area, coarse dashed plane (d) and solid plane (e) represent magnetic foliation plane. Solid squares, triangles, and circles represent mean tensor maximum, intermediate, and minimum axes, respectively (e).

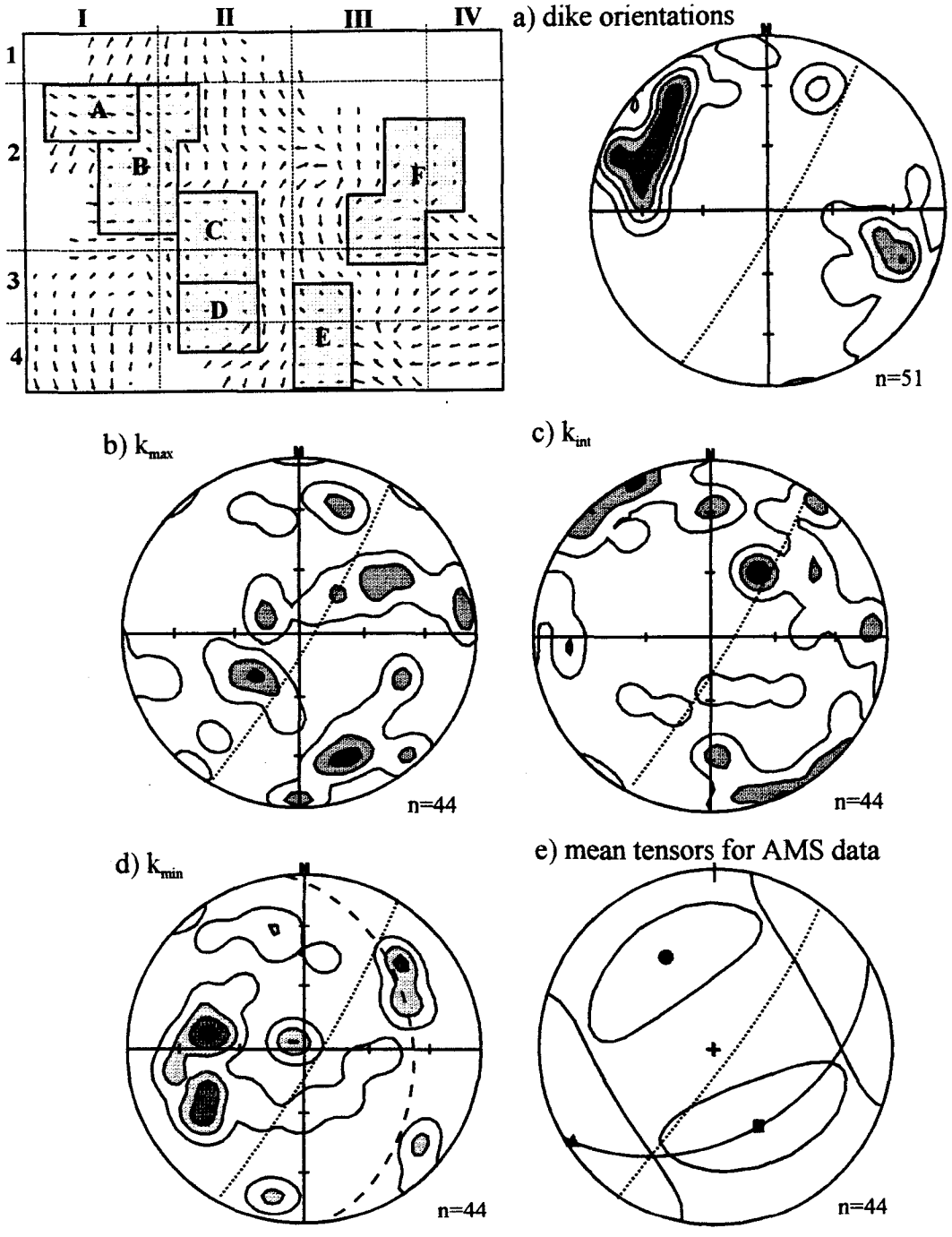

Figure 5-13. AMS data for sub-area I-3. Density contoured stereonets for dike orientations (a), k_{max} (b), k_{int} (c), k_{min} (d), and mean tensors and 95% confidence regions (e). Fine dashed plane represents the mean dike for this sub-area, coarse dashed plane (d) and solid plane (e) represent magnetic foliation plane. Solid squares, triangles, and circles represent mean tensor maximum, intermediate, and minimum axes, respectively (e).

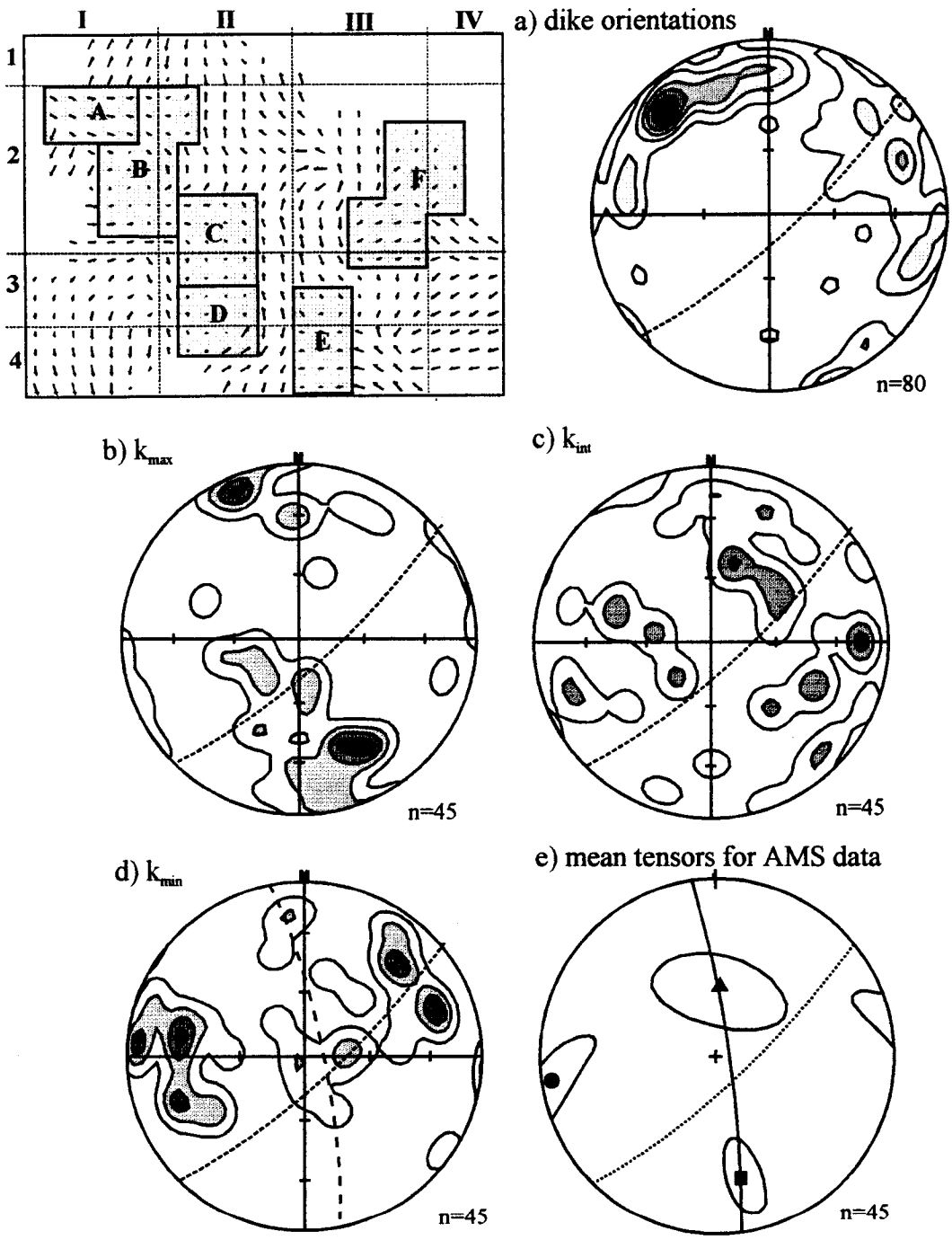

Figure 5-14. AMS data for sub-area I-4. Density contoured stereonets for dike orientations (a), k_{max} (b), k_{int} (c), k_{min} (d), and mean tensors and 95% confidence regions (e). Fine dashed plane represents the mean dike for this sub-area, coarse dashed plane (d) and solid plane (e) represent magnetic foliation plane. Solid squares, triangles, and circles represent mean tensor maximum, intermediate, and minimum axes, respectively (e).

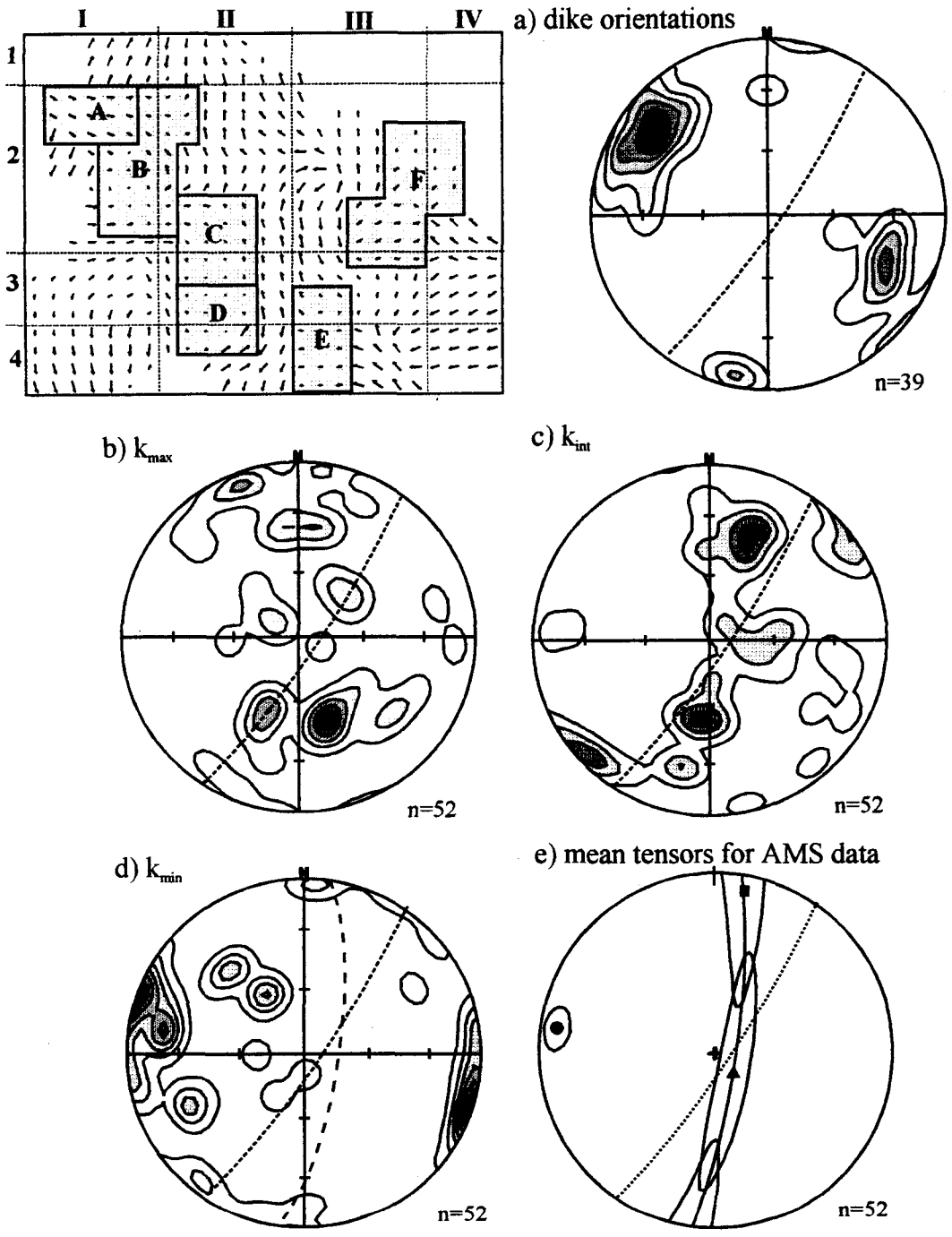

Figure 5-15. AMS data for sub-area II-1. Density contoured stereonets for dike orientations (a), k_{max} (b), k_{int} (c), k_{min} (d), and mean tensors and 95% confidence regions (e). Fine dashed plane represents the mean dike for this sub-area, coarse dashed plane (d) and solid plane (e) represent magnetic foliation plane. Solid squares, triangles, and circles represent mean tensor maximum, intermediate, and minimum axes, respectively (e).

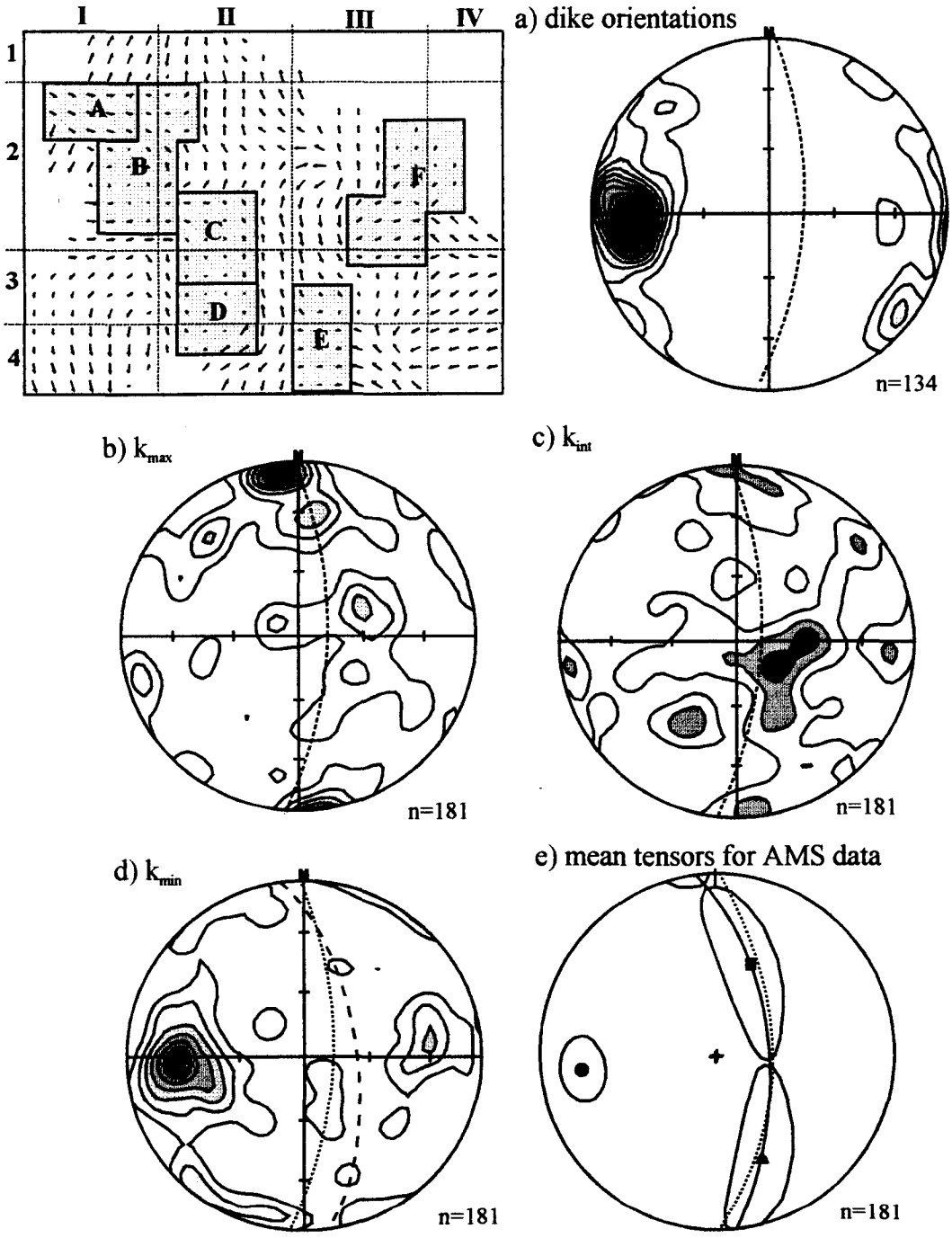

Figure 5-12. AMS data for sub-area II-2. Density contoured stereonets for dike orientations (a), k_{max} (b), k_{int} (c), k_{min} (d), and mean tensors and 95% confidence regions (e). Fine dashed plane represents the mean dike for this sub-area, coarse dashed plane (d) and solid plane (e) represent magnetic foliation plane. Solid squares, triangles, and circles represent mean tensor maximum, intermediate, and minimum axes, respectively (e).

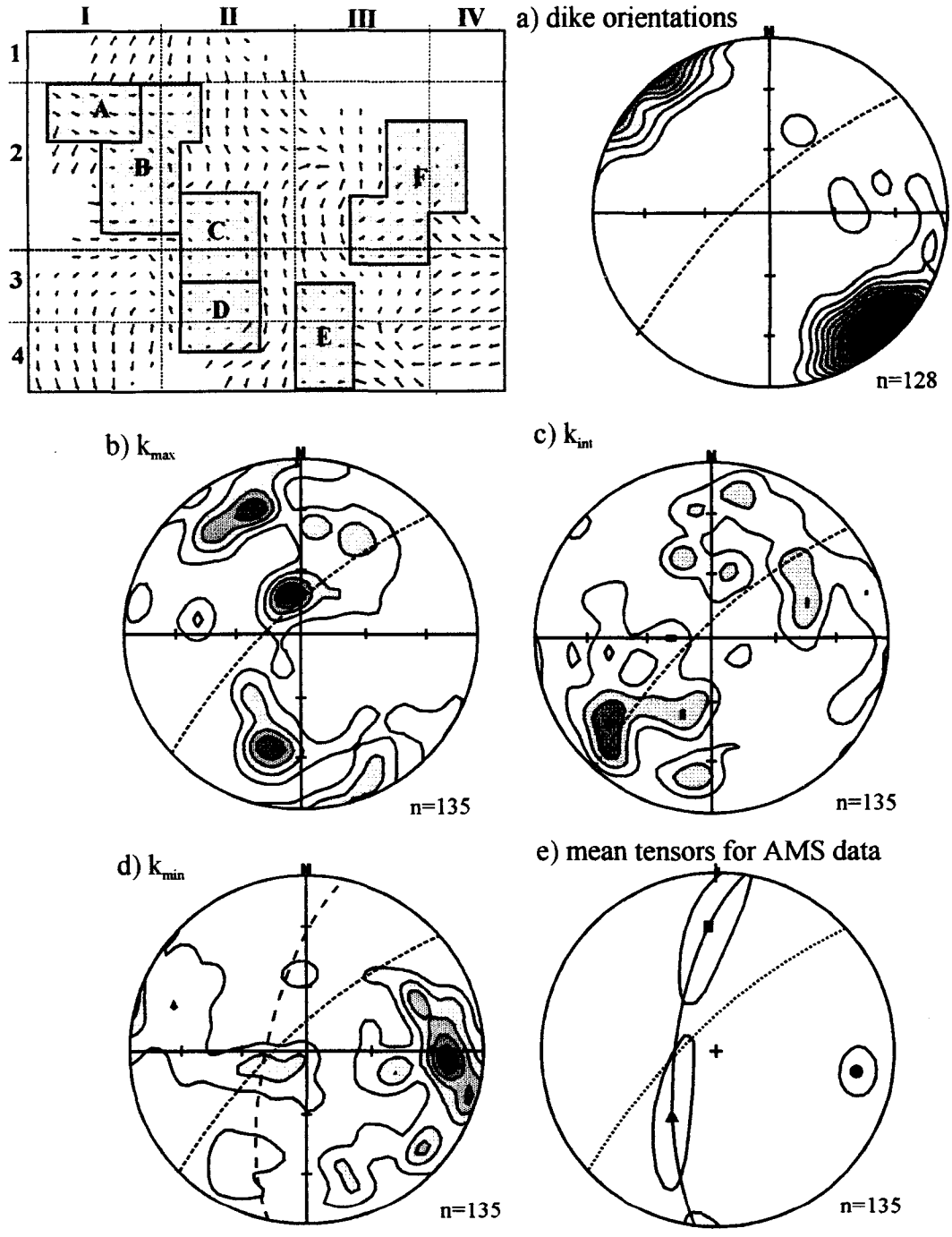

Figure 5-17. AMS data for sub-area II-3. Density contoured stereonets for dike orientations (a), k_{max} (b), k_{int} (c), k_{min} (d), and mean tensors and 95% confidence regions (e). Fine dashed plane represents the mean dike for this sub-area, coarse dashed plane (d) and solid plane (e) represent magnetic foliation plane. Solid squares, triangles, and circles represent mean tensor maximum, intermediate, and minimum axes, respectively (e).

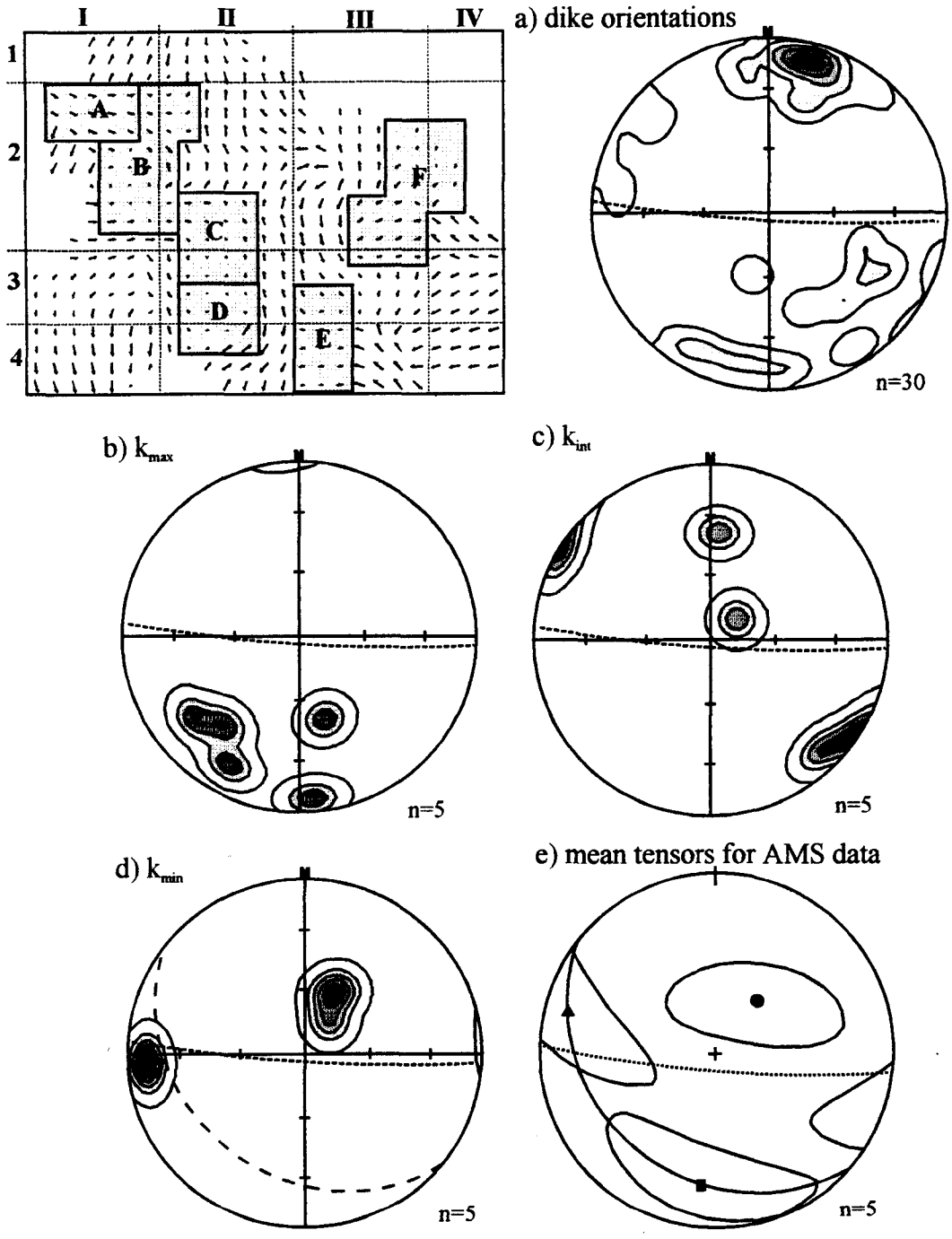

Figure 5-18. AMS data for sub-area II-4. Density contoured stereonets for dike orientations (a), k_{max} (b), k_{int} (c), k_{min} (d), and mean tensors and 95% confidence regions (e). Fine dashed plane represents the mean dike for this sub-area, coarse dashed plane (d) and solid plane (e) represent magnetic foliation plane. Solid squares, triangles, and circles represent mean tensor maximum, intermediate, and minimum axes, respectively (e).

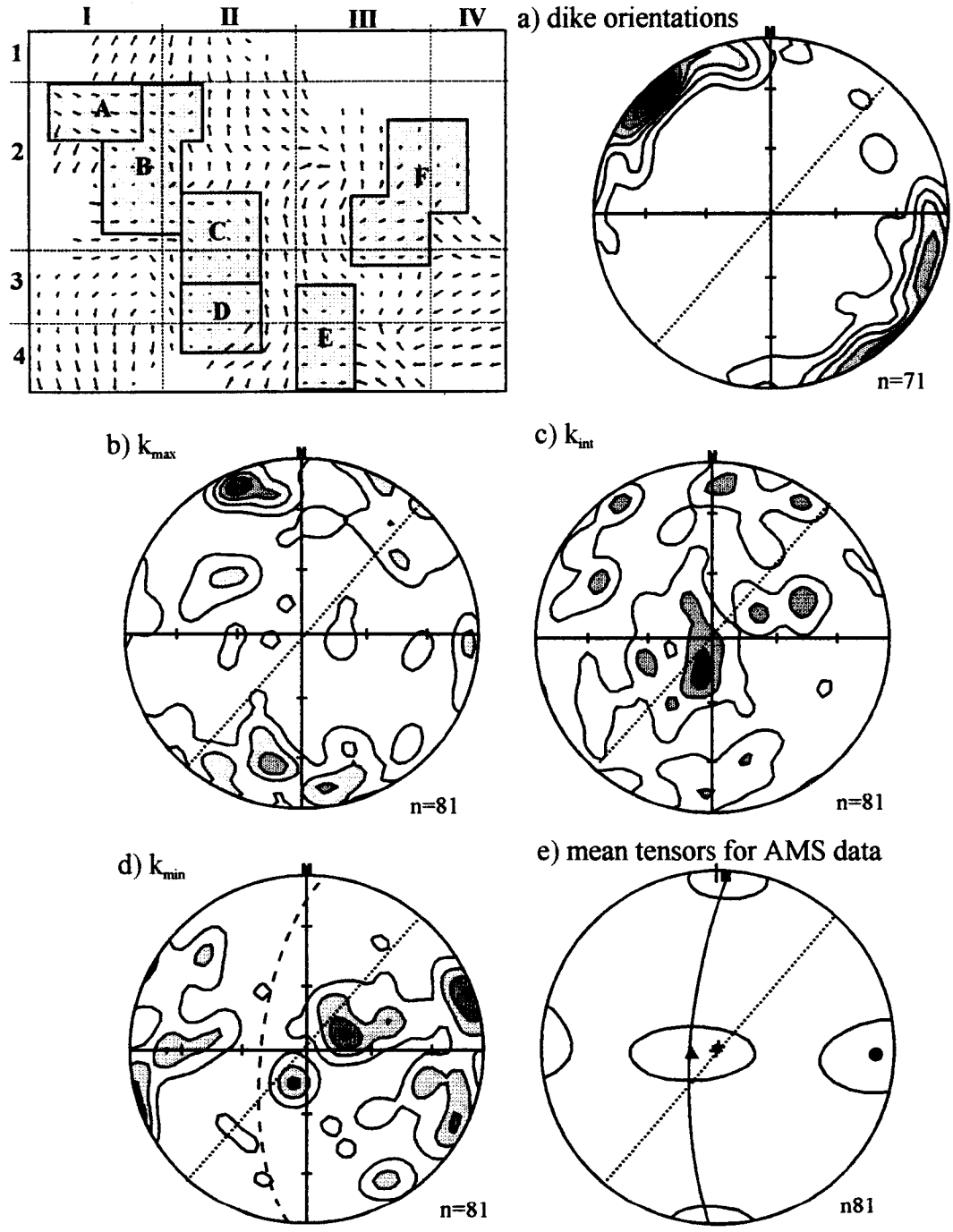

Figure 5-19. AMS data for sub-area III-2. Density contoured stereonets for dike orientations (a), k_{max} (b), k_{int} (c), k_{min} (d), and mean tensors and 95% confidence regions (e). Fine dashed plane represents the mean dike for this sub-area, coarse dashed plane (d) and solid plane (e) represent magnetic foliation plane. Solid squares, triangles, and circles represent mean tensor maximum, intermediate, and minimum axes, respectively (e).

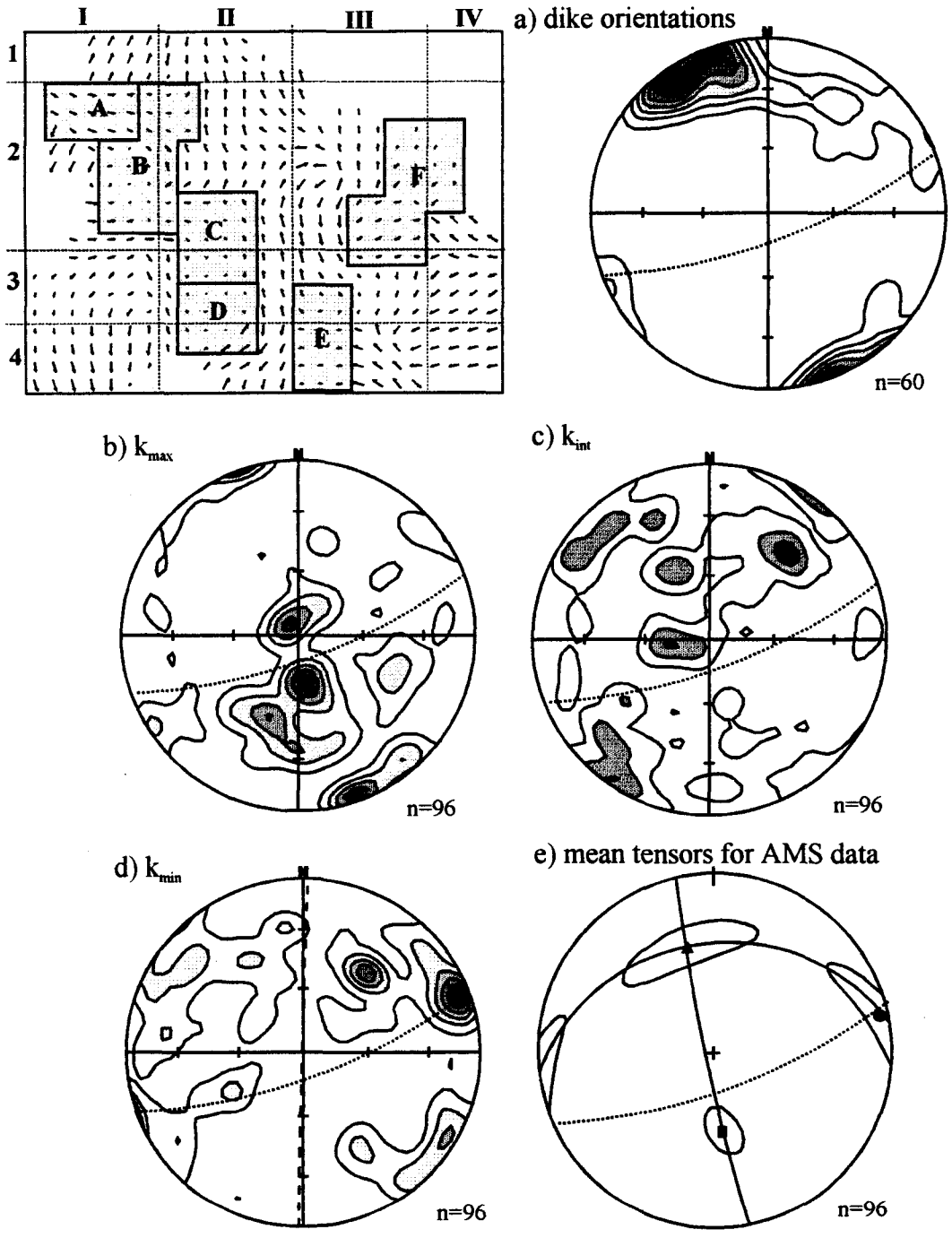

Figure 5-20. AMS data for sub-area III-3. Density contoured stereonets for dike orientations (a), k_{max} (b), k_{int} (c), k_{min} (d), and mean tensors and 95% confidence regions (e). Fine dashed plane represents the mean dike for this sub-area, coarse dashed plane (d) and solid plane (e) represent magnetic foliation plane. Solid squares, triangles, and circles represent mean tensor maximum, intermediate, and minimum axes, respectively (e).

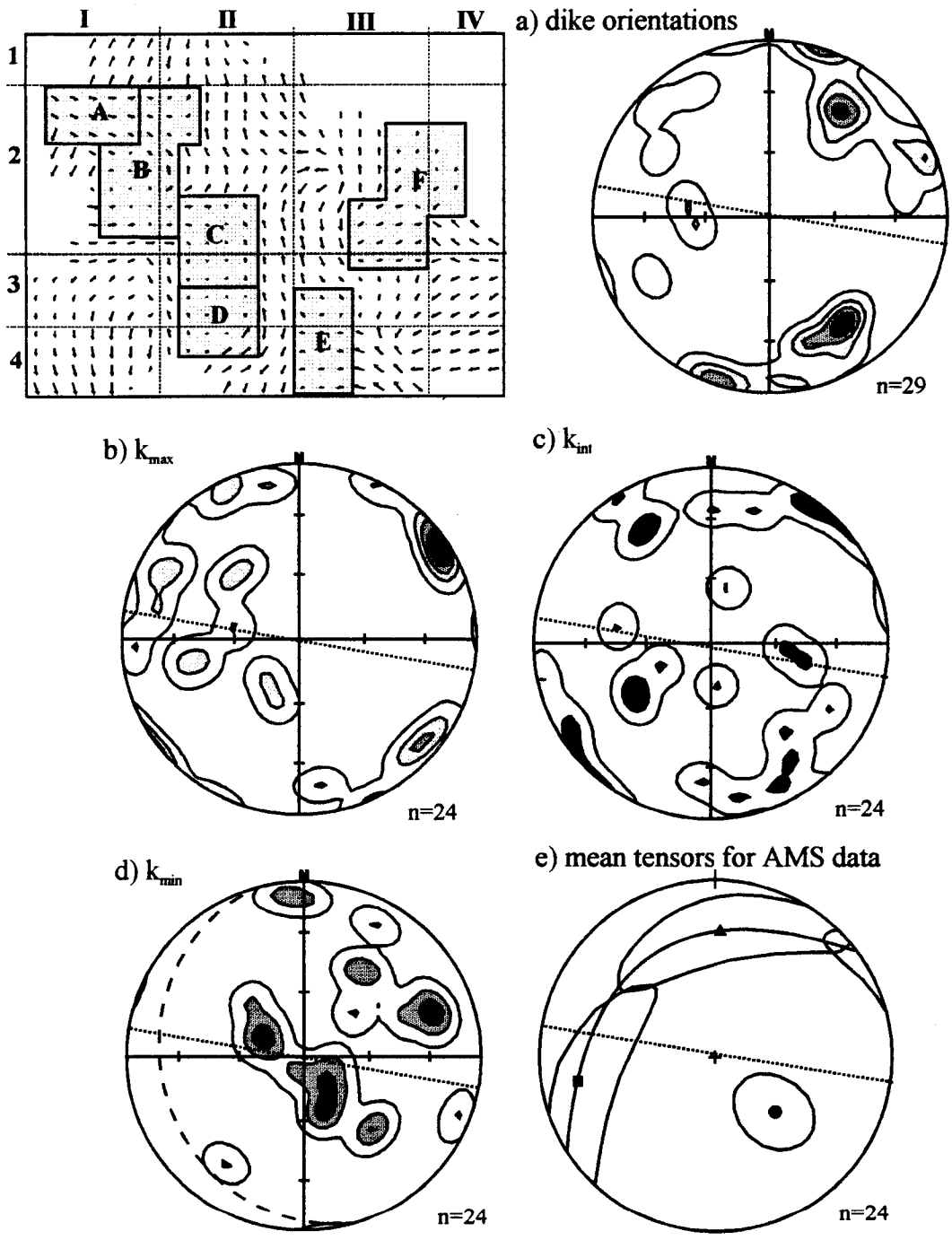

Figure 5-21. AMS data for sub-area III-4. Density contoured stereonets for dike orientations (a), k_{max} (b), k_{int} (c), k_{min} (d), and mean tensors and 95% confidence regions (e). Fine dashed plane represents the mean dike for this sub-area, coarse dashed plane (d) and solid plane (e) represent magnetic foliation plane. Solid squares, triangles, and circles represent mean tensor maximum, intermediate, and minimum axes, respectively (e).

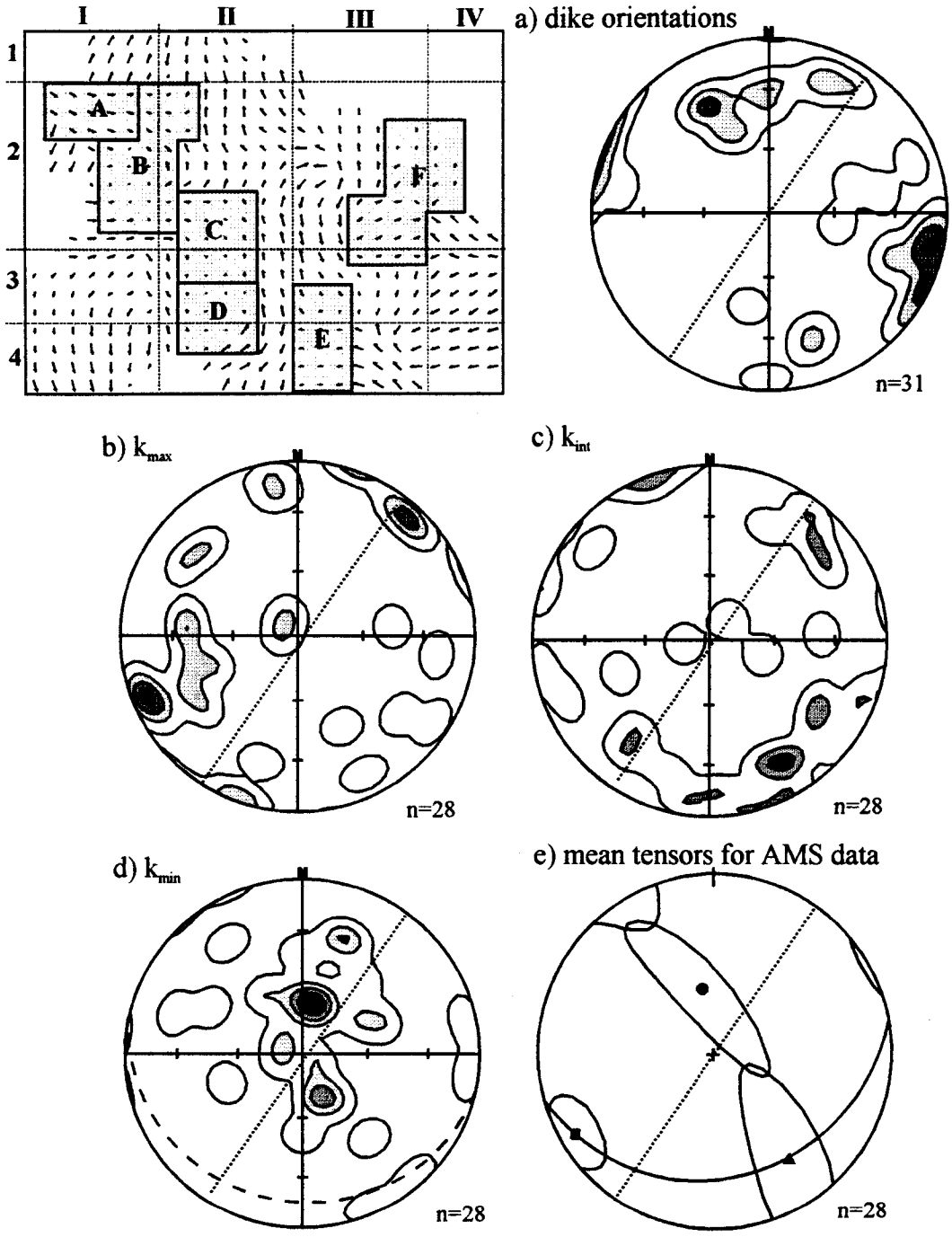

Figure 5-22. AMS data for sub-area IV-3. Density contoured stereonets for dike orientations (a), k_{max} (b), k_{int} (c), k_{min} (d), and mean tensors and 95% confidence regions (e). Fine dashed plane represents the mean dike for this sub-area, coarse dashed plane (d) and solid plane (e) represent magnetic foliation plane. Solid squares, triangles, and circles represent mean tensor maximum, intermediate, and minimum axes, respectively (e).

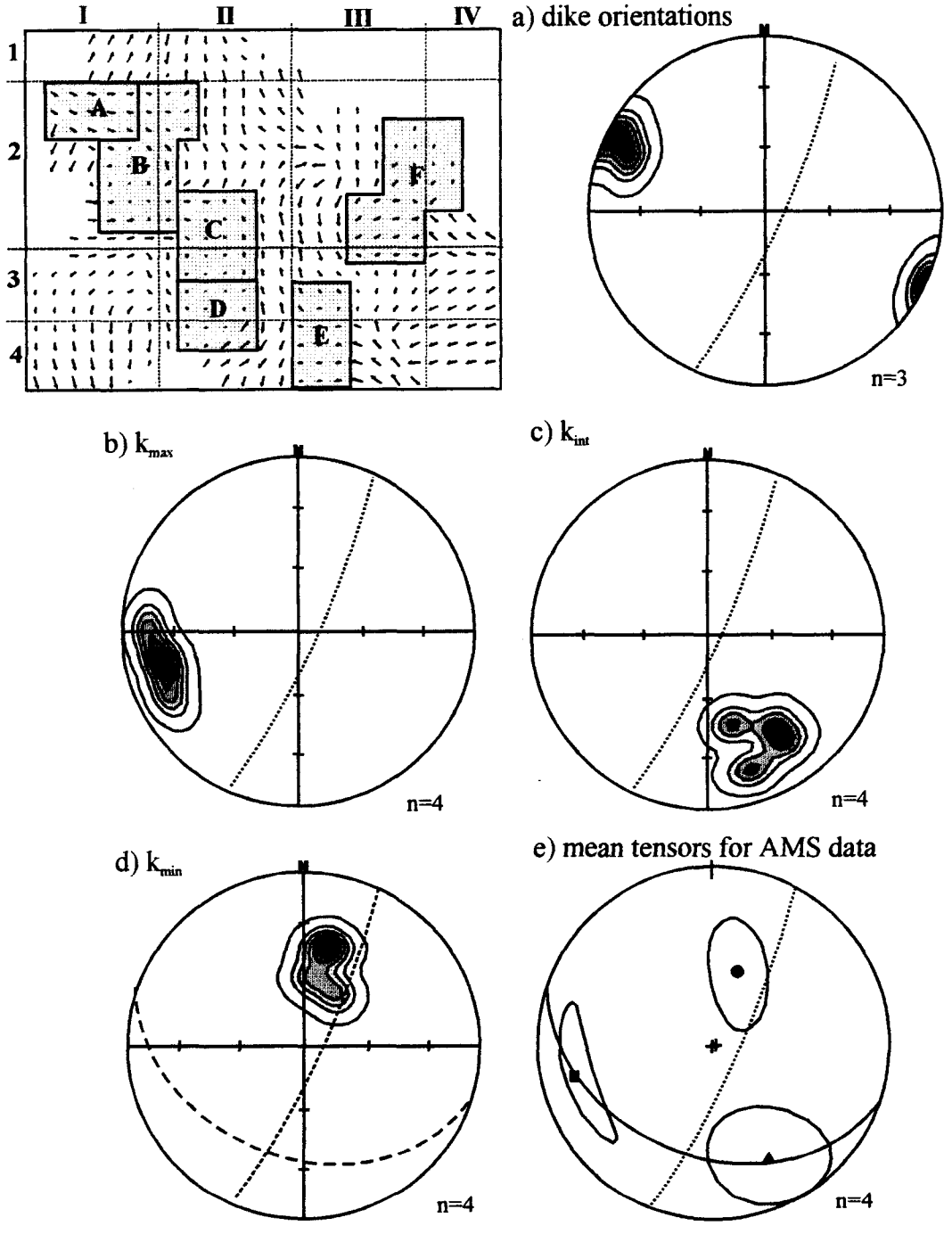

Figure 5-23. AMS data for sub-area IV-4. Density contoured stereonets for dike orientations (a), k_{max} (b), k_{int} (c), k_{min} (d), and mean tensors and 95% confidence regions (e). Fine dashed plane represents the mean dike for this sub-area, coarse dashed plane (d) and solid plane (e) represent magnetic foliation plane. Solid squares, triangles, and circles represent mean tensor maximum, intermediate, and minimum axes, respectively (e).

6. Interpretation guidelines

This chapter describes the AMS, AARM, and rock magnetic investigations of specimens collected at two structurally homogenous sites within the present study area (Figure 6-1). Based on the results of this small-scale but detailed study, guidelines for the interpretation of the AMS fabrics described in Chapter 5 will be proposed. The results of this detailed study are presented in Borradaile and Gauthier (2002).

6.1. Purpose and study areas

While the AMS fabrics of many of the sub-areas described in Chapter 5 conform nearly perfectly to those expected on kinematic grounds (Section 4.3), others have fabrics that completely or partially depart from this theoretical, flow-derived fabric. In both the cases of flow-compatible and anomalous fabrics, it may be instructive to have more information regarding the mineralogical source of the fabric, the (non-) existence of competing sub-fabrics, and the effect of post-emplacement dike shear on the AMS fabrics. In order to assess these factors, two structurally homogenous sites were selected. They are considered representative of the orientations of the dikes and of their mineralogy and alteration. At a road-cut exposure near the forest station at Panagea, 20 samples were taken from 7 dikes with an average orientation of north strike and 60° dip to the east (Figure 6-1a). At another site, close to the Konia observation post, 7 dikes with a consistent northeast strike and 60° dip to the southeast (Figure 6-1b) yielded a further 23 oriented hand samples.

6.2.AMS and AARM results

6.2.1. Panagea site

AMS was measured on 63 core-samples from this site, 19 of which were also suitable for AARM determination. As this site is ~13km north of the STTFZ, no obvious dike rotation related to shear along the transform is evident (Figure 6-1a), nor are the dikes pervasively deformed. Therefore, any departure of the magnetic fabrics from that expected based on the arguments in section 4.3 cannot be related to shear or deformation. Fortunately, the AMS fabrics of these samples agree perfectly with the flow-kinematic model: k_{max} axes are distributed along the trace of the dike plane, with a strong grouping and mean tensor axis that plunges shallowly to the north, within the dike plane (Figure 6-2a). The intermediate mean tensor axis also lies within the dike plane, while k_{min} axes cluster strongly around the group of dike poles for this outcrop (Figure 6-2c). As expected for a group of specimens from within meters of each other and from similar dikes, there is little scatter in the AMS results with all axes having tightly constrained mean tensor orientations and small 95% confidence regions. These results strongly suggest that a preferred orientation caused by flowing magma exists, and that flow may have been very shallow and consistently oriented in this area.

While AMS fabrics describe the orientation-distribution of all grains of a specimen, AARM fabrics successfully isolate the ferromagnetic component. Interestingly, the AARM fabrics do not correspond to the AMS fabrics, except in that they have roughly parallel symmetry planes (Figure 6-2c,d). $AARM_{int}$ is close to parallel with k_{min}, and the AARM foliation is perpendicular to the AMS foliation and mean dike planes. In most cases where there are two distinct paramagnetic and ferromagnetic sub-fabrics, the high-susceptibility of the ferromagnetic fabric swamps the paramagnetic

contribution to AMS. In this case, a poorly defined orientation-distribution of a complex mixture of primary and secondary ferromagnetics has too low an *anisotropy* to disturb significantly the well-defined and strongly oriented (by magmatic flow) paramagnetic AMS.

6.2.2. Konia site

Seventy-four core samples were recovered form this site. AMS was measured on all, while 21 of these were found suitable for AARM determination. At less than 7km north of the STTFZ, and with a mean dike strike of northeast-southwest (Figure 6-1b), these dikes were clearly affected by shear along the transform, causing their clockwise rotation. While the exact sequence of rotations affecting these dikes remains elusive, it is clear that they are at least rotated 45° clockwise. This is due to their proximity to the transform and is observed in their departure from the north-south strike which is considered primary for the SDC. They remain free from penetrative deformation, however. Despite the difference in dike orientation, AMS fabrics from Konia are very similar in orientation to those described for Panagea. k_{max} axes are distributed along the trace of the dike plane, with a strong grouping, and mean tensor axis for k_{max} plunging moderately to the east/northeast, within the dike plane (Figure 6-3a). k_{int} axes group with a shallow plunge to the south, displaced anti-clockwise from the mean dike plane. Minimum axes and their mean tensor cluster close to but with anti-clockwise displacement from the group of dike poles for the area (Figure 6-3b). In contrast to the oblate symmetry of the mean tensor confidence regions of the Panagea samples, those for Konia show a distinct prolate symmetry. Clearly, the clockwise rotation of the dikes of this area due to shear along the STTFZ is responsible for the misalignment of the AMS principal axes and the dike plane.

Removing this offset, the magnetic fabrics appear compatible with magma flow described in Section 4.3, meaning that k_{max} may indicate magma flow that was relatively steep in this area. As at Panagea, AARM fabrics for Konia share symmetry planes with AMS fabrics, but show perpendicular magnetic foliation planes (Fig 6-3c,d). Again, a low-anisotropy ferromagnetic oxide subfabric may be present which, while highly susceptible, is insufficiently anisotropic to disturb the paramagnetic-orientation distribution expressed in the AMS fabric.

6.3. Interpretation of magnetic fabrics

It has been shown that in both sheared and non-sheared area, AMS may be a useful magma-flow indicator as described in previous chapters. The correspondence of AMS axes and magnetic foliation with those expected for magma-flow based on kinematic arguments (Section 4.3) leaves little room for doubt as to the origin of the orientation distribution of grains found in rocks of the SDC. Despite the apparent simplicity in interpreting AMS data alone in terms of magma-flow, AARM fabrics are somewhat ambiguous and difficult to reconcile with a simple kinematic model. Interestingly, the k_{max} and $AARM_{max}$ mean tensors are similarly oriented in both areas described above, whereas k_{min} roughly corresponds to $AARM_{int}$, and k_{int} roughly corresponds to $AARM_{min}$. The most noticeable disparity between the AMS and AARM fabrics is the difference in variability within the data. The 95% confidence regions about the mean tensors for AMS principal axes are very small and well constrained, whereas those for AARM principal axes are large. Clearly, there exist at least two petrofabrics in these rocks; a 'primary' preferred orientation of paramagnetic silicates (AMS), and a feeble, low-anisotropy

orientation distribution in late crystallizing and altered primary ferromagnetic oxides. With the data presented thus far in this chapter, the following may be concluded:

1) That AMS fabrics may proxy for magmatic flow in areas where 'primary' dike-strikes persist
2) Despite the misalignment of AMS fabrics and dike planes related to shear along the STTFZ in areas of rotated dikes, magma flow may still be inferred by qualitatively restoring the dike strike and then evaluating the fabrics as described in Section 4-5 (Figure 6-4)
3) There may be an oxide sub-fabric that, while overwhelming the bulk susceptibility of the samples, is of low-anisotropy and therefore is unable to swamp the strong preferred orientation of the paramagnetic fabric described by AMS results.

In general, a ferromagnetic sub-fabric that is oriented differently from that of the paramagnetic silicates will dominate both the magnitude and orientation of the resulting AMS fabric (Borradaile and Henry, 1997). The late, low-temperature sea-floor alteration and topotactic recrystallization of oxides in ophiolitic and oceanic basalt and diabase is a well known process (Section 3.3.2). This process does not implicitly retain any features of the orientation-distribution of primary oxides that may have been aligned by magmatic flow. Fortunately, in this study the oxide sub-fabric due to sea-floor alteration appears to be unable to affect the flow-derived orientation-distribution of the paramagnetic silicates. Nonetheless, in light of the potential for confusion resulting from a alteration oxide fabric masking a flow-aligned AMS, the nature of the oxides should be investigated further. The main question that must be addressed is; what is the nature of the oxide sub-fabric

revealed by AARM? Moreover, why is its orientation not expressed in the AMS fabric? It is also possible that there are multiple oxide sub-fabrics, an early one corresponding to the AMS signal, and an alteration fabric as suggested.

6.4. Rock magnetism tests

To answer the questions above, and to further understand the nature of the AMS results presented in Chapter 5, several rock magnetic properties were evaluated for the Panagea and Konia sites.

6.4.1. Thermomagnetic experiments

As described in section 3.3.2, different oxides occur in oceanic basalt and diabase at different stages of alteration, *and* at different depths in the crust. Each of these oxides has a distinct Curie temperature (T_c), and as such may be identified via thermomagnetic tests. For this study, a Sapphire Instruments (Canada) horizontal-translation Curie Balance was used. With this instrument, T_c of ferromagnetic grains is determined by heating a specimen from room temperature to some predetermined maximum, and measuring the displacement of the specimen relative to a large solid-state neodynium-cobalt magnet. When a given oxide reaches its Curie temperature, the specimen instantly loses some attraction to the magnet. Results of this experiment are shown in Figure 6-5. Inflexion points occur in most samples between 300°C and 350°C. In 50% of samples tested, all ferro-magnetism is lost at temperatures between 350°C and 550°C. Weak inflexion points in the remaining samples occur at 560°C. However, >30% of original magnetization persists beyond that temperature in these specimens. The primary oxides in sea-floor basaltic rocks, TM_{60} and magnetite, have Curie temperatures of 150-200°C and 560°C, respectively. Only weak inflexion points are found at these temperatures,

indicating that while these phases are present in the specimens, much of the magnetization is carried elsewhere. Oxidised TM_{60}, or titanomaghemite, has Curie temperatures in the 300-400°C range, corresponding better to the inflexion points observed in this study (Figure 6-5). Also, the Curie temperature of oxidized magnetite, or maghemite, is >600°C, and presumably those specimens in this study that were not fully demagnetized at 600°C contain some proportion of it.

These tests reveal that the following oxides are present within the tested specimens:

- small amounts of magnetite, possibly both primary and exsolved from TM_{60}
- small amounts of primary TM_{60}
- oxidised TM_{60}, or titanomaghemite
- oxidised magnetite, or maghemite

6.4.2. AF Demagnetization of SIRM

In order to rule out the single domain effect of inverse fabrics (Section 4.4.1.2), oxide grain-size was inferred from domain-response studied by AF-demagnetization of saturation isothermal remanence (SIRM). An SIRM was imposed at 1.0 Tesla using a Sapphire Instruments (Canada) SI-6 pulse-magnetiser. The SIRM intensity was measured following each step of AF-demagnetization in a Sapphire Instruments SI-4 demagnetizer. SIRM was removed completely at a peak AF demagnetising field of 130 mT (Figure 6-6a). Differentiating the cumulative curve gives a remanence-coercivity spectrum (Figure 6-6a inset), which indicates the proportions of IRM carried in different ranges of the AF-field. Most remanence is carried in the 0-15mT range, slightly less between 15 and 30 mT. These ranges correspond to multi-domain (MD) and pseudo-

single domain *magnetite*, respectively. Therefore, it appears that single-domain magnetite does not contribute to the AMS fabrics in these specimens.

6.4.3. ARM Acquisition

A second test of coercivity of remanence is accomplished by investigating the acquisition of anhysteretic remanent magnetism (ARM). Following complete demagnetization, ARM is acquired using a DC bias field of 0.1mT and a peak alternating field of 180mT. The DC field was applied over AF-windows of different sizes, in 2mT steps. After each step, remanence intensity was measured. Differentiating the cumulative acquisition curves (Figure 6-6b) yields a remanence coercivity spectrum (Figure 6-6b inset). The majority of ARM was acquired over remanence-coercivity windows corresponding to MD-magnetite, and to a slightly lesser extent by PSD-magnetite. These results confirm those found via demagnetization of SIRM (Section 6.4.1).

6.5.Discussion and conclusions

Three main conclusions may be drawn from the AMS, AARM, and rock magnetic results presented here for samples collected at Panagea and Konia, and by extension the Troodos SDC:

1) The topotactic growth of secondary oxides (magnetite, maghemite, titanomaghemite) at the expense of primary oxides (magnetite, TM_{60}) may occur without orientation-bias, resulting in weakly anisotropic oxide sub-fabrics. The secondary oxide sub-fabric may dominate the bulk susceptibility of the rock. However, it cannot suppress the strongly aligned and anisotropic paramagnetic (and residual primary oxide) flow fabric because it is nearly isotropic. This is

especially clear where AMS tensors of individual specimens have been normalized to equivalent volumes (thus the magnitude of susceptibility of each is not considered), and evaluated in structurally homogenous subareas.

2) When interpreting anomalous magnetic fabrics where an oxide subfabric is suspected, it is common practice to conclude that a mixing of aligned, paramagnetic and ferromagnetic anisotropic fabrics is present. The resulting AMS in that case may be controlled more by the relative susceptibilities of two (or more) sub-fabrics. In this study, mixing of subfabrics of differing anisotropies is suspected. Fortuitously, in this study the oxide sub-fabric is of low-anisotropy and poor alignment, so it is not able to mask the strong flow-alignment and high anisotropy of the paramagnetic fabric.

Rotation of dikes due to shear along the STTFZ may misalign the AMS fabric and dike plane, potentially leading to kinematically ambiguous fabrics. Clearly, in many cases, offset dikes and fabrics may be rectified in terms of magmatic flow *within* the dike plane, even where k_{max} does not lie within the dike plane.

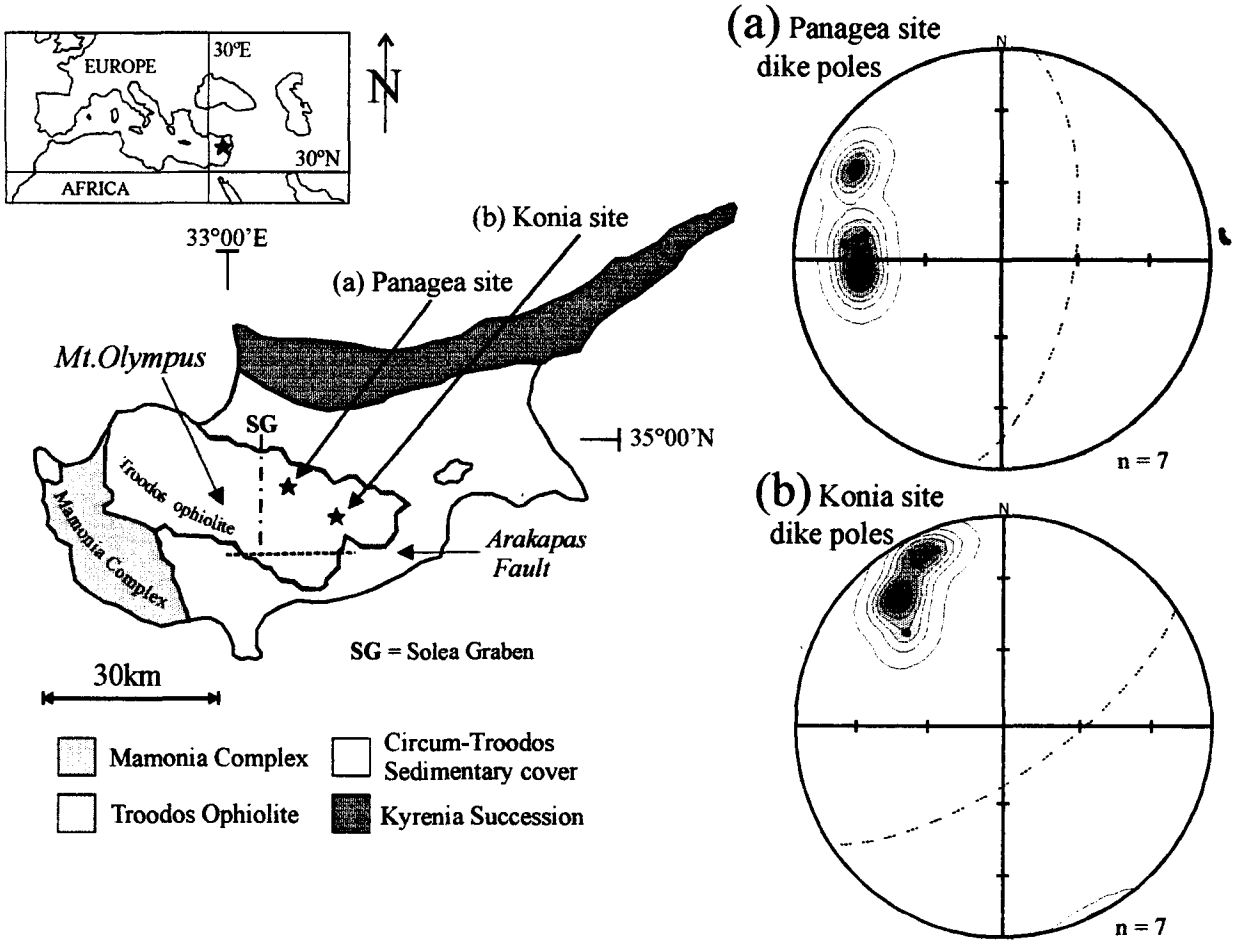

Figure 6-1. Generalized geological map of Cyprus, showing the location and dike orientations of the Panagea (a) and Konia (b) dike study sites. (From Borradaile and Gauthier, 2002)

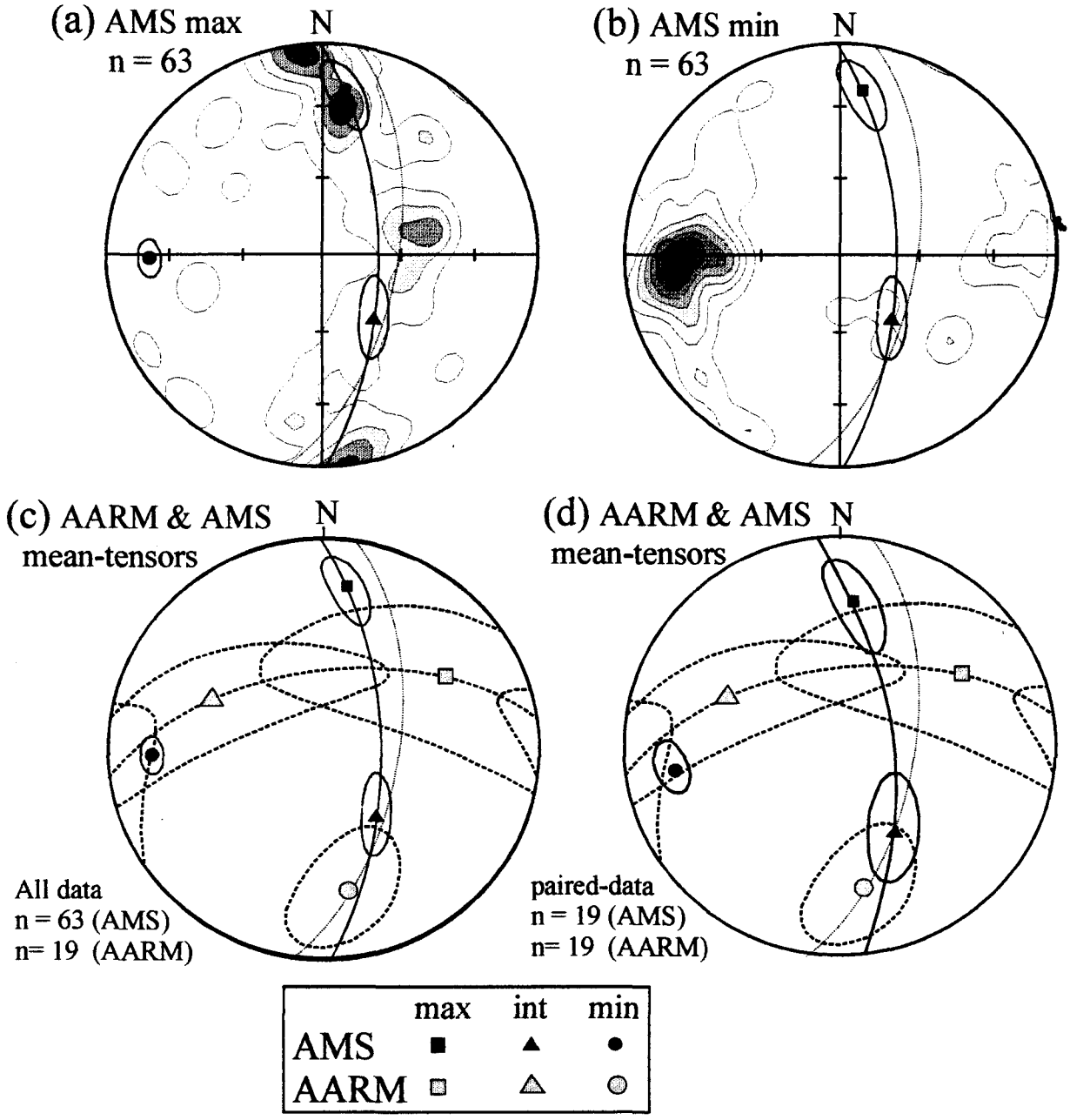

Figure 6-2. AMS and AARM results for specimens collected at the Panagea site. Mean AMS tensors and confidence ellipses are plotted over density contoured stereonets of maximum (a) and minimum (b) AMS axes, and AARM mean tensors and confidence regions (c). In (d) only the 19 specimens for which AARM was performed are included in the AMS mean tensors, for comparison. (From Borradaile and Gauthier, 2002)

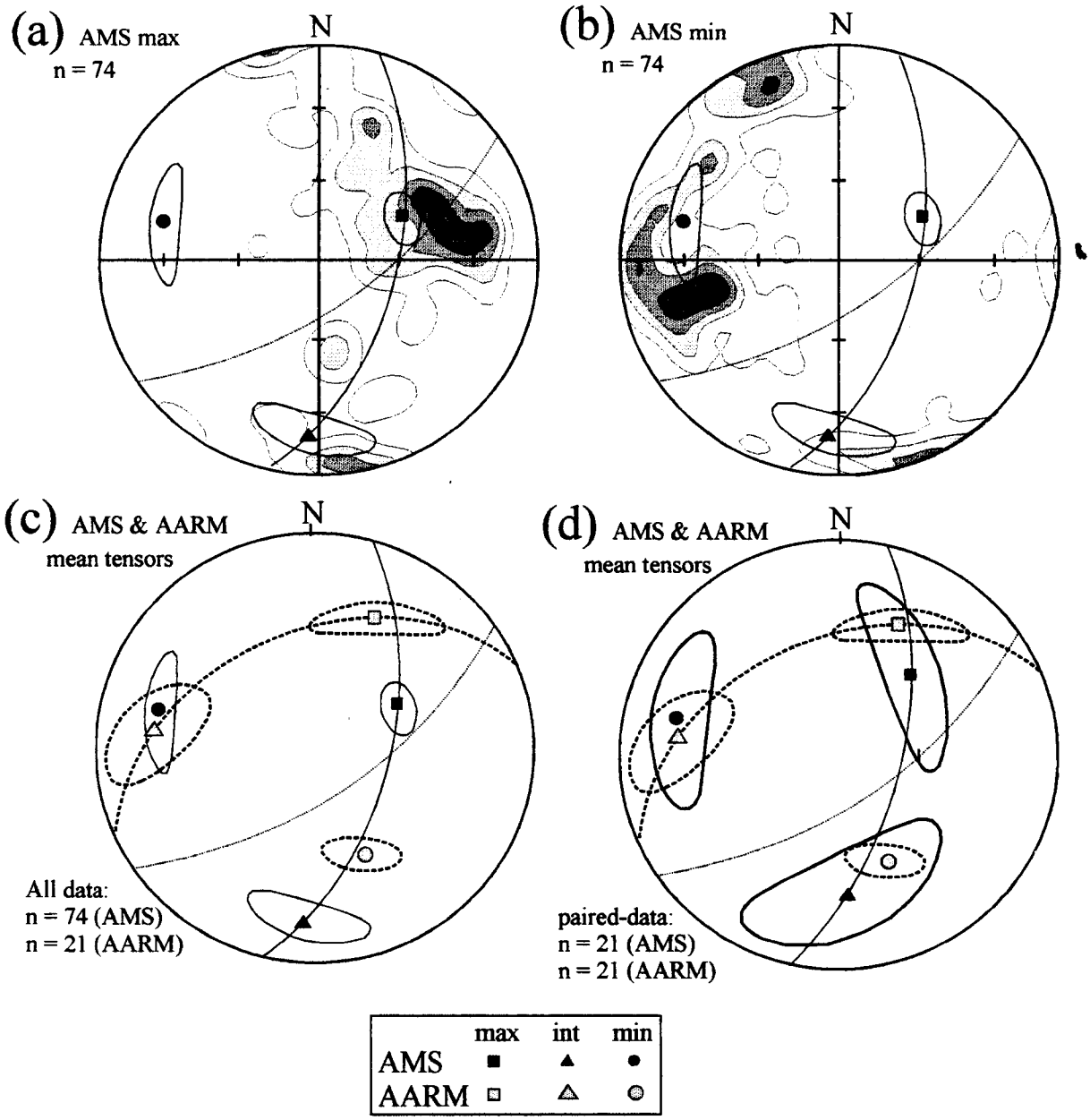

Figure 6-3. AMS and AARM results for specimens collected at the Konia site. Mean AMS tensors and confidence ellipses are plotted over density contoured stereonets of maximum (a) and minimum (b) AMS axes, and AARM mean tensors and confidence regions (c). In (d) only the 21 specimens for which AARM was performed are included in the AMS mean tensors, for comparison. (From Borradaile and Gauthier, 2002)

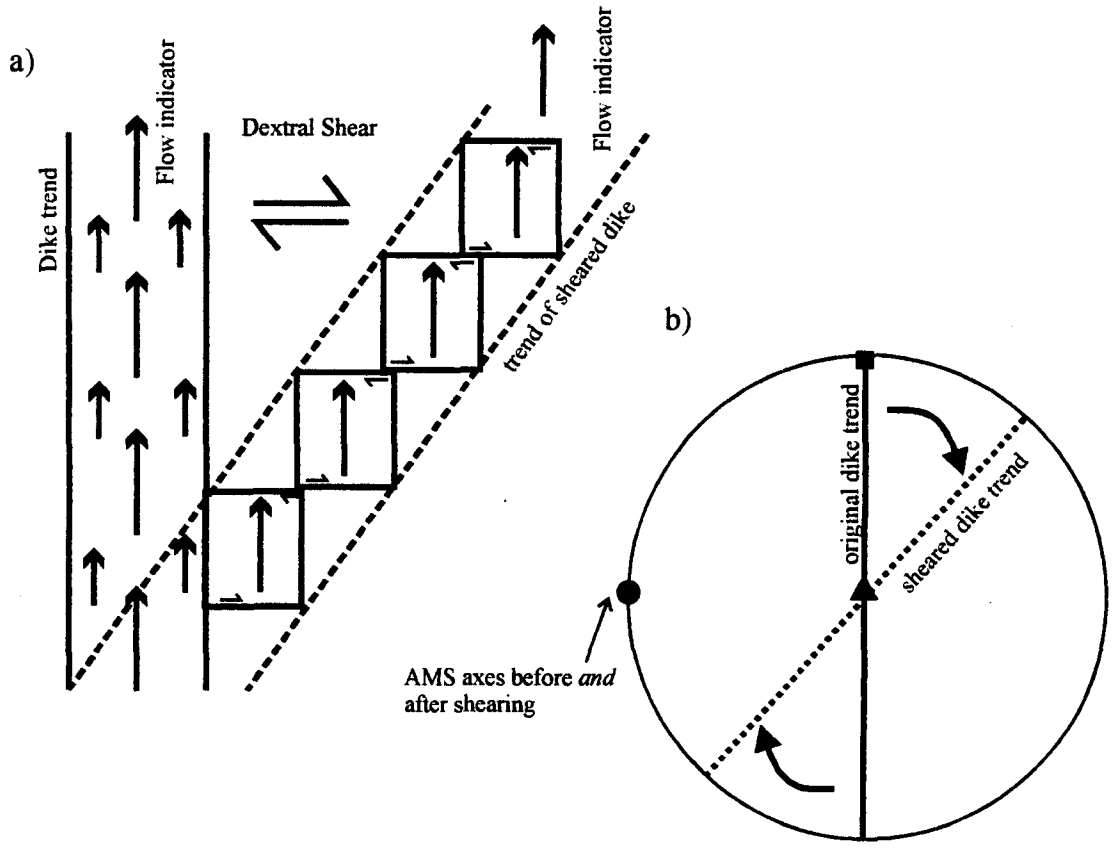

Figure 6-4. (a) Plan view sketch idealizong macroscopic or megascopic cataclastic shear on E-W fractures. The internal penetrative flow fabric, defined magnetically, retains its orientation, despite cataclasis (from Borradaile and Gauthier, 2002). (b) Example of a theoretical AMS fabric resulting from the process described in (a).

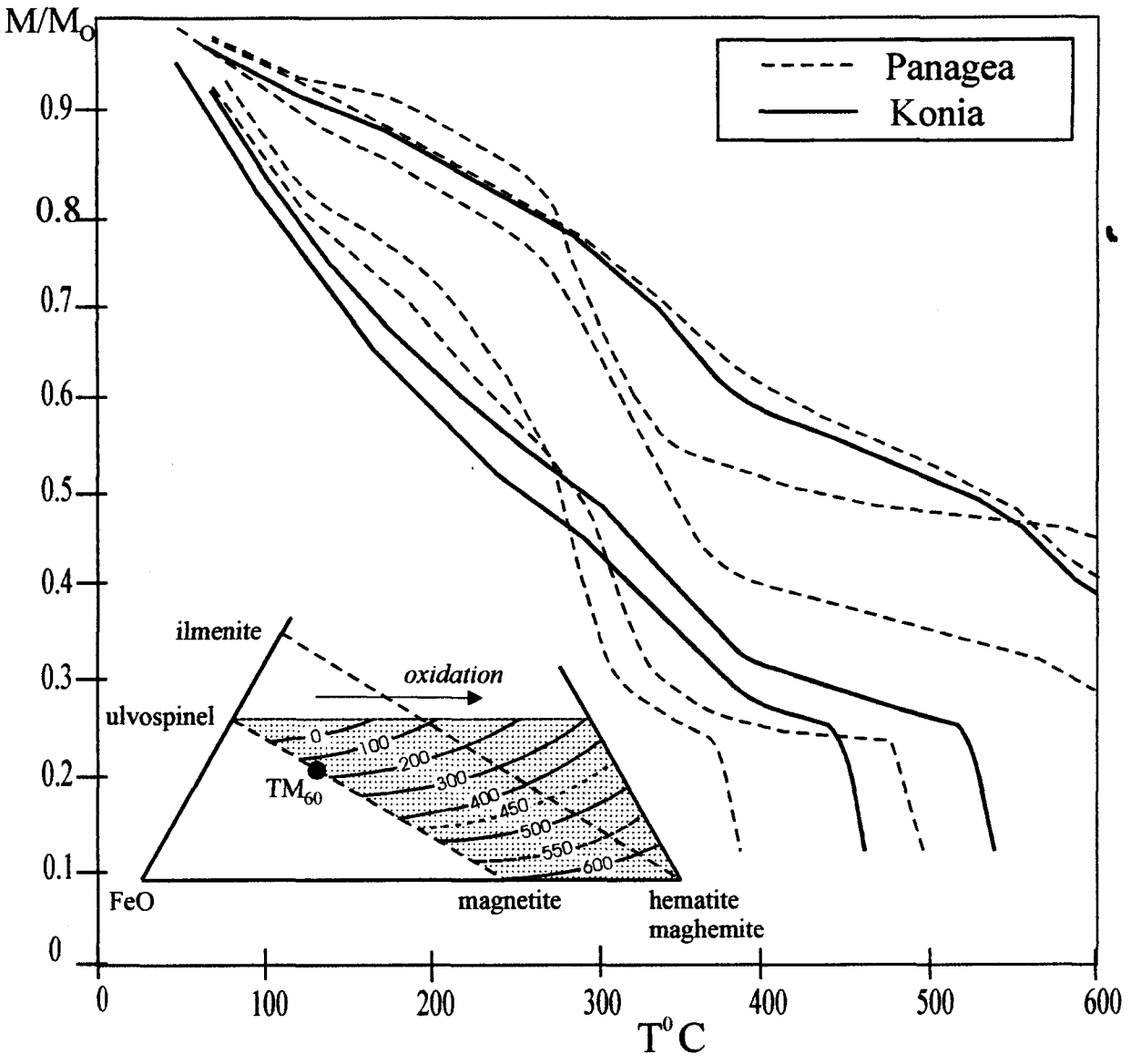

Figure 6-5. Curie temperatures on heating typical dike-samples in this study. Inflection points near ~250°C may be due to TM_{60}, but the most prominent inflection points ~300-350°C suggest more oxidised versions such as titanomaghemite. Traces of magnetite are indicated by Curie points ~560-580°C. (Inset diagram after Dunlop and Ozdemir, 1997)(From Borradaile and Gauthier, 2002)

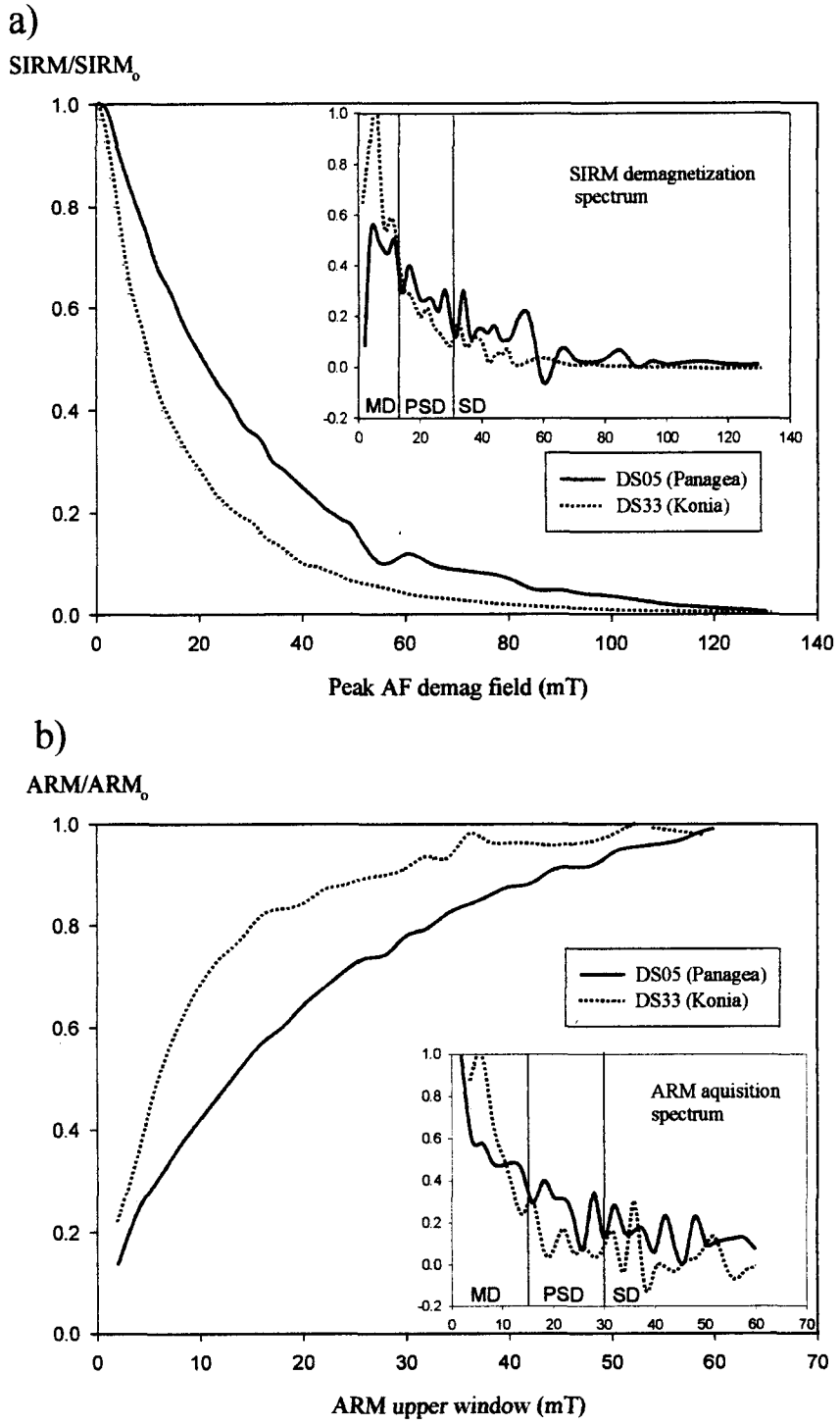

Figure 6-6. (a) Alternating field (AF) demagnetization of isothermal remanence (IRM) acquired at 1 Tesla. Inset of spectrum of coercivity of remanence (Bcr) and, for comparison only, domain -state ranges commonly reported for magnetite (MD=multi-domain, PSD=pseudo-single domain, SD=single-domain). (b) Intensity of anhysteretic remanence (ARM) acquired with successively higher upper window-frame for the AF over which the DC bias field was applied. In all cases, the peak AF was 180 mT and the DC bias field was o.1mT, as in the experiments where anisotropy of ARM was measured. (From Borradaile and Gauthier, 2002)

7. Interpretation and discussion

This chapter attempts to use the magnetic fabrics described in Chapter 5 to infer the magma-flow patterns in the sheeted dikes of the study-area. In turn, these are used to infer the location and dimensions of mid-ocean ridge magma-chambers. A brief review of the popular models of mid-ocean ridge magma-chambers prefaces the discussion. The implications of these interpretations on the spreading structure of the Troodos oceanic crust are discussed.

7.1.Magma-chambers and magnetic fabrics

The terms *magma-chamber*, *magma resevoir*, and *melt-lens* must be qualified when they are used, as they describe different features of the crust depending on the model being discussed. In this study, the *magma-chamber* and *magma reservoir* will be used to refer to the small melt lens that is thought to develop at the top of the crystal mush zone from which sheeted dikes are injected.

7.1.1. Review of magma-chamber models

Geophysical studies of the East Pacific Rise (EPR) fast-spreading mid-ocean ridge (e.g. Detrick et al., 1987) have confirmed the presence of a 1km wide, ~100m thick magma-chamber that may be continuous along the ridge. The presence of the large, steady state or permanent magma-chambers of Cann (1974) have never been observed. Along slow-spreading ridges no geophysical evidence for large or small magma-chambers was observed until relatively recently; Calvert (1995) and Sinha et al. (1998) reported a 4km wide, 100m thick magma pocket extending approximately for 30km along the slow-spreading Mid-Atlantic Ridge (MAR) at one location.

Sinton and Detrick (1992) reviewed the expected features of mid-ocean ridge magma-chambers in popular models, which have been subsequently confirmed by geophysical evidence. Fast-spreading ridges are expected to have a three-part chamber. A large tent shaped (wide at the base) crystalline transition zone between partially molten material to hot surrounding rock tapers upwards to a volume of partially solidified crystal mush above and within the transition zone, capped by a small sill shaped melt lens. Magma resevoirs along slow-spreading ridges are believed to be ephemeral. Where an eruptable magma supply exists along a slow-spreading ridge, it should differ somewhat from the fast-spreading reservoir. The crystal mush zone may be more dike-like, surrounded by a transition zone of mostly crystalline material. The uppermost part of the crystal mush 'dike' may pool molten material which both passively supplies the ridge and crystallizes into sill-like bodies that form the lower crust. Seismic velocity data and theoretical models predict, for both fast and slow-spreading ridges, that the crystal mush zone is ~25% crystalline, while the transition zone should contain up to 80% crystals (Nicolas et al., 1993).

The existence of magma reservoirs at mid-ocean ridges as described above reconciles the current geophysical and petrological data obtained from both in situ crust and ophiolite analogues. In terms of the current study, the specific features of the transition and crystal mush zones are of little significance. It is the existence and extent of the upper magma-lens that is of interest.

At fast-spreading ridges with abundant magma supply, most areas along the ridge axis would be expected to be underlain by an axial magma reservoir or chamber. This implies that magma flow in the sheeted dikes should be preferentially vertical, as all

dikes are fed from directly below. Along slow-spreading ridges, however, there are intermittently spaced magma-rich and magma-starved regions. Magma-rich regions are fed by a magma-chamber, allowing for magmatic extension and crustal growth, while magma-starved regions lack an axial magma-chamber and spread via tectonic or mechanical extension. Sheeted dikes forming directly above a slow-spread axial magma-chamber may also show preferentially vertical flow. Areas further from the chamber are more likely to be intruded laterally, with magmatic flow shallowing with distance from the source. Following the cessation of magmatic extension and a switch in a particular area from magma-rich to magma-starved, tectonic extension takes over and the crust formed by dike intrusion may be faulted and stretched to accommodate plate separation (Figure 7-1).

7.1.2. Magnetic fabrics

As described in Chapter 5, the majority of the magnetic fabrics throughout this study area may be used as magma-flow indicators. By reducing the data into sub-areas of steep k_{max} and shallow k_{max} with similar dike orientations, regions of steep magma flow and shallow magma flow were delineated (Figure 5-4). Four of the shallow-k_{max} sub-areas were found to have an insufficient number of specimens to interpret magnetic fabrics in terms of magma-flow. In most of these cases the magnetic fabrics were similar in orientation to adjacent sub-areas. Two sub-areas originally identified as 'shallow' k_{max} sub-areas (I-2 and III-3) may be better suited to designation as steep-flow sub-areas.

Based on a detailed study of magnetic fabrics and other properties of samples from two outcrops (Chapter 6), it was suggested that the magnetic fabrics presented in Chapter 5 may be influenced by two distinct populations of ferromagnetic minerals. To

test this hypothesis for the entire study area, the mixing model of Henry (1983) is presented in Figure 7-2. By plotting k_i (where i= max, int, min) against k_{mean} for each specimen, a linear relationship of principal axes may occur, and the mutual intersection of these trend lines may represent a theoretical, isotropic, paramagnetic matrix, provided that Henry's assumptions about the magnetic mineralogy of the specimens are met. These assumptions are that there is one group of paramagnetic matrix minerals and one group of ferromagnetic minerals, and that their respective orientation distributions are co-axial. The intersection of the principal lines for the entire data set at k_{mean} = 6482 μSI is greater than the theoretical maximum susceptibility for a pure paramagnetic silicate (Borradaile and Henry, 1997), indicating the presence of ferromagnetic inclusions in the matrix paramagnetics. The same test for samples with k_{mean} < 20 000 μSI and < 2000 μSI (insets of Figure 7-2) show intersections at k_{mean} = 486 μSI and 210 μSI respectively, proving that the ferromagnetic inclusions in paramagnetic matrix minerals may dominate in the higher susceptibility samples. The assumption of a single ferromagnetic population may not apply here, thereby confirming the conclusion of Chapter 6 that suggested that multiple oxide sub-fabrics may be present. One of these fabrics is co-axial with the flow-aligned paramagnetic fabric, while the other may be of such low alignment as not to disrupt the primary fabric.

It was also shown in Chapter 6 that in many cases the mean dike plane and magnetic fabrics may become misaligned by shear along the STTFZ, implying that trend variation in k_{max} (flow) axes may be less important than plunge variation. In light of this, Figure 7-3 only maps spatially averaged k_{max} *inclinations*. Inclination data was smoothed using similar parameters to previously described spatial-averaging of dike and k_{max} orientations,

however in this case the smoothed inclinations are colour contoured. Regions of steep and shallow flow axes are easily identified by inspection of the map.

7.2.Size, location, and scale of Troodos magma-chambers

In terms of the original aim of this study, regions of steep k_{max}, and therefore steep magma-flow, are thought to have been underlain by an axial magma-chamber. Conversely, regions of shallow flow may have been further from the magma supply. In the models for slow-spreading ridges described above, the existence of active magma-chambers, and therefore regions of steep and shallow flow must vary *along* the spreading-axis. The temporal stability of these features, however, must be evaluated perpendicular to the axis. In order to evaluate the along-axis and axis-perpendicular variation in the results of this study, the position of lines of equal time (as in Figure 6-1) must be determined for the study area. These lines do not necessarily represent the position of a paleo-spreading centre, but do tie together portions of the crust that resided along a spreading-axis at the same time. The trend of this 'ridge-chron' can be defined by the average orientation of its extensional structures, the most obvious of which are the dikes of the sheeted complex (Nicolas, 1989) (Figure 7-4). The spatially averaged dike orientations shown in Figure 7-3 may therefore be used to approximate the orientation of the ridge-chrons for the current study area. Also, the axis of the Mitsero Graben, which may represent a paleo-spreading axis (Van Everdingen and Cawood, 1995), supports the trend of the ridge-chron as defined by dike orientation (Figure 7-3).

7.2.1. Along-axis length

Evaluation of the magnetic fabrics presented in Chapter 5 in terms of the requirements for magmatic origin have shown that each of the steep k_{max} (flow) sub-areas

may be used to approximately indicate magma flow. As such, these areas may have been underlain by, or were close to, an axial magma-chamber when they were intruded. In each of these sub-areas, the ridge-chron may be defined by the average dike-orientation within the sub-area. The *along*-axis extent of the regions of steep flow, and therefore of the magma-chambers themselves, must be evaluated in this direction (Figure 7-5). To accomplish this, seven representative traverses along dike-orientation defined ridge-chrons were selected, including one traverse along the Mitsero Graben axis. From west to east, the traverses are labeled W1, W2, W3, Mitsero, E3, E2, E1. Six of the seven terminate in the south at northern boundary of the Arakapas dike domain (Figure 3-4). This southern termination is considered the starting point of each south to north traverse and is assigned a position of 0m in the distance scale on a plot of k_{max} plunge versus distance (Figure 7-6a).

One important observation based on Figure 7-6a is that the region of *very* steep flow (ie. >80° inclination) along each line is narrow, indicating a *point source* of magma supply to the ridge. On a plot of flow-inclination versus distance, such as Figure 7-6a, a traverse along a line that had a magma source with some along-axis extent would yield constant steep inclinations above the source, as very-steep flow would be expected to exist along the length of the source. Each of curves plotted for this study area have narrow peaks with very-steep flow, but these regions do not continue along the traverse (ridge). Regions of generally shallow flow tend to be flat on Figure 7-6a, meaning that the space between magma-chambers must be larger than the chambers themselves.

The along-axis spacing of the magma sources identified by very-steep flow in Figure 7-6a was investigated using Fast Fourier Transform (FFT) analysis of the

waveforms of each traverse. The power of each peak (normalized to the power of the first peak) is plotted against the wavelength (1/frequency) of the peak (Figure 7-6b). The highest power (most significant) peaks of each traverse (relative power = 1) occur at a wavelength of between 2000m and >8000m (Figure 7-6bi), with a mean wavelength of ~4000m. The majority of the lesser-power peaks have wavelengths of less than 4000m (Figure 7-6bii), with a mean of ~1200m. Clearly, there is a bimodal distribution in the peaks (Figure 7-6b): a high-power group representing the spacing of areas of very steep k_{max} seen in Figure 7-6a, and a set of lesser-power peaks corresponding to the small peaks in the distance vs. inclination curves (Figure 7-6a). The short wavelength of ~4000m (high frequency) of steep k_{max}, and therefore magma sources, means that the diameter of the sources themselves must be less than 2000m (<1/2 x 4000m).

7.2.2. Temporal stability of magma-chambers

The scale of the magma sources described in Section 7.2.1 perpendicular to the spreading axis will allow for an estimate to be made on their temporal stability. Simply put, the wider the region of steep flow, the longer the magma source was in operation. Similar to the analysis described above for axis-parallel traverses, spatially averaged k_{max} inclinations were collected along five traverses perpendicular to dike strike, therefore representing temporal variations in magma supply at a given point along the ridge. These traverses are plotted on a distance versus inclination plot (Figure 7-7a). The traverses are numbered N1 to N5, where N1 is the northernmost and N5 the southernmost. Each traverse begins at the far west side of the study area, and as such this is considered the starting point of each and assigned a position of 0m on the distance scale. Inspection of the graph shows that while the peaks in flow inclination are not as narrow as those on the

along-axis plot (but are nonetheless not plateaus), the change from shallow to steep flow tends to take place over a short distance (steep curves on Fig. 7-7a)).

FFT analysis was performed on these waveforms as well, with the relative powers of peaks (steep flow) compared with their wavelength (1/frequency) (Figure 7-7b). There exists a large range in the wavelength of the maximum-power peaks, with values from ~2000m to >12 000m, and a mean at ~6000m (Figure 7-7bi). The lesser-power peaks are consistently around a wavelength <2000m (Figure 7-7bii). The spacing, or wavelength, of these peaks is a measure of the across-axis distance between regions of steep-flow, which in turn is directly related to the spacing in *time* between active magmatism at a given location along the ridge.

Before making any firm interpretations based on the magma-source spacing described above, it is necessary to discuss the role of the Mitsero Graben as a spreading-centre. As the graben axis passes through the present study area, it is important to understand if the graben axis does represent a paleo-spreading axis. Also, it is important to recognize the areas of crust within the study area that were formed at the Solea or Mitsero axes. Without that knowledge it will be impossible to make interpretations with confidence based on spreading-rate or ridge processes, as crust formed along different ridge systems may not be directly comparable.

7.3.Mitsero Graben axis as a spreading-ridge

As described in Chapter 2, there has been some debate in the literature regarding the role of the Mitsero Graben in the spreading structure and evolution of the Troodos ophiolite. For example, some models claimed that the graben was formed 'off-axis', possibly related to tectonic (amagmatic) crustal growth along the Solea spreading axis

(Allerton and Vine, 1991). A more recent model regards the Mitsero Graben and axis to represent a fossil spreading centre (Van Everdingen and Cawood, 1995; Figure 2-6).

Interestingly, the Mitsero Graben axis cuts across the steep-flow sub-areas C and D (Chapter 5). In fact, inspection of Figure 7-5 shows that the region of steep flow associated with these subareas is almost perfectly symmetrical about the axis, while Figure 7-6a shows that magma-flow reaches >85° inclination at the axis' south end. This data alone is sufficient to consider the Mitsero graben axis to represent a fossil spreading centre and support the model of Van Everdingen and Cawood (1995). In that model, all of the dikes that are part of the current study area are thought to have formed at the Mitsero ridge. Therefore, the current study area must encompass a complete mid-ocean ridge system: the spreading axis itself, and portions of crust formed on both sides of it.

Dilek et al. (1998) compare the constructional features of several ophiolite complexes with modern oceanic crust, and conclude that Troodos matches best the crust along the Mid-Atlantic Ridge (MAR). The MAR is slow-spreading at a *full* spreading-rate of between 2.5 and 4.6 cm/a (Moores and Twiss, 1995). This probably gives the best estimate of the spreading rate of the Troodos crust formed along the Mitsero spreading axis, provided of course that it was, in fact, a slow-spreading ridge. The evidence presented by Dilek et al. (1998) is compelling, and as the data presented here does not exclude the slow-spread origin for Troodos, a full spreading rate of 2.5-5 cm/a will be assumed for the Mitsero crust.

7.4. Troodos as slow-spreading crust

7.4.1. Along-axis processes

The point-source magma-chamber interpretation described above contradicts popular models for both fast and slow-spreading oceanic crust, which call for a magma source that is continuous along the ridge on at least a scale of a few kilometers (Section 7.1). Certainly, the data does exclude the fast-spreading models entirely, as there are regions of lateral magma flow in the SDC of Troodos.

Based on the along-axis size and spacing of magma sources described above, one of two-conclusions may be drawn:

1) While magmatism along slow-spreading ridges is thought to be highly focused (Dilek et al., 1998), the point source magma-chambers that fed the Troodos SDC seem to contradict to the popular magma chamber models and geophysical evidence (Sihna et al., 1998), which require magma-chambers with some along-axis extent.

or,

2) The results presented here may only apply to the plumbing system and magma-delivery systems from magma-chamber to mid-ocean ridge, which may be more complicated than previously thought. The popular models and geophysical evidence for magma-chamber dimensions may not be contradicted by this data, however these results would be inconsistent with a direct delivery from the chambers to the dikes.

Analysis of the along-axis spacing of these small magma sources indicates that their mean separation may be approximately 4km. Again, it is possible that geophysical and other ophiolite evidence for a much longer magma-chamber can be reconciled with

these results. These results only require that the SDC be directly fed by point source chambers spread every 4km along the ridge, while no comment can be made regarding the magma source or delivery to the point-source chambers.

7.4.2. Time-dependant processes

As with the along axis extent of magma sources, the axis-perpendicular traverse data suggests two main ideas: that the magma sources do not persist for any great length of time (ie. point-source in *time* as well as *space*); and that the change from magma rich to magma starved at a given point on the ridge takes place over a short time.

Across-axis distance between regions of steep flow may be directly correlated with time via a given spreading rate, following Table 7-1.

Table 7-1. Seafloor spreading rates and corresponding time-distance factors

distance/time (spreading rate) (cm/year)	distance/million years (km/Ma)	time/distance (years/km)
1	10	100,000
2	20	50,000
3	30	33,300
4	40	25,000
5	50	20,000
10	100	10,000
15	150	7,500
20	200	5,000

It is important, however, to realize that the crust on each side of the ridge is moving away from that ridge at half of the full spreading rate. In this study, across-axis spacing of features which only occur on one side of the Mitsero axis must be related to time by a half-spreading rate, while those that traverse the ridge must be evaluated in terms of full spreading rate. For example, the mean maximum power peak spacing (Figure 7-7bi) of around 6000m, as well as the individual 8000m and 12000m spaced peaks, clearly extend across the Mitsero axis and represent double-sided features. Regions of steep magma

flow, and therefore magma-chambers, spaced 6km across axis would represent a time interval of between 120,000 and 240,000 years, at a *full*-spreading rate of between 2.5 and 5 cm/a. Lesser-power peaks, which have a mean spacing of <2000m (Figure 7-7bii) and appear to be one sided relative to the Mitsero axis, may be 100,000 to 200,000 years of sea-floor spreading apart.

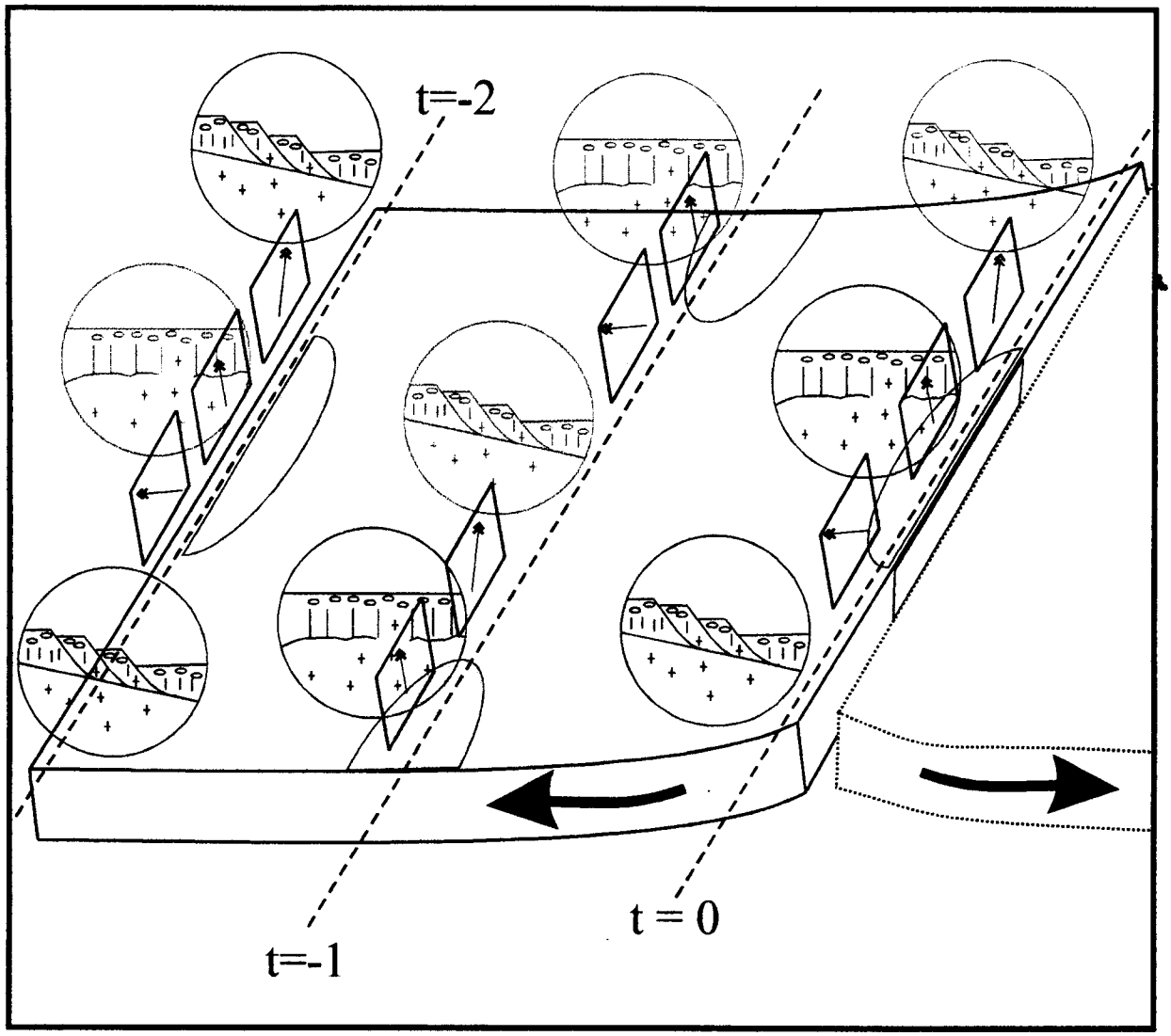

Figure 7-1. Schematic representation of axial processes at slow-spreading ridges with time. Relative time scale of t=0 (present),-1,-2 etc. Shaded areas show the location of magma chambers, vertical planes are dikes with arrows showing magma flow direction, coloured insets represent magma generations vs. tectonic and magmatic extension.

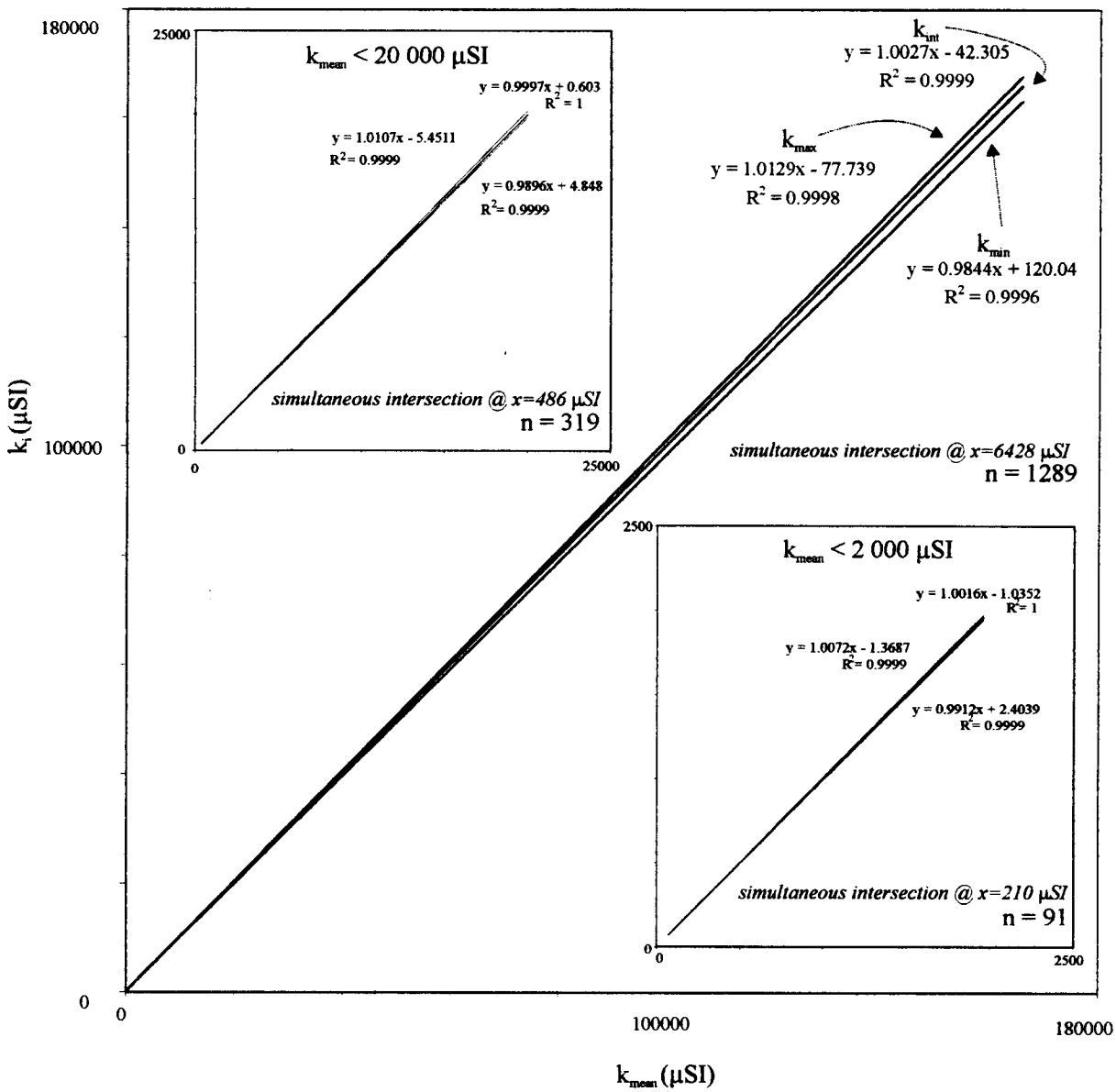

Figure 7-2. Plot of k_i vs. k_{mean} (i= max, int, min) as per the mixing model of Henry (1983) for all specimens, and those with kmean <20 000μSI and <2000 μSI (insets). The simultaneous intersections of the linear functions for maximum, intermediate, and minimum axes are indicated. See text for discussion.

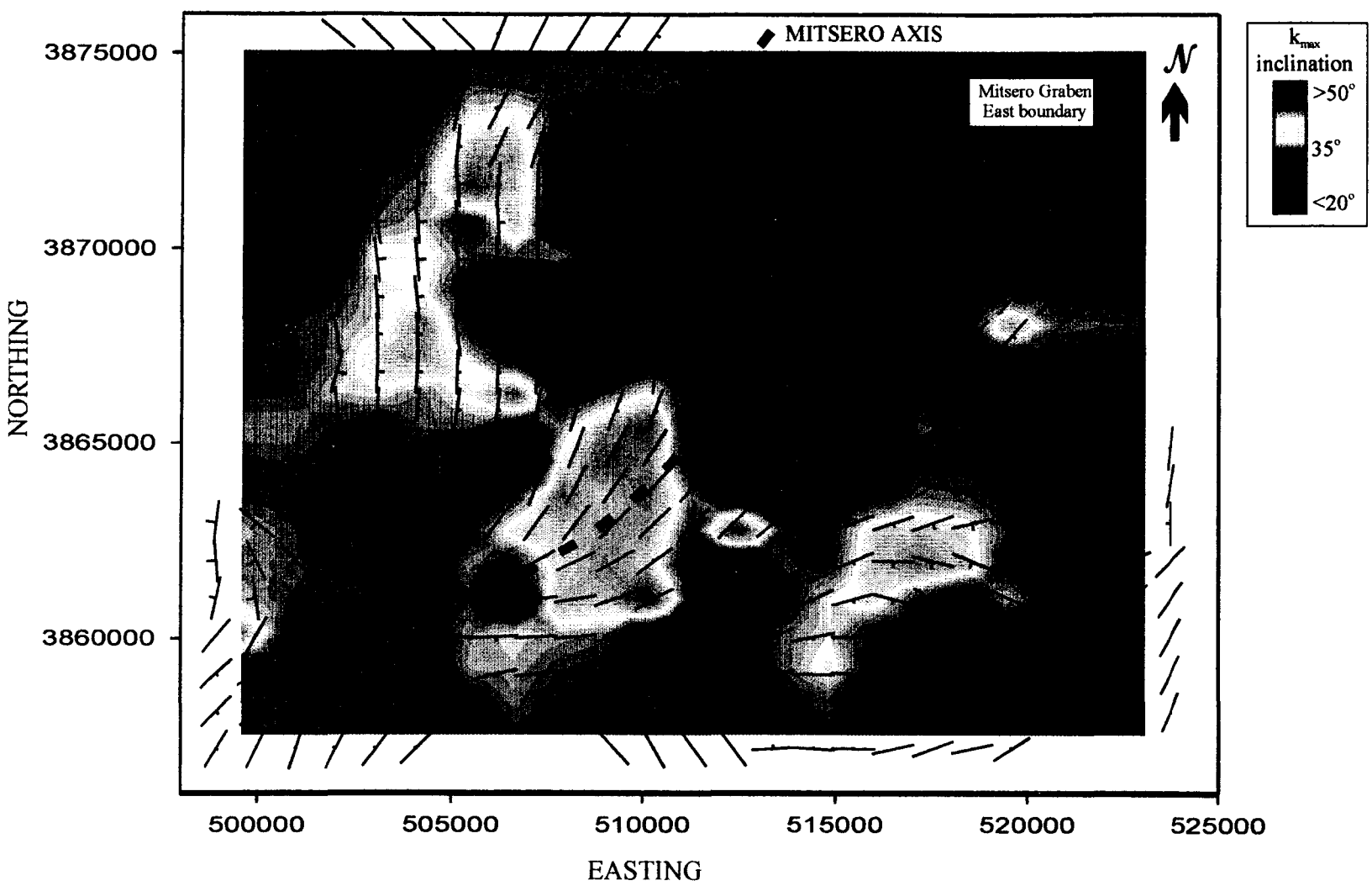

Figure 7-3. Spatially averaged and colour contoured k_{max} inclinations, with spatially averaged dike orientations (strike/dip symbols) and trace of Mitsero Graben axis (thick dashed line).

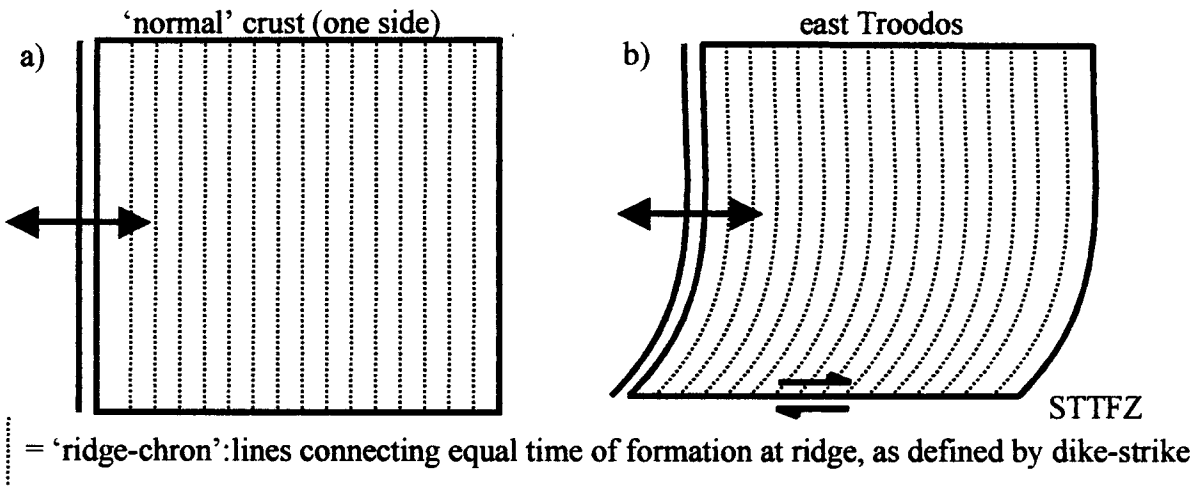

Figure 7-4. a) plan-view schematic of a mid-ocean ridge and one side of its associated crust, showing the orientation of the 'ridge referential' of Nicolas (1989), here referred to as the 'ridge-chron'. b) The concept of (a) modified for the eastern portion of the Troodos ophiolite, showing the effect of shear along the Southern Troodos Transform Fault Zone (STTFZ).

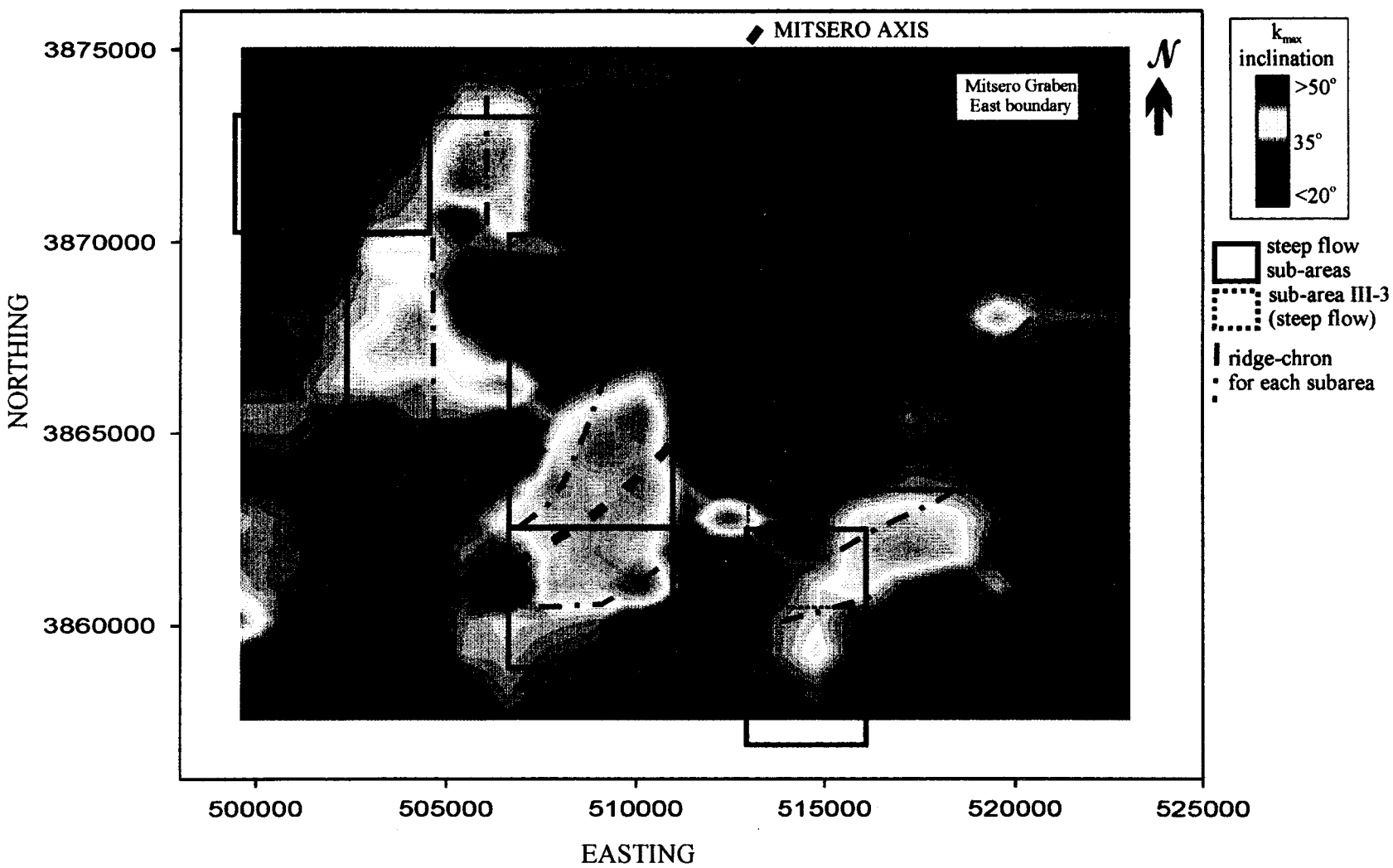

Figure 7-5. Spatially averaged and colour contoured k_{max} inclinations, with location of steep k_{max} sub-areas and the orientation of the 'ridge-chron' within each. The Mitsero graben axis (thick dashed line) and east boundary (thin dashed line) are indicated.

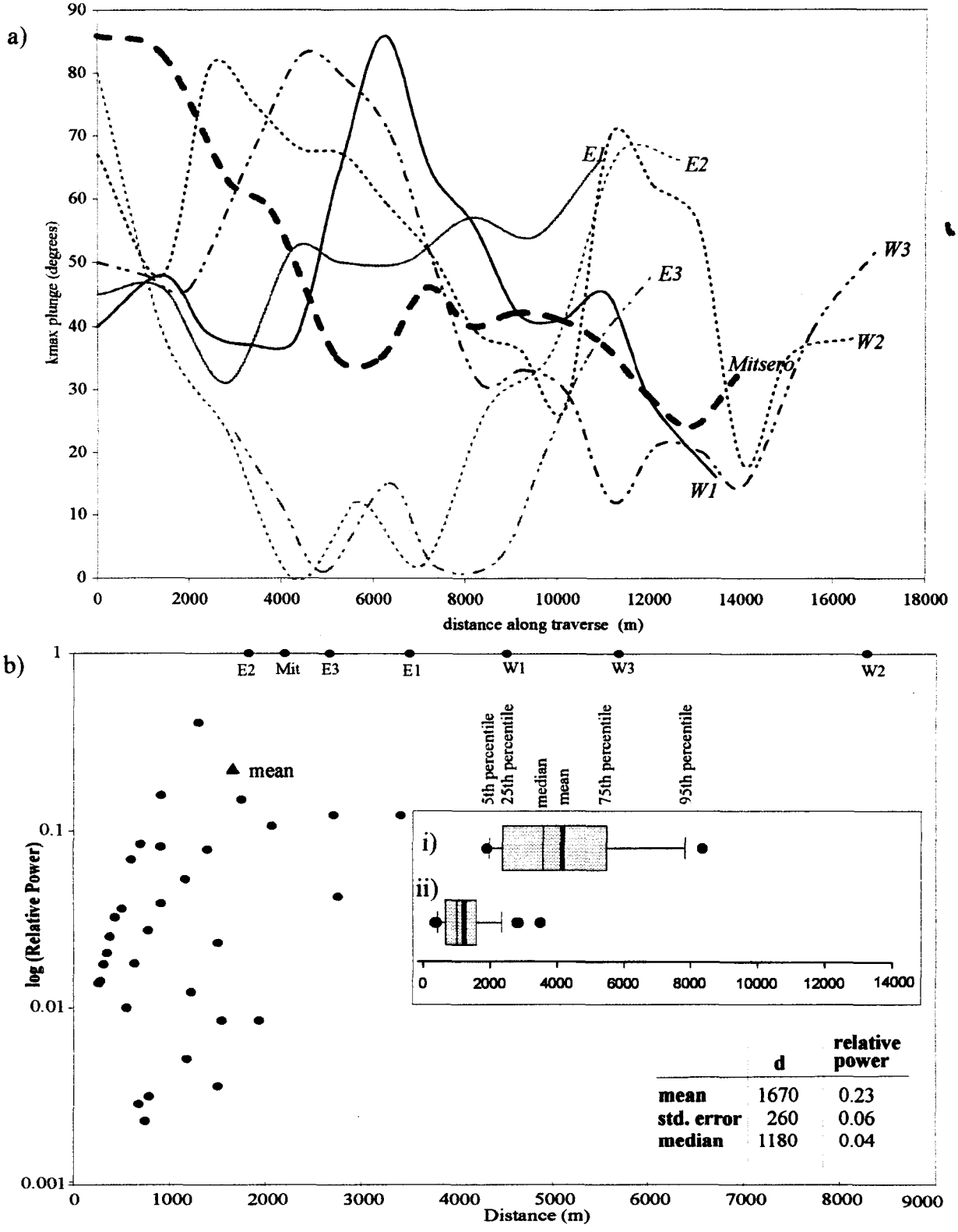

Figure 7-6. a) k_{max} inclination vs. distance plot for several representative *along axis* traverses through the study area. b) Results of Fast Fourier Transform (FFT) analysis of magma chamber spacing, with statistics of maximum power (i) and lesser power (ii) peaks. For clarity, only the maximum-power peaks are labelled.

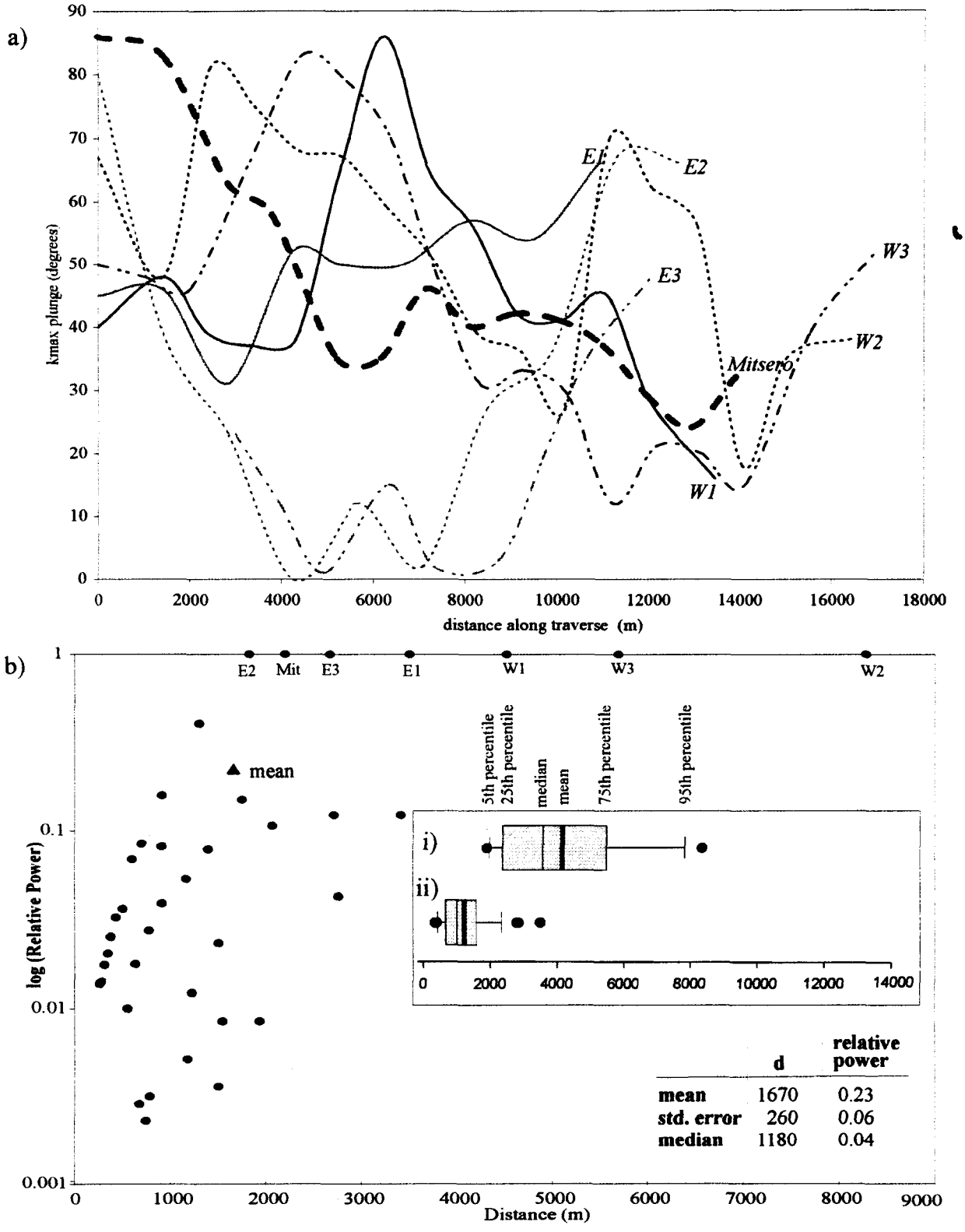

Figure 7-6. a) k_{max} inclination vs. distance plot for several representative *along axis* traverses through the study area. b) Results of Fast Fourier Transform (FFT) analysis of magma chamber spacing, with statistics of maximum power (i) and lesser power (ii) peaks. For clarity, only the maximum-power peaks are labelled.

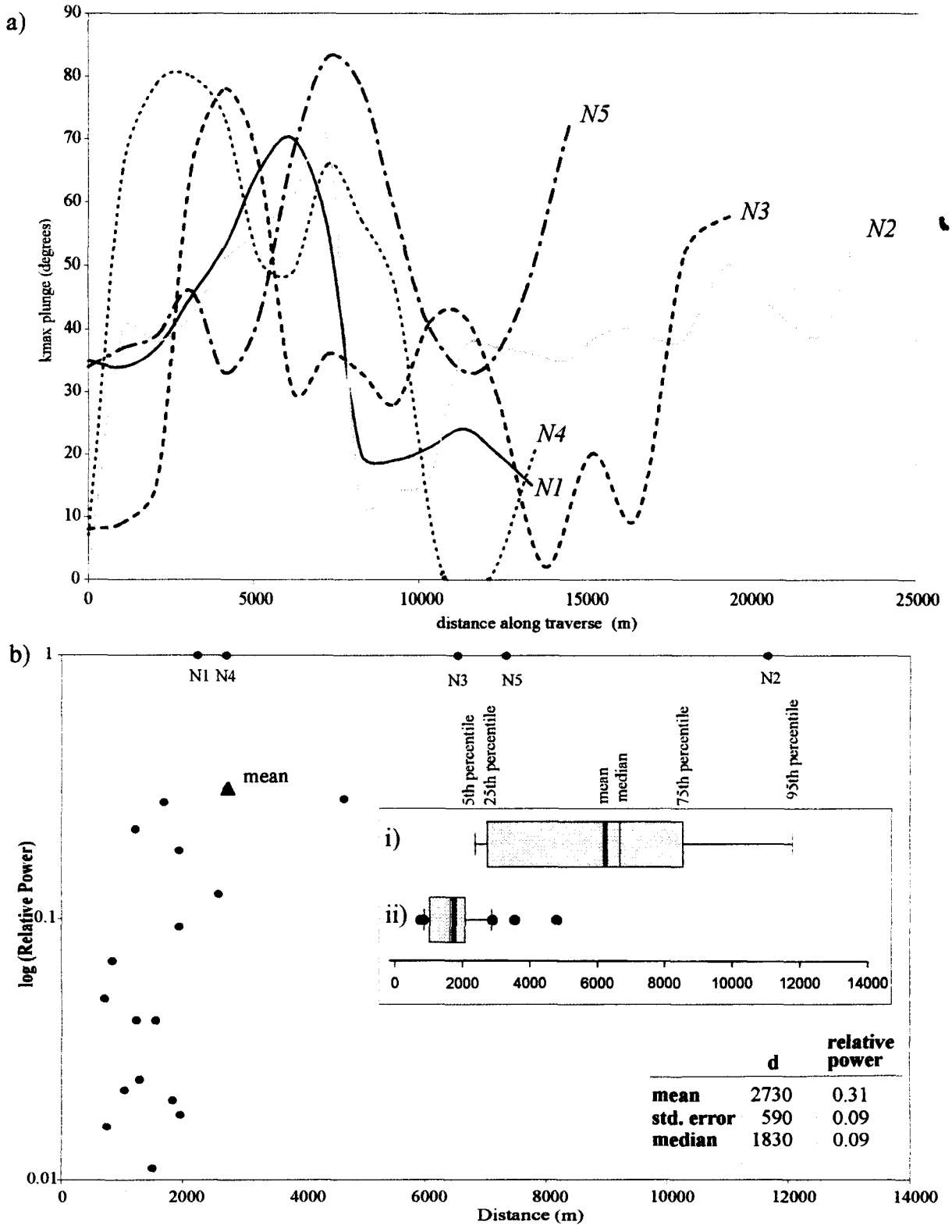

Figure 7-7. a) k_{max} inclination vs. distance plot for several representative *across axis* traverses through the study area. b) Results of Fast Fourier Transform (FFT) analysis of magma chamber spacing, with statistics of maximum power (i) and lesser power (ii) peaks. For clarity only the maximum power peaks are labelled.

8. Conclusions

The intent of this study was to determine the pattern of spatial variation in magma flow directions in the Sheeted Dike Complex (SDC), Troodos ophiolite, Cyprus. This pattern, as defined by AMS fabrics, made it possible to infer the location, size, stability, and frequency of the mid-ocean ridge magma chambers feeding the Troodos crust. Using Troodos as an analogue for modern ocean crust allowed the application of these ideas to mid-ocean ridges in general.

In Chapter 2 it was established that rocks of the Troodos ophiolite represent a relatively undeformed and uninterrupted sample of oceanic crust that was formed ~90Ma within the Paleo-Tethys Sea. The simple tectonic history and well preserved nature of the Troodos ophiolite make it an ideal location to study mid-ocean ridge processes and the details of the creation of new oceanic crust. The sheeted dike complex is the most and best exposed of the Troodos units, and is the focus of this study (Chapter 3). The 1289 standard-size cores used in this study were recovered from 356 locations spread over a 400km^2 area east of Mt. Olympus. The orientation of 1169 dikes were measured and recorded at these locations. The three principal susceptibility axes (k_{max}, k_{int}, k_{min}) were determined for each specimen, and it was shown that the orientation k_{max} may faithfully represent the orientation of the magmatic-flow axis of each specimen (Chapter 4).

AMS results were grouped into sub-areas, containing both homogenous dike orientations and magnetic fabric orientations. Six of these were deemed to have predominantly steeply inclined k_{max} axes, were shown to approximate the magma-flow

axis of the area. The remainder had predominantly shallowly inclined k_{max} axes. Overall, the majority of the AMS fabrics determined in this study were shown to be reliable indicators of magma-flow (Chapter 5).

To aid in the interpretation of magnetic fabrics, two sites were selected, one at Panagea and the other at Konia, to be studied in detail. AMS and AARM were determined for specimens collected at these sites. In addition, several rock magnetism experiments were performed on these samples to determine the specific minerals, phases, and grain-sizes contributing to the AMS fabrics (Chapter 6). The results of the detailed study showed that both a flow-aligned paramagnetic and blended ferromagnetic component contribute the AMS. The ferromagnetic component was shown to consist of a flow-aligned primary fabric combined with a poorly oriented alteration fabric of secondary minerals, which together are unable to mask the flow-aligned paramagnetic fabric. It was also observed that shear along the Southern Troodos Transform Fault Zone (STTFZ) may cause the magnetic foliation plane and the dike plane to become misaligned. Despite this, the AMS axes and flow-axis retain their primary orientation (Chapter 6; Borradaile and Gauthier, 2002).

Analysis of the spacing of the regions of very steep magma flow was described in Chapter 7. The data was analyzed in traverses that were both parallel and perpendicular to the paleo-spreading axis. This allowed the following observations to be made:

1) There exists a variation on magma-flow directions in the SDC from steep in some areas to shallow in others. This means that was never a continuous and stable magma supply to the Troodos SDC, and as such it must have been formed along a slow-spreading ridge.

2) The magma supply to the Troodos ridge may have been *point-source* in that there appears to be a very limited along-axis extent to regions of very steep flow. These point-source magma chambers may also have been short-lived, as the regions of steep-flow are very narrow when observed in traverses perpendicular to the spreading axis.
3) Statistical analysis indicates that magma-chambers were spaced in ~4km intervals along the spreading axis. At a given location, the change from magma-rich to magma starved may have taken place rapidly, and 100,000 to 250,000 years may have elapsed before the onset of another magma-rich episode.

While these observations are incompatible with a fast-spread origin for Troodos, they do not necessarily contradict the popular models for slow-spreading processes. Geophysical and theoretical evidence suggests that magma-chambers along slow-spreading ridges have some along-axis extent, at least on the scale of a few kilometers, and are spread intermittently along a mid-ocean ridge. The data presented here seems to contradict this idea, however the observations described above can only apply to the direct source of magma to the SDC. It is entirely possible that the point-source and short lived magma-chambers may simply deliver magma to the SDC from some lower reservoir that matches the size and scale predicted by the popular models. In that case, this study may have provided some insight on the plumbing system in operation at slow-spreading ridges to deliver magma from chamber to dike.

9. References

Abelson, M., Baer, G., Agnon, A. Evidence from gabbro of the Troodos ophiolite for lateral magma transport along a slow-spreading mid-ocean ridge. Nature, 409, 72-75, 2000.

Allen, C., 1975. The petrology of a portion of the Troodos plutonic complex, Cyprus. Unpublished Ph.D. thesis, University of Cambridge.

Allerton, S. and Vine, F. J., 1987, Spreading structure of the Troodos ophiolite, Cyprus: Some paleomagnetic constraints: Geology, 15, 593-597

Allerton, S. and Vine, F. J., 1991, Spreading evolution of the Troodos ophiolite, Cyprus: Geology, 19: 637-640

Anon, 1972. Penrose field conference on ophiolites. Geotimes, 17, 24-25.

Baragar, W., Lambert, M., Baglow, N., and Gibson, I., 1987. Sheeted dykes of the Troodos ophiolite, Cyprus. In: Halls, H. and Fahrig, W. (eds), Mafic dyke swarms. Geological Association of Canada Special Paper 34, 257-272.

Baragar, W., Lambert, M., Baglow, N., and Gibson, I., 1990. The sheeted dike zone in the Troodos ophiolite. In: Malpas, J. (Ed.), Ophiolites: Oceanic crustal analogues. Geol. Surv. Dept, Nicosia, Cyprus. 37-52.

Bender, J., Langmuir, C., and Hanson, G., 1984. Petrogenesis of basaltic glasses from the Tamayo Region, East Pacific Rise. Journal of Petrology, 25, 213-254.

Bonhommet, N., Roperch, P. and Calza, F. Paleomagnetic arguments for block rotations along the Arakapas fault (Cyprus). Geology, 16, 422-425, 1988.

Borradaile, G., 1987. Anisotropy of magnetic susceptibility: rock composition versus strain. Tectonophysics, 138, 327-329

Borradaile, G., 1994. Paleomagnetism carried by crystal inclusions: the effect of preferred crystallographic orientations. Earth and Planetary Science Letters, 126, 171-182.

Borradaile, G., 2001. Magnetic fabrics and petrofabrics: their orientation distributions and anisotropies. Journal of Structural Geology, 23, 1581-1596.

Borradaile, G. and Werner, T., 1994. Magnetic anisotropy of some phylloslicates. Tectonophysics, 235, 233-248.

Borradaile, G. and Stupavsky, M., 1995. Anisotropy of magnetic susceptibility: Measurement schemes. Geophysical Research Letters, 22, 1957-1960.

Borradaile, G. and Henry, B., 1997. Tectonic applications of magnetic susceptibility and its anisotropy. Earth Science Reviews, 42, 49-93.

Borradaile, G., and Lagroix, F., 2001. Magnetic fabrics reveal Upper Mantle flow fabrics in the Troodos Ophiolite Complex, Cyprus. Journal of Structural Geology, 23, 1299-1317.

Borradaile, G. and Gauthier, D., 2001. AMS-detection of inverse fabrics without AARM, in ophiolite dikes. Geophysical Research Letters, 28, n.18, 3517-3520.

Borradaile, G and Gauthier, D., 2002. Interpreting anomalous fabrics in ophiolite dikes. Journal of Structural Geology, IN PRESS

Borradaile, G., Keeler, W., Alford, C., and Sarvas, P., 1987. Anisotropy of magnetic susceptibility of some metamorphic minerals. Physics of the Earth and Planetary Interiors, 48, 161-166.

Borradaile, G., Fralick, P., and Lagroix, F., 1999. Acquisition of anhysteretic remanence and tensor subtraction from AMS isolates true paleocurrent grain alignments. In: D. Tarling and P. Turner (eds), Paleomagnetism and sedimentation, Geological Society of London Special Publication.

Butler, R.F., 1992, Paleomagnetism: Magnetic Domains to Geologic Terranes, Blackwell Scientific Publications, Boston, 319 pp.

Calvert, A., 1995. Seismic evidence for a magma chamber beneath the slow-spreading Mid-Atlantic Ridge. Nature, 377, 410-414

Cann, J., 1974. A model for oceanic crustal structure developed. Geophysical Journal of the Royal Astronomical Society, 39, 169-187

Carmichael, R., 1982. Magnetic properties of minerals and rocks. *In:* R. West and M. Ashe (eds.), CRC Handbook of Physical Constants for Rocks. CRC Press, Roca Baton, pp. 229-287.

Clube, T. and Robertson, A., 1986. The paleorotation of the Troodos microplate, Cyprus, in the Late Mesozoic - Early Cenozoic plate tectonic framework of the Eastern Mediterranean. Surveys in Geophysics, 8, 375-437

Detrick, R., Buhl, P., Vera, E., Mutter, J., Orcutt, J., Madsen, J., Brocher, T., 1987. Multi-channel seismic imaging of a crustal magma chamber along the East Pacific Rise. Nature, 326, 35-41

Dietrich, D., and Spencer, S., 1993. Spreading induced faulting and fracturing of oceanic crust: examples from the Sheeted Dike Complex of the Troodos ophiolite, Cyprus. In: Prichard, H., Alabaster, T., Harris, N., and Neary, C. (eds). Magmatic processes and plate tectonics, Geological Society Special Publication, 76, 121-139.

Dilek, Y., Thy, P., Moores, E.M. and Ramsden, T. W., 1990, Tectonic evolution of the Troodos ophiolite within the Tethyan framework: Tectonics, 9, 811-823

Dilek, Y., Moores, E.M., and Furnes, H.,1998. Structure of modern oceanic crust and ophiolites and implications for faulting and magmatism at oceanic spreading centers. Geophysical monograph, 106, 219-265

Elthon, D., and Stern, S., 1978. Metamorphic petrology of the Sariento Ophiolite complex, Chile. Geology, 6, 464-468.

Fernandez, A., and Laporte, D., 1991. Significance of low-symmetry fabrics in magmatic rocks. Journal of Structural Geology, 13, n.3, 337-347

Gass, I., 1990. Ophiolites and oceanic lithosphere. In: Malpas, J. (Ed.), Ophiolites: Oceanic crustal analogues. Geol. Surv. Dept, Nicosia, Cyprus. 1-12

Gass, I., 1968. Is the Troodos Massif of Cyprus a fragment of Mesozoic ocean floor? Nature, 220, 39-42

Gillis, K., and Roberts, M., 1999. Cracking at the magma-hydrothermal transition: evidence from the Troodos ophiolite, Cyprus. E. Plan. Sci. Lets., 169, 227-244.

Greenbaum, D., 1972. Magmaic processes at oceanic ridges: evidence from the Troodos Massif, Cyprus. Nature, 242, 26-29

Henry, B., 1983. Interpretation quantitative de l'anisotropie de susceptibilitie magnetique. Tectonophysics, 91, 165-177.

Hall, J., Fisher, B., Walls, C., Hall, S., Johnson, H., Baker, A., Agrawal, V., Persaud, M., and Sumaiang, R., 1987. The vertical distribution and alteration of dikes in a profile through the Troodos ophiolite. Nature, 326, 780-782.

Hrouda, F., 1986. The effect of quartz on the magnetic susceptibility of quartzite. Studies in Geophysics and Geodynamics, 30, 39-45.

Hurst, S., Versoub, K., and Moores, E., 1992. Paleomagnetic constraints on the formation of the Solea Graben, Troodos ophiolite. Tectonophysics, 208, 431-445

Jackson, M., 1991. Anisotropy of magnetic remanence: A brief review of mineralogical sources, physical origins, and geological applications, and comparison with susceptibility anisotropy. Pure and applied geophysics, 136, 1-28.

Jeffrey, G., 1922. The motion of ellipsoidal particles immersed in a viscous fluid. Proc. of the Royal Society, London, 102, 161-179.

Jelinek, V., 1978. Statistical processing of anisotropy of magnetic susceptibility measured on groups of specimens. Studia Geophysica. et Geodetica., 22: 50-62.

Jelinek, V., 1981. Characterization of the magnetic fabrics of rocks. Tectonophysics, 79, 63-67.

Kidd, R., and Cann, J., 1974. Chilling statistics indicate an ocean-floor spreading origin for the Troodos complex, Cyprus. E. Plan. Sci. Let., 24, 151-155.

Lagroix, F. and Borradaile, G., 2000. Magnetic fabric interpretation complicated by inclusions in mafic silicates. Tectonophysics, 325, 207-225.

Laurent, R., 1990. Parental magma and crystal fractionation modeling of the CY-4 plutonic rocks, Troodos ophiolite, Cyprus. In: Malpas, J. (Ed.), Ophiolites: Oceanic crustal analogues. Geol. Surv. Dept, Nicosia, Cyprus. 139-148.

Macleod, C. and Murton, B., 1995. On the sense of slip of the Southern Troodos transform fault zone, Cyprus. Geology, 23, 257-260

Macleod, C., Allerton, S., Gass, I., and Xenophontos, C., 1990. Structure of a fossil rodge-transform intersection in the Troodos ophiolite. Nature, 348, 717-720

Malpas, J., Calon, T., and Squires, G., 1993. The development of a late Cretaceous microplate suture zone in SW Cyprus. In: Prichard, H. (Ed.), Magmatic Processes and Plate Tectonics, Geological Society, Special Publication 76, 177-195

Miyashiro, A., 1973. The Troodos ophiolite complex was probably formed in an island arc: Earth and Planetary Science Letters, 19, 218-224

Moores, E., and Vine, F., 1971. The Troodos Massif, Cyprus, and other ophiolites as ocean crust; evaluation and implications. Phil. Trans. Roy. Soc. Lon., A268, 433-466

Moores, E.M., Robinson, P.T., Malpas, J. and Xenophontos, C., 1984. A model for the origin of the Troodos Massif, Cyprus and other mid-east ophiolites. Geology, 12, 500-503

Moores, E., Varga, R., Versoub, K., and Ramsden, T., 1990. Regional structure of the Troodos dyke complex. In: Malpas, J. (Ed.), Ophiolites: Oceanic crustal analogues. Geol. Surv. Dept, Nicosia, Cyprus. 27-35.

Morris, A., Creer, K., and Robertson, A., 1990. Paleomagnetic evidence for clockwise rotations related to dextral shear along the Southern Troodos Transform Fault. Earth and Planetary Science Letters, 99, 250-262

Morris, A., Anderson, M.W., and Robertson, A.H.F., 1998. Multiple tectonic rotations and transform tectonism in an intraoceanic suture zone, S.W. Cyprus. Tectonophysics, 299; 229-253.

Murton, B., 1986. The tectonic evolution of the western Limassol Forest Complex, Cyprus. Unpublished Ph.D. Thesis, Open University, 322pp

Murton, B., 1987. Suprasubduction transform activity along the southern Troodos ophiolite: a microplate margin. In: Troodos 87, Ophiolites and oceanic lithosphere. Abstracts. Cyprus Geological Survey Dept., 27

Murton, B., 1990, Was the Southern Troodos transform fault a victim of microplate rotation? In: Malpas, J. (Ed.), Ophiolites: Oceanic crustal analogues. Geol. Surv. Dept, Nicosia, Cyprus, 87-98

Nicolas, A., 1989. Structures of ophiolites and dynamics of oceanic lithosphere. Kluwer Academic, Boston. 365pp.

Nicolas, A., 1992. Kinelatics in magmatic rocks with special reference to gabbros. Journal of Petrology, 33, part 4, 891-915

Nicolas, A., Freydier, C., Godard, M., Vauchez, A., 1993. Magma chambers at oceanic ridges: How large? Geology, 21, 53-56

Nye, J., 1957. The physical properties of crystals. Clarendon Press, Oxford. 322pp.

Passchier, C., 1987. Stable positions of rigid objects in non-coaxial flow-a study in vorticity analysis. Journal of Structural Geology, 8, 831-843

Robertson, A., 1990. The tectonic evolution of Cyprus. In: Malpas, J. (Ed.), Ophiolites: Oceanic crustal analogues. Geol. Surv. Dept, Nicosia, Cyprus. 235-251

Robertson, A., Dixon, J., Brown, S., Collins, A., Morris, A., Pickett, E., Sharp, I., Ustaomer, T., 1996. Alternative tectonic models for the Late Paleozoic-Early Tertiary development of Tethys in the eastern Mediterranean region. In: Morris, A. and Tarling, D. (Eds.), Paleomagnetism and tectonics of the Mediterranean region. Geological Society of London, Special Publication 105, 239-263

Robinson, P., 1987. The Troodos ophiolite of Cyprus: new perspectives on its origin and emplacement. In: Troodos 87, Ophiolites and oceanic lithosphere. Abstracts. Cyprus Geological Survey Dept., 3

Robinson, P., Melson, W., and Schmincke, H. , 1983. Volcanic glass compositions of the Troodos ophiolite, Cyprus. Geology, 11, 400-404

Rochette, P., Jackson, J., and Aubourg, C., 1992. Rock magnetism and the interpretation of anisotropy of magnetic susceptibility. Reviews of Geophysics, 30: 209-226.

Rochette, P., Reuber, I., Jenatton, L., Dupuy, C., Boudier, F., 1991. Diabase dikes emplacement in the Oman ophiolite: a magnetic fabric study with reference to geochemistry. In: Peters, T. (Ed), Ophiolite genesis and evolution of the oceanic lithosphere. Proc. conference, Muscat. 55-82.

Shau, Y., Torii, M., Horng, C., Peacor, D., 2000. Subsolidus evolution and alteration of titanomagnetite in ocean ridge basalts from Deep Sea Drilling Project/Ocean Drilling Program Hole 504B, Leg 83: Implications for the timing of magnetization. Journal of Geophysical Research, 105, B10, 23635-23649.

Simonian, K. O. and Gass, I.G., 1978. Arakapas fault belt, Cyprus: A fossil transform fault. Geol. Soc. Am. Bull., 89: 1220-1230.

Sinha, M., Constable, S., Pierce, C., White, A., Heinson, G., MacGregor, L., and Navin, D., 1998. Magmatic processes at slow spreading ridges: implications of the RAMESSES experiment a 57°45'N on the Mid-Atlantic Ridge. Geophysical Journal International, 135, 731-745

Sinton, J. and Detrick, R., 1992. Mid-ocean ridge magma chambers. Journal of Geophysical Research, 97, 197-216

Staudigel, H., Gee, J., Tauxe, L., and Varga, R.,1992. Shallow intrusive directions of sheeted dikes in the Troodos ophiolite: Anisotropy of magnetic susceptibility and structural data. Geology, 20, 841-44

Staudigel., H., Tauxe, L., Gee, J., Bogaard, P., Haspels, J., Kale, G., Leenders, A., Meijer, P., Swaak, B., Tuin, M., Van Soest, M., Verdurmen, E., Zevenhuizen, A. Geochemistry and intrusive directions in sheeted dikes in the Troodos ophiolite: Implications for mid-ocean ridge spreading centres. Geochem. Geophys. Geosys. [online] 1, 1999GC000001, 1999.

Swarbick, R., 1993. Sinistral strike-slip and transpressional tectonics in an ancient oceanic setting: the Mamonia Complex, southwest Cyprus. Journal of the Geological Society, London, 150, 381-392

Swarbick, R., and Robertson, A., 1980. Revised stratigraphy of the Mesozoic rocks of southern Cyprus. Geological Magazine, 117, 547-563

Tarling, D. and Hrouda, F., The magnetic anisotropy of rocks. Chapman and Hall. 217pp.

Tauxe, L., Gee, J. S. and Staudigel, H., 1998, Flow directions in dikes from anisotropy of magnetic susceptibility data: The bootstrap way. Journal of Geophysical Research. 103, 17:775-790.

Thy, P. and Ebeson, K., 1993. Seafloor spreading and the ophiolite sequence of the Troodos complex: A principal component analysis of lava and dike compositions. Journal of Geophysical Research, 98, B7, 11799-11805.

Thy, P., Schiffman, P., and Moores, E., 1989. Igneous mineral stratigraphy and chemistry of the Cyprus Crustal Study Project drill core in the plutonic sequences of the Troodos ophiolite. In: Gibson, I., Malpas, J., Robinson, P., and Xenophontos, C. (eds), Cyprus Crustal Study Project, Initial Report, Hole CY-4. Geological Survey of Canada, Paper 88-9, 147-186.

van Everdingen, D., 1995. fracture characteristics of the Sheeted Dike Complex, Troodos ophiolite, Cyprus: Implications for permeability of oceanic crust. Journal of Geophysical Research, 100, B10, 19957-19972.

van Everdingen, D., and Cawood, P., 1995. Dyke domains in the Mitsero Graben, Troodos ophiolite, Cyprus: an off-axis model for graben formation at a spreading centre. Journal of the Geological Society, London, 152, 923-932.

Varga, R., and Moores, E., 1985. Spreading structure of the Troodos ophiolite. Geology, 13, 846-850.

Varga, R., and Moores, E., 1990. Intermittent magmatic spreading and tectonic extension in the Troodos ophiolite: implications for exploration for black smoker-type ore deposits. In: Malpas, J. (Ed.), Ophiolites: Oceanic crustal analogues. Geol. Surv. Dept, Nicosia, Cyprus. 53-64.

Varga, R. J., Gee, J. S., Staudigal, H., and Tauxe, L., 1998. Dike surface lineations as magma flow indicators within the sheeted dike complex of the Troodos Ophiolite, Cyprus. Journal of Geophysical Research, 103, B3: 5241-5256.

Versoub, K., and Moores, E., 1981. Tectonic rotations in extensional regimes and their paleomagnetic consequences for oceanic basalts, Journal of Geophysical Research, 86, 6335-6349.

Vine, F., and Matthews, D., 1963. Magnetic anomalies over oceanic ridges. Nature, 199, 947-949

Werner, T. and Boradaile, G., 1996. Paleoremanence dispersal across a transpressional Archean terrane: Deflection by anisotropy or by late compression? Journal of Geophysical Research, 101, 5531-5545

Whitechurch, H., Juteau, T., and Montigny, R., 1986. Role of the eastern Mediterranean ophiolites (Turkey, Syria, Cyprus) in the histiry of the Neo-Tethys. In: Dixon, J., and Robertson, A. (Eds.), Geological evolution of the eastern Mediterranean, Geological Society, London, Special Publication 17, 301-317

Appendix A: Outcrop Data

Outcrop	Easting	Northing	Elevation
1999-001	0510787	3856244	n/a
1999-002	0510841	3856340	n/a
1999-003	0511006	3856445	n/a
1999-004	0510917	3856583	n/a
1999-005	0510905	3856955	n/a
1999-006	0510863	3856974	n/a
1999-007	0510708	3857245	n/a
1999-008	0510623	3857341	n/a
1999-009	0510698	3857530	n/a
1999-010	0510623	3857614	n/a
1999-011	0510804	3857620	n/a
1999-012	0510814	3857839	n/a
1999-013	0510886	3857876	n/a
1999-014	0510872	3858011	n/a
1999-015	0510876	3858183	n/a
1999-016	0510772	3858246	n/a
1999-017	0510620	3859249	n/a
1999-018	0510858	3859141	n/a
1999-019	0511019	3858979	n/a
1999-020	0510777	3858766	n/a
1999-021	0510809	3858417	n/a
1999-022	0510187	3859634	n/a
1999-023	0510370	3859540	n/a
1999-024	0509857	3859641	n/a
1999-025	0509904	3859856	n/a
1999-026	0509871	3859991	n/a
1999-027	0509326	3860452	n/a
1999-028	0510066	3860706	n/a
1999-029	0509681	3860768	n/a
1999-030	0509613	3861129	n/a
1999-031	0509577	3861501	n/a
1999-032	0509518	3861939	n/a
1999-033	0509114	3862142	n/a
1999-034	0508958	3862232	n/a
1999-035	0508688	3862563	n/a

Outcrop	Easting	Northing	Elevation
1999-036	0508726	3862936	n/a
1999-037	0508518	3862802	n/a
1999-038	0508189	3862656	n/a
1999-039	0507518	3862515	n/a
1999-040	0508231	3863131	n/a
1999-041	0508476	3863341	n/a
1999-042	0508830	3864775	n/a
1999-043	0510139	3858883	n/a
1999-044	0509805	3859494	n/a
1999-045	0509496	3859544	n/a
1999-046	0509310	3859376	n/a
1999-047	0509145	3859579	n/a
1999-048	0508779	3859346	n/a
1999-049	0508638	3858953	n/a
1999-050	0507908	3858957	n/a
1999-051	0506842	3858699	n/a
1999-052	0506412	3858477	n/a
1999-053	0505370	3858211	n/a
1999-054	0504993	3857968	n/a
1999-055	0504872	3857896	n/a
1999-056	0504779	3857486	n/a
1999-057	0504566	3857374	n/a
1999-058	0504334	3857594	n/a
1999-059	0504255	3857308	n/a
1999-060	0504209	3857046	n/a
1999-061	0504069	3856851	n/a
1999-062	0503812	3856538	n/a
1999-063	0504180	3856888	n/a
1999-064	0504690	3856636	n/a
2000-001	0509646	3861105	
2000-002	0510006	3860933	
2000-003	0510438	3861225	
2000-004	0510839	3861273	
2000-005	0511365	3861617	
2000-006	0511914	3861433	
2000-007	0512109	3862539	
2000-008	0512129	3863831	

Outcrop	Easting	Northing	Elevation
2000-009	0511927	3863354	
2000-010	0511887	3863322	
2000-011	0512220	3864189	
2000-012	0512128	3865007	
2000-013	0511640	3865642	
2000-014	0503255	3860303	
2000-015	0503131	3860110	
2000-016	0502816	3860037	
2000-017	0502766	3859388	
2000-018	0502746	3859155	
2000-019	0502667	3858920	
2000-020	0502640	3858500	
2000-021	0502665	3857887	948
2000-022	0502176	3857510	877
2000-023	0501044	3857609	n/a
2000-024	0501029	3858278	n/a
2000-025	0500922	3858746	n/a
2000-026	0510627	3865524	n/a
2000-027	0510338	3865561	n/a
2000-028	0510100	3865425	n/a
2000-029	0509557	3865147	n/a
2000-030	0509221	3864905	n/a
2000-031	0504228	3866256	n/a
2000-032	0504497	3866378	n/a
2000-033	0504918	3866312	n/a
2000-034	0505198	3865913	n/a
2000-035	0505495	3866274	n/a
2000-036	0506464	3866343	n/a
2000-037	0506716	3866096	n/a
2000-038	0507127	3865970	n/a
2000-039	0506776	3865599	n/a
2000-040	0500723	3861226	n/a
2000-041	0500104	3860903	n/a
2000-042	0500265	3860388	n/a
2000-043	0499589	3859990	n/a
2000-044	0501140	3858489	n/a
2000-045	0501145	3858485	n/a

Outcrop	Easting	Northing	Elevation
2000-046	0500290	3858203	n/a
2000-047	0499964	3858390	n/a
2000-048	0505219	3862988	n/a
2000-049	0505103	3863264	n/a
2000-050	0504783	3863323	n/a
2000-051	0504740	3863583	n/a
2000-052	0504425	3864041	n/a
2000-053	0504451	3864849	n/a
2000-054	0504557	3865181	n/a
2000-055	0504183	3864892	n/a
2000-056	0503647	3864991	n/a
2000-057	0508441	3871638	n/a
2000-058	0508264	3870912	n/a
2000-059	0508050	3870182	n/a
2000-060	0507607	3869764	n/a
2000-061	0507105	3869393	n/a
2000-062	0506857	3868960	n/a
2000-063	0508004	3873905	470
2000-064	0508670	3872070	511
2000-065	0506442	3868098	720
2000-066	0506315	3867680	803
2000-067	0508048	3864865	960
2000-068	0508105	3864236	970
2000-069	0507850	3863568	927
2000-070	0506125	3863746	1074
2000-071	0505458	3863345	1123
2000-072	0504741	3862616	1225
2000-073	0503929	3863411	1182
2000-074	0503114	3863089	1135
2000-075	0507947	3866227	851
2000-076	0507598	3866041	816
2000-077	0507406	3866580	800
2000-078	0507373	3867130	857
2000-079	0504328	3862091	1204
2000-080	0503663	3861885	1182
2000-081	0503274	3863683	1207
2000-082	0503048	3864202	1260

Outcrop	Easting	Northing	Elevation
2000-083	0503572	3864014	1315
2000-084	0504343	3864090	1391
2000-085	0514461	3866948	1020
2000-086	0515144	3866214	1030
2000-087	0515472	3865558	1030
2000-088	0514808	3865293	1080
2000-089	0514680	3864326	1050
2000-090	0514816	3863700	1070
2000-091	0514241	3863469	1065
2000-092	0513879	3863934	1060
2000-093	0513360	3864411	1050
2000-094	0517577	3866075	985
2000-095	0517994	3865098	1112
2000-096	0517992	3863293	1231
2000-097	0517683	3863203	1206
2000-098	0517843	3862130	1120
2000-099	0518331	3861207	1040
2000-100	0518340	3860400	999
2000-101	0509820	3859506	745
2000-102	0515707	3864390	949
2000-103	0515520	3862905	1015
2000-104	0515744	3863227	1071
2000-105	0515511	3862650	1105
2000-106	0515393	3862308	1146
2000-107	0514786	3861945	1153
2000-108	0514083	3862058	1114
2000-109	0514601	3868548	779
2000-110	0515296	3868509	860
2000-111	0515824	3868808	854
2000-112	0516103	3869477	780
2000-113	0519487	3868186	695
2000-114	0519115	3867459	735
2000-115	0518675	3866145	813
2000-116	0517550	3865725	922
2000-117	0517571	3866341	915
2000-118	0516989	3865404	840
2000-119	0516328	3866550	855

Outcrop	Easting	Northing	Elevation
2000-120	0515018	3867086	890
2000-121	0515559	3867144	980
2000-122	0515085	3867382	900
2000-123	0514002	3868297	700
2000-124	0513713	3868249	690
2000-125	0513320	3867204	693
2000-126	0513530	3867429	690
2000-127	0513199	3866800	705
2000-128	0512938	3865957	740
2000-129	0512760	3865201	784
2000-130	0512546	3864960	810
2000-131	0512392	3864619	842
2000-132	0512351	3864180	875
2000-133	0515170	3859419	700
2000-134	0521720	3864152	667
2000-135	0522084	3863733	675
2000-136	0522390	3863295	708
2000-137	0522192	3862838	680
2000-138	0521745	3862266	744
2000-139	0521670	3861395	830
2000-140	0520634	3860620	850
2000-141	0519700	3860844	804
2000-142	0519753	3860255	820
2000-143	0519036	3859921	901
2000-144	0518250	3860055	812
2000-145	0518083	3863345	1185
2000-146	0518420	3862544	1153
2000-147	0519058	3862490	1199
2000-148	0520551	3862155	1069
2000-149	0520207	3861714	1001
2000-150	0521025	3861650	915
2000-151	0521841	3860902	825
2000-152	0522530	3860750	855
2000-153	0523060	3859957	796
2000-154	0517650	3859278	689
2000-155	0517832	3859102	667
2000-156	0517838	3858860	630

Outcrop	Easting	Northing	Elevation
2000-157	0517676	3858714	573
2000-158	0517504	3857760	505
2000-159	0516981	3858085	553
2000-160	0516420	3858430	530
2000-161	0515355	3858014	530
2000-162	0515201	3858755	575
2000-163	0515181	3859385	608
2000-164	0514713	3859286	626
2000-165	0514573	3859680	665
2000-166	0514492	3859746	715
2000-167	0514077	3859994	800
2000-168	0512549	3862801	1027
2000-169	0512553	3862656	1030
2000-170	0512654	3862490	1031
2000-171	0512634	3862225	1035
2000-172	0512313	3862127	1067
2000-173	0512266	3861799	1095
2000-174	0512365	3861465	1117
2000-175	0512640	3861348	1139
2000-176	0512759	3861017	1150
2000-177	0513146	3861008	1116
2000-178	0513342	3860936	1096
2000-179	0512428	3861949	974
2000-180	0511981	3861893	978
2000-181	0511830	3861400	990
2000-182	0511287	3861447	1010
2000-183	0510660	3861122	1035
2000-184	0510620	3860882	1093
2000-185	0511109	3860992	1127
2000-186	0510162	3861027	1054
2000-187	0509906	3860997	1022
2000-188	0510229	3863360	842
2000-189	0510450	3863750	815
2000-190	0510439	3864189	744
2000-191	0510505	3864615	718
2000-192	0510605	3865093	682
2000-193	0510337	3865244	707

Outcrop	Easting	Northing	Elevation
2000-194	0510048	3865132	730
2000-195	0509667	3864830	770
2000-196	0509240	3864684	806
2000-197	0509150	3864336	830
2000-198	0508971	3863954	850
2000-199	0508707	3863359	872
2000-200	0506636	3861031	1318
2000-201	0506943	3861204	1295
2000-202	0506714	3861162	1272
2000-203	0506639	3861599	1219
2000-204	0506996	3861922	1165
2000-205	0507138	3862245	1123
2000-206	0507199	3862626	1093
2000-207	0506799	3862376	1105
2000-208	0507118	3862975	1092
2000-209	0507352	3862943	1053
2000-210	0507537	3863019	1025
2000-211	0507816	3863299	1003
2000-212	0508089	3863411	959
2000-213	0509145	3861977	1028
2000-214	0509072	3861589	976
2000-215	0508922	3861847	934
2000-216	0508837	3861134	888
2000-217	0508860	3861222	870
2000-218	0508683	3861071	840
2000-219	0508653	3861000	811
2000-220	0508760	3860620	797
2000-221	0508714	3860676	776
2000-222	0508647	3860610	736
2000-223	0509282	3862219	1018
2000-224	0509417	3862189	972
2000-225	0509791	3862181	958
2000-226	0510046	3862207	975
2000-227	0510197	3862226	983
2000-228	0513358	3861205	1030
2000-229	0513492	3861420	1006
2000-230	0513659	3861158	970

Outcrop	Easting	Northing	Elevation
2000-231	0513551	3860885	942
2000-232	0513485	3860516	897
2000-233	0513944	3860709	843
2000-234	0514311	3861584	954
2000-235	0514231	3861247	941
2000-236	0513933	3860853	892
2000-237	0512703	3860623	1005
2000-238	0512842	3860902	1055
2000-239	0512314	3859966	1016
2000-240	0512481	3860241	1047
2000-241	0512518	3860786	1099
2000-242	0512630	3862904	995
2000-243	0512792	3863040	1030
2000-244	0511794	3863094	808
2000-245	0511586	3862996	790
2000-246	0511356	3862681	818
2000-247	0511266	3862497	831
2000-248	0512202	3864824	783
2000-249	0512078	3864520	786
2000-250	0511995	3864165	764
2000-251	0511857	3863745	782
2000-252	0511756	3863344	797
2000-253	0511473	3863946	838
2000-254	0511470	3863224	884
2000-255	0511374	3863472	926
2000-256	0511336	3863792	965
2000-257	0511651	3864537	820
2000-258	0511833	3864628	788
2000-259	0511692	3864420	807
2000-260	0511575	3864174	819
2000-261	0511761	3863879	806
2000-262	0511693	3863504	805
2000-263	0511653	3863208	798
2000-264	0512891	3863660	1012
2000-265	0511377	3866725	667
2000-266	0511513	3867501	649
2000-267	0511423	3867813	639

Outcrop	Easting	Northing	Elevation
2000-268	0511662	3863773	624
2000-269	0511831	3863773	624
2000-270	0511850	3871864	555
2000-271	0511910	3870818	590
2000-272	0509613	3873348	652
2000-273	0509544	3873734	648
2000-274	0509169	3873915	612
2000-275	0508950	3873914	600
2000-276	0508738	3873891	600
2000-277	0508341	3873940	556
2000-278	0508224	3874069	538
2000-279	0507786	3874453	525
2000-280	0507199	3874206	525
2000-281	0506879	3873484	557
2000-282	0506529	3872675	597
2000-283	0506414	3872088	611
2000-284	0505815	3871438	630
2000-285	0505340	3870664	680
2000-286	0505117	3869948	714
2000-287	0507816	3864931	1018
2000-288	0507559	3865112	1033
2000-289	0504707	3864662	1045
2000-290	0507130	3864652	1063
2000-291	0506883	3864565	1085
2000-292	0506607	3864593	1105
2000-293	0506573	3865065	1135
2000-294	0506316	3864951	1143
2000-295	0506135	3864937	1126
2000-296	0505948	3865156	1120
2000-297	0506107	3865483	1111
2000-298	0506297	3865636	1109
2000-299	0506470	3865932	1103
2000-300	0506682	3865890	1105
2000-301	0507937	3867897	760
2000-302	0507791	3867388	999
2000-303	0507847	3867686	822
2000-304	0507674	3867570	838

Outcrop	Easting	Northing	Elevation
2000-305	0507496	3867339	862
2000-306	0507375	3867220	868
2000-307	0507413	3866908	854
2000-308	0507397	3866567	811
2000-309	0507434	3866330	800
2000-310	0507630	3866228	816
2000-311	0507576	3866033	830
2000-312	0513011	3863920	986
2000-313	0513101	3864342	1007
2000-314	0513383	3864173	995
2000-315	0513820	3864249	976
2000-316	0513958	3863649	1010
2000-317	0514521	3863131	1025
2000-318	0514767	3863260	1028
2000-319	0514615	3863933	1022
2000-320	0514751	3864315	1008
2000-321	0514698	3864755	998
2000-322	0515382	3865164	1020
2000-323	0515321	3865812	977
2000-324	0510072	3860727	942
2000-325	0509930	3860285	903
2000-326	0510117	3859942	879
2000-327	0509936	3859828	860
2000-328	0510374	3859409	744
2000-329	0510800	3859000	699
2000-330	0507441	3874979	507
2000-331	0507039	3875103	545
2000-332	0503551	3874230	601
2000-333	0503528	3873699	613
2000-334	0503562	3873145	624
2000-335	0501706	3870211	885
2000-336	0501458	3870535	850
2000-337	0501648	3870937	800
2000-338	0501900	3871153	767
2000-339	0502419	3871446	728
2000-340	0503288	3872025	692
2000-341	0502708	3871528	720

Outcrop	Easting	Northing	Elevation
2000-342	0502828	3871621	773
2000-343	0502873	3871288	809
2000-344	0503368	3871082	854
2000-345	0503336	3871412	899
2000-346	0503625	3871489	920
2000-347	0504006	3871023	961
2000-348	0504195	3871060	930
2000-349	0504260	3870633	900
2000-350	0504644	3870516	907
2000-351	0504549	3870135	918
2000-352	0504152	3869918	907
2000-353	0504120	3869450	849
2000-354	0504176	3868450	822
2000-901	0508665	3872227	524
2000-902	0517930	3865001	1096

Appendix B: Dike Data

Subarea	dike #	Strike Dip	From Outcrop#
A			
	1035	334/ 54	2000-336
	1036	352/ 60	2000-336
	1037	330/ 67	2000-336
	1038	328/ 69	2000-337
	1039	316/ 61	2000-337
	1040	339/ 61	2000-337
	1041	325/ 45	2000-338
	1042	323/ 49	2000-338
	1043	302/ 44	2000-338
	1044	340/ 55	2000-339
	1045	342/ 63	2000-339
	1046	334/ 77	2000-339
B			
	870	219/ 84	2000-282
	871	210/ 81	2000-282
	872	230/ 66	2000-282
	873	172/ 51	2000-283
	874	168/ 69	2000-283
	875	209/ 69	2000-283
	876	028/ 87	2000-284
	877	024/ 82	2000-284
	878	029/ 89	2000-284
	879	302/ 51	2000-284
	880	340/ 45	2000-284
	881	302/ 70	2000-284
	882	340/ 52	2000-285
	883	349/ 51	2000-285
	884	349/ 70	2000-285
	1029	208/ 61	2000-334
	1030	200/ 86	2000-334
	1031	210/ 70	2000-334
	1047	310/ 45	2000-340
	1048	329/ 40	2000-340
	1049	331/ 52	2000-340
	1050	352/ 52	2000-341
	1051	000/ 59	2000-341
	1052	358/ 57	2000-341

Subarea	dike #	Strike Dip	From Outcrop#
	1053	020/ 56	2000-342
	1054	006/ 43	2000-342
	1055	036/ 81	2000-342
	1056	350/ 48	2000-343
	1057	345/ 44	2000-343
	1058	348/ 46	2000-343
	1059	011/ 36	2000-344
	1060	334/ 56	2000-344
	1061	350/ 53	2000-344
	1062	324/ 51	2000-345
	1063	339/ 61	2000-345
	1064	318/ 51	2000-345
	1065	060/ 59	2000-346
	1066	019/ 57	2000-346
	1067	012/ 44	2000-346
	1068	020/ 62	2000-347
	1069	004/ 54	2000-347
	1070	000/ 86	2000-347
	1071	350/ 51	2000-348
	1072	352/ 49	2000-348
	1073	008/ 41	2000-348
	1074	000/ 52	2000-349
	1075	354/ 46	2000-349
	1076	345/ 43	2000-349
	1077	354/ 46	2000-350
	1078	352/ 61	2000-350
	1079	359/ 48	2000-350
C			
	105	320/ 71	2000-026
	106	100/ 37	2000-027
	107	080/ 40	2000-027
	108	092/ 28	2000-027
	109	160/ 75	2000-028
	110	140/ 88	2000-028
	111	140/ 88	2000-028
	112	040/ 62	2000-029
	113	040/ 64	2000-029
	114	060/ 55	2000-029
	115	038/ 76	2000-030
	116	200/ 88	2000-030
	117	210/ 80	2000-030

Subarea	dike #	Strike Dip	From Outcrop#
	138	000/ 80	2000-037
	139	045/ 70	2000-037
	140	220/ 84	2000-037
	141	000/ 89	2000-037
	142	040/ 48	2000-038
	143	040/ 46	2000-038
	144	045/ 50	2000-038
	145	030/ 46	2000-038
	146	081/ 89	2000-039
	147	084/ 80	2000-039
	148	074/ 79	2000-039
	238	190/ 81	2000-067
	239	004/ 79	2000-067
	240	000/ 69	2000-067
	241	010/ 88	2000-067
	242	208/ 70	2000-068
	243	208/ 88	2000-068
	244	208/ 82	2000-068
	245	352/ 82	2000-069
	246	358/ 86	2000-069
	247	030/ 78	2000-069
	264	010/ 73	2000-075
	265	008/ 66	2000-075
	266	008/ 65	2000-075
	267	200/ 80	2000-076
	268	198/ 82	2000-076
	269	210/ 78	2000-076
	270	351/ 80	2000-077
	271	190/ 80	2000-077
	272	192/ 80	2000-077
	590	051/ 71	2000-188
	591	052/ 72	2000-188
	592	051/ 81	2000-188
	593	080/ 70	2000-189
	594	060/ 61	2000-189
	595	081/ 63	2000-189
	596	088/ 79	2000-190
	597	100/ 64	2000-190
	598	106/ 67	2000-190
	599	334/ 64	2000-191
	600	334/ 76	2000-191

Subarea	dike #	Strike Dip	From Outcrop#
	601	130/ 81	2000-191
	602	080/ 57	2000-192
	603	120/ 62	2000-192
	604	118/ 50	2000-192
	605	218/ 69	2000-193
	606	218/ 74	2000-193
	607	216/ 71	2000-193
	608	000/ 81	2000-194
	609	346/ 66	2000-194
	610	354/ 80	2000-194
	611	038/ 73	2000-195
	612	352/ 88	2000-195
	613	348/ 73	2000-195
	614	044/ 65	2000-196
	615	010/ 66	2000-196
	616	050/ 71	2000-196
	617	200/ 87	2000-197
	618	211/ 84	2000-197
	619	041/ 72	2000-197
	620	041/ 74	2000-198
	621	040/ 78	2000-198
	622	030/ 79	2000-198
	623	232/ 71	2000-199
	624	229/ 80	2000-199
	625	042/ 79	2000-199
	644	197/ 64	2000-206
	645	218/ 51	2000-206
	646	202/ 55	2000-206
	650	036/ 59	2000-208
	651	040/ 66	2000-208
	652	048/ 71	2000-208
	653	111/ 86	2000-209
	654	114/ 88	2000-209
	655	119/ 89	2000-209
	656	228/ 81	2000-210
	657	230/ 76	2000-210
	658	224/ 82	2000-210
	659	172/ 54	2000-211
	660	175/ 59	2000-211
	661	192/ 64	2000-211
	662	231/ 75	2000-212

Subarea	dike #	Strike Dip	From Outcrop#
	663	218/ 73	2000-212
	664	220/ 66	2000-212
	889	059/ 69	2000-287
	890	100/ 89	2000-287
	891	097/ 81	2000-287
	892	005/ 79	2000-288
	893	034/ 81	2000-288
	894	340/ 87	2000-288
	898	010/ 76	2000-290
	899	014/ 80	2000-290
	900	012/ 81	2000-290
	901	010/ 75	2000-291
	902	002/ 77	2000-291
	903	004/ 79	2000-291
	949	309/ 67	2000-307
	950	335/ 67	2000-307
	951	338/ 68	2000-307
	952	267/ 70	2000-308
	953	272/ 84	2000-308
	954	266/ 80	2000-308
	955	010/ 89	2000-309
	956	036/ 84	2000-309
	957	036/ 87	2000-309
	958	110/ 81	2000-310
	959	100/ 88	2000-310
	960	290/ 89	2000-310
	961	100/ 70	2000-311
	962	090/ 84	2000-311
	963	090/ 71	2000-311
	1141	252/ 80	1999-036
	1142	274/ 82	1999-037
	1143	062/ 70	1999-038
	1145	254/ 84	1999-040
	1146	238/ 65	1999-041
	1147	210/ 80	1999-041
	1148	210/ 75	1999-042
D			
	17	238/ 84	2000-001
	18	114/ 84	2000-001
	19	110/ 79	2000-001
	20	240/ 80	2000-002

Subarea	dike #	Strike Dip	From Outcrop#
	21	248/ 74	2000-002
	22	250/ 75	2000-002
	23	238/ 86	2000-002
	24	225/ 74	2000-003
	25	222/ 80	2000-003
	26	230/ 85	2000-003
	341	130/ 80	2000-101
	342	124/ 75	2000-101
	343	124/ 72	2000-101
	578	238/ 88	2000-183
	579	234/ 86	2000-183
	580	246/ 89	2000-183
	581	248/ 80	2000-184
	582	240/ 72	2000-184
	583	222/ 88	2000-184
	584	228/ 88	2000-186
	585	280/ 62	2000-186
	586	242/ 60	2000-186
	587	067/ 82	2000-187
	588	060/ 85	2000-187
	589	218/ 86	2000-187
	629	274/ 81	2000-201
	630	090/ 88	2000-201
	631	082/ 71	2000-201
	632	148/ 61	2000-202
	633	150/ 51	2000-202
	634	168/ 71	2000-202
	638	071/ 86	2000-204
	639	069/ 87	2000-204
	640	080/ 86	2000-204
	641	172/ 84	2000-205
	642	174/ 70	2000-205
	643	179/ 71	2000-205
	647	057/ 71	2000-207
	648	052/ 76	2000-207
	649	046/ 81	2000-207
	665	153/ 39	2000-213
	666	152/ 45	2000-213
	667	268/ 89	2000-215
	668	089/ 84	2000-215
	669	082/ 29	2000-215

Subarea	dike #	Strike Dip	From Outcrop#
	670	062/ 87	2000-216
	671	266/ 84	2000-216
	672	262/ 63	2000-216
	673	211/ 62	2000-217
	674	218/ 51	2000-217
	675	194/ 52	2000-217
	676	298/ 79	2000-218
	677	304/ 81	2000-218
	678	303/ 74	2000-218
	679	274/ 88	2000-219
	680	092/ 83	2000-219
	681	104/ 84	2000-219
	682	256/ 83	2000-220
	683	095/ 74	2000-220
	684	246/ 86	2000-220
	685	084/ 81	2000-221
	686	078/ 75	2000-221
	687	072/ 81	2000-221
	688	105/ 76	2000-222
	689	272/ 88	2000-222
	690	062/ 64	2000-223
	691	078/ 69	2000-223
	692	063/ 68	2000-223
	693	207/ 81	2000-224
	694	039/ 89	2000-224
	695	210/ 89	2000-224
	696	210/ 67	2000-225
	697	202/ 74	2000-225
	698	198/ 79	2000-225
	699	312/ 81	2000-226
	700	314/ 78	2000-226
	701	319/ 86	2000-226
	702	231/ 87	2000-227
	703	230/ 86	2000-227
	704	222/ 84	2000-227
	1000	260/ 71	2000-324
	1001	252/ 69	2000-324
	1002	261/ 74	2000-324
	1003	071/ 86	2000-325
	1004	271/ 81	2000-325
	1005	248/ 84	2000-325

Subarea	dike #	Strike Dip	From Outcrop#
	1006	192/ 79	2000-326
	1007	060/ 89	2000-326
	1008	200/ 89	2000-326
	1009	200/ 89	2000-326
	1010	320/ 79	2000-327
	1011	329/ 74	2000-327
	1012	030/ 80	2000-328
	1013	041/ 83	2000-328
	1014	021/ 74	2000-328
	1015	318/ 84	2000-329
	1016	330/ 84	2000-329
	1017	322/ 85	2000-329
	1113	015/ 85	1999-017
	1116	064/ 72	1999-020
	1118	050/ 62	1999-022
	1119	238/ 85	1999-023
	1120	276/ 54	1999-024
	1121	100/ 50	1999-025
	1122	094/ 68	1999-025
	1123	082/ 76	1999-025
	1124	235/ 78	1999-026
	1125	086/ 86	1999-026
	1126	262/ 80	1999-026
	1127	262/ 78	1999-027
	1128	245/ 83	1999-027
	1129	072/ 88	1999-027
	1130	260/ 74	1999-028
	1131	236/ 68	1999-028
	1132	245/ 78	1999-029
	1133	250/ 82	1999-030
	1134	248/ 84	1999-030
	1135	225/ 76	1999-031
	1136	226/ 82	1999-032
	1137	232/ 84	1999-033
	1138	240/ 80	1999-034
	1139	230/ 76	1999-035
	1140	232/ 74	1999-035
	1144	258/ 86	1999-039
	1149	256/ 90	1999-043
	1150	124/ 72	1999-044
	1151	150/ 56	1999-045

Subarea	dike #	Strike Dip	From Outcrop#
	1152	194/ 40	1999-045
	1153	275/ 70	1999-046
	1154	254/ 85	1999-047
	1155	270/ 82	1999-048
	1156	300/ 60	1999-049
	1157	104/ 75	1999-050
E			
	354	050/ 84	2000-106
	355	050/ 82	2000-106
	356	040/ 85	2000-106
	357	150/ 62	2000-107
	358	052/ 75	2000-108
	359	042/ 65	2000-108
	360	072/ 81	2000-108
	432	271/ 79	2000-133
	433	082/ 88	2000-133
	434	091/ 84	2000-133
	510	262/ 72	2000-161
	511	268/ 89	2000-161
	512	256/ 59	2000-161
	513	298/ 87	2000-162
	514	294/ 86	2000-162
	515	289/ 79	2000-162
	516	070/ 69	2000-163
	517	262/ 84	2000-163
	518	264/ 71	2000-163
	519	100/ 73	2000-164
	520	090/ 56	2000-164
	521	094/ 88	2000-164
	522	152/ 51	2000-165
	523	112/ 46	2000-165
	524	088/ 64	2000-165
	525	076/ 59	2000-166
	526	068/ 57	2000-166
	527	332/ 56	2000-167
	528	312/ 52	2000-167
	529	296/ 56	2000-167
	536	222/ 77	2000-170
	537	208/ 76	2000-170
	538	238/ 74	2000-170
	539	228/ 84	2000-170

Subarea	dike #	Strike Dip	From Outcrop#
	540	226/ 80	2000-170
	541	208/ 85	2000-170
	542	050/ 78	2000-171
	543	052/ 68	2000-171
	544	058/ 75	2000-171
	554	078/ 80	2000-175
	555	052/ 75	2000-175
	556	054/ 84	2000-175
	557	032/ 86	2000-176
	558	204/ 84	2000-176
	559	058/ 80	2000-176
	560	064/ 78	2000-177
	561	024/ 80	2000-177
	562	056/ 68	2000-177
	563	070/ 75	2000-178
	564	075/ 74	2000-178
	565	055/ 60	2000-178
	705	067/ 87	2000-228
	706	061/ 88	2000-228
	707	063/ 84	2000-228
	708	082/ 82	2000-229
	709	081/ 79	2000-229
	710	073/ 84	2000-229
	711	210/ 88	2000-230
	712	020/ 79	2000-230
	713	030/ 79	2000-230
	714	060/ 74	2000-231
	715	234/ 63	2000-231
	716	236/ 64	2000-231
	717	057/ 81	2000-232
	718	059/ 74	2000-232
	719	040/ 71	2000-232
	720	140/ 50	2000-233
	721	142/ 60	2000-233
	722	086/ 56	2000-233
	723	069/ 64	2000-234
	724	068/ 64	2000-234
	725	062/ 59	2000-234
	726	159/ 74	2000-235
	727	164/ 59	2000-235
	728	164/ 67	2000-235

Subarea	dike #	Strike Dip	From Outcrop#
	729	238/ 86	2000-236
	730	216/ 89	2000-236
	731	241/ 86	2000-236
	732	116/ 79	2000-237
	733	312/ 81	2000-237
	734	111/ 86	2000-237
	735	121/ 89	2000-238
	736	296/ 87	2000-238
	737	320/ 55	2000-238
	744	095/ 76	2000-241
	745	091/ 81	2000-241
	746	101/ 83	2000-241
F			
	9	062/ 83	2000-902
	10	062/ 76	2000-902
	11	044/ 54	2000-902
	12	050/ 70	2000-902
	13	049/ 69	2000-902
	14	052/ 64	2000-902
	15	069/ 79	2000-902
	16	051/ 57	2000-902
	321	040/ 70	2000-094
	322	060/ 79	2000-094
	323	065/ 68	2000-094
	324	052/ 66	2000-095
	325	030/ 69	2000-095
	326	032/ 69	2000-095
	370	228/ 79	2000-112
	371	206/ 80	2000-112
	372	208/ 82	2000-112
	373	034/ 74	2000-113
	374	038/ 72	2000-113
	375	050/ 64	2000-113
	376	052/ 69	2000-114
	377	036/ 76	2000-114
	378	035/ 69	2000-114
	379	130/ 79	2000-115
	380	132/ 73	2000-115
	381	130/ 79	2000-115
	382	058/ 66	2000-116
	383	070/ 56	2000-116

Subarea	dike #	Strike Dip	From Outcrop#
	384	050/ 71	2000-116
	385	074/ 74	2000-117
	386	100/ 60	2000-117
	387	050/ 60	2000-117
	388	050/ 51	2000-118
	389	038/ 41	2000-118
	390	060/ 66	2000-119
	391	030/ 74	2000-119
	392	040/ 72	2000-119
I1			
	1023	300/ 73	2000-332
	1024	302/ 81	2000-332
	1025	311/ 81	2000-332
	1026	164/ 74	2000-333
	1027	150/ 86	2000-333
	1028	142/ 83	2000-333
I2			
	118	028/ 38	2000-031
	119	024/ 58	2000-031
	120	021/ 49	2000-031
	121	022/ 56	2000-031
	122	348/ 60	2000-032
	123	000/ 70	2000-032
	124	352/ 60	2000-032
	125	001/ 64	2000-032
	126	184/ 84	2000-033
	127	161/ 80	2000-033
	128	170/ 78	2000-033
	129	350/ 58	2000-034
	130	030/ 72	2000-034
	131	040/ 89	2000-034
	132	008/ 78	2000-035
	133	008/ 88	2000-035
	134	174/ 88	2000-035
	192	028/ 55	2000-053
	193	040/ 66	2000-053
	194	020/ 70	2000-053
	195	310/ 62	2000-054
	196	030/ 58	2000-054
	197	340/ 60	2000-054
	198	010/ 55	2000-054

Subarea	dike #	Strike Dip	From Outcrop#
	199	350/ 45	2000-055
	200	000/ 55	2000-055
	201	010/ 58	2000-055
	202	342/ 58	2000-056
	203	320/ 60	2000-056
	204	318/ 50	2000-056
	885	342/ 66	2000-286
	886	000/ 55	2000-286
	887	009/ 81	2000-286
	888	342/ 61	2000-286
	895	032/ 87	2000-289
	896	038/ 87	2000-289
	897	028/ 89	2000-289
	1032	352/ 67	2000-335
	1033	012/ 64	2000-335
	1034	010/ 68	2000-335
	1080	357/ 57	2000-351
	1081	355/ 45	2000-351
	1082	339/ 54	2000-351
	1083	342/ 43	2000-352
	1084	357/ 38	2000-352
	1085	357/ 38	2000-352
	1086	359/ 46	2000-352
	1087	010/ 75	2000-353
	1088	000/ 51	2000-353
	1089	353/ 56	2000-353
	1090	350/ 72	2000-354
	1091	357/ 82	2000-354
	1092	342/ 87	2000-354
I3			
	149	088/ 76	2000-040
	150	112/ 58	2000-040
	151	112/ 64	2000-040
	152	114/ 72	2000-040
	153	192/ 44	2000-041
	154	186/ 32	2000-041
	155	190/ 54	2000-041
	156	198/ 57	2000-041
	179	222/ 78	2000-048
	180	235/ 80	2000-048
	181	222/ 44	2000-048

Subarea	dike #	Strike Dip	From Outcrop#
	182	225/ 55	2000-048
	183	210/ 61	2000-049
	184	201/ 64	2000-049
	185	215/ 84	2000-049
	186	024/ 64	2000-050
	187	044/ 66	2000-050
	188	038/ 63	2000-050
	189	202/ 72	2000-051
	190	188/ 70	2000-051
	191	192/ 55	2000-052
	252	040/ 65	2000-071
	253	030/ 60	2000-071
	254	022/ 55	2000-071
	255	020/ 88	2000-072
	256	050/ 69	2000-072
	257	052/ 71	2000-072
	258	040/ 65	2000-073
	259	030/ 70	2000-073
	260	018/ 80	2000-073
	261	020/ 80	2000-074
	262	027/ 82	2000-074
	263	020/ 78	2000-074
	276	200/ 71	2000-079
	277	200/ 73	2000-079
	278	170/ 75	2000-079
	279	060/ 81	2000-080
	280	056/ 74	2000-080
	281	070/ 60	2000-080
	282	020/ 62	2000-081
	283	010/ 58	2000-081
	284	006/ 60	2000-081
	285	030/ 58	2000-082
	286	358/ 64	2000-082
	287	000/ 54	2000-082
	289	010/ 64	2000-083
	290	012/ 70	2000-083
	291	020/ 69	2000-083
	292	050/ 78	2000-084
	293	080/ 86	2000-084
	294	050/ 79	2000-084

I4

Subarea	dike #	Strike Dip	From Outcrop#
	59	090/ 42	2000-014
	60	092/ 60	2000-014
	61	072/ 62	2000-014
	62	061/ 65	2000-014
	63	140/ 85	2000-015
	64	142/ 87	2000-015
	65	142/ 87	2000-015
	66	002/ 65	2000-015
	67	158/ 70	2000-015
	68	008/ 71	2000-016
	69	010/ 74	2000-016
	70	020/ 69	2000-016
	71	040/ 68	2000-016
	72	140/ 65	2000-017
	73	132/ 70	2000-017
	74	155/ 69	2000-017
	75	335/ 70	2000-018
	76	070/ 87	2000-018
	77	004/ 70	2000-018
	78	160/ 70	2000-018
	79	204/ 74	2000-019
	80	210/ 65	2000-019
	81	270/ 58	2000-019
	82	230/ 44	2000-019
	83	040/ 71	2000-020
	84	045/ 75	2000-020
	85	050/ 82	2000-020
	86	250/ 89	2000-021
	87	240/ 85	2000-021
	88	234/ 79	2000-021
	89	230/ 79	2000-021
	90	199/ 70	2000-022
	91	180/ 65	2000-022
	92	200/ 78	2000-022
	93	192/ 45	2000-022
	94	180/ 85	2000-023
	95	184/ 89	2000-023
	96	190/ 75	2000-023
	97	120/ 40	2000-024
	98	132/ 48	2000-024
	99	152/ 55	2000-024

Subarea	dike #	Strike Dip	From Outcrop#
	100	138/ 64	2000-024
	101	130/ 71	2000-025
	102	122/ 80	2000-025
	103	100/ 68	2000-025
	104	110/ 87	2000-025
	157	164/ 52	2000-042
	158	160/ 32	2000-042
	159	154/ 41	2000-042
	160	180/ 68	2000-042
	161	154/ 75	2000-042
	162	048/ 74	2000-043
	163	044/ 68	2000-043
	164	055/ 72	2000-043
	165	042/ 77	2000-043
	166	058/ 82	2000-043
	167	058/ 72	2000-044
	168	082/ 74	2000-044
	169	066/ 60	2000-044
	170	066/ 68	2000-044
	171	252/ 89	2000-045
	172	194/ 82	2000-046
	173	028/ 79	2000-046
	174	165/ 65	2000-046
	175	048/ 68	2000-047
	176	064/ 55	2000-047
	177	046/ 72	2000-047
	178	041/ 66	2000-047
	1160	120/ 58	1999-053
	1161	088/ 70	1999-054
	1162	020/ 74	1999-055
	1163	095/ 74	1999-056
	1164	050/ 82	1999-057
	1165	042/ 76	1999-058
	1166	082/ 62	1999-059
	1167	082/ 74	1999-060
	1168	092/ 76	1999-061
	1169	180/ 85	1999-062
	1170	072/ 70	1999-063
	1171	070/ 70	1999-064
III			
	225	280/ 82	2000-063

Subarea	dike #	Strike Dip	From Outcrop#
	226	284/ 80	2000-063
	227	280/ 88	2000-063
	839	032/ 63	2000-272
	840	038/ 69	2000-272
	841	028/ 80	2000-272
	842	045/ 86	2000-273
	843	022/ 60	2000-273
	844	041/ 74	2000-273
	845	052/ 61	2000-274
	846	042/ 77	2000-274
	847	010/ 58	2000-274
	848	032/ 66	2000-275
	849	033/ 64	2000-275
	850	025/ 81	2000-275
	851	048/ 71	2000-276
	852	052/ 66	2000-276
	853	042/ 54	2000-276
	854	228/ 61	2000-277
	855	209/ 69	2000-277
	856	214/ 67	2000-277
	857	036/ 71	2000-278
	858	039/ 63	2000-278
	859	026/ 74	2000-278
	860	040/ 81	2000-279
	861	230/ 89	2000-279
	862	018/ 69	2000-279
	863	202/ 64	2000-280
	864	194/ 35	2000-280
	865	189/ 63	2000-280
	866	202/ 56	2000-280
	867	211/ 63	2000-280
	868	216/ 89	2000-281
	869	190/ 60	2000-281
	1018	000/ 59	2000-330
	1019	020/ 79	2000-330
	1020	010/ 80	2000-330
	1021	200/ 59	2000-331
	1022	090/ 60	2000-331
II2			
	1	006/ 65	2000-901
	2	352/ 62	2000-901

Subarea	dike #	Strike Dip	From Outcrop#
	3	030/ 72	2000-901
	4	032/ 70	2000-901
	5	352/ 56	2000-901
	6	010/ 56	2000-901
	7	358/ 55	2000-901
	8	355/ 51	2000-901
	53	190/ 60	2000-012
	54	180/ 60	2000-012
	55	200/ 72	2000-012
	56	050/ 65	2000-013
	57	052/ 62	2000-013
	58	052/ 72	2000-013
	135	165/ 86	2000-036
	136	174/ 80	2000-036
	137	160/ 80	2000-036
	205	346/ 72	2000-057
	206	351/ 72	2000-057
	207	350/ 75	2000-057
	208	332/ 82	2000-057
	209	000/ 61	2000-058
	210	002/ 58	2000-058
	211	004/ 60	2000-058
	212	002/ 68	2000-059
	213	352/ 72	2000-059
	214	324/ 75	2000-059
	215	000/ 65	2000-059
	216	004/ 62	2000-060
	217	010/ 65	2000-060
	218	358/ 62	2000-060
	219	020/ 45	2000-061
	220	000/ 55	2000-061
	221	010/ 45	2000-061
	222	010/ 76	2000-062
	223	358/ 71	2000-062
	224	344/ 72	2000-062
	228	350/ 70	2000-064
	229	000/ 69	2000-064
	230	010/ 88	2000-064
	231	357/ 71	2000-064
	232	310/ 80	2000-065
	233	342/ 88	2000-065

Subarea	dike #	Strike Dip	From Outcrop#
	234	316/ 76	2000-065
	235	340/ 80	2000-066
	236	160/ 88	2000-066
	237	340/ 82	2000-066
	273	000/ 59	2000-078
	274	356/ 66	2000-078
	275	354/ 66	2000-078
	420	212/ 76	2000-129
	421	210/ 79	2000-129
	422	212/ 84	2000-129
	423	022/ 79	2000-130
	424	030/ 81	2000-130
	425	190/ 85	2000-130
	426	350/ 78	2000-131
	427	022/ 74	2000-131
	428	350/ 69	2000-131
	765	044/ 88	2000-248
	766	042/ 76	2000-248
	767	049/ 80	2000-248
	768	213/ 76	2000-249
	769	222/ 81	2000-249
	770	044/ 72	2000-249
	794	123/ 84	2000-257
	795	134/ 89	2000-257
	796	148/ 80	2000-257
	797	132/ 78	2000-258
	798	121/ 86	2000-258
	799	114/ 71	2000-258
	800	231/ 81	2000-259
	801	221/ 81	2000-259
	802	221/ 72	2000-259
	818	002/ 86	2000-265
	819	010/ 81	2000-265
	820	022/ 71	2000-265
	821	000/ 70	2000-266
	822	010/ 70	2000-266
	823	350/ 89	2000-266
	824	152/ 71	2000-267
	825	356/ 71	2000-267
	826	338/ 40	2000-267
	833	221/ 88	2000-270

Subarea	dike #	Strike Dip	From Outcrop#
	834	220/ 84	2000-270
	835	217/ 50	2000-270
	836	170/ 50	2000-271
	837	201/ 50	2000-271
	838	184/ 56	2000-271
	904	000/ 81	2000-292
	905	356/ 84	2000-292
	906	004/ 84	2000-292
	907	000/ 76	2000-293
	908	004/ 69	2000-293
	909	004/ 89	2000-293
	910	358/ 69	2000-294
	911	359/ 75	2000-294
	912	348/ 71	2000-294
	913	350/ 66	2000-295
	914	352/ 66	2000-295
	915	344/ 63	2000-295
	916	000/ 75	2000-296
	917	010/ 81	2000-296
	918	010/ 79	2000-296
	919	008/ 86	2000-297
	920	002/ 81	2000-297
	921	026/ 86	2000-297
	922	358/ 86	2000-298
	923	352/ 81	2000-298
	924	350/ 74	2000-298
	925	008/ 71	2000-299
	926	009/ 79	2000-299
	927	000/ 62	2000-299
	928	032/ 86	2000-300
	929	010/ 79	2000-300
	930	010/ 79	2000-300
	931	252/ 57	2000-301
	932	254/ 77	2000-301
	933	240/ 68	2000-301
	934	344/ 59	2000-302
	935	012/ 66	2000-302
	936	358/ 53	2000-302
	937	030/ 56	2000-303
	938	340/ 66	2000-303
	939	008/ 64	2000-303

Subarea	dike #	Strike Dip	From Outcrop#
	940	019/ 54	2000-304
	941	006/ 51	2000-304
	942	030/ 54	2000-304
	943	350/ 64	2000-305
	944	009/ 64	2000-305
	945	346/ 64	2000-305
	946	350/ 63	2000-306
	947	318/ 61	2000-306
	948	342/ 59	2000-306
II3			
	27	240/ 70	2000-004
	28	250/ 64	2000-004
	29	242/ 72	2000-004
	30	242/ 72	2000-004
	31	184/ 38	2000-005
	32	160/ 55	2000-005
	33	107/ 68	2000-005
	34	169/ 55	2000-005
	35	185/ 43	2000-005
	36	230/ 85	2000-006
	37	218/ 85	2000-006
	38	250/ 82	2000-006
	39	250/ 82	2000-006
	40	240/ 75	2000-006
	41	219/ 75	2000-007
	42	030/ 87	2000-007
	43	224/ 78	2000-007
	44	242/ 50	2000-008
	45	250/ 75	2000-008
	46	232/ 76	2000-008
	47	234/ 82	2000-008
	48	052/ 78	2000-008
	49	042/ 56	2000-008
	50	235/ 36	2000-010
	51	310/ 75	2000-011
	52	300/ 80	2000-011
	248	030/ 68	2000-070
	249	052/ 70	2000-070
	250	070/ 68	2000-070
	251	072/ 76	2000-070
	429	230/ 81	2000-132

Subarea	dike #	Strike Dip	From Outcrop#
	430	220/ 71	2000-132
	431	222/ 79	2000-132
	530	224/ 83	2000-168
	531	198/ 83	2000-168
	532	240/ 84	2000-168
	533	222/ 85	2000-169
	534	212/ 60	2000-169
	535	216/ 77	2000-169
	545	212/ 88	2000-172
	546	214/ 86	2000-172
	547	216/ 78	2000-172
	548	257/ 84	2000-173
	549	232/ 64	2000-173
	550	228/ 74	2000-173
	551	238/ 84	2000-174
	552	056/ 88	2000-174
	553	244/ 84	2000-174
	566	054/ 84	2000-179
	567	052/ 84	2000-179
	568	038/ 76	2000-179
	569	228/ 84	2000-180
	570	236/ 76	2000-180
	571	224/ 86	2000-180
	572	050/ 88	2000-181
	573	245/ 80	2000-181
	574	246/ 88	2000-181
	575	230/ 76	2000-182
	576	222/ 66	2000-182
	577	218/ 80	2000-182
	626	064/ 79	2000-200
	627	064/ 86	2000-200
	628	062/ 74	2000-200
	635	114/ 41	2000-203
	636	108/ 40	2000-203
	637	107/ 44	2000-203
	747	249/ 86	2000-242
	748	049/ 86	2000-242
	749	242/ 84	2000-242
	750	211/ 86	2000-243
	751	030/ 81	2000-243
	752	060/ 89	2000-243

Subarea	dike #	Strike Dip	From Outcrop#
	753	193/ 80	2000-244
	754	199/ 70	2000-244
	755	190/ 81	2000-244
	756	221/ 59	2000-245
	757	214/ 73	2000-245
	758	236/ 66	2000-245
	759	241/ 59	2000-246
	760	246/ 60	2000-246
	761	232/ 59	2000-246
	762	240/ 69	2000-247
	763	242/ 60	2000-247
	764	229/ 67	2000-247
	771	049/ 86	2000-250
	772	054/ 77	2000-250
	773	059/ 81	2000-250
	774	219/ 76	2000-251
	775	224/ 68	2000-251
	776	204/ 71	2000-251
	777	237/ 83	2000-252
	778	241/ 79	2000-252
	779	242/ 66	2000-252
	780	032/ 76	2000-253
	781	216/ 87	2000-253
	782	231/ 74	2000-254
	783	051/ 81	2000-254
	784	210/ 89	2000-254
	785	220/ 69	2000-255
	786	188/ 84	2000-255
	787	214/ 83	2000-255
	788	041/ 76	2000-256
	789	034/ 84	2000-256
	790	051/ 83	2000-256
	791	242/ 71	2000-256
	792	221/ 68	2000-256
	793	219/ 66	2000-256
	803	219/ 78	2000-260
	804	234/ 86	2000-260
	805	232/ 86	2000-260
	806	021/ 88	2000-261
	807	211/ 86	2000-261
	808	031/ 79	2000-261

Subarea	dike #	Strike Dip	From Outcrop#
	809	232/ 69	2000-262
	810	214/ 81	2000-262
	811	230/ 68	2000-262
	812	222/ 63	2000-263
	813	224/ 76	2000-263
	814	230/ 69	2000-263
	815	092/ 86	2000-264
	816	244/ 83	2000-264
	817	229/ 84	2000-264
	827	170/ 71	2000-268
	828	170/ 76	2000-268
	829	180/ 79	2000-268
	830	182/ 35	2000-269
	831	164/ 35	2000-269
	832	160/ 35	2000-269
II4			
	738	238/ 79	2000-239
	739	206/ 64	2000-239
	740	008/ 74	2000-239
	741	039/ 86	2000-240
	742	039/ 71	2000-240
	1093	080/ 76	1999-001
	1094	110/ 72	1999-001
	1095	105/ 55	1999-002
	1096	098/ 78	1999-003
	1097	104/ 80	1999-003
	1098	296/ 74	1999-004
	1099	094/ 83	1999-005
	1100	108/ 80	1999-006
	1101	215/ 55	1999-007
	1102	250/ 48	1999-008
	1103	130/ 80	1999-009
	1104	106/ 78	1999-010
	1105	285/ 76	1999-010
	1106	200/ 48	1999-011
	1107	082/ 64	1999-012
	1108	275/ 75	1999-012
	1109	114/ 85	1999-013
	1110	264/ 78	1999-014
	1111	285/ 30	1999-015
	1112	118/ 70	1999-016

Subarea	dike #	Strike Dip	From Outcrop#
	1114	018/ 90	1999-018
	1115	232/ 54	1999-019
	1117	303/ 80	1999-021
	1158	098/ 72	1999-051
	1159	110/ 58	1999-052
III			
	338	150/ 69	2000-100
	339	140/ 64	2000-100
	340	142/ 64	2000-100
III2			
	295	020/ 70	2000-085
	296	030/ 85	2000-085
	297	018/ 69	2000-085
	298	040/ 82	2000-086
	299	042/ 76	2000-086
	300	045/ 86	2000-086
	301	100/ 80	2000-087
	302	080/ 70	2000-087
	303	080/ 69	2000-087
	304	260/ 80	2000-088
	305	248/ 88	2000-088
	306	040/ 88	2000-089
	307	038/ 88	2000-089
	308	270/ 76	2000-089
	318	034/ 82	2000-093
	319	042/ 80	2000-093
	320	250/ 82	2000-093
	344	060/ 88	2000-102
	345	070/ 85	2000-102
	346	240/ 85	2000-102
	361	192/ 82	2000-109
	362	192/ 80	2000-109
	363	208/ 82	2000-109
	364	190/ 80	2000-110
	365	192/ 88	2000-110
	366	010/ 86	2000-110
	367	210/ 79	2000-111
	368	212/ 76	2000-111
	369	182/ 74	2000-111
	393	040/ 81	2000-120
	394	050/ 84	2000-120

Subarea	dike #	Strike Dip	From Outcrop#
	395	028/ 74	2000-120
	396	200/ 81	2000-121
	397	030/ 81	2000-121
	398	235/ 85	2000-121
	399	208/ 89	2000-122
	400	280/ 84	2000-122
	401	030/ 86	2000-122
	402	080/ 88	2000-123
	403	230/ 56	2000-123
	404	200/ 81	2000-123
	405	230/ 79	2000-124
	406	238/ 78	2000-124
	407	234/ 76	2000-124
	408	178/ 79	2000-125
	409	180/ 79	2000-125
	410	174/ 76	2000-125
	411	220/ 69	2000-126
	412	224/ 89	2000-126
	413	052/ 87	2000-126
	414	182/ 88	2000-127
	415	202/ 84	2000-127
	416	350/ 81	2000-127
	417	188/ 55	2000-128
	418	194/ 64	2000-128
	419	198/ 69	2000-128
	967	231/ 89	2000-313
	968	050/ 81	2000-313
	969	244/ 87	2000-313
	988	051/ 86	2000-320
	989	050/ 79	2000-320
	990	052/ 83	2000-320
	991	152/ 61	2000-321
	992	128/ 71	2000-321
	993	150/ 57	2000-321
	994	080/ 77	2000-322
	995	060/ 76	2000-322
	996	079/ 79	2000-322
	997	071/ 86	2000-323
	998	050/ 83	2000-323
	999	070/ 79	2000-323

III3

Subarea	dike #	Strike Dip	From Outcrop#
	309	080/ 69	2000-090
	310	078/ 88	2000-090
	311	250/ 88	2000-091
	312	250/ 88	2000-091
	313	042/ 82	2000-091
	314	074/ 74	2000-091
	315	048/ 85	2000-092
	316	064/ 82	2000-092
	317	062/ 76	2000-092
	327	062/ 64	2000-096
	328	072/ 71	2000-096
	329	072/ 62	2000-096
	330	050/ 76	2000-097
	331	080/ 74	2000-097
	332	054/ 66	2000-097
	333	145/ 56	2000-098
	334	100/ 60	2000-098
	335	094/ 60	2000-099
	336	130/ 69	2000-099
	337	114/ 68	2000-099
	347	158/ 86	2000-103
	348	140/ 89	2000-103
	349	142/ 79	2000-103
	350	050/ 84	2000-104
	351	130/ 55	2000-105
	352	125/ 68	2000-105
	353	114/ 55	2000-105
	453	070/ 60	2000-141
	454	081/ 64	2000-141
	455	084/ 60	2000-141
	465	053/ 71	2000-145
	466	041/ 81	2000-145
	467	046/ 72	2000-145
	468	132/ 41	2000-146
	469	099/ 54	2000-146
	470	122/ 60	2000-146
	471	332/ 88	2000-147
	472	166/ 78	2000-147
	473	338/ 81	2000-147
	964	221/ 74	2000-312
	965	229/ 84	2000-312

Subarea	dike #	Strike Dip	From Outcrop#
	966	216/ 69	2000-312
	970	061/ 76	2000-314
	971	059/ 84	2000-314
	972	048/ 87	2000-314
	973	242/ 84	2000-315
	974	250/ 82	2000-315
	975	060/ 83	2000-315
	976	051/ 86	2000-316
	977	243/ 79	2000-316
	978	071/ 89	2000-316
	979	074/ 81	2000-317
	980	078/ 76	2000-317
	981	240/ 86	2000-317
	982	074/ 86	2000-318
	983	057/ 76	2000-318
	984	071/ 86	2000-318
	985	072/ 81	2000-319
	986	058/ 80	2000-319
	987	054/ 76	2000-319
III4			
	456	122/ 60	2000-142
	457	130/ 69	2000-142
	458	128/ 46	2000-142
	459	121/ 61	2000-143
	460	118/ 73	2000-143
	461	128/ 59	2000-143
	462	333/ 64	2000-144
	463	351/ 34	2000-144
	464	010/ 40	2000-144
	490	231/ 60	2000-154
	491	238/ 64	2000-154
	492	234/ 61	2000-154
	493	238/ 66	2000-155
	494	252/ 64	2000-155
	495	254/ 64	2000-155
	496	283/ 84	2000-156
	497	258/ 87	2000-156
	498	110/ 89	2000-156
	499	292/ 84	2000-157
	500	268/ 81	2000-157
	501	104/ 87	2000-157

Subarea	dike #	Strike Dip	From Outcrop#
	502	242/ 79	2000-158
	503	160/ 85	2000-158
	504	030/ 61	2000-159
	505	044/ 79	2000-159
	506	060/ 71	2000-159
	507	149/ 71	2000-160
	508	169/ 66	2000-160
	509	158/ 81	2000-160
IV3			
	435	160/ 74	2000-134
	436	010/ 73	2000-135
	437	010/ 88	2000-135
	438	020/ 88	2000-135
	439	190/ 76	2000-136
	440	160/ 41	2000-136
	441	200/ 60	2000-136
	442	070/ 40	2000-137
	443	062/ 45	2000-137
	444	090/ 51	2000-137
	445	112/ 74	2000-138
	446	112/ 66	2000-138
	447	124/ 74	2000-138
	448	282/ 45	2000-139
	449	250/ 60	2000-139
	450	190/ 32	2000-140
	451	170/ 54	2000-140
	452	200/ 69	2000-140
	474	192/ 79	2000-148
	475	196/ 83	2000-148
	476	184/ 85	2000-148
	477	081/ 60	2000-149
	478	064/ 56	2000-150
	479	062/ 63	2000-150
	480	056/ 60	2000-150
	481	271/ 83	2000-151
	482	252/ 69	2000-151
	483	094/ 64	2000-151
	484	208/ 84	2000-152
	485	219/ 86	2000-152
	486	208/ 89	2000-152
IV4			

Subarea	dike #	Strike Dip	From Outcrop#
	487	028/ 81	2000-153
	488	022/ 71	2000-153
	489	204/ 89	2000-153

Appendix C: AMS Data

Subarea	Sample#	k_{min}			k_{int}			k_{max}		
		dec.	inc.	int.	dec.	inc.	int.	dec.	inc.	int.
A										
	DG 369 A	321.6	3.1	49270	229.7	31.2	49706	56.7	58.7	49991
	DG 369 B	298.7	6.3	62361	199	56.8	62845	32.7	32.4	63190
	DG 370 A	280.5	35.3	26634	95.6	54.6	27313	188.9	2.3	27408
	DG 370 B	280.6	36.4	26537	118.8	52.2	27365	17.2	8.9	27448
	DG 371 A	316.2	28.4	515.3	61.7	26.4	516.7	187	49.4	520.2
	DG 371 B	343	17.4	696.1	240.9	33.7	698.5	95.7	50.9	700.6
	DG 371 C	242.4	75.3	473.9	51.6	14.4	474.4	142.3	2.8	475.9
	DG 371 D	292.1	57.9	584	180	13.2	586.1	82.6	28.7	587
	DG 372 A	214.9	6.7	33511	313.4	51.5	33629	119.7	37.7	34029
	DG 372 B	241.4	60.7	19938	47.9	28.6	20030	141	5.8	20168
	DG 372 C	191.7	79.2	10489	69.9	5.8	10600	339	9.2	10728
	DG 372 D	35.3	8.6	27342	291.7	57.3	27553	130.6	31.3	27716
	DG 373 A	349.1	15.9	62823	245.9	38.8	63525	96.9	46.9	64006
	DG 373 B	344.5	19.1	63690	234.4	44.9	64335	90.8	39	64821
	DG 374 A	250	41.5	88479	356.9	18.2	89577	104.7	42.9	89993
	DG 374 B	242.9	48.9	101530	356.7	19.4	102300	100.8	34.5	103120
	DG 374 C	263	62	110570	23.1	15	111470	119.7	23.1	112330
	DG 374 D	249.6	54.3	118660	8.7	19.3	119330	109.7	28.8	120500
	DG 375 A	253.2	57.8	88130	10.1	15.9	89142	108.6	27.2	89402
	DG 375 C	260.3	50.1	91092	10.8	16.3	92070	112.7	35.2	92355
	DG 375 D	265.5	53.7	92678	4.2	6.3	93854	98.8	35.6	94075
B										
	DG 290 A	69.7	8.1	53145	298.1	78	53636	161	8.9	53798
	DG 291 A	244.3	21.9	72923	147	17.6	73796	21.5	61.3	74298
	DG 291 B	258.8	14.6	67332	165.4	12.8	67879	35.9	70.4	68005
	DG 291 C	258.2	23	68307	155.3	27.9	69193	21.8	52.5	69469
	DG 292 A	243.7	41.9	74156	335.3	1.9	75487	67.4	48	76306
	DG 292 C	261.9	48.6	74172	1.8	8.6	75896	99.1	40.1	76841
	DG 292 D	263.7	41.8	78720	356.2	2.7	80145	89.2	48.1	81180
	DG 293 A	258.4	14.9	76851	166.7	6.3	79672	54.5	73.8	80946
	DG 293 B	255.3	24.1	74678	345.7	0.9	77458	77.8	65.9	78805
	DG 293 C	232.7	14.7	76338	325	8.7	78807	84.8	72.8	80143
	DG 294 A	2.4	6.1	584.7	269.2	27.9	592.7	103.7	61.3	596.2
	DG 294 B	352.4	10.7	554.7	259.3	16.1	562.8	114.7	70.5	567.6

AMS intensity in μ SI units

Subarea	Sample#	k_{min}			k_{int}			k_{max}		
		dec.	inc.	int.	dec.	inc.	int.	dec.	inc.	int.
	DG 294 C	350.5	7.5	550	256.9	25.5	553.8	95.7	63.2	555.8
	DG 294 D	335.7	13	573	239	26.6	578.6	89.3	59.9	580.4
	DG 295 A	8.4	3.2	617.1	278.2	4.6	619.6	133.2	84.4	622
	DG 295 B	348.8	14.5	603.6	82.7	15.1	606.6	216.9	68.9	610.5
	DG 295 C	346.7	11.7	592.8	256.6	0.3	593.6	165.4	78.3	594.4
	DG 296 A	212.9	37	52467	332	32.8	52607	89.8	35.9	52812
	DG 296 B	277.3	67.7	47696	35.9	11.1	47922	129.7	19.1	48164
	DG 297 A	68.4	31.7	46937	322.1	24.6	47168	201.6	48	47409
	DG 297 B	69.6	28.3	47789	257.1	61.5	48200	161.3	3.1	48445
	DG 297 C	234	28.6	45818	83.9	57.9	46057	331.5	13.4	46468
	DG 297 D	65.2	22.3	46541	303.5	52.1	46873	168.3	28.9	47180
	DG 365 A	108.8	20.4	78256	6.9	28.9	79675	228.8	53.4	80359
	DG 365 B	114.7	24.2	79567	22.7	4.4	80633	283	65.4	81325
	DG 366 A	117.8	45.1	48580	254.9	36.1	49399	2.8	22.8	50121
	DG 366 B	106.9	42	42394	227	29.1	43105	339.2	34.2	43596
	DG 366 C	99.9	32.1	54759	241.1	51.1	55584	357.1	19.5	56051
	DG 366 D	116.6	41.9	36453	241.6	32.6	37365	354.1	30.9	37879
	DG 376 A	301.7	6.9	23173	197.4	63.8	23402	34.9	25.2	23424
	DG 376 B	307.6	4.7	25665	208.5	62.7	25847	39.9	26.8	25949
	DG 376 C	302	4.9	26258	208.9	33	26525	39.4	56.5	26590
	DG 376 D	300.8	4.4	24892	203.8	58.1	25066	33.5	31.5	25191
	DG 377 A	293.4	2.4	8328.6	189.5	79.9	8352	23.8	9.8	8370.8
	DG 377 B	129.2	30.7	7463.6	356.8	48.6	7484.6	235.1	24.8	7500.8
	DG 378 A	241.1	4.3	76396	342.8	69.7	76905	149.5	19.8	77211
	DG 378 B	238.2	30.9	77761	20.1	52.8	78114	136.5	18.7	78745
	DG 379 A	4.5	7.3	25687	98	25.7	26015	259.9	63.1	26277
	DG 379 B	185.4	11.1	42132	90.9	21.6	42786	300.8	65.4	42838
	DG 379 C	181.3	2.3	52799	88.7	48.5	53411	273.3	41.4	54008
	DG 380 A	17.4	13.5	9187.4	252.1	67.4	9203.6	111.8	17.8	9224.7
	DG 380 B	7	1.3	9912.9	98.5	50.3	9983.3	275.9	39.7	10034
	DG 380 C	337.2	25.3	5484.3	241.5	11.9	5491.5	128.5	61.7	5515.6
	DG 381 A	243.9	82.7	42210	74.7	7.2	42312	344.6	1.4	42558
	DG 381 B	248	82.2	42226	43.9	7.1	42417	134.3	3.2	42672
	DG 382 A	261.3	42	8062.3	355.6	4.7	8163.1	90.8	47.6	8435.3
	DG 382 B	259.9	41.7	9605.2	350.1	0.2	9698.8	80.3	48.3	10016
	DG 383 A	16.3	1	2153.7	106.6	20.9	2154.8	283.7	69.1	2185.4
	DG 383 B	184.8	14.9	2071.6	89.3	20	2075.3	309	64.7	2092.3
	DG 383 C	165.3	18	2776.6	69.6	16.8	2789.9	299.4	64.9	2823.5

** AMS intensity in μ SI units*

Subarea	Sample#	k_{min}			k_{int}			k_{max}		
		dec.	inc.	int.	dec.	inc.	int.	dec.	inc.	int.
	DG 384 A	178.5	44.4	65521	26.3	42.1	66436	283	14.3	67466
	DG 384 B	171.9	48.5	63169	18.7	38.3	63963	277.7	13.6	64758
	DG 384 C	165	67.3	60514	8.1	21.1	62053	275	8.1	62665
	DG 385 A	19.8	30.3	31440	119	15.3	31665	232.2	55.3	31989
	DG 385 B	20	24.4	43315	112.2	4.8	43746	212.6	65.1	44060
	DG 386 A	45.3	42.6	94405	170.7	32.2	94942	282.5	30.6	95846
	DG 386 A	199.8	28.4	43004	300.2	18.4	43334	58.8	55.2	43665
	DG 386 B	198	25.6	40824	299.3	22.3	41111	65	54.9	41423
	DG 386 C	220.2	36.6	44436	312.4	3	44708	46.5	53.3	45095
	DG 386 D	226.5	30.7	32985	317.9	2.3	33215	51.8	59.2	33459
	DG 387 B	11.6	24	93357	134.3	50.6	94061	267.2	29.2	94395
	DG 387 C	28	32.9	95855	148.1	37.8	96407	271	35	96825
	DG 387 D	15.2	30.7	87600	141.8	45.2	87975	265.9	29.2	88588
	DG 388 A	206.2	17	64173	351	69.5	64496	112.7	11.1	65130
	DG 388 B	217.7	26	56626	345.9	51.7	56850	114	26	57083
	DG 388 C	206.1	46.3	56715	18.6	43.4	56930	112.1	3.8	57371
	DG 389 A	221.8	11.3	64405	314.2	11.8	65007	89.3	73.5	65461
	DG 389 B	203.3	22.1	74561	325.4	52.6	75099	100.6	28.5	75522
	DG 389 C	208.4	16	78011	310.2	35.4	78305	98.4	50.1	78951
	DG 389 D	221.2	19.3	78048	326.2	36.5	78530	109.1	47.1	79034
	DG 390 A	318.7	67.7	48362	49.5	0.3	48911	139.6	22.3	49086
	DG 390 B	310.9	54.7	54118	211.5	6.6	54581	117	34.5	54795
	DG 390 C	325.9	52.3	53352	224	9	54246	127.4	36.2	54353
	DG 390 D	314.1	40.3	53465	192.5	31.7	53932	78.4	33.6	54054
	DG 390 E	316.4	46.1	53396	222.7	3.6	53956	129.2	43.7	54064
	DG 391 A	255.8	54	56415	350.6	3.5	56725	83.1	35.7	57244
	DG 391 B	270.8	47.7	46521	1.2	0.4	46763	91.5	42.3	47305
	DG 391 C	291.2	45.2	52145	185.5	15.1	52243	82	40.9	52648
	DG 392 A	207.9	9.3	32732	300.2	13.7	32894	84.6	73.3	33158
	DG 392 B	227	19.2	31616	332.1	36.9	31782	115.2	46.8	31979
	DG 392 C	20.4	1.4	31472	289.9	18.9	31632	114.5	71	31902
	DG 392 D	218.9	14.8	31984	319	33.6	32266	108.8	52.4	32430
	DG 393 A	309.8	6.4	36336	45.9	43.2	36445	213	46.1	37055
	DG 393 B	308.5	2.9	32335	42.2	52.2	32464	216.3	37.7	32873
	DG 393 C	322.1	22.2	37582	75.9	44.6	37671	214.1	37.1	38199
	DG 393 D	320.8	4.1	33338	53.6	35.1	33475	225	54.6	33923
	DG 394 A	4.2	38.2	111270	229.3	41.9	111890	115.2	24.5	112200
	DG 395 A	0.2	17.9	4170.8	266.1	12.3	4300.6	143.5	68	4304.4

AMS intensity in μ SI units

Subarea	Sample#	k_{min}			k_{int}			k_{max}		
		dec.	inc.	int.	dec.	inc.	int.	dec.	inc.	int.
	DG 395 B	350.5	19.2	5217.4	252.4	22	5351.7	117.7	60	5394.4
	DG 395 C	345.7	27	4850	240.1	27.9	4919.1	112	49.3	4943.2
	DG 395 D	352.7	16.8	4442.8	247	41.9	4543.9	99.3	43.3	4560.4
C										
	DG 028 A	204.1	12.7	135120	53.2	75.6	136810	295.7	6.8	138930
	DG 028 B	213.9	37	108000	21.4	52.4	109730	119.3	6.1	112080
	DG 028 C	205.3	28.9	107650	49.6	58.7	110440	301.3	10.8	112230
	DG 028 D	210.9	20.4	130670	68.7	64.8	134050	306.3	14.1	136690
	DG 029 A	14.1	45.3	696.8	104.7	0.6	705.2	195.2	44.7	710
	DG 029 B	1.3	15.6	675.2	105.4	41.3	678.7	255.3	44.6	681.4
	DG 029 C	337.3	21	681.7	80.7	31	682.7	218.8	51.1	686.7
	DG 030 A	293.5	21.1	43720	25.8	5.9	43788	130.7	68	43976
	DG 030 B	233.7	6.5	40734	327.5	30.8	40957	133.1	58.4	41072
	DG 031 A	212.1	9.6	25689	115.1	35.4	26011	315.1	52.9	26112
	DG 031 B	216.5	14.7	25246	115.7	35.5	25627	325.2	50.7	25747
	DG 031 C	210.6	18.6	24828	107.5	34.1	25177	324.1	49.8	25212
	DG 032 A	208	43.9	580.8	359.4	42.4	583.6	103.3	14.8	584.3
	DG 032 B	348.1	69.3	602.5	112.5	12	604.4	206.1	16.6	605.5
	DG 039 A	228.2	4.4	38589	322.5	44.8	39237	133.8	44.9	39499
	DG 039 B	225.6	10.3	37102	342.8	68.3	37571	132.1	18.9	37824
	DG 040 A	232.2	42.6	40589	327.5	5.7	41101	63.5	46.9	41587
	DG 040 B	210.2	25.7	43162	329.8	45.7	43418	101.9	33.2	43989
	DG 040 C	226.9	52	38202	133	3	38776	40.7	37.8	39369
	DG 040 D	359.4	25.5	35898	232.5	51.5	36204	103.3	26.7	36680
	DG 041 A	262.4	36.7	10746	133.1	40.4	10985	15.9	28.2	11302
	DG 069 A	357.6	16.9	77584	95.6	24.5	79200	236.5	59.5	80505
	DG 070 A	18	7	71464	287.2	6.7	72793	153.6	80.3	73748
	DG 070 B	21.8	13.3	75011	287	19.5	76013	144.1	66.1	77420
	DG 070 C	27.5	10.3	80657	292.5	25.8	81722	137.6	62	82954
	DG 071 A	25.9	10.1	70128	116.5	3.8	70244	227	79.2	70611
	DG 071 B	25.2	28.6	111420	116.6	2.5	116500	211	61.2	117700
	DG 071 C	8.1	7.3	70389	108.5	54.5	70728	273	34.5	70886
	DG 071 C	21.2	32.2	127510	286.4	7.4	133950	185	56.8	134320
	DG 071 D	15.3	30.5	117730	106.3	1.8	123520	199.3	59.4	124420
	DG 077 A	299.7	45.6	61630	87.8	39.7	61839	192.1	16.5	62049
	DG 077 B	316.5	65.7	59122	113	22.5	59384	206.7	8.7	59591
	DG 077 C	26.5	67.6	38396	252.6	15.9	38678	158.1	15.3	38839
	DG 077 D	325.5	39.2	56336	86.8	32.4	56578	202.1	34	56754

** AMS intensity in μ SI units*

Subarea	Sample#	k_{min}			k_{int}			k_{max}		
		dec.	inc.	int.	dec.	inc.	int.	dec.	inc.	int.
	DG 078 A	350.6	31.3	62939	85	7.2	64313	186.6	57.7	65250
	DG 078 B	349.3	32	44939	88.5	14.3	45925	199.2	54.2	46366
	DG 079 A	192.5	2.6	82479	289.2	68.8	86240	101.5	21.1	87608
	DG 079 B	184.1	2.1	82568	14.9	87.9	86266	274.1	0.4	87315
	DG 079 C	15.8	3.6	82605	228.1	85.8	86062	106	2.3	87292
	DG 191 A	177	2.6	69882	267.6	13.6	71190	76.5	76.1	71636
	DG 191 B	187.9	4	72803	281.1	38	74456	92.8	51.7	74752
	DG 191 C	354.4	8.5	61109	258.5	34.5	61789	96.4	54.2	62073
	DG 192 A	218.9	9.5	29977	121.9	36.2	30330	321.3	52.1	30598
	DG 192 B	224.4	5.7	38607	131.9	23.9	39011	327.1	65.3	39347
	DG 192 C	214.9	18.7	26817	113	31.3	27071	331	52.3	27219
	DG 192 D	227.4	8.7	36579	131.6	33.8	36922	329.9	54.8	37291
	DG 193 A	245.1	10.2	52168	148.7	31.6	52592	350.8	56.4	53324
	DG 193 B	239.9	14.7	51289	142.6	26	51829	356.6	59.6	52568
	DG 193 C	222.2	28.8	49147	112.2	31.9	49606	344.7	44.3	50290
	DG 193 D	220.8	27.8	50363	111.9	31.7	50812	343.1	45.4	51526
	DG 194 A	255.8	44.3	62756	165.4	0.5	64639	74.9	45.7	64923
	DG 194 B	256.8	37.4	62288	352.2	7	63872	91.1	51.7	64582
	DG 194 C	217.6	33.6	63197	127.5	0.2	64767	37.3	56.4	65497
	DG 195 A	224.7	45.1	118100	94.5	32.8	119320	345.3	26.9	120170
	DG 195 B	223.1	46.3	123250	81.8	36.7	124010	335.8	20.2	125580
	DG 195 C	237.9	38.6	118420	103.6	41.1	119160	349.7	24.9	120670
	DG 196 A	213.5	19	122200	111.3	31.6	124570	329.5	52	125480
	DG 196 B	222.9	16.7	125190	124.3	26.5	127420	341.5	58	128570
	DG 197 A	174.6	5.7	71030	82.1	23.2	71595	277.6	66	72277
	DG 197 B	177.2	9	74930	83.5	22.5	75499	287.5	65.6	76159
	DG 197 C	176.9	6	79474	85.4	14	80138	289.4	74.7	80678
	DG 197 D	179.4	11.5	76115	85.1	20.3	76676	297.2	66.4	77398
	DG 198 A	124.9	38.1	97354	226	13.8	98968	332.2	48.6	99939
	DG 198 B	121.3	41.8	109950	221.7	11.4	111890	323.8	46	113180
	DG 198 C	128.1	41.2	119020	229.5	12.8	121200	333.1	46	122580
	DG 198 D	117.5	35.5	96376	220.9	18.1	97688	332.8	48.9	98906
	DG 199 A	199.8	1.5	16434	290.8	32.4	16658	107.4	57.6	16810
	DG 199 B	20.9	3.3	16663	289.5	22.7	16934	118.7	67.1	17103
	DG 199 C	16.1	5.1	21913	281.1	44.1	22390	111.3	45.4	22562
	DG 199 D	11.1	7	20009	269.2	59.4	20403	105.1	29.6	20563
	DG 200 A	207.3	0.5	56503	297.6	33	59683	116.4	57	60825
	DG 200 B	206.4	0.8	52491	296.9	30.8	56027	115.1	59.2	56597

** AMS intensity in μ SI units*

Subarea	Sample#	k_{min}			k_{int}			k_{max}		
		dec.	inc.	int.	dec.	inc.	int.	dec.	inc.	int.
	DG 200 C	201.3	2.3	54556	292.4	26.3	57595	106.6	63.6	58806
	DG 200 D	211.3	1.6	63625	302.4	34.1	67928	118.9	55.9	68643
	DG 201 A	230.9	13.8	75566	124.5	49.1	76962	331.8	37.5	77520
	DG 201 B	235.5	14.3	77689	129.3	47.5	78985	337.4	39	79623
	DG 201 C	229.2	17.5	76708	122.7	42.1	78195	336.1	42.7	78816
	DG 202 A	9.6	36.9	87552	138.1	39.6	88232	255.2	28.8	88491
	DG 202 B	17.7	41.4	86598	145.9	35	87079	258.6	28.8	87400
	DG 202 C	351.3	36.8	90463	96	18.7	91142	207.5	47.1	91253
	DG 202 D	341.6	32.8	89351	195.5	52.1	90016	82.7	16.7	90130
	DG 209 A	249.3	7.5	46856	152	43.7	48059	346.9	45.3	48712
	DG 209 B	247.6	8.6	51085	149.5	42.9	52396	346.5	45.8	53087
	DG 211 A	90.6	16.7	14325	186.1	17.6	14620	319.8	65.3	14859
	DG 211 B	88.2	11.9	14622	184	25.7	14899	335.5	61.3	15142
	DG 211 C	79.3	11.8	15902	174.6	23.9	16225	325	63	16510
	DG 211 D	95.2	14.3	15046	191.2	22.5	15351	335.3	62.9	15576
	DG 212 A	53.6	28.4	25906	316.1	13.5	26331	203.5	57.9	26499
	DG 212 B	64.1	28.8	27143	321.1	22.2	27612	199.2	52.2	27911
	DG 212 C	69.6	28.7	28046	332.7	12.4	28538	221.9	58.3	28845
	DG 212 D	51.6	29.8	25584	318.1	6.1	25957	217.7	59.4	26067
	DG 213 A	145.9	5.7	1472.3	243.3	52.2	1492.7	51.5	37.2	1495
	DG 213 B	326.7	6.8	1242.4	233.1	28	1258	69.1	61	1262.1
	DG 213 C	296.5	7.9	2290.3	34.8	45.9	2328.7	199.1	43	2334.4
	DG 213 D	296.8	10	3256.3	49.7	65.5	3327.8	202.7	22.1	3338.7
	DG 214 A	280	63.8	56276	166.5	11.1	56822	71.6	23.4	57118
	DG 214 B	241.5	0.5	24583	148.8	79	24854	331.6	11	25082
	DG 215 A	58.1	16.1	22317	173	55.5	22441	318.7	29.6	22682
	DG 215 B	59.6	7.3	52267	189.7	78.7	52632	328.5	8.5	52912
	DG 215 C	231.1	10.3	24208	120.8	62.4	24385	326	25.3	24688
	DG 301 A	10.4	12.8	69012	108	30.3	71259	260.4	56.6	72125
	DG 301 B	3.7	8.6	80924	94.5	5.8	83742	218.2	79.6	84480
	DG 301 B	3.6	5.4	63423	267	50.3	67955	98	39.2	68524
	DG 302 A	17.8	3.9	98994	108.9	15.5	103569	274.1	74	106520
	DG 304 A	357.4	0.1	87310	267.2	47.6	95529	87.5	42.4	96052
	DG 305 A	213.3	22.3	41753	351.4	61.1	44341	116	17.4	46022
	DG 305 B	222.2	26.8	42006	357.5	54.6	44498	120.8	21.3	46045
	DG 305 C	219.9	26.2	37616	351.2	53.2	39845	117.3	23.8	41225
	DG 321 A	322.7	25.4	61125	220.4	24.2	61489	92.8	53.6	61930
	DG 321 B	332.7	23.7	56625	229.5	27.5	57011	97.2	52.2	57213

** AMS intensity in μ SI units*

Subarea	Sample#	k_{min}			k_{int}			k_{max}		
		dec.	inc.	int.	dec.	inc.	int.	dec.	inc.	int.
	DG 321 C	336.5	9.8	101550	87.7	64.3	102900	242.2	23.5	104040
	DG 322 A	351.4	32.1	73659	90.1	13.6	76950	199.8	54.5	78128
	DG 322 C	350.2	28	61572	84.7	8.4	65060	189.9	60.6	66482
	DG 323 A	12.8	31.8	85071	117.6	22.3	87679	236.3	49.5	88706
	DG 323 B	14.7	29.3	79729	112.1	12.9	82177	223.2	57.4	83481
	DG 325 A	5.7	4	49345	271.6	45.3	53233	99.6	44.4	53789
	DG 325 B	10.6	4.9	48231	255.7	78.5	51990	101.5	10.4	52275
	DG 325 C	14.7	2.9	43428	283.9	15.2	45829	115.4	74.5	46332
D										
	DG 001 A	256	36	44228	28.3	42.8	44638	145.2	26.1	45030
	DG 001 B	269.1	51.2	50907	47.4	31	51059	150.7	21	51399
	DG 002 A	240	41	31751	132.5	19.1	32058	23.7	42.9	32509
	DG 002 B	247.9	39.1	30172	134.4	26.1	30557	20.4	39.7	31089
	DG 003 A	208.7	44.9	29927	55	41.9	30214	312.6	13.5	30386
	DG 003 B	208.3	46.9	26180	54.5	40	26426	313	13.4	26628
	DG 003 C	209.4	45.1	38366	65.7	38.8	38763	319.6	19	39137
	DG 103 A	282.6	49.8	63611	137.5	34.8	63983	34.7	17.7	64641
	DG 103 B	285.2	44.1	63541	150.9	35.8	64140	41.6	24.7	64727
	DG 186 A	290.9	18.2	14945	186.2	37.7	15148	41.3	46.6	15254
	DG 186 B	297	17.7	13691	193.4	36.3	13903	47.9	48.2	14054
	DG 187 A	323.4	10.9	41749	229.7	18.7	41948	82.1	68.2	42092
	DG 187 B	315.2	17.8	51001	45.4	0.7	51278	137.6	72.2	51378
	DG 187 C	113.2	1.9	49716	22.5	18	50179	209.2	71.9	50439
	DG 187 D	114	5.5	46893	22	19.7	47178	218.9	69.5	47456
	DG 189 A	106.4	13.9	10878	12	17.2	11022	233.3	67.6	11161
	DG 189 B	112.5	6.1	9977.7	18.9	30.2	10114	212.8	59.1	10286
	DG 190 A	75.6	6.4	15982	343.3	19.4	16064	183	69.5	16133
	DG 190 B	267	11.5	17137	174.3	13.3	17185	36.5	72.3	17323
	DG 204 A	276.3	6.2	10936	177.4	54.8	11095	10.5	34.4	11255
	DG 204 B	287.1	4.4	11617	191.7	51.3	11737	20.6	38.4	11898
	DG 204 C	98.2	0.1	10275	188.3	45.3	10361	8.1	44.7	10473
	DG 204 D	271.9	3.6	11841	176.8	55.3	11995	4.4	34.4	12160
	DG 205 A	166.1	10.8	83011	72.7	17.2	83878	286.8	69.6	84525
	DG 205 B	161.1	8	83971	69.8	9.4	84665	290.8	77.7	85398
	DG 207 A	224.2	37.2	32342	52.8	52.5	32501	317.4	4.2	33234
	DG 207 B	223.6	35	32754	57	54.2	32908	318.1	6.3	33679
	DG 207 C	226.1	6.2	32194	57.9	83.7	32292	316.3	1.3	32916
	DG 207 D	221.3	18	34605	48.4	71.8	34740	311.9	2.1	35349

** AMS intensity in μ SI units*

Subarea	Sample#	k_{min}			k_{int}			k_{max}		
		dec.	inc.	int.	dec.	inc.	int.	dec.	inc.	int.
	DG 208 A	98.1	2.2	17921	7.1	25.5	18138	192.6	64.4	18336
	DG 208 B	96.6	1.5	18582	6	21.8	18763	190.3	68.1	19019
	DG 208 C	264.8	0.3	19091	354.9	16.4	19329	173.7	73.5	19552
	DG 210 A	257.6	6.8	17469	350.5	22.6	17755	151.8	66.3	17844
	DG 210 B	260.5	11.1	22136	0.5	41.3	22565	158.5	46.5	22733
	DG 210 C	254.1	11.1	18385	356.2	46.8	18707	154.2	41.1	18823
	DG 210 D	263	8.3	23347	1.6	45.6	23775	165.1	43.2	24025
	DG 210 E	248.8	11.3	22744	347.3	36.5	23178	144.4	51.2	23353
	DG 216 A	337.2	16	26311	74.6	24.1	26549	216.7	60.5	26724
	DG 216 B	327.9	14.6	25859	237.3	2.1	26005	139.4	75.2	26171
	DG 216 C	337	17	24754	70.5	11.5	24915	193.1	69.3	25059
	DG 217 A	158.6	6.5	46679	19.2	81.4	47145	249.3	5.5	47221
	DG 217 B	163.1	3.9	47494	66.7	58.9	47962	255.5	30.8	48081
	DG 217 C	161.1	4.2	45871	61.8	65.3	46352	253	24.3	46493
	DG 217 D	158.3	7.4	48407	67	9.8	48966	285	77.7	48992
	DG 218 A	150.4	10.7	14125	251.7	45.8	14234	50.6	42.2	14394
	DG 218 B	312.1	0.6	21317	221.7	34.6	21524	43	55.4	21562
	DG 218 C	133.2	20.6	19534	246.9	47	19668	27.5	35.8	19738
	DG 219 A	145.3	5.3	36128	237.3	21.2	36635	42	68.1	36822
	DG 219 B	143.1	5.5	33309	235.2	20.7	33904	39	68.5	34097
	DG 220 A	153.9	36.9	36396	259.2	19.5	36783	11.2	46.6	36821
	DG 220 B	152.9	31.9	33817	247.8	7.8	34130	350	56.9	34217
	DG 220 C	148.2	30.6	32073	248.4	16.8	32334	3.1	54.2	32431
	DG 221 A	175.3	7.1	83059	65.3	70.1	84037	267.6	18.5	84623
	DG 221 B	185.1	2.4	78333	94.7	8.4	79165	291.1	81.2	79925
	DG 222 A	126.4	9.4	13637	21.4	57.5	13669	222.1	30.8	13775
	DG 222 B	342.6	40.9	14771	123.7	42	14793	233.6	20.7	14883
	DG 222 C	324.7	27.4	13492	92.7	49.9	13558	219.6	26.8	13635
	DG 223 A	28.4	33.1	35307	127.2	13.2	35377	235.9	53.7	35922
	DG 223 B	145.8	0.5	35994	55.4	39.5	36133	236.4	50.5	36679
	DG 223 C	126.4	15.4	35874	23.3	39.5	35996	233.2	46.4	36527
	DG 223 D	356	19.3	32548	96.8	28.1	32635	236.1	54.8	33057
	DG 224 A	146.8	35.3	72063	318.1	54.4	72304	53.9	4.1	72351
	DG 224 B	302.1	14.5	46112	43.3	36.8	46373	194.5	49.5	46483
	DG 225 A	266.2	10.2	66740	357	4.6	67744	110.8	78.8	68587
	DG 225 B	251.4	7.7	70977	341.8	3.2	71904	94.4	81.7	72873
	DG 225 C	262.5	8.7	59917	354.1	10.3	60835	133.2	76.4	61929
	DG 225 D	268.3	11.3	61278	359.3	5	62101	112.8	77.6	63084

** AMS intensity in μ SI units*

Subarea	Sample#	k_{min}			k_{int}			k_{max}		
		dec.	inc.	int.	dec.	inc.	int.	dec.	inc.	int.
	DG 226 A	266.2	22.7	42994	5.5	21.1	43179	134	58.1	44195
	DG 226 B	301.7	35.3	44680	37.2	7.8	44864	137.9	53.6	46291
	DG 226 C	285.6	26.3	50047	184.4	21.5	50090	60.3	54.9	50331
	DG 226 D	157.5	15.8	49595	258.7	34.4	49685	47	51.2	49900
	DG 227 C	171.4	18.9	49711	275.3	35	49776	58.3	48.8	50028
	DG 227 D	290.2	21.2	51545	185.8	32.7	51695	47.2	49.5	51837
	DG 228 A	88.8	7.3	7421.4	193.8	63.7	7460.3	355.4	25.1	7474.8
	DG 228 B	267.4	24.8	5868.4	136.4	54.8	5899.2	8.9	23.3	5921
	DG 228 C	262.5	14	8282.1	166.7	22.1	8314.7	22.4	63.4	8348.8
	DG 229 A	136.5	59.5	37872	297.1	29.1	38263	31.9	8.5	38346
	DG 230 A	332.9	0.6	10605	63	11.3	10722	240	78.7	10843
	DG 230 B	122.9	2.8	10664	32.5	9	10726	230.1	80.6	10857
	DG 230 C	146.5	5.1	9802.7	56.3	2.5	9875.7	299.9	84.3	9961.1
	DG 230 D	311.2	5.3	12698	42.5	13.3	12853	200	75.7	12967
	DG 346 A	85.5	3.4	56331	343.2	74.3	56406	176.5	15.3	56977
	DG 346 B	266	11	61806	34.9	72.8	61935	173.4	13	62375
	DG 346 C	54.1	40.6	59459	256.6	47.1	59697	154.1	11.4	60148
	DG 346 D	66.8	9.5	61803	251.9	80.4	61854	156.9	0.8	62508
	DG 346 E	53.4	54	59099	249.7	34.9	59200	154.2	7.8	59728
	DG 346 F	238.2	3.7	61614	4.9	83.8	61707	147.9	4.9	62445
	DG 347 A	273.8	1.2	13521	7.2	70.8	13615	183.4	19.1	13694
	DG 347 B	102.7	7.1	12990	4.8	47.7	13123	199	41.4	13181
	DG 348 A	264	24.6	46059	3.6	20	46183	128.2	57.4	46259
	DG 348 B	9.6	80.7	49619	172.3	8.9	49841	262.7	2.7	50116
	DG 348 C	331.2	26.1	48863	187.1	58.9	49283	69.2	15.8	49506
	DG 348 D	147.4	4.9	45484	274.5	81.8	45552	56.9	6.5	45709
	DG 349 A	151.7	30	36070	58.1	6.1	36350	317.7	59.3	36499
	DG 349 B	184.2	40.8	38860	89.8	5.1	39111	354	48.7	39166
	DG 350 A	352.9	69	14795	163.5	20.7	14824	254.6	3.1	14917
	DG 350 B	149.1	75	19059	335.4	14.9	19105	244.9	1.6	19439
	DG 350 D	351.9	34.5	15944	149.7	53.4	16054	254.4	10.7	16210
	DG 351 A	174.6	35.3	36407	298.7	38.4	36725	58.4	32	36993
	DG 351 B	168.3	32.4	35330	284.2	34.6	35604	47.8	38.7	35913
	DG 352 A	134.7	28.9	15197	242.2	28.6	15335	8.2	47.1	15357
	DG 352 B	117.8	34.3	17499	210.1	3.3	17633	304.8	55.5	17670
	DG 353 3	285.5	35.5	40308	192.8	3.8	41007	97.6	54.3	41254
	DG 353 3	99.4	71.4	57706	349.1	6.6	58174	257	17.3	58905
	DG 353 3	137.9	58.1	59604	328.1	31.5	60149	235.3	4.6	60663

** AMS intensity in μ SI units*

Subarea	Sample#	k_{min}			k_{int}			k_{max}		
		dec.	inc.	int.	dec.	inc.	int.	dec.	inc.	int.
	DG 353 3	280.3	15.8	40405	60.6	69.9	41826	186.8	12.2	42103
	DG 353 3	172.7	73	19369	33	13.1	19565	300.5	10.6	19581
	DG 353 3	85.4	68.5	61408	315.9	14.1	61985	221.8	16	62203
	DG 353 A	277.2	38.1	52672	32.3	28.4	53391	148.1	38.8	53554
	DG 353 B	292.6	39.2	54293	202.6	0.1	54954	112.5	50.8	55074
	DG 353 C	296.4	37.6	46807	197	11.9	47350	92.5	49.8	47528
	DG 355 A	86.7	34.8	32793	308.5	47	32850	193	21.9	33264
E										
	DG 108 A	81.8	36.7	28365	198.4	31	29006	316.3	37.9	29097
	DG 108 B	81.5	42.6	24985	181.7	10.9	25289	283	45.3	25380
	DG 108 C	84.9	47.4	25277	176.6	1.5	25795	268	42.5	25913
	DG 108 D	81.9	36.8	28384	347.2	6.2	29060	249	52.5	29158
	DG 109 A	226.6	10.8	43850	347.3	69.5	44234	133.2	17.2	44838
	DG 109 B	306	15.5	18417	203.6	37.8	18782	53.9	48.1	19074
	DG 109 B	232.4	11.4	44365	340.8	57.5	44794	135.8	30	45503
	DG 110 A	19	31.3	35585	286.9	3.6	35984	191	58.5	36125
	DG 110 B	33.1	19.9	43106	287.6	36.5	43674	145.8	46.7	43869
	DG 110 C	29.9	29.2	37671	285.7	23.6	37912	163.2	50.8	38203
	DG 110 D	6.8	32.3	32176	261.6	22.6	32396	143.2	48.9	32648
	DG 135 A	86.1	0.1	1001.8	356.1	41.2	1008.5	176.3	48.8	1011.2
	DG 135 B	266.3	39.2	39272	41.2	40.9	39366	154.5	24.5	39742
	DG 164 A	354.5	8.5	37496	87	16.6	37685	238.4	71.2	38329
	DG 165 A	258.2	40.8	34334	115.8	42.6	35513	6.4	19.9	35843
	DG 166 A	324.9	2.3	16215	55.7	19.5	16252	228.5	70.4	16384
	DG 166 B	336.3	10.4	17441	68.7	12.8	17553	208.3	73.4	17682
	DG 167 A	177.4	4.9	61169	85.4	21.9	61442	279.3	67.5	61874
	DG 167 B	183.1	1.5	58187	92.1	34.7	58576	275.3	55.3	58853
	DG 167 C	191.3	25.9	63024	13.1	64.1	63284	281.7	0.7	63530
	DG 168 A	101	26.3	61108	192.6	3.2	61561	289.1	63.5	62093
	DG 168 B	103.3	27.6	62602	195.1	3.4	62902	291.6	62.2	63537
	DG 168 C	112.2	25	63600	202.3	0.3	63889	293	65	64534
	DG 168 D	107.5	26	61146	199.1	3.4	61486	296	63.8	62161
	DG 169 A	354.2	37.1	4742.3	187	52.2	4897.7	88.9	6.2	4968.6
	DG 169 B	358.7	40.4	3100.4	206.2	46.2	3181.2	101.1	14.1	3205.6
	DG 170 A	83.7	19.8	52781	348.2	15	53157	223.6	64.8	53743
	DG 170 B	94.6	21.5	59201	1.6	7.7	59694	252.9	67	60276
	DG 170 C	102.2	21.2	58861	8.9	8.5	59338	258.2	67	59891
	DG 173 A	131.8	37.2	591.4	358.2	42.3	596.4	242.8	25.3	597.3

** AMS intensity in μ SI units*

Subarea	Sample#	k_{min}			k_{int}			k_{max}		
		dec.	inc.	int.	dec.	inc.	int.	dec.	inc.	int.
	DG 174 A	116.1	33.2	18812	243.3	42.7	18924	4.6	29.3	19196
	DG 174 B	132.9	36.7	22121	245.2	26.9	22223	1.8	41.4	22641
	DG 174 C	150.1	48	18125	258.6	15.9	18320	1.3	37.6	18648
	DG 174 D	148.8	48.9	19783	253.9	12.8	19942	354.2	38.2	20304
	DG 178 A	46.1	19.1	40688	151.6	37.7	40951	295.1	46.1	41143
	DG 178 B	40.2	11.9	43820	144.2	48.8	44083	300.4	38.7	44205
	DG 178 C	21.9	4.4	47448	113.5	19.9	47620	279.9	69.6	47878
	DG 179 A	86	19.6	4365	207.4	55.6	4382.5	345.6	27	4466.8
	DG 179 B	80.4	5.8	3046.8	209.2	80.8	3076.2	349.7	7.1	3132.7
	DG 179 D	85.8	16.3	3726.6	226.6	69.3	3775.4	352.2	12.4	3847.5
	DG 180 A	213.2	41.4	60705	86.6	34.1	60825	333.7	29.9	62387
	DG 180 B	49	8.4	64445	151.6	55.9	65626	313.5	32.8	66454
	DG 180 C	60.7	13	57431	172	57.5	57882	323.2	29.2	58874
	DG 180 D	75.8	36.5	57647	207.3	41.9	58031	324.1	26.6	59277
	DG 180 E	79.1	30.3	63770	203.8	44.3	63891	328.9	30.5	65420
	DG 181 A	344.3	20.4	28787	94.7	43.2	29230	236.2	39.8	29402
	DG 181 B	341.4	16.4	35336	160.4	73.6	36012	251.3	0.2	36138
	DG 181 C	346.3	21.6	37431	214	59.5	38332	84.8	20.5	38600
	DG 231 A	305.6	4.3	20258	37.5	23.5	20401	205.9	66	20817
	DG 231 A	307.5	1.2	22700	37.8	12.2	22893	211.9	77.8	23262
	DG 231 B	302.9	4.6	17956	34.2	16.7	18116	198.1	72.6	18473
	DG 232 A	39.7	12.4	53762	282.7	64.2	53998	134.9	22.3	54544
	DG 232 B	37	14.3	54038	278.2	62.2	54506	133.4	23.3	55075
	DG 233 A	281.3	57.9	27068	147	23.7	27204	47.6	20.4	27315
	DG 233 B	235.4	14.7	30643	140.6	17.5	30892	3.2	66.8	31139
	DG 233 C	237.8	56.5	27783	31.6	30.7	28039	128.9	12.1	28069
	DG 234 A	299.2	28.1	6714.5	123.8	61.9	6790.8	30.2	1.9	6887.9
	DG 234 B	283.5	17.8	3968.8	191.7	5.4	4004.4	85.4	71.3	4017.6
	DG 234 C	283.2	11.2	4423.1	25.9	48.1	4466.2	183.7	39.7	4483.4
	DG 234 D	280.3	38.6	7048.2	83.3	50.2	7126.5	183.5	8.4	7203.2
	DG 235 A	83.5	35.4	23640	196.5	28.9	23683	315.2	41.1	23876
	DG 235 B	89.9	21.2	30990	194.5	33	31095	333.3	49.1	31140
	DG 235 C	291.7	1.5	25361	24.9	65.5	25436	201	24.5	25566
	DG 235 D	87.5	23	28167	348.9	19.3	28254	222.8	59.2	28336
	DG 235 E	77.8	23.4	28362	346.9	2.2	28581	251.7	66.5	28647
	DG 236 A	55.7	26.4	57603	214.6	62	59042	321.4	8.7	59079
	DG 236 B	47.8	32.8	48324	317.6	0.3	49787	227.2	57.2	50058
	DG 236 C	49.1	23	57659	187.7	60.5	58859	311.5	17.4	59168

** AMS intensity in μ SI units*

Subarea	Sample#	k_{min} dec.	k_{min} inc.	k_{min} int.	k_{int} dec.	k_{int} inc.	k_{int} int.	k_{max} dec.	k_{max} inc.	k_{max} int.
	DG 237 A	286.4	2.1	27918	193.6	53.3	27996	18	36.6	28048
	DG 238 A	62.5	7.9	45879	153.2	4.9	47125	274.6	80.6	47746
	DG 238 B	51.3	8	48895	320.9	2.8	49899	211.9	81.5	50231
	DG 238 C	48.1	12.6	44353	141.1	13.2	45418	276.1	71.6	45901
	DG 239 A	242.1	0	79916	332.9	86.2	82465	152	3.8	83139
	DG 239 B	78	20.1	78230	276.9	68.9	80841	170.3	6.3	81220
	DG 240 A	235.6	19.2	3527.5	326.5	2.5	3570	63.6	70.6	3607.8
	DG 240 B	256.7	3	11924	164.7	32.9	12052	351.4	56.9	12101
	DG 240 C	79.1	9.4	8732.5	341.2	39.5	8815.6	180	48.9	8840.7
	DG 240 D	280.3	3.4	8384.1	188.6	26	8487.3	17.1	63.7	8536
	DG 241 A	174.1	14.6	1343.6	61.4	56.1	1347.3	272.7	29.9	1355
	DG 241 B	105.6	21.5	1528.5	310.3	66.5	1530.2	199.1	8.9	1541.6
	DG 241 C	165	29.9	1582.6	49.7	36.7	1592.3	282.7	39	1597.8
	DG 241 D	93.3	40.9	2061.7	296.7	46.6	2075	193.8	11.9	2096.4
	DG 244 A	280.1	62.3	17383	122.9	25.8	17635	28.3	9.3	17861
	DG 244 B	276.8	41.7	24040	135.5	41.2	24157	26.3	20.6	24587
	DG 244 B	124.5	25.8	20099	279.1	61.9	20157	29.4	10.5	20657
	DG 244 C	253.7	65	21312	102.3	22.3	21439	7.8	10.8	21875
F										
	DG 096 A	280.4	15.2	24320	185.1	18.7	24670	47	65.5	24948
	DG 096 B	300.5	18.8	23425	202.7	21.9	23740	67.4	60.5	24031
	DG 096 C	286.5	22	19617	184.4	27.3	19919	49.9	53.6	20164
	DG 097 A	87.7	2.3	55302	178.4	15	56047	349.2	74.8	56126
	DG 097 B	259.2	8.9	52013	162	39	52563	359.8	49.6	52951
	DG 097 C	81.6	4.6	48696	342.3	63.5	49084	173.9	26	49324
	DG 114 A	204.1	50.5	102950	87.2	20.5	103240	343.7	32.1	103570
	DG 114 B	214.5	39.2	106410	113.2	13.5	106550	7.9	47.6	107070
	DG 114 C	239.1	21.3	100460	141.3	19	100600	13.3	60.8	101210
	DG 114 D	175.7	42.1	105030	76.6	9.9	105220	336.1	46.1	105620
	DG 115 A	99.5	7.6	116120	330.6	78.1	116350	190.7	9.2	116531
	DG 115 B	280.6	11.3	111960	186.2	21.1	112624	37.1	65.8	112770
	DG 115 C	108.8	2.6	110050	199.3	9.9	110500	4.4	79.8	111040
	DG 115 D	106.2	9.1	123430	200.5	24.8	123570	357.6	63.3	123920
	DG 116 A	21.1	74	72242	137.4	7.2	72595	229.3	14.2	73286
	DG 116 B	136.3	32.4	67237	10.9	42.4	67431	248.3	30.5	68129
	DG 116 C	101.5	37.8	77566	344.8	30.1	77859	228.2	37.6	78290
	DG 116 D	127.8	2.8	75531	30.9	67.7	75753	219	22.1	76636
	DG 117 A	334.4	52.6	113120	223.1	15.5	119720	122.7	33	122540

** AMS intensity in μ SI units*

Subarea	Sample#	k_{min}			k_{int}			k_{max}		
		dec.	inc.	int.	dec.	inc.	int.	dec.	inc.	int.
	DG 117 B	331.5	53.2	112460	225.2	11.9	118800	127	34.2	121400
	DG 117 C	318.3	52.7	111320	214	10.6	118050	116.4	35.3	120680
	DG 117 D	327	54.1	115840	216.8	14	122743	117.8	32.3	125150
	DG 118 A	298.5	55.3	14546	196.2	8.4	14747	100.6	33.3	14995
	DG 118 B	289.9	55.1	15510	186.3	9.3	15714	90.1	33.3	15984
	DG 119 A	272.7	80.1	12526	63.6	8.7	12583	154.3	4.8	12791
	DG 119 B	288.4	88.1	13022	64.9	1.4	13087	154.9	1.3	13256
	DS 12 A	325.3	6.4	61226	232.6	23.1	62157	69.9	65.9	62636
	DS 12 B	150.5	1.7	56494	241.2	21.3	57477	56.1	68.6	57767
	DS 12 C	341.9	0.9	56390	250.8	51.8	57177	72.6	38.2	57723
	DS 12 D	167.3	5.5	55882	271.2	68.2	56495	75.2	21	56763
	DG 120 A	299	39.6	44887	192.9	18.5	46630	83.7	44.5	47634
	DG 120 B	290.2	41.2	55038	185.1	16.6	57675	78.3	44.1	58830
	DG 120 C	296	39.7	28021	178.7	28.8	28949	64.4	36.8	29364
	DG 121 A	103.9	0.5	103610	194.6	54.7	104380	13.6	35.3	104950
	DG 121 B	245.8	2.4	87189	154.2	35.1	87621	339.2	54.8	88396
	DG 121 C	86.5	1.8	86552	177.8	36.6	86887	354.1	53.3	87525
	DS 13 A	324	2.7	62546	232.5	30.5	63680	58.5	59.4	64407
	DS 13 B	340.5	8.6	66727	245.2	31.7	68184	83.9	56.9	68813
	DS 13 C	340.5	5.4	66928	245	45.6	68449	75.7	43.9	68893
	DS 13 D	323.7	13.1	62136	220.9	43.7	63246	66.3	43.4	64101
	DS 14 A	253.4	32.3	27436	349.4	9.5	27898	93.7	56	27959
	DS 14 B	254.6	26.9	25907	150.4	25.7	26316	23.7	51.2	26347
	DS 15 A	254.6	16	49153	73.1	74	49638	164.5	0.4	50202
	DS 15 B	249.9	18.8	52747	77.1	71.1	53313	340.7	2.2	53777
	DS 16 A	272.8	8.3	58210	178.9	25.2	58510	19.7	63.3	58833
	DS 16 B	264.7	11.5	56715	167.7	30.9	57041	12.6	56.5	57464
	DS 16 C	288.4	20.2	60784	196.9	4.3	61191	95.4	69.3	61382
	DS 16 D	289.8	20.2	58719	190.8	23	59045	56.8	58.6	59485
	DS 17 A	152.5	1.9	63029	244.2	42.1	64402	60.4	47.8	65141
	DS 18 A	157.7	5.4	64469	255.6	55.8	65483	64.1	33.7	66060
	DS 18 B	166.1	8.5	63289	266.3	49.9	64588	69.2	38.8	65118
	DS 19 A	259.2	22.4	22260	17.4	48.9	22462	154	32.4	22544
	DS 19 B	204.7	7.2	25662	297.2	19.1	25884	95	69.4	26035
	DS 19 C	240	21.2	20508	347.2	37.3	20707	127.1	45.1	20744
	DS 19 D	340.4	12.5	22345	244	26.6	22397	93.2	60.2	22528
	DS 20 A	282.8	15.6	22020	20.5	25.5	22146	164.5	59.5	22270
	DS 20 B	272.5	11.2	22730	11.4	38.1	22873	169	49.7	23024

** AMS intensity in μ SI units*

Subarea	Sample#	k_{min}			k_{int}			k_{max}		
		dec.	inc.	int.	dec.	inc.	int.	dec.	inc.	int.
	DS 21 A	178.5	16	46965	298.8	60.4	47161	81.1	24.2	47490
	DS 21 B	235.2	65.2	38476	331.6	3	38628	63	24.6	38840
	DS 21 C	335.6	15.7	46772	226.1	49.9	46912	77.3	35.8	47203
	DS 21 D	322.1	7.2	37891	224.1	47.6	37950	58.5	41.5	38221
	DS 22 A	339.7	18.6	41009	217.4	57.8	41139	78.8	25.3	41428
	DS 22 B	314.6	57	36598	182.4	23.6	36743	82.4	21.7	36982
	DS 22 C	174.3	8.9	40568	285.7	66.7	40640	80.8	21.4	40936
	DS 22 D	336	17.7	37944	231.3	38.3	38121	85.5	46.3	38316
	DS 23 A	186.1	12.5	31599	291.3	49.7	31666	86.3	37.5	31908
	DS 23 B	347.5	14.4	32657	237	53.8	32705	86.8	32.5	32919
	DS 23 C	329	19.8	27339	224.3	35.2	27467	82.5	48	27683
	DS 23 D	284.5	52.5	28101	179.9	11	28183	82.1	35.4	28476
	DS 32 A	256.3	6.3	40227	120.8	81.2	40840	347	6.1	41243
	DS 32 B	325.2	42.3	48221	202.1	31	48449	89.9	32.1	48955
	DS 32 C	350.6	26.7	45786	219.9	52.4	45934	93.8	24.4	46525
	DS 32 D	258.5	15.5	40810	76.7	74.5	41328	168.4	0.5	41686
	DS 32 E	359.2	23.4	52531	226.4	57.5	52716	98.8	21.2	53161
	DS 33 A	309.3	29.4	46689	53.2	23.1	47123	175	51.1	47397
	DS 33 B	310.8	19.8	49148	127.4	70.2	49447	220.4	1.1	49834
	DS 33 C	308.7	27.1	46180	129.3	62.9	46622	38.8	0.2	46816
	DS 33 D	300.2	27.7	48972	73.8	52.7	49402	197.4	22.9	49699
	DS 33 E	286.2	12.7	49123	41	61.7	49674	190.2	24.9	49948
	DS 35 A	283.4	70.4	42118	85	18.7	42231	177	5.8	42822
	DS 35 B	272.1	39.5	40952	77.1	49.5	41032	175.9	7.5	41669
	DS 35 C	266.3	5.8	40171	48.3	82.6	40425	175.8	4.5	40845
	DS 35 D	280.7	8.4	40456	52.8	77.6	40587	189.3	9.1	40985
	DS 36 A	259.6	29.2	39562	120.6	53.5	39926	1.3	19.9	40407
	DS 36 B	267.2	10.5	42082	154.3	64.6	42575	1.7	22.9	42991
	DS 36 C	95.3	2.5	39339	201.4	81.2	39669	4.9	8.5	40083
	DS 37 A	258.8	36.6	38813	135.5	36.5	39112	17.2	32.6	39279
	DS 37 B	259.6	42.5	37603	133.3	32.9	37815	21.5	29.9	37988
	DS 38 A	231	49.7	37671	124.6	13.5	37723	24.1	37.1	37915
	DS 38 B	204.8	46.4	35439	114.7	0.1	35540	24.6	43.6	35772
	DS 38 C	226.6	36.4	38414	127.8	11.7	38485	22.9	51.2	38700
	DS 39 A	253.2	31.6	33702	153.3	15.7	33929	40.6	53.8	33965
	DS 39 B	238.9	20.7	35527	147.8	2.9	35778	50.2	69.1	35859
	DS 39 C	252.6	48.4	39576	155.3	6.4	39687	59.7	40.9	39733
	DS 39 D	220.1	55.7	37348	117.2	8.7	37511	21.5	32.9	37651

** AMS intensity in μ SI units*

Subarea	Sample#	k_{min}			k_{int}			k_{max}		
		dec.	inc.	int.	dec.	inc.	int.	dec.	inc.	int.
	DS 40 A	84.4	21.8	14538	177	6.5	14602	282.6	67.2	14724
	DS 41 B	86.8	4.3	34290	181.6	47.9	34612	352.9	41.7	34848
	DS 41 C	100.1	31.3	31869	220.5	39.7	32018	345.3	34.6	32224
	DS 41 D	146.4	20.3	33279	238.6	5.8	33407	343.9	68.8	33611
	DS 42 A	305.5	23.6	53437	45.5	21.5	53678	173	57.1	54404
	DS 42 B	258	36.5	54300	4	20.4	54635	117	46.4	54849
	DS 42 C	256.1	42	54194	158.7	8.2	54950	59.9	46.8	55042
	DS 42 D	256.2	44.1	53388	146.7	19	54149	40	39.8	54277
	DS 42 E	256.5	43.2	53156	154.2	12.8	53788	51.5	44	54043
	DS 43 A	251.8	22.4	52027	16.1	53.7	52525	149.8	26.9	52658
	DS 43 B	277	36.2	54390	45.4	40.3	54710	163.2	28.8	54916
	DS 43 C	266.9	23.8	56448	58.7	63.4	56735	171.9	11.2	57260
I1										
	DG 361 A	119.8	47.3	36137	273.5	39.6	36719	14.9	13.4	37023
	DG 361 B	112.7	45.8	35654	273.5	42.6	36042	12.6	9.7	36566
	DG 362 A	120.2	31.6	23058	292.7	58.2	23496	28.1	3.3	23972
	DG 362 B	140.2	31.2	23231	291.5	55.4	23743	41.9	13.5	24174
	DG 363 B	265.8	43.4	1038.1	168.8	7.4	1043.4	71.1	45.7	1047.6
	DG 364 A	152.4	75.2	29239	321.7	14.6	29403	52.4	2.6	29445
I2										
	DG 033 A	170.2	30.2	22961	42.8	46.3	23195	278.4	28.4	23429
	DG 035 A	172.2	16.8	65120	265.9	12	66016	29.9	69.2	66559
	DG 035 B	177.4	17.7	67644	270.3	9	68781	26	70	69222
	DG 036 A	188.9	11.5	41150	96.3	12.2	41519	320.8	73.1	41607
	DG 036 B	202.6	4.4	43639	112.4	3.1	43984	347.5	84.6	44193
	DG 036 C	207	12.1	43044	108.4	35.2	43390	313.1	52.2	43470
	DG 036 D	197.5	3	40111	106.5	19.2	40509	296	70.5	40631
	DG 037 A	4.1	15.4	103020	254.6	50.5	106410	105.4	35.3	106440
	DG 055 A	342.6	7.4	39016	242.2	54.3	39322	77.7	34.7	39845
	DG 055 B	169.3	6.4	41047	268.7	55.4	41228	75	33.8	41814
	DG 056 A	181	12.1	28464	70.2	58.8	28716	277.7	28.3	29067
	DG 056 B	229	53.9	12062	346	18.2	12096	86.9	29.9	12183
	DG 056 C	181	7.3	39927	80	56.3	40181	275.7	32.7	40543
	DG 057 A	225	15.5	46926	131.7	11.9	47507	5.6	70.3	47997
	DG 057 B	223.8	22.4	47393	127	16.1	47983	4.3	61.9	48315
	DG 057 C	217.8	25.4	46940	124.9	6.1	47584	22.4	63.8	47719
	DG 057 D	217.3	22.9	49456	120.6	15.4	50147	359.5	61.9	50385

** AMS intensity in μ SI units*

Subarea	Sample#	k_{min}			k_{int}			k_{max}		
		dec.	inc.	int.	dec.	inc.	int.	dec.	inc.	int.
	DG 058 A	245.8	55.7	100760	351.6	10.5	102260	88.3	32.3	105054
	DG 058 B	268	58.4	99446	6.6	5.3	100970	99.7	31.1	103630
	DG 058 C	273.6	59.8	106740	6.2	1.5	108090	97.1	30.2	111170
	DG 058 D	276.7	62.6	103080	185.3	0.7	104430	94.9	27.4	107270
	DG 298 A	57	52.7	7419.4	263.1	34.3	7506.1	164.3	12.7	7620.5
	DG 298 B	268	13.5	968.2	27	63.7	979.7	172.4	22.1	985
	DG 299 A	173.1	74	35780	311.1	12	35851	43.3	10.4	36116
	DG 300 A	186.8	4.1	46409	87.8	65.5	46452	278.6	24.1	47521
	DG 300 B	169.2	43.2	42930	41.3	33.2	43048	290.2	28.8	43738
	DG 300 C	187	9.5	49934	79.8	60.6	50252	282	27.6	51091
	DG 303 A	189.3	14.8	86696	24	74.8	89557	280.3	3.7	89854
	DG 303 B	174.9	14.8	89927	320	72.1	92996	82.3	9.8	93899
	DG 303 C	188.4	11.2	83158	335.5	76.7	85426	97	7	86277
	DG 367 A	319.6	52.1	18378	95	29	18634	198	22.1	18771
	DG 367 B	329.3	56.3	19297	127.3	31.7	19543	223.7	10.2	19637
	DG 367 C	316.3	42	18266	98.2	41.1	18479	207	20.2	18563
	DG 368 A	321	41.6	30521	108.2	43.5	30934	215.2	17.1	31218
	DG 368 B	331.9	46.7	30851	111.4	35.7	31228	217.6	21.2	31667
	DG 396 A	56	1.4	99046	326	2.4	99326	175.2	87.2	100463
	DG 396 B	66.2	0.7	95037	336	15.7	95463	158.6	74.3	96359
	DG 397 A	278.1	32.5	83637	17.3	14.1	85278	127.3	53.8	86172
	DG 397 B	277.3	34.2	79200	18.6	16.1	80058	129.7	51.2	81420
	DG 398 A	65.1	47.2	39617	172.6	15.6	39831	275.5	38.7	40395
	DG 398 B	49.6	45.2	39776	163.5	21.9	39971	271	36.7	40523
	DG 398 C	63.1	30.2	46283	160.8	12.9	46517	271.1	56.6	47065
	DG 398 D	40.8	30.7	29279	147.9	26.4	29385	270.6	47.4	29828
	DG 399 A	164.3	5.6	74713	68.7	44.9	75387	259.9	44.6	76212
	DG 400 A	44.8	40.7	14473	204.7	47.5	14550	306	10.1	14676
	DG 400 B	224.1	2	19259	132.4	40.2	19399	316.5	49.7	19561
	DG 400 C	56	5.3	27158	149.9	36.4	27250	318.9	53.1	27625
	DG 400 D	108.7	51	21297	209.9	9	21332	306.9	37.5	21600
	DG 401 A	352.4	10.1	62824	260.2	12.1	64317	121.2	74.2	65299
	DG 401 B	351	21	55425	258.2	7	56396	150.7	67.7	57588
	DG 401 C	0.7	16	68519	267.4	11.5	70689	143.1	70.1	71154
I3										
	DG 042 A	350	29.2	38567	144.4	58.2	41266	253.5	11.5	42803
	DG 042 B	345.4	39.4	51833	84.8	11.2	57249	187.7	48.4	58203
	DG 043 A	52.2	27.8	39269	320.3	3.6	40216	223.5	62	40958

** AMS intensity in μ SI units*

Subarea	Sample#	k_{min}			k_{int}			k_{max}		
		dec.	inc.	int.	dec.	inc.	int.	dec.	inc.	int.
	DG 043 B	45.6	27.3	30728	309.3	12	31292	198	59.8	31547
	DG 043 C	46.2	26.4	37907	314.9	2.7	38670	219.5	63.4	39278
	DG 050 A	230.9	34.8	23045	42.6	54.9	23533	138.2	3.9	23551
	DG 050 B	237.2	33.6	36188	33.9	54.1	36919	139.7	11.1	37220
	DG 051 A	139	1.8	13724	230.7	42.6	13771	47.1	47.3	13828
	DG 051 B	296.4	36.7	14795	175.2	34.8	14834	56.9	34.3	14906
	DG 051 C	277.9	37.2	15458	170.4	21.6	15536	57.1	45	15648
	DG 052 A	278	43.8	20612	87	45.7	20698	182.7	5.5	20735
	DG 052 B	272.6	29.2	27867	39.4	47	28214	164.9	28.5	28284
	DG 053 A	94.3	51.4	68286	322.4	28.1	68337	218.6	24.2	68543
	DG 053 A	312	82.5	48066	87.3	5.3	48234	177.8	5.2	48687
	DG 053 B	282.9	53.4	49733	59.7	28.4	50016	161.7	21	50620
	DG 053 C	213.6	52.7	24358	80.3	27.6	24686	337.5	23	24726
	DG 053 C	259.3	28.4	45685	32.8	51.9	45871	156	23.2	46528
	DG 053 D	284.9	42.3	47596	61.6	38.6	47813	171.7	23.4	48483
	DG 054 B	11.4	87.9	63876	128	0.9	64777	218	1.9	64916
	DG 073 A	274.3	44.2	87815	27.9	22.5	88785	136.4	37.4	89399
	DG 073 B	278	52.3	80219	48.2	26.6	81310	151.5	24.7	81918
	DG 074 A	234.2	26.9	14814	140.2	7.8	14959	35.5	61.8	15264
	DG 074 B	11.9	45.5	27230	261.2	19.2	27422	155.2	38.3	28095
	DG 074 B	260	22	13560	166	9.8	13689	53.4	65.7	13837
	DG 075 A	127.8	18.5	40278	36.8	3.1	41773	297.7	71.2	42165
	DG 075 B	190.4	17.9	30637	94.3	18.1	30826	321.9	64.1	30893
	DG 075 C	131.1	13.5	39641	39.8	5.3	41011	288.8	75.5	41198
	DG 075 D	193.3	12.3	30276	283.9	3	30489	27.5	77.3	30560
	DG 076 A	231.6	55.8	14762	119.4	14.4	14931	20.8	30.3	15076
	DG 076 B	241.4	24.3	23098	124.8	44.7	23235	350.1	35.4	23450
	DG 081 A	321.2	18.8	74547	206.5	50.8	74849	63.9	32.9	75726
	DG 081 B	314.4	49.4	66612	179	31.4	67187	74	23	67612
	DG 081 C	339.4	23.8	77954	177.2	65.1	79168	72.4	6.7	80014
	DG 082 A	66.7	39.4	1116.2	330.2	7.9	1137.7	230.9	49.5	1144.2
	DG 082 B	69.1	29.8	1079.1	336.1	5.2	1091.3	237.2	59.7	1106.6
	DG 082 C	61.2	38.4	1158	156.3	6.5	1174.4	254.3	50.9	1180
	DG 083 A	290	80.8	29077	173.4	4.2	29157	82.8	8.2	29515
	DG 083 B	105.6	64	15301	346.1	13.5	15335	250.6	21.7	15471
	DG 083 C	183.5	57.6	16899	352.3	31.9	16940	85.5	5.1	17124
	DG 084 A	249	42.5	43272	2.3	23.4	43979	112.4	38.4	44025
	DG 084 B	245.2	38.8	41370	335.3	0.1	41987	65.4	51.2	42055

AMS intensity in μ SI units

Subarea	Sample#	k_{min}			k_{int}			k_{max}		
		dec.	inc.	int.	dec.	inc.	int.	dec.	inc.	int.
	DG 084 C	244.8	42	41215	4.2	28.6	41791	116.4	34.7	41900
	DG 085 A	140.2	58.1	814.5	270.2	21.9	818	9.6	22.1	822.5
	DG 085 B	166.9	64.5	787	285.2	12.7	791.7	20.3	21.7	794.9
I4										
	DG 016 A	344.3	39.6	48841	89.6	17.7	49283	198.2	45.1	49723
	DG 017 A	124.7	5.8	37522	230	69.1	37587	32.6	20	38186
	DG 018 A	276.2	29.3	38338	60.3	55.3	39924	176.4	16.9	40204
	DG 018 B	277.8	31	42028	138.5	51.6	43457	20.7	20.3	43921
	DG 018 C	286	31.5	35883	57.5	47.2	37154	178.8	25.7	37573
	DG 018 D	273.8	29.6	30106	47.2	50.4	31189	169.3	23.8	31537
	DG 019 A	36.9	14.3	17737	130.1	12.5	17874	259.8	70.8	17925
	DG 019 B	34.7	13.1	16642	138.1	44.8	16776	292.4	42.3	16897
	DG 020 A	77	72	17249	256.4	18	17452	346.5	0.2	17544
	DG 020 B	102.7	72.8	33351	248	14.3	33549	340.5	9.4	33846
	DG 021 A	272.5	54.9	32830	85	34.9	33111	177.5	3.5	33955
	DG 022 A	356.1	16.9	34262	90.7	14.8	34621	219.8	67.2	35097
	DG 022 B	351.5	23.9	28643	89.3	17	28899	211.3	60.1	29522
	DG 023 A	274.8	8.1	48263	179.8	31.2	51784	17.6	57.6	53185
	DG 024 A	175.6	72.8	622	356.6	17.2	624.4	266.5	0.3	629
	DG 024 B	286.1	26.4	592.6	77.1	60.4	594	189.9	12.4	595.6
	DG 025 A	68.9	23.1	3144.8	283.5	62.6	3163.4	165	13.9	3169.8
	DG 025 B	74.5	23.8	2955.8	275.7	64.7	2973.1	168.1	8.1	2996.7
	DG 025 C	71.5	21.4	3612.3	219.7	65.2	3640.6	336.8	11.9	3669.8
	DG 025 D	84.6	45.1	3854.2	232	40.1	3881.3	336.9	16.9	3897.8
	DG 026 A	15	49.7	1937.3	112.1	6	1966	207.1	39.7	1968.3
	DG 027 A	67.1	21.9	50372	334.9	5.3	52031	231.9	67.4	53614
	DG 027 B	41.5	26.7	56355	138.6	13.7	57800	253	59.5	59631
	DG 044 A	43.7	26.2	1527.4	282.4	46.5	1561.4	151.5	31.9	1570.8
	DG 044 B	49.7	24.1	2658	295	43.1	2737.1	159.6	37.3	2768.3
	DG 044 C	47.1	31	4101.9	287.1	39.8	4214.9	161.8	34.8	4293.1
	DG 045 A	290.4	9.9	48681	23.4	17	49425	171.4	70.2	49853
	DG 045 B	272.8	4.8	51283	6.3	35.9	51719	176.2	53.7	51975
	DG 045 C	274.5	6	51285	6.4	17.6	51797	166.2	71.3	52240
	DG 045 D	286	13	44216	22.2	24.9	44807	170.8	61.5	45089
	DG 046 A	239.5	32.9	23843	115.4	40.9	24198	353.1	31.7	24549
	DG 046 B	236.7	39.7	28523	115.1	32.3	29027	0.3	33.7	29445
	DG 046 C	242.2	42.6	28539	109.6	36.4	28918	358.6	25.9	29252
	DG 047 A	287.8	41.8	1121.2	43.9	26.2	1127.6	155.6	36.9	1134.5

** AMS intensity in μ SI units*

Subarea	Sample#	k_{min} dec.	k_{min} inc.	k_{min} int.	k_{int} dec.	k_{int} inc.	k_{int} int.	k_{max} dec.	k_{max} inc.	k_{max} int.
	DG 047 B	250.6	27.2	14682	16	48.4	14841	144.2	28.7	15067
	DG 047 C	262.5	31.5	2198.6	37.8	49.2	2236.1	157.4	23.1	2258.5
	DG 047 D	247.4	21.7	15238	15.1	56.8	15382	147.4	23.7	15647
	DG 047 E	251.7	24.6	15329	16.3	51.2	15510	147.7	28	15751
	DG 048 A	322.3	69.5	777.3	198.3	11.8	781.2	104.8	16.5	784.6
	DG 048 B	311.4	86	807.1	143.8	3.9	814.6	53.8	0.9	819.6
	DG 048 C	199	83.2	798.1	61.6	5	804.5	331.2	4.6	809.9
	DG 048 D	151.3	60.1	858.8	342.2	29.5	859.5	249.5	4.7	862.9
	DG 049 A	66.4	38.2	2014	160.4	5.1	2021.4	256.8	51.3	2031
	DG 049 B	42.4	53.3	1189.2	284.8	19.1	1197.9	183.3	30.1	1202.6
	DG 049 C	82.2	65.2	1388.1	243.3	23.7	1392.3	336.5	7.2	1395.3
II1										
	DG 065 A	221.1	10.2	53622	94.3	73.2	53766	313.6	13.1	53881
	DG 065 B	208.8	0.6	59954	118.6	12.1	60072	301.5	77.9	60149
	DG 065 C	49.5	3.4	58224	140.1	9.6	58389	300.1	79.8	58471
	DG 065 D	58.9	28.5	58193	187.7	49.2	58343	313.1	26.6	58497
	DG 278 A	217.5	7.1	61620	123.4	30.2	61770	319.4	58.8	61958
	DG 278 B	174.6	80.7	66628	59.2	4	67253	328.6	8.4	67452
	DG 279 A	291	11.8	56612	195.4	25	57206	44.1	62	57378
	DG 279 B	289.9	19.9	55602	189.8	25.8	56094	53	56.5	56421
	DG 279 C	286.5	7.6	57262	192.3	28.6	57518	30	60.3	57687
	DG 280 A	247.1	38.4	64046	82	50.7	64447	342.9	7.4	64693
	DG 280 C	247.6	27.7	69307	110.1	54.6	69825	348.8	20.3	69945
	DG 280 C	193.9	6.9	32443	101.4	19.9	32802	302.1	68.9	32871
	DG 280 D	243.7	28.4	68721	85.7	59.8	69066	338.9	9.6	69437
	DG 281 A	329.3	55.9	56206	225.5	9.1	56699	129.7	32.5	56985
	DG 281 B	326	59.1	56224	212	13.7	56806	114.8	27.2	56976
	DG 281 C	328.9	56.6	55985	233	3.8	56376	140.5	33.1	56765
	DG 281 D	324.9	56.9	55230	222.1	8.2	55669	127	31.8	55962
	DG 282 A	309.7	35.7	118920	52	16.5	119870	162.3	49.6	120110
	DG 282 B	321.5	37.2	112210	231.4	0.1	112900	141.2	52.8	113320
	DG 282 C	320.8	37.3	124410	58.1	9.4	125240	159.9	51.1	125560
	DG 282 D	318	36.6	112700	223.9	5.5	113190	126.6	52.8	113430
	DG 283 A	280.2	23	59997	25.4	31.8	61568	160.9	49.1	62027
	DG 283 B	282.5	21.9	62001	26.6	31.3	63742	163.6	50.2	64213
	DG 283 C	278.7	23.8	61657	21	25.9	63811	152.1	53.5	63885
	DG 284 A	276.7	16.3	37968	103.6	73.6	38825	7.3	1.9	39096
	DG 284 B	276.1	23.8	37090	114.7	65	37690	9.3	7.1	38114

** AMS intensity in μ SI units*

Subarea	Sample#	k_{min}			k_{int}			k_{max}		
		dec.	inc.	int.	dec.	inc.	int.	dec.	inc.	int.
	DG 284 C	292.4	9.5	37186	175.6	69.7	37826	25.5	17.8	38363
	DG 285 A	257.3	8.3	92036	356.2	46.8	94651	159.7	42	94957
	DG 285 B	260.2	6.5	93331	357.6	48.4	95766	164.6	40.9	96033
	DG 286 A	292.4	3.6	40143	48	81.7	40857	201.9	7.4	41266
	DG 286 B	244.7	29.4	70470	82.1	59.5	70904	339	7.6	71125
	DG 286 C	124.6	0	42728	34.4	77.3	43442	214.6	12.7	43857
	DG 287 A	106.1	3.4	42601	13.6	36.4	43004	200.7	53.4	43781
	DG 287 B	113.2	0.5	41645	22.7	47	42167	203.7	43	42424
	DG 287 C	96.7	9.5	42175	0.7	31.9	42585	201.3	56.3	43388
	DG 288 A	178.6	14.3	24668	274.9	23.3	24733	59.8	62.2	24822
	DG 288 B	3.2	4.2	26501	95.8	32	26629	266.5	57.7	26696
	DG 288 D	3.6	4.1	33929	272.9	10.7	34238	114.5	78.5	34386
	DG 289 A	270.4	1.6	41384	175.1	73.6	42032	0.9	16.3	42352
	DG 289 B	88.7	2.4	49174	182.6	58.7	49728	357.3	31.1	50044
	DG 289 C	282.2	0.3	46217	191.8	53.7	46787	12.5	36.3	47028
	DG 357 B	276.6	15.9	43098	21.9	42.9	44593	171.3	42.8	44804
	DG 358 A	110.1	3	39656	18.2	32.6	40983	204.8	57.2	41258
	DG 358 B	293.6	0.1	45009	23.8	49.7	46559	203.6	40.3	46803
	DG 358 C	103.6	0.2	42406	13.2	62.1	43919	193.7	27.9	44117
	DG 358 D	111.8	2.4	38684	19.8	40.8	39867	204.6	49.1	40141
	DG 359 A	269.3	68	32835	167.6	4.7	33108	75.8	21.4	33361
	DG 359 B	213.3	66.1	25950	358.7	20	26135	93.4	12.5	26288
	DG 360 A	105.8	4.6	30812	201.8	52.7	31527	12.4	37	32327
	DG 360 B	96.2	3.8	31481	190.9	51	32227	3.2	38.7	32918
	DG 360 C	80.5	3	30135	174.3	51.9	31002	348.2	37.9	31771
	DG 360 D	82.6	2.2	32247	175.3	50.3	33174	350.8	39.6	33987
II2										
	DS 01 A	166.6	49.6	38954	263.5	5.8	39099	358.3	39.8	39201
	DS 01 B	303.7	43.9	30846	53.8	19.7	30975	161	39.6	31158
	DS 01 C	310.4	34.7	30127	48.7	11.7	30219	154.6	52.9	30469
	DS 01 D	153.5	49.7	39889	247.3	3.2	40075	340	40.1	40227
	DG 013 A	318.8	5	703.2	225.9	29.6	708.7	57.5	59.9	713.2
	DG 013 B	318.4	6	648.5	49.6	11.9	654.4	202.1	76.6	656.5
	DG 013 C	160.7	6.4	674.7	254.5	30.3	679.4	60	58.9	685
	DG 014 A	10.3	45.4	21215	227.4	38.2	21305	121.3	19.4	21326
	DG 014 B	343.5	1.9	23932	78.5	69.5	24019	252.8	20.4	24067
	DG 015 A	236.2	85.1	486.1	85.5	4.2	488.9	355.4	2.4	492
	DS 02 A	257.7	24.5	19204	144.5	40.8	19432	9.6	39.3	19719

AMS intensity in μ SI units

Subarea	Sample#	k_{min}			k_{int}			k_{max}		
		dec.	inc.	int.	dec.	inc.	int.	dec.	inc.	int.
	DS 02 B	255.8	14.3	24628	155.3	35.5	24951	4	50.9	25477
	DS 02 C	268.2	11.6	18859	166.5	44.5	19174	9.3	43.2	19416
	DS 02 D	258.1	21.8	28878	143.8	45.9	29215	5.1	36.1	29628
	DS 03 A	129.2	33.1	29913	18.1	28.9	30096	256.8	43.2	30242
	DS 03 B	127.1	36.8	26548	10.4	31	26751	252.6	37.8	26888
	DG 038 A	189.7	8.4	97457	279.9	1.3	103230	18.5	81.5	105260
	DG 038 B	188.2	7.4	106240	96.9	9.9	112240	314.2	77.6	114180
	DG 038 C	184.2	4.9	98794	93.2	10.8	104750	298.3	78.1	106110
	DG 038 D	180.2	7.8	90246	88	15.4	96434	296.1	72.6	97968
	DS 04 A	256.1	2.2	19730	150.1	82.1	19838	346.4	7.6	20047
	DS 04 B	262.5	11.4	18489	108.7	77.3	18602	353.6	5.4	18844
	DS 04 C	258.3	5.7	19401	146.9	74.6	19572	349.8	14.2	19725
	DS 05 A	137.7	64.4	45748	230.1	1.1	45858	320.6	25.6	46159
	DS 05 B	178.6	67.8	46366	58.9	11.4	46702	325	18.7	47241
	DG 059 A	235.3	27	881.1	122.6	37.2	885.4	351.5	40.9	904.1
	DG 059 B	276.5	33.2	865	15	12.6	872.5	122.8	53.9	887.5
	DG 059 C	287.4	37.9	783.5	25.6	10.4	790.4	128.3	50.2	798.7
	DG 059 D	277.3	28	833.3	14.3	12.9	848.5	126.5	58.7	856
	DS 06 A	96.4	37.5	28815	199.5	16.5	29037	308.6	47.8	29160
	DS 06 B	91.2	10	31504	217.2	73.3	31947	358.8	13.3	31971
	DG 060 A	249.1	41.4	22199	37.7	44.1	22502	144.2	16.3	22561
	DG 060 B	249.3	42.2	26386	93.5	45.2	26789	350.7	12.3	26896
	DG 060 C	249.9	50.8	24771	59.8	38.8	25175	153.8	4.9	25289
	DG 060 D	251	48.9	21991	11.9	24.1	22337	117.5	31	22372
	DG 061 A	146.7	4.7	39041	55.5	14.1	39167	254.7	75.1	39435
	DG 062 A	220.9	4.4	36845	121	66.1	37153	312.9	23.4	37272
	DG 062 B	213.3	3.4	35298	122.6	10.3	35688	321.1	79.2	35703
	DG 062 C	226.1	4	35737	128.4	62.3	36013	318.2	27.4	36078
	DG 062 D	221.4	4.8	34599	311.5	1.5	34983	58.7	84.9	35118
	DG 063 A	219.9	53.3	23961	91.8	24.7	24267	349.2	25.3	24352
	DG 063 B	217.8	56.2	25438	81.1	26	25822	340.8	20.1	25890
	DG 063 D	210.9	54	22826	93.6	18.4	23059	352.6	29.7	23151
	DG 064 A	202.5	1.3	64194	293.9	46.6	64590	111.3	43.4	65013
	DG 064 B	235.5	50.5	71056	7.1	28.7	71096	111.7	24.6	71838
	DG 064 C	22	1.7	60934	290.1	49.7	61240	113.4	40.2	61782
	DG 066 A	258.8	57.4	18362	94.1	31.7	18413	359.8	7	18612
	DG 066 B	257.5	34.6	21362	100.4	53.2	21476	355.2	11.1	21637
	DG 067 A	179.2	60.1	9717.7	86.9	1.3	9820	356.1	29.8	10003

** AMS intensity in μ SI units*

Subarea	Sample#	k_{min}			k_{int}			k_{max}		
		dec.	inc.	int.	dec.	inc.	int.	dec.	inc.	int.
	DG 067 B	117.8	34.6	7991.1	257.1	47.7	8142.7	12.3	21.2	8200.7
	DG 067 C	209.8	50.6	9409.9	97.4	17.4	9465.8	355.1	34.1	9665.3
	DG 068 A	157.7	34.6	71008	357.3	53.8	72776	254.2	9.4	74494
	DG 068 B	159.2	26.6	71019	353.5	62.7	72401	252.1	5.9	74291
	DS 07 A	272.5	31.8	84891	176	10.4	85965	70.1	56.2	86257
	DS 07 B	267.7	46.7	88676	167.3	9.6	89174	68.7	41.7	89398
	DS 07 C	279.2	31.1	87379	184.2	8.2	87743	81.2	57.6	88060
	DS 07 D	272	31.6	89954	158.6	32.8	90340	34.5	41.1	90424
	DS 07 E	271.8	30.8	87455	171.8	16.3	88212	57.8	54.3	88490
	DS 08 A	267.2	43.1	58099	67.6	45.2	58618	167.8	9.9	59037
	DS 08 B	250.7	28.1	55593	349.8	16.6	56222	106.7	56.6	56339
	DS 08 C	246.5	27.5	54087	337.7	2.4	54563	72.3	62.4	54676
	DS 08 D	268.1	48.8	57117	72.3	40.1	57492	169	7.9	57789
	DG 080 A	336.8	0.9	61657	246.2	35.6	62368	68	54.4	62678
	DG 080 B	333.2	3	62640	242.1	21.1	63336	70.8	68.7	63844
	DG 080 C	333.2	2.3	59609	242.5	16.5	60332	70.8	73.4	60788
	DS 09 A	266.3	30.3	73384	104.2	58.4	73992	1	8	74281
	DS 09 B	255.4	42.1	73967	101.3	44.8	74576	357.8	13.3	74922
	DS 09 C	270	27.7	71940	44.7	53.3	73204	167.7	22.1	73279
	DS 09 D	266	32.4	70692	86.2	57.6	71760	176.1	0	72097
	DS 10 A	265.3	23.6	62201	135	56	64909	5.9	23	65838
	DS 10 B	259.1	21.9	62726	142.5	48	64705	4.6	33.7	65304
	DS 10 C	270.2	19.5	63130	149	55.6	64835	10.7	27.1	65820
	DS 10 D	267.3	21	61358	148.6	51.4	63381	10.5	30.7	64286
	DS 11 A	242.9	24.9	57394	144.2	18	58483	22.2	58.5	58535
	DS 11 B	258.1	16.2	56929	355.8	24.8	57471	138.2	59.8	57813
	DG 132 A	43.4	34	73219	213.9	55.7	73819	310.4	4.4	74281
	DG 132 B	38.2	37.3	72544	207.1	52.2	73151	304.1	5.4	73479
	DG 133 A	252.2	36.8	40379	46.9	50.4	40700	152.6	12.6	40932
	DG 133 B	282.3	49.4	40229	59.5	32.2	40847	164.2	22	41037
	DS 24 A	81.5	12.5	29474	340.1	41.6	29870	184.6	45.7	30091
	DS 24 B	93.3	10.4	26140	347	56.7	26585	189.7	31.2	26703
	DS 25 A	91.6	24.8	23044	312.9	58.4	23170	190.4	18.3	23340
	DS 25 B	83.9	30.8	24564	305.1	51.7	24673	186.8	20.5	24786
	DS 25 C	102.2	1.7	26180	203.3	81.2	26416	12	8.7	26499
	DG 251 A	300.6	31	68242	51.8	31.1	71245	176.3	43.2	71478
	DG 251 B	292.9	29.4	71334	40.4	28.1	74332	165.5	47.1	74484
	DG 252 A	21.3	43	31709	209.3	46.7	31859	115	4	32243

** AMS intensity in μ SI units*

Subarea	Sample#	k_{min}			k_{int}			k_{max}		
		dec.	inc.	int.	dec.	inc.	int.	dec.	inc.	int.
	DG 252 B	19.3	25.6	33070	246.1	55	33325	120.6	22.1	33482
	DG 252 C	26.1	46.1	34961	214	43.6	35173	120.2	3.9	35510
	DS 26 A	241.3	18.3	23525	149.8	4.5	23643	46.5	71.1	23650
	DS 26 B	226.8	11.9	28312	344.8	65.8	28398	132.3	20.7	28475
	DS 26 C	205.4	5.3	44410	104	64.9	44615	297.8	24.5	44809
	DS 26 D	209.2	8.6	39463	84	75.3	39607	301	11.8	39813
	DG 261 A	276.6	35.6	71006	84.2	53.7	71744	182.3	5.9	72252
	DG 261 B	270.3	21.2	64915	3.4	7.9	65819	112.6	67.3	66042
	DG 261 C	266.8	28.1	68693	111.8	59.5	69456	2.7	10.9	69600
	DG 261 D	266.4	32.7	71213	84.6	57.3	71827	175.9	0.8	72114
	DG 262 A	244.3	43.6	31637	122.2	29.2	31864	11.5	32.4	31952
	DG 262 B	247	43.5	33698	88.2	44.5	33913	347.4	10.8	34030
	DG 263 A	338.9	32.8	33705	215.6	40.4	34214	93	32.3	34297
	DG 263 B	214.8	2	33250	309.3	65.7	33728	123.9	24.2	33906
	DG 263 X	235.4	47.1	70240	327.4	1.9	71618	59.1	42.9	72244
	DG 269 A	290.8	19.9	61551	190.7	26	63007	53.7	56.3	63342
	DG 269 B	282.4	19.9	63570	27.7	36	64821	169.3	47.2	65440
	DG 269 C	285.2	21	68626	164.2	53.2	69663	27.3	28.6	69967
	DS 27 A	65.2	15.5	15325	282.7	70.8	15380	158.3	11.1	15433
	DS 27 B	88.4	24.7	17880	268.5	65.3	17939	178.4	0	18074
	DS 27 C	264.4	27.7	15492	70.4	61.6	15542	171.3	5.8	15633
	DS 27 D	80.5	10.4	15934	246.5	79.3	16005	350.1	2.5	16122
	DG 270 A	142.5	27.7	44867	235.4	5.5	45042	335.6	61.7	45547
	DG 270 B	135.8	43.6	45408	240.3	14.7	45599	344.3	42.7	45979
	DG 271 A	262.5	58.8	28427	134.7	20.4	28836	35.8	22.6	28929
	DG 271 C	263.1	43.3	30988	129.2	36.4	31328	19.1	25	31436
	DG 271 D	234	37.4	21651	135	11.5	21778	30.8	50.3	21906
	DG 274 A	87.7	30.9	38277	337.6	29.9	39377	213.4	44.3	39996
	DG 274 B	84.9	30.9	38675	333.4	31.4	39837	208.8	43	40496
	DG 275 A	80.6	22.9	28261	243.8	66.2	29178	348	6.2	29328
	DG 275 B	73.7	22.3	28678	202.9	57	29619	333.7	22.9	29781
	DG 275 C	70.7	27.4	29986	241.3	62.3	30745	338.7	3.9	31083
	DG 275 D	67.3	26.7	28889	185.4	43.1	30106	316.6	35.1	30241
	DG 276 A	68.8	49.8	61654	213.5	34.6	61833	316.3	17.9	62150
	DG 276 B	84.3	34.9	62178	219	45.3	62488	336	24.2	62674
	DG 276 C	69.7	41.4	61796	206	39.4	62044	317	23.6	62376
	DG 277 A	97.8	42.1	57916	352.6	16.1	59003	246.8	43.4	59614
	DG 277 B	106.3	39.5	58230	7.5	10.5	59269	265.4	48.5	59927

** AMS intensity in μ SI units*

Subarea	Sample#	k_{min}			k_{int}			k_{max}		
		dec.	inc.	int.	dec.	inc.	int.	dec.	inc.	int.
	DG 277 C	90.7	38.3	58071	357.8	3.7	59200	263.1	51.4	59635
	DS 28 A	281.9	38.6	82633	190.3	2	83518	97.8	51.3	83998
	DS 28 B	276.9	41.8	83435	178.8	8.9	84281	79.2	46.8	84670
	DS 28 C	227.5	15.4	82285	330.6	39.6	82603	120.8	46.3	83022
	DS 28 D	269.2	43.6	88173	174.3	5.2	88719	78.8	45.9	89055
	DS 28 E	260.8	44.6	85644	170.6	0.2	86422	80.5	45.4	86704
	DS 29 A	295.7	29.7	70439	166.5	48	71057	42.4	26.8	71717
	DS 29 B	289.3	35.2	70666	157.8	43.2	71204	39.9	26.5	71963
	DS 30 A	269.6	15.8	62680	154.1	56.7	65604	8.5	28.4	66462
	DS 30 B	267.9	19.9	62746	142.1	58.3	65688	7	23.6	66820
	DG 306 A	130.8	15.4	58002	294.3	74	58768	39.6	4.3	59208
	DG 306 B	121.1	6.2	49770	0.1	78	50368	212.2	10.2	50722
	DG 306 C	126.2	1.4	52395	354.5	87.9	53271	216.3	1.6	53670
	DG 306 D	309.5	9.1	53008	180.5	75.7	53476	41.2	10.9	54107
	DG 307 A	351.8	5.6	84788	213.6	82.4	87114	82.3	5	87942
	DG 308 A	183.1	28.7	90886	23.4	59.7	91829	278	8.9	92545
	DG 308 B	164.8	28.2	87202	6.9	60	88292	259.9	9.6	88859
	DG 309 A	77.8	25.5	68759	265.1	64.3	69644	169.1	2.9	70360
	DG 309 B	267	13.4	68447	92.7	76.5	69006	357.3	1.3	69963
	DS 31 A	333.5	15.3	53631	123.3	72.5	54584	241.1	8.4	54833
	DS 31 B	311.5	25.4	49707	121.2	64.2	50820	219.6	4	51204
	DS 31 C	315.5	18.9	50903	103.4	68	51767	221.7	10.9	52463
	DG 310 A	221.5	11.5	63312	131.4	0.3	63669	39.9	78.5	64523
	DG 311 A	249.5	13.8	71647	350.7	38.4	72267	143.4	48.3	72733
	DG 311 B	253.5	14.8	74862	349.3	21	75746	130.9	63.9	76352
	DG 312 A	351	17.3	20134	138.5	69.7	20823	257.7	10.2	20950
	DG 312 B	346.9	20.1	20633	146.6	68.7	21281	254.4	6.8	21521
	DG 312 C	344.6	17.9	19847	132	69.1	20564	251.2	10.6	20751
	DG 313 A	194.3	10.2	62501	87.1	58.9	64247	290.1	29.1	65465
	DG 313 B	200.1	12.7	64080	88.7	58.3	65917	297.1	28.5	66981
	DG 313 C	195	13.4	69484	85.3	54.6	71193	293.6	32	72716
	DG 314 A	40.3	1.5	37307	310.3	2.9	37446	156.7	86.7	37791
	DG 314 B	13.5	1.2	37287	103.8	12	37410	278	78	37494
	DG 315 A	155.1	15.6	35934	265.7	51.5	36029	54.2	34.1	36244
	DG 315 B	166.6	10.9	35805	310	76.4	36046	75.1	7.9	36169
	DG 315 C	257.1	65.7	33746	152.4	6.5	34006	59.6	23.3	34262
	DG 316 A	135.2	78.6	34539	261.5	6.8	34802	352.6	9.1	35447
	DG 316 B	133.2	79.1	35495	257.4	6.2	35690	348.3	8.9	36333

** AMS intensity in μ SI units*

Subarea	Sample#	k_{min}			k_{int}			k_{max}		
		dec.	inc.	int.	dec.	inc.	int.	dec.	inc.	int.
	DG 316 C	132.2	78.1	34690	260.1	7.4	34979	351.4	9.2	35799
	DG 316 D	101.5	69	33893	258	19.4	34104	350.8	7.8	34781
	DG 317 A	97.1	47.9	36746	257	40.3	37036	355.7	10.1	37438
	DG 317 B	91.3	48.5	31962	252.8	40	32295	350.6	9.3	32573
	DG 317 C	72.3	32.8	33542	206	47	33887	325.2	24.5	33984
	DG 317 D	68.7	32.4	33652	195.3	43.2	34049	317.6	29.6	34107
	DG 318 A	157.9	57.1	42758	46.3	13.4	43062	308.6	29.5	43602
	DG 318 B	151.4	65.6	41213	34.9	11.5	41750	300.4	21.3	42215
	DG 319 A	306.1	67.1	36480	150.7	21	38134	57.3	8.7	38607
	DG 319 B	311.9	68.8	36495	158.8	19.1	38088	65.7	8.9	38479
	DG 319 C	317.3	67.6	35871	152.9	21.6	37356	60.7	5.4	37840
	DG 319 D	318.8	68.2	37314	145.4	21.6	38922	54.5	2.3	39434
	DG 320 A	262.3	34.3	33838	355.3	4.4	34436	91.8	55.4	34742
	DG 320 B	261.7	30.7	36048	171.4	0.4	37016	80.8	59.2	37392
	DG 320 C	260.2	31.3	33734	161.2	14.4	34721	49.8	54.8	35082
	DS 66 A	270.9	27.2	16243	5.9	9.6	16449	113.5	60.9	16632
	DS 66 B	283.1	16.8	16199	17.1	13	16443	143	68.5	16619
	DS 66 C	287	17.2	13556	25.4	25.5	13888	166.7	58.5	14010
II3										
	DG 004 A	359.8	54.3	26774	254.8	10.6	26967	157.6	33.7	27548
	DG 005 A	52.3	33.7	14514	289.1	39.4	14663	167.5	32.5	14774
	DG 005 B	39.3	47.2	15589	253.9	37.4	15774	149.6	17.8	15909
	DG 005 C	42	38.9	13551	260.6	44.1	13664	149.5	20.5	13781
	DG 005 D	61.7	31	13628	266.2	56.6	13729	158.6	11.3	13797
	DG 006 A	157.7	14.7	27547	65.4	8.6	27978	306	72.9	28617
	DG 006 B	167.3	11.6	25605	75.6	8.1	25977	311.6	75.8	26662
	DG 006 C	161.9	15.4	26291	69.6	8.3	26751	312.2	72.4	27361
	DG 007 A	182.2	56.7	9035.7	20	32	9082.2	284.8	8.2	9158.2
	DG 007 B	178.8	70.8	7716.7	6.8	19	7767.9	275.9	2.5	7844.4
	DG 007 C	165.8	67	8392.3	14.8	20.4	8452.1	280.9	10.2	8541
	DG 008 A	75	16.5	52829	273.7	72.7	53025	166.5	5.3	53276
	DG 008 B	235.3	12.2	46505	99.1	73.3	46664	327.8	11.2	47007
	DG 009 A	282.1	6.4	66870	22.8	58.8	67502	188.3	30.4	68185
	DG 010 A	66.7	58.7	38796	288.2	24.5	38832	189.6	18.2	39354
	DG 010 B	289.9	16.5	40840	50.1	59.6	41015	192	24.8	41491
	DG 011 A	130.6	11.2	42338	223.4	13.5	42945	2	72.3	43488
	DG 011 B	122.6	7.1	43490	214.6	15.8	44261	9.1	72.6	44753
	DG 011 C	127.7	14.7	31097	220.1	9.2	31569	341	72.6	32201

AMS intensity in μ SI units

Subarea	Sample#	k_{min}			k_{int}			k_{max}		
		dec.	inc.	int.	dec.	inc.	int.	dec.	inc.	int.
	DG 012 A	254	49	45792	61.9	40.3	46354	157	6	46424
	DG 012 B	265.5	54.6	41000	47.7	29.3	41576	148.3	18	41734
	DG 072 A	302.2	35.8	80588	76.6	44.1	82945	193	24.6	83418
	DG 072 B	309.7	30.7	79039	63.8	34.5	81544	189.4	40.3	82095
	DG 072 C	305.7	34.2	85025	67.6	37.9	87155	188.9	33.6	88346
	DG 134 A	121.5	24.1	34852	232.6	38.8	34998	8.1	41.6	35374
	DG 134 B	144.2	45.6	37498	259.6	22.8	37636	7.1	35.6	38168
	DG 134 C	109.4	19.3	32639	220.2	45.3	32792	3.3	38.3	33130
	DG 134 D	112.8	20.1	33562	223.7	44.3	33677	5.6	38.9	34083
	DG 171 A	211.6	12.2	12388	118.7	13.2	12447	342.9	71.9	12509
	DG 171 B	210	13.8	12381	116.3	14.7	12450	341.3	69.7	12517
	DG 171 C	204.4	14.3	13924	110.8	13.9	14038	338.4	69.8	14100
	DG 171 D	193.2	16.4	13326	100.5	9.2	13413	342.2	71.1	13472
	DG 172 A	102.3	1.6	17613	11.8	19.6	17846	196.9	70.4	17885
	DG 172 B	100.7	1.7	17436	191.2	15.9	17590	4.6	74	17670
	DG 172 C	91.2	10.4	15973	185.5	22	16163	337.5	65.4	16223
	DG 175 A	162.2	24.1	59514	49.9	40.3	60520	274.4	40.1	62219
	DG 175 B	179.8	13.1	60565	76.8	44.1	61632	282.4	43	63427
	DG 175 C	161.6	23.2	58356	50.8	39.7	59330	273.8	41.4	60928
	DG 175 D	162	32.2	59670	47.1	33.7	60902	283.5	39.7	62352
	DG 176 A	97	14.1	29751	261.7	75.5	29876	6	3.7	30038
	DG 176 B	277.6	6.3	35554	153.9	78.8	35726	8.6	9.2	35840
	DG 176 C	91.6	17.6	17666	338.9	50.6	17907	193.9	34	18124
	DG 177 B	92.9	19.1	17090	339.5	48.8	17316	196.9	34.9	17568
	DG 177 C	94.5	20.7	15580	338.8	49	15779	199	33.6	16016
	DG 177 D	94.3	21.4	21550	338	48.5	21753	199.4	33.6	22041
	DG 177 E	75.3	34	19594	316.4	35.6	19810	194.9	36.2	20120
	DG 182 A	206.8	36	1250.8	16.5	53.5	1252.4	113.2	5	1268.7
	DG 182 B	216.8	64.4	1163.3	48.4	25.2	1172.3	316.3	4.5	1184.8
	DG 183 A	342.9	36.8	3812.9	79.7	9	3818.7	181.3	51.7	3909.1
	DG 184 A	81.1	26.1	33570	229.1	60	34343	344.2	13.8	34668
	DG 184 B	83.6	19.9	34925	233.5	67.3	35665	349.7	10.5	36088
	DG 184 C	81.9	25.4	35717	267.6	64.5	36481	173	2.2	36927
	DG 184 D	80.5	18.7	34148	276.9	70.5	34869	172.2	5.1	35292
	DG 185 A	98.3	12.1	9137.1	358.7	37.7	9254.3	202.9	49.7	9381.6
	DG 185 B	97.2	22.6	9523.3	358.5	20	9703.6	231.1	59	9795.7
	DG 185 C	90.6	28.1	9010.2	347.2	23.4	9135.9	223.6	52	9263.2
	DG 185 D	92.1	25.2	12172	347.2	28.7	12395	216.4	50.1	12586

** AMS intensity in μ SI units*

Subarea	Sample#	k_{min}			k_{int}			k_{max}		
		dec.	inc.	int.	dec.	inc.	int.	dec.	inc.	int.
	DG 188 A	122.4	62	52774	10.7	11.1	53310	275.4	25.3	53393
	DG 188 B	114.8	51.1	52813	219.8	11.9	53077	318.7	36.4	53352
	DG 188 C	96.7	41	51472	230.4	38.5	51729	342.5	25.3	52038
	DG 188 D	104.3	58.1	51038	233.4	21.4	51400	332.7	22.5	51607
	DG 203 A	72.8	11.8	72709	188.7	64.4	73804	337.9	22.4	74485
	DG 203 B	75.4	9.7	83721	183.7	61.4	84568	340.5	26.6	85494
	DG 206 A	359	53.5	47560	236.3	21.8	48217	134.1	27.7	48478
	DG 206 B	345	53.9	50307	226.4	19.3	51171	125.1	29.2	51553
	DG 245 A	93.8	26.5	35088	216.4	47.2	35866	346.5	30.8	36122
	DG 245 B	83.9	30.8	36842	228.2	53.7	37645	343.2	17.3	37763
	DG 245 C	96.3	29.8	35078	198.8	20.7	35811	318.2	52.5	36105
	DG 246 A	165.9	36.5	48566	285	33.3	49027	43.4	36	49203
	DG 246 B	165	34	45943	269.5	20.3	46245	24.6	48.9	46514
	DG 246 C	142.2	35.5	49531	279.2	45.7	49842	34.7	22.8	50223
	DG 246 D	142.3	34.1	46896	265.3	38.8	47323	26.5	32.8	47599
	DG 247 A	77.2	58.3	63341	243	30.9	63659	336.8	6.4	64626
	DG 247 B	94.2	69.6	63079	244.2	17.9	63515	337.3	9.6	64524
	DG 248 A	69.4	18	10558	197.3	62.2	10617	332.4	20.5	10675
	DG 248 B	62	30.8	10969	196.4	49.5	11037	317	23.5	11088
	DG 249 A	264.4	32.2	33236	154.8	28	33363	33	44.7	33553
	DG 249 B	286.4	39	30424	184.6	14.2	30743	78.5	47.5	30844
	DG 249 C	257	43.7	30402	142.1	23.8	30549	32.8	36.9	30673
	DG 249 D	257.2	28.6	33125	138	41.8	33218	9.5	34.8	33413
	DG 250 A	223.9	34.5	9900.8	94.6	42.7	9981.1	335.3	27.9	10024
	DG 250 B	279.4	39.3	3176.8	33.2	26.3	3242.3	147.1	39.4	3283.2
	DG 250 C	246.9	58	3516	29.3	26.3	3574	127.9	16.9	3606.8
	DG 250 D	33.8	1.5	7315.5	128.1	70.6	7362.8	303.3	19.4	7388.8
	DG 253 A	224.1	48	55751	39.3	41.9	56287	131.5	2.4	56465
	DG 253 B	223.3	73.7	63299	28.7	15.8	63955	119.8	3.9	64580
	DG 254 A	292.9	25.6	25505	186.9	29.9	25923	56	48.7	26237
	DG 254 B	329.7	3.4	19819	239.2	9	20195	80	80.4	20269
	DG 254 C	216.5	20.4	26383	307.9	3.6	26846	47.5	69.2	27169
	DG 254 D	291.5	24.8	19626	192.4	18.8	19902	69.4	58	20021
	DG 255 A	229.4	85.1	52820	90.3	3.7	53342	0.1	3.2	53629
	DG 255 C	242.4	87.1	52906	104.6	2.1	53231	14.6	1.9	53448
	DG 255 C	237	70.9	63202	77.1	18	63603	345.1	6.1	64082
	DG 255 D	168	86.4	63378	264.1	0.4	63809	354.1	3.6	64202
	DG 256 A	140.2	31.4	4387.5	262.1	40.9	4421.2	26.6	33.2	4433.1

** AMS intensity in μ SI units*

Subarea	Sample#	k_{min}			k_{int}			k_{max}		
		dec.	inc.	int.	dec.	inc.	int.	dec.	inc.	int.
	DG 256 B	186.9	39.1	4277.6	303.1	28.5	4289.3	57.9	37.7	4290.9
	DG 256 C	313.1	0.4	4488.8	223	23.8	4504.9	44.1	66.2	4515.2
	DG 256 D	266	34.2	5620.8	18.2	29	5686.7	138.2	42	5702.6
	DG 257 A	106.4	8.2	51117	15.7	4.8	52374	255.6	80.5	52419
	DG 257 B	109.2	5.6	48514	9.1	60.9	49568	202.3	28.4	49776
	DG 257 C	102.5	6.8	51981	10.6	14.8	53399	216.5	73.7	53429
	DG 258 A	214.6	26.9	24701	88.6	49.2	24843	320.4	28.2	24901
	DG 258 B	216.7	27.4	24170	78	55.4	24303	317.2	19.4	24380
	DG 258 C	204.5	40.4	25228	71.3	38.8	25336	318.6	25.6	25420
	DG 258 D	199.2	31.3	24828	70.6	45.8	24932	307.8	27.8	25016
	DG 259 A	110.3	3.6	33749	15.5	53.6	33980	202.9	36.2	34384
	DG 259 B	306.9	13.1	27745	48.7	41.5	28142	203.2	45.6	28385
	DG 260 A	136	16.6	40158	232.3	20.3	41258	9.6	63.2	41793
	DG 260 B	130.9	16.6	50039	223.7	9.4	52080	341.9	70.8	52902
	DG 260 C	109.5	3.4	21431	8.2	73	21506	200.5	16.6	21767
	DG 260 C	127.2	17.4	49966	222.5	16.3	52521	353.1	65.8	53206
	DG 260 D	133.8	13.3	43196	230.3	25.7	44962	18.9	60.6	45649
	DG 264 A	298.8	6.9	17758	199.5	53.1	17926	33.8	36	17998
	DG 264 B	268.3	3.7	15891	175.4	37.7	16108	3.1	52	16221
	DG 265 A	276.7	15.6	67303	180	22.5	67763	38.4	62.1	68352
	DG 265 B	252.2	58.9	70774	119.8	22.1	71387	21	20.7	71893
	DG 265 C	273.1	24.1	73848	162.8	37.9	74017	27.3	42.5	74465
	DG 265 D	285.3	21.2	69321	185.2	24.4	69819	51.4	56.7	70525
	DG 266 A	96.8	20.2	9805.3	353.7	31.7	9858.1	213.8	51	9972.4
	DG 266 B	96.9	20.5	8896.4	356.2	26.5	8967.8	219.7	55.4	9053.4
	DG 267 A	214.9	77.4	107114	312.6	1.7	107250	43	12.5	107660
	DG 267 B	308.1	17.1	107900	190.4	56.5	108060	47.5	27.9	108670
	DG 268 A	108.1	6.8	20545	4.1	63.9	20647	201.2	25.1	20892
	DG 268 B	87.4	8.3	18384	345.9	53.6	18426	183.3	35.2	18690
	DG 268 D	67.2	33.1	16855	299.9	42.9	16879	178.6	29.2	17102
	DG 272 A	102.4	49.3	18169	231.7	28.6	18718	337.4	26.3	19176
	DG 272 B	103.7	47.1	15939	236.3	32.2	16320	343.5	25.1	16700
	DG 272 C	100.2	47.6	16373	225.3	27.7	16792	332.4	29.3	17286
	DG 272 D	103.3	44.3	16970	235	34.3	17293	344.6	26.2	17844
	DG 273 A	63.8	33.7	39229	206.5	50	39963	320.6	18.9	40301
	DG 273 B	254.7	69.6	37977	33	15.6	38799	126.7	12.9	38900
	DG 273 C	257.7	66	34850	58.7	22.8	35510	151.7	7	35721
	DG 273 D	265.6	70.9	39925	62.3	17.7	40712	154.6	7.1	41029

** AMS intensity in μ SI units*

Subarea	Sample#	k_{min} dec.	k_{min} inc.	k_{min} int.	k_{int} dec.	k_{int} inc.	k_{int} int.	k_{max} dec.	k_{max} inc.	k_{max} int.
	DG 273 E	71.1	29.1	37889	195.1	45.1	38559	321.7	30.8	38901
	DG 273 F	66.4	32.2	36744	204.6	49.8	37362	322.1	21.3	37623
II4										
	DG 242 A	37.3	71.5	43922	299.4	2.6	44359	208.5	18.3	44530
	DG 242 B	28.7	55.1	40530	126	5.1	40881	219.5	34.5	41071
	DG 242 C	21.6	61.1	43792	135.4	12.5	44171	231.5	25.5	44471
	DG 243 A	265.7	10.8	32589	4.5	38.9	32908	163	49.1	32987
	DG 243 B	267.3	12.6	35035	52.5	74.7	35310	175.4	8.4	35579
III										
	DG 102 A	92.8	43.2	946.6	254.4	45.3	951.3	353.9	9.3	959.1
	DG 102 B	142.1	48	864.2	269.4	28.6	867.9	16.1	27.8	871.6
III2										
	DG 087 A	66.1	49.2	23186	292.8	30.6	23470	187.4	24.2	23683
	DG 087 B	69.6	47	22637	300.7	30.4	22805	193.1	27.3	22957
	DG 088 A	75.8	33.1	1048.8	187.1	29.2	1049.8	308.5	43	1052.3
	DG 088 B	268.7	22	1135	173.9	11.7	1136.2	57.9	64.8	1142
	DG 088 C	158.5	38.1	1016.7	60.2	10.4	1017.8	317.5	50	1020.4
	DG 088 D	60.9	11.9	988.5	159.1	34.3	991.5	314.5	53.1	992.1
	DG 089 A	124.8	9.8	15548	33.1	10.2	15902	257.9	75.7	16191
	DG 089 B	302.3	15.2	17917	210.1	8.1	18297	92.9	72.7	18611
	DG 090 A	265.7	33	2164.6	32.6	42.8	2185.1	154.2	29.5	2212
	DG 090 B	273.6	39.9	1614.7	67.5	47	1619	172.2	13.3	1643.1
	DG 090 C	68.4	1.7	6465.1	335.4	60.4	6495.1	159.4	29.5	6621.1
	DG 090 D	275.4	27.6	4563.3	31.3	40	4647.2	161.6	37.6	4740.2
	DG 091 A	75.5	47.9	30742	235	40.2	30945	333.9	10.3	31783
	DG 091 B	80.2	67.7	30244	241.3	21.3	30492	333.9	6.6	31370
	DG 091 C	85.2	62	35367	244.8	26.5	35772	339	8.4	36742
	DG 095 A	163.2	53.6	534.7	286.4	21.9	537.5	28.4	27.4	538.7
	DG 095 B	281	51.3	533.4	69.5	34.3	535.8	170.5	15.7	537
	DG 095 C	258.1	2.7	525.4	50.8	86.9	526	168	1.4	527.8
	DG 095 D	301.3	3.5	526.6	195	77.8	527.8	32	11.6	529.4
	DG 104 A	67.8	12	29153	213.2	75.5	29352	336.1	8	29713
	DG 104 B	73.8	31.1	27738	229.8	56.5	27944	337	11.1	28242
	DG 104 C	69.8	14.2	25006	201.7	69.2	25361	336	14.9	25538
	DG 104 D	69.6	6.1	26708	198.7	80.4	27011	338.8	7.4	27274
	DG 111 A	207.1	70.3	115390	18.6	19.5	117050	109.6	2.7	118700
	DG 111 B	196.6	70.9	117920	357.8	18.1	120040	89.7	5.7	121720

** AMS intensity in μ SI units*

Subarea	Sample#	k_{min}			k_{int}			k_{max}		
		dec.	inc.	int.	dec.	inc.	int.	dec.	inc.	int.
	DG 111 C	223.8	79.5	114970	6.6	8.4	117460	97.5	6.3	119310
	DG 111 D	206	73.4	113090	359.9	15	115110	91.8	7	116790
	DG 112 A	48.9	39.9	49500	167.8	30	49750	282.2	35.6	50247
	DG 112 B	198.2	22.7	44006	81.9	46.6	44317	305	34.6	44558
	DG 113 A	106.5	9.8	81487	209.2	52	84195	9.2	36.3	85708
	DG 113 B	246.8	0.6	77809	339.6	78	80630	156.7	12	81608
	DG 113 C	107.5	10.8	78697	211.9	52.7	80880	9.8	35.3	82398
	DG 113 D	260	8.6	90205	147.2	68.6	93494	353.1	19.5	94730
	DG 113 E	264.2	5.4	81913	129.3	82.3	84684	354.7	5.4	85985
	DG 122 A	93.1	76.6	15682	325	8.4	15810	233.4	10.4	15948
	DG 122 B	60.9	70	25135	183.2	11	25294	276.5	16.5	25408
	DG 122 C	323.2	55.5	26187	114.2	31	26439	212.5	13.6	26730
	DG 122 D	71.9	69.4	15578	327.3	5.4	15672	235.3	19.8	15854
	DG 123 A	274.8	42.2	44130	150.6	31.8	44473	38.3	31.4	44713
	DG 123 B	306.2	33.3	51527	154.2	53.4	51685	45.3	13.5	52051
	DG 123 C	330.3	78.5	41690	72.6	2.5	41833	163.1	11.2	41941
	DG 123 D	288.8	49.7	48897	166.6	24.3	48943	61.5	29.9	49328
	DG 124 A	24.5	65.8	8895.7	232.8	21.6	8921.5	138.7	10.4	8935.6
	DG 124 B	311.9	22.7	4211.5	63.8	41.7	4270	201.5	39.7	4290.2
	DG 124 C	33.9	26.5	11746	253.7	57	11787	133.3	18.2	11800
	DG 124 D	313.3	22.5	6906	67.6	44.8	6932.6	205.3	36.7	6959.1
	DG 125 A	129.1	42.9	38374	35.1	4.3	38601	300.4	46.7	38780
	DG 125 B	136	48.4	38309	31.8	12.2	38616	291.7	39	38739
	DG 126 A	148.1	12.2	65378	256.4	55.5	66135	50.4	31.7	66577
	DG 126 B	145.6	5.3	74437	244.5	58.8	75362	52.5	30.6	75639
	DG 126 C	152.9	16	79709	286.6	67.4	81260	58.3	15.5	81649
	DG 126 D	147.2	18.1	82414	322.8	71.9	84213	56.7	1.3	84514
	DG 127 A	290.1	6.4	48405	33.1	63.5	49121	197	25.6	49436
	DG 127 B	97.7	13	49116	351.2	51	49563	197.3	36	50192
	DG 128 A	267.8	19.3	70460	56.1	67.6	71889	174	10.9	72875
	DG 128 B	270.5	22.2	65875	71.4	66.7	67046	177.6	6.9	68007
	DG 129 A	228.5	37.8	51364	346.5	31.2	51755	103.3	36.6	52177
	DG 129 B	211.2	37.6	50392	336.7	37	50684	93.6	31	51203
	DG 130 A	103.6	30.6	63419	286.5	59.4	64205	194.4	1.3	64511
	DG 130 B	109.6	35.2	62004	296.8	54.6	62676	202	3.4	63142
	DG 328 A	80.2	4.1	4161.7	179.6	66.3	4192.1	348.5	23.3	4220.5
	DG 328 B	82.8	13.1	4891	202.4	64.7	4915.9	347.6	21.2	4943.1
	DG 328 C	78.3	8.8	3632.9	191.2	68.2	3652.7	345.2	19.8	3681.6

** AMS intensity in μ SI units*

Subarea	Sample#	k_{min} dec.	k_{min} inc.	k_{min} int.	k_{int} dec.	k_{int} inc.	k_{int} int.	k_{max} dec.	k_{max} inc.	k_{max} int.
	DG 329 A	320.1	17.1	759.6	227.2	9.5	763.5	109.3	70.3	768.8
	DG 329 B	40.7	54.7	981	259	29.1	984.9	158.5	18.2	987.3
	DG 329 C	70.2	1.9	993.5	160.7	15.6	997	333.4	74.2	1000.3
	DG 341 A	64.3	75.8	72341	302	7.7	73038	210.3	11.8	73247
	DG 341 B	66	69.2	72152	305.9	10.8	72395	212.4	17.6	72794
	DG 341 C	73.4	53.3	70131	297.9	28	70328	195.6	21.7	70711
	DG 342 A	117.5	6.7	81369	281.8	83	81710	27.3	1.9	82613
	DG 342 B	124.8	20.6	83469	327.4	67.8	83853	217.8	7.8	84594
	DG 342 C	119.5	5.8	79848	254.9	81.9	80497	28.9	5.7	81109
	DG 343 A	110.2	30	3817.1	8.3	19.7	3880.7	250.1	52.9	3937.5
	DG 343 B	100.3	30.5	4629.4	8	3.9	4692.4	271.5	59.2	4742.1
	DG 343 C	100.2	19.1	2067.4	206.6	39.1	2089.6	350.2	44.7	2100.2
	DG 344 A	289.4	20.2	2775.2	63.1	61.9	2796.8	192.3	18.6	2804.1
	DG 344 B	33.3	61.7	2665.3	280.6	11.7	2684	184.9	25.3	2695.3
	DG 344 C	43.5	73.8	1548.1	184.3	12.7	1562.9	276.5	9.9	1566.9
	DG 345 A	113.6	7.7	939.3	18.3	34.9	943.6	214.3	54	944.3
	DG 345 B	184.1	75.9	904.9	324.4	11	910.1	56.1	8.8	913.9
	DG 345 C	19.1	68.8	991.3	198.3	21.2	993.6	288.4	0.3	996.6
III3										
	DG 092 A	349.6	26.3	39526	238.1	36.6	40014	106.1	42.1	41167
	DG 092 B	351.2	28.9	37123	231.8	41.7	38014	103.6	34.7	38722
	DG 093 A	148.5	41.4	57770	318.4	48.1	58321	54	5	58826
	DG 093 B	141.7	22.3	59337	287.2	63.6	60185	46.1	13.5	60387
	DG 093 C	146	30.9	56606	336.4	58.6	57280	238.7	4.7	57585
	DG 093 D	146.1	41.8	56808	330.9	48.1	57371	238.2	2.4	57625
	DG 094 A	129.4	4.6	26015	219.4	0.5	27057	315.1	85.4	27500
	DG 094 B	234.7	14.2	28599	144	2.6	29082	44	75.5	29823
	DG 094 C	127.5	9.9	25499	217.5	0.5	26527	310.6	80.1	26808
	DG 098 A	265.5	10.4	57032	173.3	12.1	58053	35	73.9	58315
	DG 098 B	248	10.7	62789	155.3	14.1	63542	13.9	72.2	64073
	DG 099 A	70.3	8.9	24881	327.4	55.1	25915	166.2	33.5	26031
	DG 099 B	67	4.2	24960	334.7	29.1	26102	164.4	60.6	26107
	DG 099 C	65.8	2.7	24434	160.7	60.8	25368	334.2	29.1	25450
	DG 099 D	70.2	3.9	24656	240.6	86.1	25626	340.2	0.6	25750
	DG 099 E	71.3	5.5	25268	166	40.7	26306	335	48.7	26438
	DG 100 A	53.4	13.4	10507	319.9	14.1	10552	185.2	70.4	10700
	DG 100 B	55.6	9.9	12277	322.5	17.5	12337	173.8	69.7	12506
	DG 100 C	35.6	17.4	10009	300.1	16.9	10046	168.6	65.4	10200

** AMS intensity in μ SI units*

Subarea	Sample#	k_{min}			k_{int}			k_{max}		
		dec.	inc.	int.	dec.	inc.	int.	dec.	inc.	int.
	DG 100 D	73.4	4.3	7003.1	341.9	19.1	7005.5	175.4	70.4	7124.9
	DG 100 E	55.6	14.5	8236.4	321.9	14.2	8270.4	189.5	69.5	8377.7
	DG 101 1	113	17.6	35793	5.8	42.9	36155	219.5	41.8	36332
	DG 101 B	317.2	3.4	33787	205.7	80.7	33837	47.7	8.7	33972
	DG 101 C	326.9	28.4	40955	103.8	53.4	41170	224.9	21	41642
	DG 101 D	112.8	15.6	36278	6.8	44.8	36481	216.9	41.1	36710
	DG 105 A	273.1	25.2	26448	22.7	35.3	26673	156	44.1	27160
	DG 105 B	295.9	25.7	30723	37.5	22.8	30866	163.6	54.5	31521
	DG 105 C	282.7	39.4	30597	40.4	29.5	30880	155.1	36.5	31390
	DG 105 D	282	24	28046	22.9	23.1	28250	151.4	55.6	28781
	DG 106 A	123.2	6.1	31577	32.8	3.5	31981	273	82.9	32455
	DG 106 B	114.5	4.9	22425	204.6	0.9	22645	305.1	85	22784
	DG 106 C	117.1	3.9	25940	207.6	8.4	26233	2.6	80.7	26503
	DG 106 D	120.2	6	27595	211	7.4	27892	351.7	80.4	28054
	DG 107 A	318.3	38.7	55891	207.5	23.9	56861	94.1	41.9	57330
	DG 107 B	340.4	41.6	67254	229.3	22.1	67866	119.2	40.3	68433
	DG 107 C	329.6	38.2	64746	224.9	17.9	65883	115.1	46.3	66605
	DG 107 D	331.7	39.8	62737	224.2	19.8	63660	114.1	43.6	63815
	DG 144 A	141.9	4.2	22428	233.6	22	22544	41.6	67.5	22644
	DG 144 B	144	13.5	20186	2.7	72.9	20227	236.5	10.3	20243
	DG 144 C	139.2	8.3	22091	47.7	9.9	22201	268.5	77	22293
	DG 144 D	137.5	5.3	20524	227.6	1	20600	328.3	84.6	20679
	DG 148 A	294.5	9.1	15388	42.5	62.6	15427	200.1	25.6	15520
	DG 148 B	278.1	21.2	16616	40.5	54.1	16654	176.5	27.5	16680
	DG 148 C	35.9	41.1	15825	275.1	30.5	15915	161.8	33.9	16064
	DG 148 D	94.3	18.4	14645	337.6	53.4	14698	195.5	30.3	14761
	DG 149 A	39.3	40.1	63826	300	10.9	64854	197.7	47.8	65824
	DG 149 B	43.2	40.8	64077	313.2	0.1	65450	223.1	49.2	66042
	DG 149 C	37.1	42.8	64255	300.7	6.8	65586	203.5	46.4	66160
	DG 149 D	38.5	39.5	63527	303.6	5.9	64840	206.6	49.9	65393
	DG 150 A	334	53.2	20255	82.3	13.2	20324	181.3	33.6	20535
	DG 150 B	348.7	54.1	22181	87.5	6.3	22196	182	35.2	22519
	DG 150 C	52.5	41	20347	298.8	24.9	20473	186.8	38.9	20741
	DG 150 D	36.7	45.3	22671	281.7	22.6	22834	174.1	36.1	23160
	DG 326 A	71.7	20.3	28011	268.8	68.9	28245	163.8	5.7	28753
	DG 326 B	67.7	16.7	26835	263.4	72.7	27068	159	4.4	27526
	DG 326 C	70.3	12.9	27850	266.4	76.6	28138	161.1	3.6	28592
	DG 327 A	305.9	14.7	24271	46	33.9	24379	196.1	52.2	25131

** AMS intensity in μ SI units*

Subarea	Sample#	k_{min}			k_{int}			k_{max}		
		dec.	inc.	int.	dec.	inc.	int.	dec.	inc.	int.
	DG 327 B	294	9.7	24017	31	35.7	24269	191	52.6	24956
	DG 327 B	355.2	30	63865	95.2	16.8	67216	210.5	54.8	68683
	DG 327 C	308.7	20.7	19714	55.7	37.7	19865	196.4	45	20392
	DG 327 D	290	11.1	21882	31.4	45.3	22084	189.6	42.6	22585
	DG 330 A	75.1	10.5	9517.2	244.6	79.3	9581.3	344.7	1.9	9737.6
	DG 330 B	71.1	46.4	17311	231.1	41.9	17465	330.3	10.1	17769
	DG 331 A	71.4	21.6	14875	261.8	68	15144	162.8	3.6	15639
	DG 331 B	59.8	28.4	13634	257.1	60.5	13784	153.8	7.4	14385
	DG 332 A	315.1	20.6	18997	212.6	30	19344	74.2	52.3	19530
	DG 332 B	310.3	28.2	24146	215.8	8.4	24790	110.7	60.3	24866
	DG 332 C	302.6	20.1	17393	196	38	17641	54.2	45.2	17773
	DG 332 D	315.5	14.5	23603	205.5	52.8	23939	55.3	33.4	24252
	DG 333 A	155.7	36.9	16736	262.1	20.6	16833	14.9	45.9	16929
	DG 333 B	151.4	27	12465	246.4	9.7	12504	354.5	61	12624
	DG 333 C	244.7	35.8	19044	132.3	27.9	19111	14.4	41.5	19232
	DG 333 D	272.4	10.6	20125	5	14	20213	146.6	72.3	20259
	DG 334 A	203.9	10.4	22231	79.9	71.8	22266	296.7	14.7	22631
	DG 334 B	226.4	4.4	21867	34.3	85.5	21902	136.3	0.9	22246
	DG 335 A	48.9	68.6	37399	252.9	19.7	37450	160	8	37977
	DG 335 B	61.3	68.9	48570	216.5	19.3	48717	309.4	8.2	49450
	DG 336 A	22	64.2	697.2	140.6	13	701.1	235.9	21.9	703.8
	DG 336 B	17	41.1	611.9	146.6	36.2	614.3	259.5	27.9	616.3
	DG 336 C	32.6	42.6	610.1	165.7	36.7	611.6	276.6	25.5	617.4
	DG 336 D	63.1	56.7	663.7	332.5	0.4	665.5	242.2	33.3	668.3
	DG 336 E	19.3	28.2	651.6	165.8	57.3	654.1	280.9	15.2	657.6
	DG 337 A	46.4	7.4	30197	314.1	16.7	30238	159.3	71.6	30850
	DG 337 B	43.9	13.9	34878	309.3	17.8	35005	169.7	67.1	35498
	DG 337 C	69.2	10.9	29675	334.5	23.4	29861	182.4	63.9	30383
	DG 337 D	68.5	6.3	34158	335.1	28.4	34418	169.9	60.8	34849
	DG 338 A	313.9	64.3	95439	176.2	19.6	96366	80.4	15.9	97155
	DG 338 B	310.2	62.7	91474	185.7	16.3	92688	89.2	21.3	93540
	DG 338 C	287.8	62.5	88386	195.5	1.2	89272	104.9	27.4	89966
	DG 339 A	244.2	40.5	48822	6.8	32.3	49124	120.8	32.8	49648
	DG 339 B	233.2	13.2	48863	342.6	54.8	48939	134.8	31.9	49652
	DG 340 A	238.4	22.4	64061	20	62.3	64416	141.8	15.5	65024
	DG 340 B	244.6	53.2	50307	40.3	34.3	50427	138.4	11.8	51010
	DG 340 C	239.7	51.6	53748	41.4	36.9	54004	138.2	8.9	54501
	DG 340 D	238.1	53	51466	45.1	36.3	51744	139.7	6.3	52389

** AMS intensity in μ SI units*

Subarea	Sample#	k_{min} dec.	k_{min} inc.	k_{min} int.	k_{int} dec.	k_{int} inc.	k_{int} int.	k_{max} dec.	k_{max} inc.	k_{max} int.
	DG 340 E	249.6	66.7	60552	57.2	22.8	61302	149.1	4.5	61521
III4										
	DG 145 A	352.2	7.1	42861	92.8	55.8	43006	257.4	33.3	43457
	DG 145 B	0.1	12.1	40889	101.8	43.6	41118	258.2	43.9	41569
	DG 146 A	212.5	82.2	62943	326.9	3.3	63333	57.3	7.1	65221
	DG 146 B	285.2	74.1	62700	154.7	10.5	63237	62.5	11.8	64703
	DG 147 A	72.7	19.8	14406	333.7	23.5	14544	198.6	58.5	14576
	DG 147 B	66	25.1	17361	245.1	64.9	17506	335.8	0.3	17553
	DG 147 C	74.2	27.6	13627	170.2	11.3	13726	280.2	59.8	13778
	DG 147 D	67.3	39.3	16321	280.2	45.7	16442	171.9	17	16513
	DG 157 A	28.5	16.1	14443	172.1	70.3	14484	295.3	11.1	14574
	DG 157 B	49.1	59.7	15422	183.6	22.3	15517	281.9	19.4	15683
	DG 158 A	132.2	43.1	36085	40.3	2	39388	308.2	46.8	40448
	DG 158 B	141.2	42.1	37915	232.4	1.3	40787	323.8	47.9	41783
	DG 159 A	289	65.9	32947	118.5	23.9	33392	26.9	3.5	33493
	DG 159 B	307.4	68.2	22979	145	20.9	23308	52.7	6	23442
	DG 159 C	315.6	54.7	30100	139.6	35.2	30444	48.3	1.9	30530
	DG 160 A	106	75.8	666.3	239.9	10	670.6	331.7	10.1	673.2
	DG 160 B	148.3	77.1	662.4	258	4.4	664.8	349	12.1	666.6
	DG 160 C	38.4	38.9	696.9	240.6	48.9	699.7	137.5	11.1	703.1
	DG 160 D	215.9	25.7	639.9	17.8	63.2	641.5	122.4	7.3	643.6
	DG 161 A	29.6	43	13777	231.1	45	13813	130	10.9	13892
	DG 162 A	111.5	8	162240	18.3	22	163950	220.3	66.4	170580
	DG 163 A	161.9	60.2	54239	325.4	28.8	54778	59.3	7.1	55122
	DG 163 B	137.9	67.8	59387	32.1	6.3	60138	299.7	21.2	60418
	DG 163 C	161.6	64.1	58801	0.5	24.7	59463	267.1	7.4	59852
IV3										
	DG 136 A	156.7	69.1	21956	259.9	5	22207	351.7	20.3	22383
	DG 136 B	145.8	63.3	18897	37.3	9.1	19017	303.1	24.9	19237
	DG 137 A	20.3	70.2	12869	248	13.7	13039	154.4	14.1	13247
	DG 137 B	9.3	65.4	9372.5	217.1	22	9542.7	122.9	10.4	9578.8
	DG 138 A	68.1	49.9	32362	176.8	15.1	32606	278.1	36.1	32873
	DG 138 B	58.4	58.9	32356	153.2	2.9	32625	244.9	30.9	32790
	DG 140 A	21.3	30.1	16324	127.1	25.2	16483	249.8	48.9	16514
	DG 140 B	359.3	41.4	17496	119.9	30	17635	232.8	34	17714
	DG 141 A	21.9	63.3	424	287.3	2.3	426.3	196.2	26.5	428.3
	DG 141 B	141.9	38.6	380.8	26.8	28	383.7	271.6	38.7	385.3

** AMS intensity in μ SI units*

Subarea	Sample#	k_{min}			k_{int}			k_{max}		
		dec.	inc.	int.	dec.	inc.	int.	dec.	inc.	int.
	DG 141 C	257.6	79.5	422.8	127.8	6.7	426.1	36.9	8	429
	DG 142 A	354	63.7	23442	155.5	25.1	23735	249	7.3	23932
	DG 142 B	6.3	65.9	21119	146.7	19	21414	241.8	14.2	21509
	DG 143 A	326.3	24.7	46631	218	34.3	50169	84.2	45.4	51199
	DG 151 A	138	6.7	720.5	261.9	78.1	723.4	46.9	9.8	728.1
	DG 151 B	162.5	69.3	635	309	17.5	639	42.4	10.7	643.8
	DG 152 A	125.9	82.5	40878	339.5	6.3	41012	249	4.1	42096
	DG 152 B	156.2	5.1	29958	43.2	77.1	30198	247.3	11.8	30997
	DG 153 B	18.3	31.9	722.4	249.8	45	723.4	127.6	28	725.6
	DG 153 C	97.3	6.2	1028.4	188.2	8.8	1038	332.3	79.2	1041.8
	DG 154 A	297.4	41.5	3322	45.6	19.4	3351.6	154.2	42.2	3377.5
	DG 154 B	78.1	7.3	1530.2	168.4	1.7	1533.9	271.7	82.5	1539.6
	DG 154 C	37.6	44.7	2570.7	148.6	19.9	2578.9	255.4	38.6	2601.9
	DG 154 D	179.7	52.2	2310.8	57.5	22.4	2321.7	314.5	28.6	2331
	DG 155 A	329.4	57.4	646	197.6	23.1	647.7	97.8	21.7	649.9
	DG 155 B	288.1	25.5	565.5	105.7	64.4	567.9	197.6	0.9	571.3
	DG 155 C	248.8	52	604.7	87	36.6	605.3	350.3	8.9	608.1
	DG 155 D	311.7	79	615.2	112	10.4	619.6	202.7	3.6	620.4
IV4										
	DG 156 A	31	61.3	69605	162.3	19.9	70081	259.8	19.8	70688
	DG 156 B	15.1	40.3	74585	164.8	45.5	74972	271.4	15.7	75652
	DG 156 C	11.2	43.3	74310	144.8	36.2	74505	254.9	25.2	75320
	DG 156 D	6.6	57.6	79385	144.2	25.1	79832	243.5	19.1	80717

** AMS intensity in μ SI units*

Appendix D: AARM Data

Outcrop	Sample#	$AARM_{min}$			$AARM_{int}$			$AARM_{max}$		
		dec.	inc.	int.	dec.	inc.	int.	dec.	inc.	int.
2000-901										
	DS 01 A	144.9	24.3	2374.1	23.2	49.4	2455.5	250.2	30.3	2491.8
	DS 02 A	155.8	33.8	876.2	48.9	23.5	964.7	291.3	46.8	1041.2
	DS 02 B	46.8	39.4	2109.8	148.8	14.2	2203.2	254.6	47.1	2289.1
	DS 03 A	169.3	15.6	1816.8	274	42.3	1926.9	63.9	43.6	1994.9
	DS 04 A	145.3	30.2	1842.6	2.8	53.8	2304.2	246.2	18.1	2412.6
	DS 06 A	167	24.8	1717.4	301.1	56.4	1779.3	66.7	21.1	1928.8
	DS 07 A	186.1	47.4	3713.8	277.3	1.1	3786.2	8.4	42.6	4045.4
	DS 07 B	134	36	182.5	261.7	40	217.3	19.9	29.4	222.5
	DS 08 A	245	47.2	3623.6	151.3	3.4	3829.3	58.2	42.7	4039.7
	DS 08 C	171.9	41	1549	75.8	7	1651.1	338	48.1	1741.7
	DS 09 A	221.4	6.5	4518.4	105.1	75.5	4667.7	312.9	12.9	4810.2
	DS 10 A	171.5	41.4	2352.3	78.7	3.2	2462.1	345.1	48.4	2594.3
	DS 10 B	147.7	32.3	5092.2	238.1	0.7	5380.6	329.1	57.7	5506.4
	DS 11 A	231.3	46.5	2814.1	140	1.2	3059.7	48.9	43.4	3388.8
	DS 25 A	301	76.8	2461.6	146.7	11.9	3036.9	55.5	5.5	3325.2
	DS 26 A	190.7	33.8	1250.4	313.9	39.3	1325.5	75.4	32.5	1365.4
	DS 27 A	6.1	3	1601.9	140.6	85.7	2636.6	275.9	3	2773
	DS 30 A	251.3	28.1	2202.5	145.9	26.4	2442.4	20.2	49.6	2582.2
	DS 31 A	194.6	26.3	3448.9	91.9	24.1	3637.7	325.5	53	3668.3
2000-902										
	DS 12 C	159.3	35.7	1736.5	254.1	6.7	1850.2	353.3	53.5	1930.5
	DS 13 A	194.6	43.1	1718.6	103.1	1.6	1755.5	11.5	46.9	1825.1
	DS 15 A	125.7	56.7	1801.6	218.6	1.9	1882.1	309.9	33.3	2023
	DS 16 D	300.5	38.7	1797.6	139.6	49.7	1864.6	38.2	9.5	2021.6
	DS 17 A	133.4	19.7	1775.2	244.1	44.8	1898.1	26.8	38.7	1999
	DS 18 A	140.3	18.8	1763.4	247.6	41.1	1857.4	31.8	42.9	1912.6
	DS 21 A	295.7	35.2	1634	161.2	44.8	1704.8	44.4	24.4	1845.5
	DS 22 A	184	49.6	1230.9	285.4	9.6	1273.6	23.3	38.8	1341.6
	DS 23 A	189	42.8	923.7	69.8	27.8	972.1	318.5	34.5	1027.4
	DS 32 A	220.8	46.8	1681	94.9	28.9	1780	347.1	29.1	1818.1
	DS 32 B	165.3	26.6	1945.6	308.9	58.1	2051.7	66.8	16.3	2144
	DS 33 D	143.9	37	1998.7	333.7	52.6	2106.5	237.5	4.7	2185.6
	DS 33 E	145.6	39	1992.5	297.8	47.5	2079.2	43.8	14.2	2144.2
	DS 35 A	128.6	30.9	1698.9	279.6	55.6	1890.2	30.3	13.6	1964.5
	DS 35 C	147.9	39.5	1700.7	292.1	44.5	1772.6	41.6	18.7	1937.8

AMS intensity in mA/m units

Outcrop	Sample#	$AARM_{min}$			$AARM_{int}$			$AARM_{max}$		
		dec.	inc.	int.	dec.	inc.	int.	dec.	inc.	int.
DS	36 A	160	68	1749.3	44.6	9.9	1786.3	311	19.5	1871.8
DS	36 B	63.3	53.3	1784.1	212.4	32.6	1822.5	312.3	15	1892.9
DS	36 C	148.5	49.6	1645.2	267.3	22.2	1781.2	11.9	31.7	1897.5
DS	39 A	171.5	46.1	1497.2	273.5	11.3	1634.2	13.8	41.7	1693.2
DS	41 B	208.5	14.4	1543.1	74.5	69.7	1615.7	302.1	14	1635.9
DS	43 B	168.2	46.3	1486.3	283	21.9	1545.9	29.8	35.6	1644.9

** AMS intensity in mA/m units*